Phase Field Modeling of Fracture in Rubbery and Glassy Polymers at Finite Thermo-Viscoelastic Deformations

Lisa-Marie Schänzel

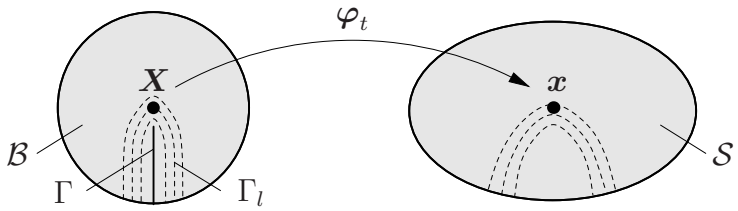

$$\eta\dot{d} = (1-d)\mathcal{H} - [d - l^2\Delta d] \quad \text{with} \quad \mathcal{H} = \max_{s\in[0,t]}\left\langle \sum_a \langle \sigma_a/\sigma_c\rangle^2 - 1 \right\rangle$$

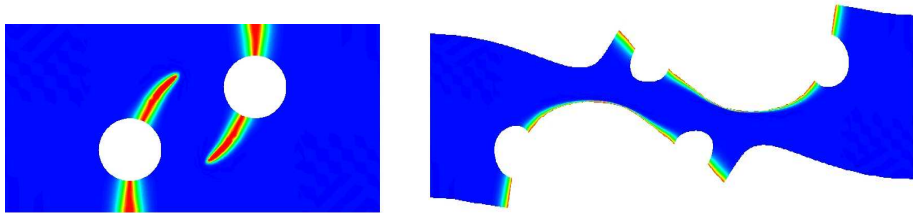

Bericht Nr.: I-31 (2015)
Institut für Mechanik (Bauwesen), Lehrstuhl I
Professor Dr.-Ing. C. Miehe
Stuttgart 2015

Phase Field Modeling of Fracture in Rubbery and Glassy Polymers at Finite Thermo-Viscoelastic Deformations

Von der Fakultät Bau- und Umweltingenieurwissenschaften
der Universität Stuttgart zur Erlangung der Würde
eines Doktor-Ingenieurs (Dr.-Ing.)
genehmigte Abhandlung

von

Lisa-Marie Schänzel

aus Waiblingen

Hauptberichter: Prof. Dr.-Ing. Christian Miehe
Mitberichter: Prof. Dr.-Ing. Alexander Lion

Tag der mündlichen Prüfung: 24. Oktober 2014

Institut für Mechanik (Bauwesen) der Universität Stuttgart

2015

Herausgeber:

Prof. Dr.-Ing. habil. C. Miehe

Organisation und Verwaltung:

Institut für Mechanik (Bauwesen)
Lehrstuhl I
Universität Stuttgart
Pfaffenwaldring 7
70569 Stuttgart
Tel.: +49 (0)711 685-66378
Fax: +49 (0)711 685-66347

ISBN 3-937859-19-5 (D 93 Stuttgart)

Acknowledgements

The work presented in this dissertation was done in the years between 2009 and 2014 during my employment as research associate at the institute of Applied Mechanics (Civil Engineering) at the University of Stuttgart. First, I would like to thank my academic teacher Prof. Christian Miehe who inspired me for engineering mechanics during my studies. He gave me the opportunity to work in his group and to deal with interesting and advanced research topics. I would like to express my gratitude for his scientific support, the fruitful discussions and for his guidance in this work. Additionally, thanks to Prof. Alexander Lion for accepting to serve as the co-referee of this thesis and for his interest in the work.

Next, I want to thank all my colleagues at the Institute for their helpfulness, the collaborations and friendship. In particular, I would like to thank Dominic Zäh for his patience, support and extraordinary helpfulness. Additionally I would like to thank my colleagues Martina Hofacker, Fabian Welschinger, Ilona Zimmermann, Heike Ulmer and Steffen Mauthe for discussions and help in my scientific questions and specifically mention Hüsnü Dal for the great support and the close cooperations. I am grateful to Andreas Krischok and Katharina Grimm whose theses contribute to the results of this dissertation and Jan Kleyersburg for the linguistic revision. Also I would like to acknowledge the financial support provided by Deutsche Forschungsgmeinschaft under grant MI 295-13.

With all my heart, I thank my beloved family for the continuous support during all the years, especially to Bastian. His calmness and confidence inspired me and the motivation during the last year was invaluable.

Zusammenfassung

Ziel dieser Arbeit ist es, einen theoretischen und computerbasierten Zugang zur spröden und duktilen Bruchmechanik zu entwickeln, welcher die Simulation von komplexen Bruchphänomenen bei großen Verzerrungszuständen ermöglicht. Ein zentraler Aspekt dieser Arbeit ist eine umfassende theoretische Untersuchung von Rissphasenfeld-Modellen in der Bruchmechanik, im Speziellen für die Anwendung zur Beschreibung von Brüchen in gummi- und glassartigen Kunststoffen bei großen thermo-viskoelastischen Deformationen. Daneben stellt die Entwicklung neuer Algorithmen für Rissfortschritt und die Erforschung der Vorhersagekraft dieser neuen Methoden einen zentralen Aspekt dar.

Unter *Bruch* versteht man die vollständige oder teilweise Trennung eines ursprünglich ganzen Körpers. Man unterscheidet häufig lineare und nichtlineare Bruchmechanik. eine Vielzahl an Versagenshypothesen ist bekannt, darunter Bedingungen bezüglich der Hauptspannungen, der Hauptdehnungen oder bezüglich eines Vergleichsspannungszustandes.

Im Jahre 1920 legte Griffith einen ersten Grundstein für eine Bruchtheorie von Rissen, indem er die für den Rissfortschritt erforderliche Energie in die Beschreibung einführte und damit das energetische Bruchkonzept schuf. Die Charakterisierung des Rissspitzenzustandes mit Hilfe von Spannungsintensitätsfaktoren geht auf Irvin zurück. Für die Beschreibung von Bruchmechanismen existieren Modelle für sowohl scharfe, als auch unscharfe Rissdiskontinuitäten. Modelle, die scharfe Rissdiskontinuitäten beschreiben, sind unter anderem Kohäsiv-Zonen-Modelle oder Konfigurations-Adaption-Modelle, welche allerdings bei komplexer Rissentwicklung versagen. Computerorientierte Modelle mit unscharfen Rissdiskontinuitäten, sogenannte Rissphasenfeld-Modelle, ermöglichen eine direkte Berechnung von gekrümmten Rissen und Rissphänomenen wie Rissinitiierung, Rissverzweigung oder Rissarrest.

Kunststoffe zeigen aufgrund ihrer molekularen Struktur ein sehr großes Spektrum an sowohl mechanischem Materialverhalten als auch Bruchverhalten. Elastomere zeigen hochgradig nichtlineares Verhalten und einen charakteristischen S-förmigen Spannungs-Dehnungs-Verlauf. Ursache der Elastizität ist überwiegend die Fähigkeit der geknäulten Polymerketten, auf eine Zugbelastung mit einer Streckung bzw. Entflechtung der Ketten zu reagieren. Die Makromoleküle richten sich bevorzugt in Richtung der Belastung aus. Der komplexe Aufbau eines Elastomers aus chemisch vernetzten und sich durchdringenden, verknäulten Makromolekülen führt zu komplexem viskoelastischem Materialverhalten. Bei kleinen Deformationsraten können sich die Moleküle leicht drehen und neu ausrichten, sodass die Verschlaufungen kaum zur Steifigkeit beitragen und sich das Material nahezu elastisch verformt. Mit steigender Deformationsgeschwindigkeit steigt auch die Materialsteifigkeit, da die Umformung der Molekülsegmente erschwert stattfindet.

Die *Bruchfestigkeit* eines Elastomers ist ebenfalls durch die molekulare Struktur bestimmt. Um einen Riss zu erzeugen, müssen die Ketten zwischen den Vernetzungspunten gebrochen werden. Diese Überlegungen resultieren in der Bestimmung einer Rissenergie, die zur Bildung einer Rissfläche nötig ist. Das Bruchverhalten von Elastomeren ist selten spröde, sondern meistens ein zähes Auseinanderreißen des Materials, das unter ständigem Energieverbrauch erfolgt. Abhängig von der Geschwindigkeit des Risszuwachses steigt die Energieaufnahme im Bruch. Dissipative Effekte im Material im Allgemeinen sowie in der Prozesszone an der Rissspitze sind Gründe dafür. Eine Zunahme der Mobilität der Polymermokleküle mit steigender Temperatur bewirkt eine Verringerung dissipativer Effekte und somit eine Verringerung der Rissenergie.

Amorphe Thermoplaste zeigen einen Bereich kleiner elastischer Verzerrungen, in dem nahezu linearelastisches Materialverhalten auftritt. Die Festigkeit wird durch Sprödbruch, Kaltverstrecken, Scherbandausbildung oder Crazing begrenzt. Unter einachsiger Zugbelastung lassen sich manche amorphe Thermoplaste kaltziehen. Nach Erreichen des Fließpunktes bleibt die Last über einen größeren Deformationsbereich nahezu konstant. Eine stabile Einschnürungszone breitet sich über die Probe aus, innerhalb derer die Moleküle gestreckt werden und sich in Richtung der Belastung zu einem Strang ausrichten. Crazing ist ein weiterer plastischer Deformationsmechanismus, welcher die Festigkeit beeinträchtigt. Crazes sind mikroskopisch kleine poröse rissartige Strukturen, bestehend aus Fibrillen und Mikroporen. Sie werden als Vorstufe einer Spannungsrissbildung in Kunststoffen betrachtet. Crazes können zu Rissen wachsen und schließlich zum Bruch des Bauteils führen. Die genannten Deformationsweisen treten nicht nur für verschiedene Polymere auf, sondern auch für ein Polymer bei unterschiedlichen Randbedingungen. Ein Übergang von duktilem zu sprödem Materialverhalten wird durch das Erhöhen der Belastungsgeschwindigkeit und das Herabsenken der Temperatur ausgelöst da durch die veränderte Mobilität der Polymermoleküle die Fließspannung über den Wert der Sprödspannung hinaus steigt.

Die vorliegende Arbeit, zur Untersuchung von Brüchen in gummi- und glassartigen Kunststoffen bei großen thermo-viskoelastischen Deformationen unter Verwendung von Rissphasenfeld-Modellen, ist wie folgt strukturiert:

In Kapitel 2 wird zunächst die Notation, die in dieser Arbeit verwendet wird, vorgestellt. Aufeinander folgend werden die Kinematik eines endlich deformierbaren materiellen Körpers, sowie grundlegende Verformungs- und Spannungsgrößen eingeführt. Die wesentlichen Bilanzgleichungen werden für einen Festkörper zusammengefasst, an dem endliche und eventuell inelastische Deformationen stattfinden.

Kapitel 3 liefert einen Überblick zur Bruchmechanik, wobei grundlegende Konzepte der klassischen Bruch- und Schädigungsmechanik in Kürze wiederholt werden. Es folgt eine Einbettung des regularisierten Rissphasenfeldmodells in den Kontext der allgemeinen Bruchkonzepte. Basierend auf einer geometrischen Interpretation der regularisierten Risstopologie wird ein umfassendes theoretisches Verständnis für das Rissfunktional entwickelt. Eine sehr anschauliche Erläuterung liefert dabei der eindimensionale Fall; anschließend wird das Funktional auf den mehrdimensionalen Fall verallgemeinert. Die Betrachtung resultiert in der Definition eines regularisierten Rissoberflächenfunktionals, das vom Rissphasenfeld abhängt und für verschwindenden Längenskalenparameter zu einer scharfen Risstopologie konvergiert. Dieses Rissfunktional kann als Rissoberfläche selbst betrachtet werden. Die regularisierte Beschreibung von Rissdiskontinuitäten durch ein Rissphasenfeld wird durch eine gradientenbasierte Bilanzgleichung getrieben. Die Theorie ist in den Rahmen gradientenbasierter standarddissipativer Festkörper eingebettet und liefert eine Art Kontinuums-Schädigungs-Bruchtheorie mit spezifischen konstitutiven Funktionen.

Ein grundlegendes Schema zur Kopplung des mechanischen Verhaltens und des Rissverhaltens wird in Kapitel 4 vorgestellt. Es wird ein klarer, rein geometrischer Zugang zur Beschreibung des Rissfortschritts unter Verwendung des Phasenfeldes vorgestellt, indem eine Bilanzgleichung für die regularisierte Rissoberfläche eingeführt wird. Unter Einbeziehung thermomechanischer Kopplung werden drei gekoppelte Bilanzgleichungen vorgestellt. Ein Konzept für spröde und duktile Rissinitiierung und -ausbreitung und deren Regularisierung in Raum und Zeit wird entwickelt. Weiterhin wird eine Zusammenstellung

von energie-, spannungs-, verzerrungs-, und inelastizitätsbasierten Kriterien vorgenommen. Für die Berechnung wird eine gestaffelte Lösungsstrategie vorgestellt, welche auf einem „one-pass“ Operator basiert. Derartige Lösungsalgorithmen sind besonders robust, einfach zu implementieren und bestens geeignet für Probleme im Ingenieurwesen. Die Leistungsfähigkeit und die enormen Möglichkeiten des Rissphasenfeld-Modells werden anhand von komplexen numerischen Beispielen in den jeweiligen Anwendungskapiteln aufgezeigt.

In Kapitel 5 wird das in Kapitel 4 vorgestellte Konzept zur Beschreibung ratenunabhängigen Rissfortschritts in gummiartigen Polymeren unter großen Verformungszuständen spezifiziert. Aus statistischen Größen der Molekülstruktur und der Netzwerkstruktur werden Materialkennwerte, sowohl des elastischen Materialverhaltens als auch der Rissfestigkeit eines idealen Netzwerkes hergeleitet. Der von Griffith eingeführte Materialkennwert der Energiefreisetzungsrate wird zur Herleitung eines energiebasierten Kriteriums zur Beschreibung von Rissinitiierung und -fortschritt verwendet. Die Vorhersagekraft des modularen Konzepts in der Anwendung auf spröde elastische Bruchvorgänge in gummiartigen Polymeren wird anhand von Vergleichen zwischen Simulationsergebnissen und experimentellen Daten belegt.

In Kapitel 6 wird das allgemeine Konzept auf die Untersuchung von Sprödbruch in thermomechanischen Problemen spezifiziert. Im Vordergrund steht die detaillierte Analyse von Wärmeflüssen durch sich gegenüberliegende Bruchflächen, sowie die Untersuchung von konvektiven Wärmeübergängen die auf Bruchflächen entstehen, die im Kontakt zu einem Umgebungsmedium stehen. Um Rissentwicklung differenziert für Zug- und Druckbelastungen beschreiben zu können, wird ein spannungsbasiertes Kriterium zur Beschreibung von Rissinitiierung und -fortschritt entwickelt. Dessen Notwendigkeit wird anhand der Simulation eines klassischen Dreipunktbiegeversuchs gezeigt. Eine Vielzahl von numerischen Simulationen veranschaulicht die entwickelte Theorie der Kopplungsphänomene zwischen den Feldgrößen Deformation, Temperatur und Bruch.

Die Beschreibung von temperatur- und ratenabhängigen Bruchvorgängen in gummiartigen Elastomeren wird in Kapitel 7 vorgestellt. Das thermo-viskoelastische Materialverhalten wird durch die Verwendung mikromechanischer Modelle beschrieben, wobei ein mehrstufiges System aus sekundären Netzwerken angenommen wird. Das raten- und temperaturabhängige Rissverhalten wird durch eine Dämpfung im Rissfortschritt und ein temperaturabhängiges, spannungsbasiertes Kriterium beschrieben. Eine Vielzahl von Simulationen wird mit Experimenten verglichen und belegt die Vorhersagekraft des modularen Konzepts in der Anwendung auf raten- und temperaturabhängige Bruchvorgänge in viskoelastischen, gummiartigen Polymeren.

Kapitel 8 beschreibt Bruchphänomene in amorphen glassartigen Polymeren, welche durch Crazing hervorgerufen werden. Die auftretenden inelastischen Deformationen sind entweder durch Kaltverstrecken (engl. shear-yielding) oder Crazing bestimmt. Ein spannungsbasiertes Kriterium für den Wechsel von shear-yielding zu Crazing wird eingeführt. Als Maß für die Entwicklung von Crazes wird eine skalare plastische Verzerrungsgröße bestimmt. Basierend auf dieser Crazing-Verzerrungsgröße wird ein Kriterium zur Beschreibung von Rissinitiierung und -fortschritt festgelegt. Die Vorhersagekraft des vorgestellten Modells wird schließlich anhand von Beispielen mit rein sprödem oder duktil-sprödem Versagensverhalten aufgezeigt.

Abstract

The goal of this work is to provide a theoretical and computer based model for brittle and ductile fracture mechanics, which enables the modeling of complex fracture phenomena with large deformations. A central aspect of this work is to provide a comprehensive theoretical study of a phase field model of fracture and its application towards the modeling of crack initiation and growth in rubbery and glassy polymers at finite thermo-viscoelastic deformations. The other main aspects are the development of new algorithms for crack propagation and investigations towards the predictive quality of these new methods.

Fracture is the partial or full separation of an object or material into two or more pieces under the influence of stress. A wide variety of failure hypotheses exist, including some related to a principal stresses, principal strains or to an equivalent tensile stress state. In 1920, Griffith introduced the so-called energy release rate for brittle elastic materials which is the energy required for crack propagation and thus, created the energetic fracture criterion. Irvin characterized the crack tip state with the help of stress intensity factors. Fracture mechanic models exist for the description of both sharp and diffusive crack discontinuities. Models describing sharp crack discontinuities include cohesive-zone models or configurational-force-driven models. These, however, suffer in situations with complex crack evolution. In contrast, phase field type diffusive crack approaches are smooth continuum formulations. These avoid the modeling of discontinuities and thus allow a straightforward computation of complex curved crack and fracture phenomena such as crack initiation, crack branching or crack arrest. This work presents the application of a fracture phase field model towards the modeling of crack initiation and growth in rubbery and glassy polymers at finite thermo-viscoelastic deformations.

Due to their molecular structure, polymeric materials show a wide range of both, mechanical material behavior as well as fracture behavior. Rubbery polymers show highly nonlinear elasticity, characterized by the typical S-shaped uniaxial nominal stress-stretch relation. The origin of the characteristic of rubber to undergo large elastic deformations, is the ability of the coiled and entangled polymer chains to elongate and disentangle under tensile stress, such that the macromolecules align in the direction of the applied force. The complex three-dimensional structure of rubbery polymers consists of chemically crosslinked and entangled macromolecules. These take up compact, random configurations, which lead to complex viscoelastic material behavior. Thermoelastic polymers and elastomers show rate dependent material behavior. During slow deformation, the molecular segments can easily rotate and realign. Thus, the entanglements contribute little to the stiffness and the material deforms almost completely elastically. However, with increasing deformation rate, the transformations of the molecular segments can no longer keep up with the rate of defomation. Hence, the stiffness of the material increases.

Macroscopic fracture of rubbery polymers is a result of the failure of the molecular network. Crack propagation takes place when molecular chains whose crosslinks lie on opposite sides of the crack plane are broken. These considerations resulted in the definition of a micromechanically motivated energy release rate, necessary for crack propagation. Crack growth in rubbery polymers is rarely brittle, but mostly a gradual tearing of the material under constant energy consumption, which strongly depends on the velocity of the crack tip. Reasons for this are dissipative effects in both the bulk material and the process zone. An increase in temperature results in an increasing polymer molecule mobility, a decrease of dissipative effects and thus a decrease of energy release rate.

Amorphous glassy polymers exhibit a small range of linear elastic deformation. The strength is limited by brittle fracture, cold drawing, shear yielding or crazing. Cold drawing is characterized by a small range of linear elastic strains up to the yield point, followed by a large amount of plastic deformation during which, the stress remains almost constant. Macroscopically a stable neck spreads over the object in question within which the molecules are stretched and align in the direction of the applied force. Crazing is also termed dilatational normal stress yielding and is a plastic deformation mechanism. Crazes consist of dense arrays of fibrils separated by voids. They can grow in width and length until the fibrils break down, which eventually leads to structural failure. Shear yielding and crazing are not completely independent, nor do they exclude each other. Changing the temperature or the rate of deformation and thus modifying the mobility and reaction of the molecules, causes a change of yield stress and brittle fracture stress. Thus a transition from ductile to brittle material response can take place.

As mentioned before, this work presents the application of a fracture phase field model towards the modeling of crack initiation and growth in rubbery and glassy polymers at finite thermo-viscoelastic deformations. It is structured as follows:

Chapter 2 outlines a short introduction to nonlinear continuum mechanics and the notation used in this work. Subsequent to the description of the kinematics of a material body at finite deformations, basic stress measures and heat flux are examined. Finally, some essential balance equations of a solid body undergoing finite, possibly inelastic deformations, are summarized.

The aim of Chapter 3 is to give an introduction to the fundamental features of fracture mechanics representing the basis of the phase field model of fracture. A geometric descriptive motivation is introduced for the one-dimensional setting and then generalized to the multidimensional case, resulting in the definition of a regularized crack surface functional dependent on the crack phase field. This crack functional is considered as the crack surface itself. The surface functional converges to a sharp crack topology when the length scale parameter tends to zero. The proposed model describes a crack discontinuity in a regularized method, using a crack phase field which is driven by a gradient type balance equation. The theory is embedded into the framework of standard dissipative solids and results in a continuum damage type theory of fracture with specific constitutive functions.

A modular scheme for the coupling of the mechanical material response and the phase field model of fracture is presented in Chapter 4. A purely geometric approach for the description of crack propagation is presented by introducing a balance equation for the regularized crack surface in terms of the regularized crack surface functional. The model bases on the introduction of a set of balance equations, describing the three field problem of finite thermo-viscoelasticity, coupled with fracture. A concept for brittle and ductile crack initiation and propagation, as well as its regularization in space and time is developed. The key aspect is the definition of a criterion for crack initiation and crack growth. Therefore, a summary of energy, stress, strain and inelasticity based criteria is presented. A staggered scheme is introduced for the numerical solution, which bases on a one-pass operator split. Such a solution algorithm is extremely robust, easy to implement and ideally suited for engineering problems. The performance and the vast possibilities of the phase field fracture model at large strains, are demonstrated by means of complex numerical examples in the respective chapters dealing with application.

In Chapter 5, the framework is specified for the description of brittle, rate independent crack propagation in rubbery polymers at large deformations. The approach accounts for micromechanically based features of both the elastic bulk response, as well as the crack toughness of idealized polymer networks. The statistically based fracture toughness of polymer networks is reviewed and an energetically based crack driving force is derived. The crack driving state function is governed by the micromechanically based critical energy release rate. The predictive capability of the modular concept, applied to brittle fracture in elastic rubbery polymers, is successfully demonstrated by comparison of simulation results and experimental data.

Chapter 6 deals with the specification of the general framework towards fully coupled thermomechanical problems at large strains. An important aspect is the constitutive modeling of degrading heat fluxes across cracks. This includes the generation of convective heat exchanges based on additional constitutive functions defined at the crack faces. The introduced maximum principal stress criterion with a critical fracture stress threshold, differentiates between tensile and compression regions. It can be extended towards complex anisotropies in material modeling. The need for such a criterion is demonstrated by means of a classic three point bending test. Various numerical simulations illustrate the developed theory and the coupling in the multifield context.

A model for rate and temperature dependent failure of viscoelastic rubbery polymers is presented in Chapter 7. Viscoelasticity in rubbery polymers is modeled on a micromechanical basis. A hierarchy of superimposed networks related to the ground state network by entanglement mechanisms is associated with the modeling of the overstress response. The rate and temperature dependent crack growth is considered by viscous damping in the fracture phase field evolution equation and by a temperature dependent, stress based fracture criterion. A variety of simulations demonstrates the predictive capability of the modular concept, applied to rate and temperature dependent failure in viscoelastic rubbery polymers.

Chapter 8 describes crazing induced fracture in amorphous glassy polymers. The ductile response is either determined by diffuse shear zones, formed by shear yielding or by crazing. The competition between shear yielding and crazing is controlled in terms of a stress based transition criterion. A scalar state variable is introduced as a measure of accumulated viscoplastic flow due to crazing. From a micromechanical point of view, this models the cumulative distribution of broken fibrils. A ductile fracture criterion based on a critical accumulated viscoplastic flow is introduced. It is devised, such that the crack phase field develops solely under craze flow. Finally, we demonstrate the capability of the phase field model for crazing induced fracture with representative boundary value problems. The model successfully captures the temperature dependent ductile to brittle failure mode transitions.

Contents

1. Introduction

The prediction of failure mechanisms in polymeric materials is of utmost importance for engineering applications. The forecasting of crack growth in rubber products such as tires, seals, conveyor belts and base insulations of buildings is a major issue. Furthermore, the prediction of failure of glassy polymers in applications ranging from micro-electronics over housewares to aerospace components is of high interest. The goal of this work is to provide a phase field model for brittle and ductile fracture mechanisms, which is capable of modeling complex fracture phenomena with large deformations. The emphases are on the description of brittle crack propagation in elastic rubbery polymers and thermoelastic solids. Besides this, the main focus is on the rate and temperature dependent failure of viscoelastic rubbery polymers and crazing induced fracture in amorphous glassy polymers.

1.1. Motivation and State of the Art

Any polymeric material is created from simple molecules, monomers, which are polymerized to long chain molecules. Polymer molecules are either in a crystalline or random amorphous structure. *Amorphous glassy polymers* are made up of molecules in random configurations, which build a network via entanglements. Polymers of this group are termed thermoplastic and are essentially viscous liquids, however they are in solid state at room temperature. By heating, the material can be melted and the solid state turns to a viscous liquid state in which the material can easily be reshaped and formed or welded. Examples of the group of glassy thermoplastic polymers are Polycarbonate PC or Poly(methyl methacrylate) (PMMA). *Thermoplastic elastomers* are viscoelastic soft solids at room temperature. However, as thermoplastic glassy polymers, they can be melted to a viscous liquid state, which is attractive for manufacturing processes. Block co-polymers consisting of polystyrene blocks and rubber blocks, for example SBS are composed of styrene-butadiene-styrene molecules.
Chemical crosslinking creates a second class of polymeric materials, called *thermosets*. A fixed molecular network is generated by bonding the long molecules together at relatively large distances. Thermosets or thermosetting resins, for example epoxy resin, are solid at room temperature and the material is in fixed shape and size after crosslinking. Thermosets are used as the matrix component in many fiber reinforced plastics such as glass reinforced plastic and graphite reinforced plastic. Elastomers or *rubbery polymers* are thermosets which are viscoelastic soft solids at room temperature. Examples are natural rubber or polybutadiene, among many others. After crosslinking by vulcanization, thermosets cannot be melted or reshaped. For a deeper insight see Gent [84], Ashby & Jones [16] or Strobl [203].

1.1.1. Elasticity of Rubbery Polymers. *Rubbery polymers* consist of long flexible molecules that are in continuous Brownian motion at room temperature due to thermal agitation. As a result, the rubber molecules take up a variety of random configurations. The molecules are highly flexible and therefore highly extensible; upon loading, the molecules elongate and disentangle. On the other hand, in the absence of an external force they adopt rather compact, random configurations; when the load is released, they spring back to random shapes as fast as their thermal motion allows. This is the origin of the unique ability of rubber to undergo large elastic deformations and recover completely. To give rubber a permanent shape, the molecules are tied together by a few chemical bonds in a process known as crosslinking or vulcanization. Molecular sequences or strands between

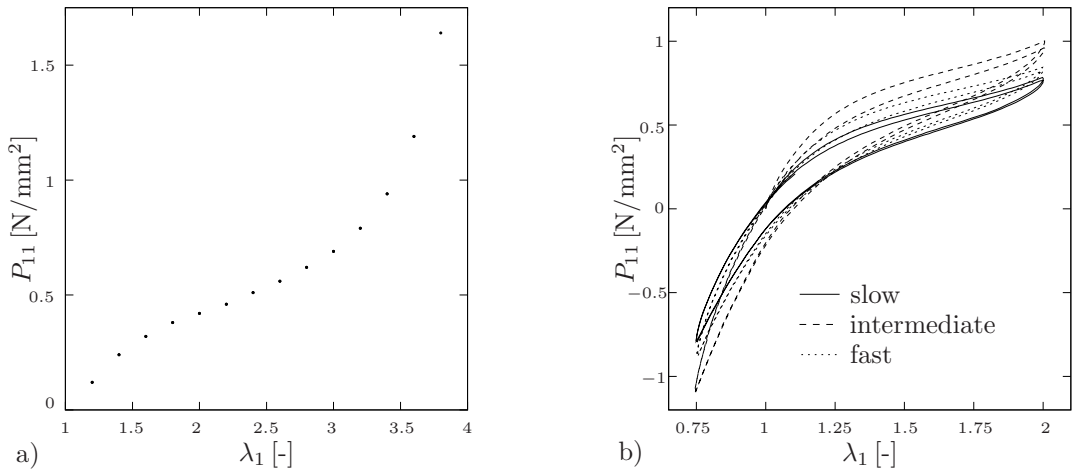

Figure 1.1: a) typical S-shaped material response in uniaxial tension, see Miehe et al. [158]. b) Rate dependent hysteresis loops of stress cycles from Miehe & Göktepe [152]

sites of interlinking still move about and change their shape, but they are now subject to the restrictions that the crosslinks remain in more or less stationary positions. Network strands are formed both by crosslinking and by molecular entanglement. Even though the original rubber molecules are very long (typically 10,000 to 50,000 main chain atoms), the degree of crosslinking is rather narrow, typically within one crosslink site for every 100 to 1,000 main chain atoms. On the other hand, long polymer molecules tend to entangle with each other, forming temporary physical crosslinks at a spacing, characteristic to the particular molecular structure. This spacing ranges from one crosslink site for 250 to 1,000 main chain atoms. For further details the reader is referred to Gent [84]. Practically, rubbery polymers are incompressible materials possessing the volumetric stiffness nearly four powers of ten larger than the shear modulus, while they are readily deformable in shear. The highly nonlinear elasticity is characterized by the typical S-shaped uniaxial nominal stress-stretch relation, see Figure 1.1a from Miehe et al. [158].

The dominant contribution to the *elastic bulk response* of rubbery polymers is due to changes in conformations of network constituents, yielding the so-called entropy elasticity theory. Entropic elasticity of chain molecules is well established in the context of statistical mechanics, see Kuhn [128, 129], Kuhn & Grün [130],Treloar [216], Flory [70] and references cited therein. A vast number of constitutive models for the macroscopic elastic response of rubbery polymers has been developed, see Boyce & Arruda [33] and Miehe et al. [158] for a literature overview. *Purely phenomenological macro-models* involve invariant or principal stretch based isotropic free energy functions Recently, Lion & Johlitz [139] suggested ageing in an invariant based model. They often base on polynomial functions, whereas the most advanced formulations are those of Ogden [174, 175]. However, the direct relation to the molecular structure of the material is missing. This is achieved by *micromechanically based network models*, such as the three chain model proposed by James & Guth [115], the eight chain model suggested by Arruda & Boyce [12] and the affine full network models considered in Treloar [215], Treloar & Riding [217] and Wu & van der Giessen [226]. It is well known that the affinity assumption between microscopic and macroscopic deformation is not in agreement with experimental observations, in particular in the range of large deformations. Consequently, Boyce & Arruda [33] argued that the eight chain model yields more realistic results

than the seemingly more precise affine full network models. A further improvement provides the non-affine microsphere model proposed in MIEHE ET AL. [158], which allows a flexible modeling of the locking stretches in multi-dimensional deformations. The above mentioned micromechanically based models consider idealized polymer networks with free motions of its single chains. In real networks, topological constraint effects arise due to entanglements. Molecular based statistical approaches, that incorporate these effects are *constrained junction theories* and *constrained segment theories*. The constraint junction theories formulate the topological constraints around the junctions. The constraint junction part of the model proposed by FLORY & ERMAN [71] was used by BOYCE & ARRUDA [33] to improve the performance of the eight chain model. The constraint segment approach is consistent with the so called tube model of rubber elasticity, see DEAM & EDWARDS [55], EDWARDS & VILGIS [64], HEINRICH & STRAUBE [106] and HEINRICH & KALISKE [105]. In MIEHE ET AL. [158], the microsphere model was equipped with a characteristic tube deformation that is linked to the macroscopic deformation.

1.1.2. Viscoelasticity of Rubbery Polymers. The assumed elastic behavior, that the relation between load and displacement is fully reversible, is an idealization. In practice, deviations from such ideal elastic behavior are to be expected. The differences between the loading and unloading curves reflect mechanical energy losses from internal dissipation processes, such as viscous flow or internal bond breaking. Introduction to viscoelastic material response can be found in BHOWMICK [25], or EIRICH [65] among others. The main cause of the viscoelastic response of rubbery solids is the internal viscosity between molecular chains. In the three-dimensional network of the rubbery solid, small segments of a molecule move to new positions as a result of random Brownian motions from thermal agitation. Below the glass transition temperature T_g the molecular strands appear to be stationary and the material becomes glass stiff. At a temperature T above T_g, the response of an elastomer depends on the temperature. Macroscopically one observes a decreasing elastic stiffness with increasing temperature. This observation results from the internal viscosity between molecular chains, which is strongly affected by temperature through the thermally activated Brownian motions. With increasing temperature, the frequency of molecular jumps increases strongly. The segments of the chains can slip more easily in relation to each other. When the temperature is raised, the rate of Brownian motion increases. The characteristic response of molecular segments speeds up and the elastic stiffness and the viscosity decrease. At a temperature T above T_g, the response of a rubbery solid also depends on the rate of deformation. When subjected to a stress cycle, the stress-strain curve is a hysteresis loop instead of a reversible curve, with the deformation lagging behind the stress, see Figure 1.1b from MIEHE & GÖKTEPE [152]. Typically, dynamic mechanical analyses with oscillating cyclic stresses are performed, to derive stress-strain relations and dissipation measures that characterize the material through the dynamic storage and loss modulus see Figure 1.2. During deformation at low rates (frequency in oscillation test) molecular segments respond readily, the dynamic modulus is low and nearly constant. As the frequency is raised, the molecular segment transformations are retarded in relation to the applied deformation and load is carried through the entanglement sites. Hence, the stiffness of the material increases. Eventually, the molecules can no longer keep up with the rate of deformation and the polymer material theoretically becomes glass hard. Figure 1.2 from BHOWMICK [25] shows the dynamic storage modulus measured over a range of frequencies at various temperatures. The increasing stiffness with increasing frequency is clearly visible, as well as the effect of

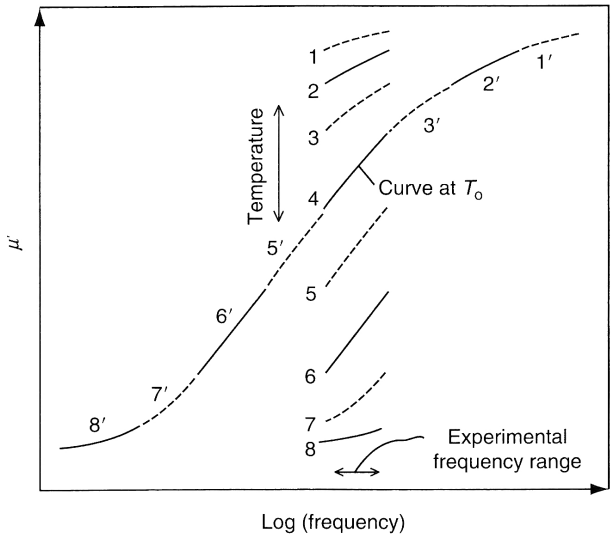

Figure 1.2: Construction of a master curve of dynamic modulus μ' versus log(frequency) by lateral shifting of experimental results made over a small frequency range but at several different temperatures, taken from Bhowmick [25].

temperature on the storage modulus which increases with decreasing temperature. For thermorheologically simple materials, it is observed that a change in temperature from T_0 to T is equivalent to changing the frequency, see also Gent [84].

Finite viscoelasticity has been investigated by many researchers from different viewpoints. Comprehensive reviews are outlined in the textbooks Ferry [68], Tanner [206], Doi & Edwards [56], Findley et al. [69] and Drozdov [60]. Purely phenomenological approaches to finite viscoelasticity usually introduce *tensorial* stress or strain like internal variables. The recent formulations Simó [200], Govindjee & Simó [87], Holzapfel & Simó [109], Lion [137] and Kaliske & Rothert [117] use internal variables of the *stress type*. These approaches exploit the structure of linear viscoelastic standard solids and can be interpreted as special cases of the general theory of a simple materials with fading memory such as outlined in Truesdell & Noll [218] and Coleman & Noll [47]. The K-BKZ model of Kaye [121] and Bernstein et al. [24] represents a class of optimal single-integral models of viscoelasticity, see Tanner [207] for an comprehensive review. Besides these theories employing stress-like internal variables in the form of convolution integrals, the formulations of Sidoroff [198], Lubliner [143], Lion [138], Keck & Miehe [122], Bergström & Boyce [23], Reese & Govindjee [187], Haupt & Sedlan [104] and Reese [186] use the multiplicative *split of the deformation gradient* into elastic and inelastic parts. The inelastic part enters the formulation as a *strain-like* tensorial state variable in the sense of Coleman & Gurtin [46]. A different kinematic approach to viscoelasticity, based on the introduction of evolving *viscous metric tensors* as internal variables, was outlined by Miehe & Keck [154] and Miehe et al. [158]. This framework avoids a priori difficulties of the above mentioned intermediate configuration theories, in particular questions concerning a separate modeling of viscous rotations.

Some of the above mentioned approaches are purely phenomenological while others are motivated by the micromechanical material structure. Several molecular theories for the modeling of viscous behavior of molten polymers and physically cross linked concentrated polymer networks were proposed in the last decades. Following Wientjes et al. [223],

these molecular approaches can be classified into three groups. The first group consists of *bead-spring models* conceptually in line with ROUSE [192] and ZIMM [232], see BIRD ET AL. [26] for an extensive review. The *reptation type tube models* proposed by DE GENNES [53] and DOI & EDWARDS [56] can be considered to define a second group of more advanced versions of bead-spring models. Ideas of the reptation model have already been utilized in the above mentioned macroscopic model of BERGSTRÖM & BOYCE [23], see also LULEI & MIEHE [144] and MIEHE ET AL. [158]. The *transient network model* was originally proposed by GREEN & TOBOLSKY [88] and further developed and revised by LODGE [141], YAMAMOTO [230], PHAN-THIEN [181] and TANAKA & EDWARDS [204, 205]. In this third group of micromechanical approaches, polymer segments located between junction points are assumed to be destroyed and reformed during the deformation process. The effect of the chain breakage and formation on the network distribution was investigated in SCOTT & STEIN [193] and FURUKAWA [75]. Basic ideas of transient network models have been employed in the macroscopic models of LUBLINER [143], DROZDOV [61], DROZDOV & DORFMANN [62], REESE [186], among others. Recently, LINDER ET AL. [136] derived the viscous evolution equation by Lubliner from a diffusion problem.

In order to determine temperature dependent mechanical properties of linear viscoelastic materials from known properties at a reference temperature, the *time-temperature superposition principle* is used. A shift factor a_T gives the ratio of internal viscosity at operating to internal viscosity at reference temperature. WILLIAMS ET AL. [224] proposed a simple, empirical function for the shift factor a_T. The so-called *Williams-Landel-Ferry Equation* depends on operating temperature, glass transition temperature and two constants. It is found to be of general validity for most thermorheologically simple elastomers. It applies to temperatures at or above the glass transition temperature only. Alternative functions for the shift factor use the Arrhenius equation, which describes the temperature dependence of reaction rates. It depends on the activation energy associated with the relaxation, the operating and a reference temperature. The Arrhenius equation is typically used to describe behavior below the glass transition region, see GENT [84]. On frequency dependence of thermomechanical response, see LION & PETERS [140].

1.1.3. Fracture Toughness of Rubbery Polymers. Fracture of rubber can initiate from imperfections anywhere in the specimen, either in the interior or on the surface. Cracks may grow under an applied load, often slowly at first, until one or more of them reaches sufficient size for gross fracture to occur. When a rubber-like material is deformed, the network constituents change their conformation and polymer chains align. At a critical load level, the first molecular chain ruptures, inducing the overload and breakage of neighboring chains. Further loading of the body leads to rupturing of additional chains and finally a macroscopic crack is generated. Thus, the occurrence of macroscopic fracture of rubbery polymers is a result of failure within the molecular network. A measure for the fracture toughness is the energy release rate. GRIFFITH [97] originally had the idea that a crack grows, if the energy needed for crack growth is provided by the material. For glass, the basic strength property appears to be the surface energy. For rubber this is not true. When a crack grows, irreversible processes occur in the vicinity of the moving crack tip, leading to energy losses that must be made up for from the available elastic energy. In some elastomers, energy losses may occur in the bulk of the sample under the applied loading. These must also be taken into account. Thus, the energy necessary to propagate a crack at a particular rate is likely to be a characteristic of the rubber itself, even though it greatly exceeds the thermodynamic surface free energy. The characteristic

of the polymer to be strain-crystallizing or amorphous, affects the tear behavior significantly. Tearing of strain-crystallizing elastomers such as natural rubber, occurs typically in a stick-slip manner. The energy release rate does not depend strongly on the rate of tearing. Greensmith & Thomas [91] documented the stick-slip tearing processes in a simple extension tearing test. The force and rate of crack propagation fluctuate in a regular manner, resembling frictional phenomena. The stick-slip process is associated with a decreasing stored energy with increasing rate of crack propagation, see Greensmith & Thomas [91]. The influence of strain crystallization on crack propagation in natural rubber is also discussed in Persson et al. [179] or Kadir & Thomas [116]

This work focuses on non-crystallizing elastomers which exhibit steady tearing behavior. Elastomers that do not crystallize upon stretching are often found to tear in a steady, time dependent manner. Tear measurements on non-crystallizing styrene-butadiene rubber have been carried out and the derived values of energy release rate can be expressed in terms the rate of crack growth. In Figure 1.3a, the experimental results from Gent [82] are visualized, showing the variation of energy release rate g to crack speed v. The energy release rate increases for increasing crack speed. Energy dissipation at the advancing crack in a viscoelastic solid has two contributors, see Persson et al. [179] for a review. According to Müller & Knauss [167] the two contributors can be additively decomposed. The first is associated with the innermost region at the crack tip, where a new macroscopic crack surface is created by cavity forming, stringing, chain pull out or bond breaking. This contribution is related to the basic molecular strength of the material. In their pioneering work, Lake & Thomas [133] proposed a simple *molecular theoretical model*, which determines this critical surface energy in terms of the parameters of the network. As noted by Ahagon & Gent [1], a reasonably good agreement between the theoretical results and experimental measurements can be obtained under near equilibrium conditions, such as reported in Müller & Knauss [167]. The second contribution to energy dissipation at the advancing crack comes from the viscoelastic dissipation in front of the crack tip and in the bulk, see for example Persson & Brener [178] and Kroon [126]. Rupture of rubber has been investigated by many researchers from different viewpoints. Thomas, Greensmith, Gent, Knauss and coworkers [82, 91, 92, 116, 167, 209, 91, 89, 90, 208, 210, 132] performed experiments on tearing of rubber to show that the energy release rate increases with increasing rate of crack propagation. Gent [82] pointed out that the strength properties are greatly enhanced by viscous resistance to internal motion or, more generally, by internal losses. Persson et al. [179] proposed that this results from the molecular network flexibility. During fast loading, the polymer chains do not have enough time to rearrange themselves by thermally activated flipping of the polymer segments. Thus, the external tensile forces acting onto the rubber volume element will distribute themselves rather uniformly in the rubber matrix. A large stress is necessary to break the chemical bonds in the block. On the other hand, for a very low crack tip velocity, the tensile loading is very slow and the polymer chain segments between the crosslinks rearrange themselves such that much of the external load will be distributed on the crosslinked bonds. Thus, the bond breaking at slow rates will start much earlier than at high velocities.

The tear strength of non-crystallizing elastomers depends not only on the rate of crack growth, but also on temperature. These variations closely parallel the variations of viscoelastic properties with rate and temperature. Gent & Lai [83] performed fracture tests on simple unfilled rubbery solids at various temperatures and measured the energy release rate and the crack speed, see Figure 1.3b. As the test conditions change from low

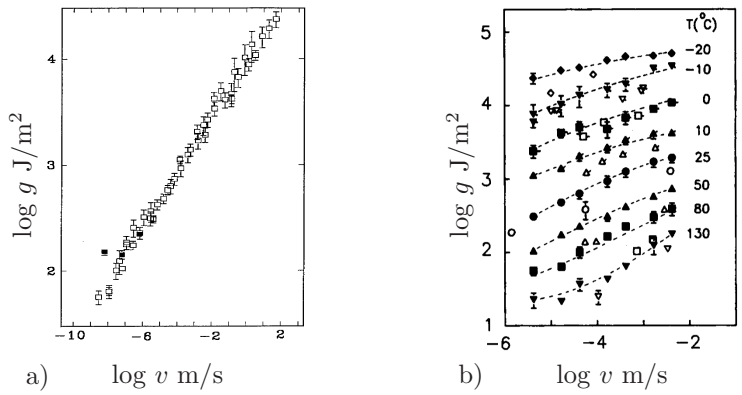

Figure 1.3: Experimental results from Gent [82] and Gent & Lai [83] on the variation of energy release rate g with crack speed v and temperature.

tear speeds at high temperatures to high tear speeds at low temperatures, the values of the energy release rate are seen to change by a large factor, see Fig. 1.3b. The change in energy release rate shows that the internal dissipation from segmental motion governs the strength of elastomers and that reduced molecular mobility is associated with high strength. At low crack speeds and high temperatures the viscous energy dissipation is minimized and the strength approaches a lower limit g_c. The values of energy release rate appear to be superposeable by horizontal shifts using time-temperature shift factors. Figure 1.3a shows the shifted experimental values from 1.3b. In this context, the shift factor a_T gives a relation between temperature and crack speed. The crack speed is multiplied by the shift factor a_T to obtain the master curve containing high and low crack speeds that cannot be easily obtained experimentally. In Bhowmick [25] it is observed that the wide range of tear rates needed to cover the complete rubber to glass transition, is about twice as large as the corresponding range of frequency needed to cover the change in the dynamic modulus function. Molecular rearrangements are apparently much slower in fracture than under an imposed deformation.

Studies from Carbone & Persson [43] and Persson & Brener [178] predict the viscoelastic contribution to fracture toughness numerically. Recently, some time dependent cohesive models were introduced in Rahul-Kumar et al. [184, 185], Nguyen & Govindjee [172], Elmukashfi & Kroon [66] with rate dependent cohesive laws of traction separation. Kroon [126] introduced a model for steady-state crack growth in rubber-like solids, where the crack speed is a primary variable to a steady problem. Geissler et al. [78], Geissler & Kaliske [77], Nase et al. [170] analyzed peeling tests with cohesive zone modeling, Netzker et al. [171] analyzed global energy balance during stable crack propagation. Grellmann et al. [94] covers lecture notes on fracture mechanics of elastomer blends. Nguyen et al. [173] introduced a material force method for inelastic fracture. Experiments from Gent & Schultz [80], Gent [82], Maugis & Barquins [147] and theoretical investigations D'Amico et al. [51], Greenwood [93], de Gennes [54] Carbone & Persson [43, 42], Persson & Brener [178], Baney & Hui [17] show that the energy release rate depends on the crack tip velocity and on the temperature. However, a three-dimensional thermodynamically consistent thermomechanically coupled continuum model is of high importance for modern computational material design.

1.1.4. Finite Viscoplasticity of Amorphous Glassy Polymers. Amorphous glassy polymers exhibit strong rate and temperature dependent mechanical responsive-

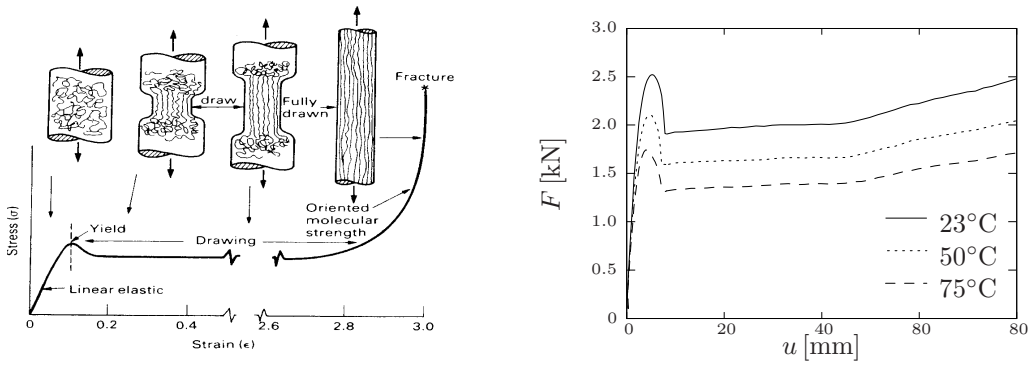

Figure 1.4: a) Schematic true stress-strain diagram of an amorphous glassy polymer under tension taken from Ashby & Jones [15]. The picture clearly shows the molecular re-arrangements taking place when the material is drawn, yielding a frozen reversible plastic deformation. b) Temperature dependence of polycarbonate under isothermal uniaxial tension results in a drop in yield stress, see Miehe et al. [162].

ness, accompanied by volume preserving inelastic deformations. The elasto-viscoplastic response stems from the inherent disordered microstructure of the material, that is formed by polymer chains in a frozen state. The basic deformation mechanism of amorphous glassy polymers is of entropic nature. The molecules, initially forming an amorphous agglomerate, can be rearranged in such a way that the flow orients the strings. The molecules thus align up to a certain level, building a fibrous structure, see Figure 1.4a. The stress-strain curve can be separated into a reversible range of linear elastic strains up to the yield point. The polymer yields at high stresses, followed by a strain softening at moderate strains. A drawing region follows, characterized by a large increase of plastic strain during which the stress remains almost constant. A strain hardening is observed at large strains when the drawing is complete. Bauwens-Crowet et al. [20] measured the yield stress over a wide range of true strain rates and temperatures on polycarbonate and poly(vinyl chloride) in tension tests. Their study revealed that the yield stress in amorphous glassy polymers appears to be dependent on the true strain rate, i.e. a larger imposed strain rate invariably results in a greater yield stress. Furthermore, the yield stress as well as yield strain increase with decreasing temperature, see Figure 1.4b from Miehe et al. [162]. Over the past decades, considerable effort was undertaken to develop three-dimensional constitutive models which account for the finite viscoplastic behavior of glassy polymers. The fundamental works of Argon [7], Boyce et al. [34], Arruda & Boyce [12], Arruda et al. [14] and Hasan & Boyce [102] have been followed, for instance, by Wu & van der Giessen [226, 227, 228], Tomita & Tanaka [213], Govaert et al. [86], Anand & Gurtin [3], Miehe et al. [159]. In most of these works, the thermally activated viscoplastic flow is described by the molecular *double-kink theory*, developed by Argon [7] and extended to the three-dimensional setting by Boyce et al. [34]. The framework yields an abrupt transition from a linear elastic to a plastic response. An overview and further developments of advanced flow models for amorphous polymers which account for temperature and strain rate dependencies are given in Richeton et al. [189, 190], however, restricted to the one-dimensional setting. An advanced *free volume flow theory*, developed in Hasan & Boyce [102], takes into account several micromechanically motivated internal variables and makes for a smooth transition. A three-dimensional, thermomechanical extension of this approach is proposed in Miehe et al. [162].

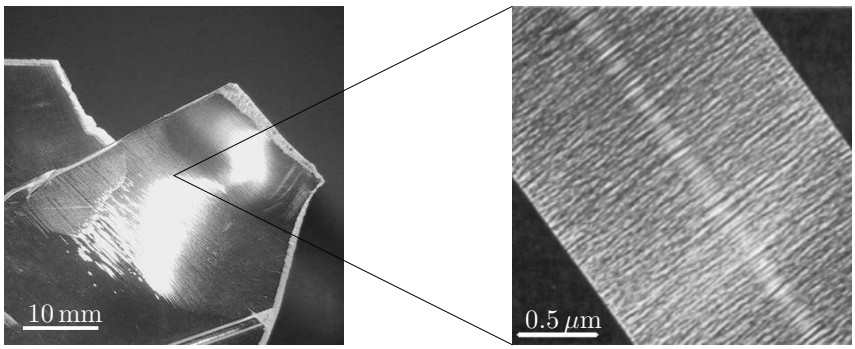

Figure 1.5: Photograph of crazing near a fracture surface in polystyrene from [220]. Micrograph of a single craze from Berger & Kramer [22].

1.1.5. Crazing in Amorphous Glassy Polymers. Crazes consist of dense arrays of fibrils, separated by voids, see Figure 1.5. Crazing can occur due to surface degradation under combined mechanical and chemical action in the interior of a specimen, due to mechanical loading. Alternatively, it can occur at a crack tip. Crazing is also termed dilatational normal stress yielding and is a plastic deformation mechanism. The fibrils in a craze lie perpendicular to the craze-bulk interface and grow in the direction of maximum principal stress in the unoriented material. The plane including the craze fibrils grows in a direction normal to the maximum principal stress. Three phases can be associated with crazing phenomena. An overview will be given on craze initiation, growth and breakdown, respectively in the following sections. For more comprehensive information, we refer to reviews of Kambour [119], Kramer [124], Kinloch & Young [123], Narisawa & Yee [169], Donald [59] and references therein.

Craze Nucleation. Craze nucleation is accompanied by cavitation which later stabilizes in terms of a fibrillar form along the maximum principal stress direction. Despite the abundance of experimental work on the morphology, growth and failure of the crazes, craze initiation remains the most controversial issue and there exists no unified explanation agreed upon this phase. This fact stems from the difficulties associated with monitoring the embryonic crazes having an initial width ranging between $5 - 20\,\text{nm}$. In addition, craze nucleation is very sensitive to surface imperfections, such as scratches or flaws and to internal defects such as air bubbles, voids, dust particles or molecular inhomogeneities, which are very difficult to eliminate during production. These defects provide the stress concentrations necessary for the formation of the initial microvoids, which then turn into the stable fibrillar crazes. This makes the criteria developed from the far field stress measurements questionable. Craze nucleation is enhanced by both tensile, hydrostatic and deviatoric components of the applied stress. Sternstein & Myers [201], Sternstein & Ongchin [202] carried out combined torsion and tension loading tests on specimen, revealing four distinct regions of loading in the principal stress planes. They stated that the stress bias loosens the tight molecular structure, permitting the mean normal stress σ_{vol} to initiate a craze in terms of plastic dilatation. Oxborough & Bowden [176] formulated an alternative criterion for craze initiation in terms of principal strains. Gent [81] suggested that negative pressure locally decreases the glass transition temperature to room temperature and crazing results from cavitation of the rubbery phase under hydrostatic tension. Gent's approach was disproved by further investigations, which showed that the local decrease in the glass transition temperature is not strong enough to cause

glass to rubber transition at room temperature. ARGON [8] proposed a kinetic equation for craze nucleation, treating the problem of craze nucleation in terms of cavitation. This approach was further advanced by ARGON & HANNOOSH [5] and supported by experimental results. Argon and Hannoosh considered the incipient cavities of cellular form growing under plastic expansion to form embryonic crazes, which finally transform into a stable craze in fibrillar form. The microscopic scenario proposed by KRAMER [124] considers the phenomenon in three steps. First, the local plastic deformation by shear in the neighborhood of a previously existing defect leads to a development of lateral stresses. Secondly, voids nucleate to release the triaxial components of the stress. Finally, the void growth and strain hardening of the intervening polymer ligaments occur, as the molecular orientation proceeds. Owing to the sensitivity of craze nucleation to imperfections and sharp crack tips, ANDREWS & BEVAN [4] have suggested a craze toughness K_{craze} as an intrinsic material parameter for craze nucleation around a notch. This approach has not gained much popularity due to the insensitivity of the critical stress at fracture for crack lengths $a_0 < 1$ mm. This led the researchers to dismiss the fracture mechanics criterion for craze initiation in favor of the void nucleation mechanism. Recently, BUCKNALL [39] criticized the void nucleation mechanism, stating that the craze initiation mechanism in terms of cellular voids and the craze growth mechanism due to meniscus instability contradict each other, since these two mechanisms lead to the coexistence of two most unlikely microstructures. He described the failure mechanism of a high molecular weight glassy polymer in a similar manner to the failure of a fiber reinforced composite, where the failure of the matrix material and the fiber occurs at two different stages. In glassy polymers, the first phase of the fracture occurs due to partial failure in the secondary intermolecular bonds leading to the fibrillar structure, whereas the final failure is dictated by rupture of the intramolecular primary covalent bonds. Then, the fracture toughness is characterized by two parameters K_{craze} and $K_{failure}$ for craze initiation and macroscopic crack initiation, respectively. Bucknall described the misinterpretation of macroscopic cracks with lengths $a_0 < 1$ mm due to the existence of microscopic surface or volume imperfections, randomly distributed in the bulk acting as craze nucleation sites. These lead to the failure mechanisms with identical macroscopic critical stress for craze initiation. Bucknall's explanation seems quite reasonable for crazes nucleating around an existing crack and is less complicated, since it does not require complex stress analysis. It simplifies the overall kinetics and mechanisms with one critical parameter, which is quite attractive for engineering design, as are the various stress based initiation criteria. However, the crazes cannot be completely eliminated even at geometrically smooth surfaces where the linear elastic fracture mechanics does not apply. According to ARGON [10] cavities emerge in cellular form, which eventually turn oblate and form a fibrillar structure, surrounded by continuous voids. Argon's approach is theoretically sound and elaborate. However, it includes many micromechanical parameters whose identification involves considerable effort. While the fracture mechanics approach derives the total energy required to transform a unit surface of uncrazed into crazed matter at a crack or craze tip in a discrete setting, it is better suited as a craze growth, rather than an initiation criterion. Argon's kinetic equation, on the other hand, explains the micro mechanisms leading to this transformation in a continuum setting.

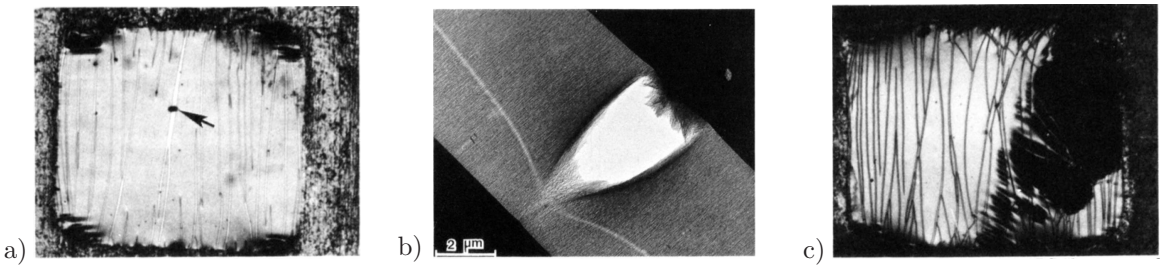

Figure 1.6: Micrographs from YANG ET AL. [231] showing fibril breakdown using a) light microscopy, b) transmission electron microscopy. Micrograph c) shows craze breakdown inducing catastrophic fracture using light microscopy.

Craze Elongation and Widening. Two descriptions exist for the elongation of the craze fibrils. The craze fibrils can grow in length due to drawing of new material from the craze-bulk interface into the craze fibrils, where the stretch of the fibrils remains constant for a given stress level. Alternatively, fibrils grow by a creep mechanism whereby the craze elongates by an increase in stretch and decrease in fibril diameter without significant amount of new material drawn into the craze fibrils. In the former mechanism, the fibrils elongate under constant stretch without significant damage in the fibril matter whereas the latter mechanism precedes the final breakdown of the fibrils. LAUTERWASSER & KRAMER [134] have shown that craze fibrils elongate with constant thickness by cold-drawing from the bulk material at the craze wall. When a craze grows in width, a midrib region becomes clearly visible under an electron microscope. Within the midrib, the fibrils have lower density, which proves the existence of a creep mechanism. The growth of a plane containing the craze fibrils is reasonably well explained in terms of the *meniscus instability* mechanism, which is observed when two rigid plates with a liquid in between are pulled apart. It was first introduced as a craze growth mechanism at a craze front by ARGON [9]. Later on it was elaborated as a detailed model and calibrated with respect to experiments carried out on polystyrene (PS) by ARGON & SALAMA [6]. Unlike emerging crazes, where the cavities have a cellular isolated form, the pores in a stable craze are interconnected. According to the meniscus instability mechanism, the yielded polymer at an air-polymer interface at a craze tip is unstable to perturbations of a well-defined wavelength. The polymer breaks up due to repeated convolutions leading to the topologically correct form of a stable craze in a cyclic and continuous manner. Electron microscopy observations around the craze tip, reveal no cellular voids supporting the meniscus instability as a driving mechanism for craze widening, see DONALD & KRAMER [58], KRAMER [124].

Craze Breakdown. Crazes grow both in width and length, until somewhere within one craze the fibrils break down to form large voids see Figure 1.6a,b. YANG ET AL. [231] investigated the failure events in a large number of independent film specimens under a reflected light microscope. They have shown that craze fibril breakdown is a statistical event and obeys a Weibull distribution which can be characterized by two additional material parameters. On further loading, a large void can become a sub-critical crack, which grows and leads to catastrophic fracture. Thus, fibril breakdown is of crucial importance for fracture. A variety of craze breakdown criteria exist, including some related to a craze opening displacement, a critical inelastic strain or to a fracture toughness. The assumption of a critical craze opening displacement is based on the interferometric measurements carried out by DÖLL [57] and depends on various factors such as molecular weight and

crack tip velocity. The critical crack tip opening displacement is incorporated into cohesive zone type discrete models e.g. Tijssens et al. [211, 212]. A critical inelastic strain criterion is utilized in Gearing & Anand [76], whereas Brown [38] and Hui et al. [111] made use of a fracture toughness criterion.

1.1.6. Phase Field Modeling of Fracture. Fracture is the partial or full separation of an object or material into two or more pieces under the influence of stress. The prediction of crack initiation and propagation through computational models is of great importance for engineering applications. Theoretical foundations of the classical theory of brittle fracture in solids are outlined in the works of Griffith [95, 96], Irwin [112, 113] and Barenblatt [18]. Following the energetic considerations of Griffith, a crack propagates if the available energy to extend a crack reaches a critical value, the so called critical energy release rate. For brittle materials like glass, it is the thermodynamic surface energy. In 1957, Irwin [112] proposed the concept of a stress intensity factor K. Instead of considering the energy of a whole system with a given crack, it describes the intensity of the stress in the neighborhood of a crack tip as a function in terms of the crack geometry and the loading. These theories provide criteria for crack propagation. However, they all require a precracked specimen as they are unable to predict crack initiation in an ideal body.

Fracture mechanic models exist for both the sharp and diffusive description of crack discontinuities. Models describing sharp crack discontinuities include cohesive-zone models or configurational-force-driven models. The numerical implementation of sharp crack discontinuities based on interface finite element formulations, or on element/nodal enriched finite elements, suffers in cases of three-dimensional applications with crack branching. Successful computational formulations with adaptive interface elements are Xu & Needleman [229] Camacho & Ortiz [41], Pandolfi & Ortiz [177], Geissler et al. [79], Kaliske et al. [118] and Miehe & Gürses[153, 99], with the latter describing the modeling of configurational-force-driven sharp crack propagation. Finite element formulations with embedded discontinuities, which allow velocity-based crack branching, were recently outlined in Armero & Linder [11] and Linder & Armero [135].

Smooth continuum formulations avoid the modeling of discontinuities and allow a straightforward computation of complex curved cracks and fracture phenomena such as crack initiation, crack branching or crack arrest. The diffusive approximation of a sharp crack surface topology in the solid, is governed by a scalar auxiliary variable. This variable is a phase field, which interpolates between the intact and the broken state of the material. To numerically deal with such problems, smooth approximation functionals may be defined. These may be obtained from the original variational problem via Γ-convergence, see Dal Maso [49]. Variational methods for brittle fracture mechanisms based on Griffith-type energy minimization were suggested by Francfort & Marigo [72], see also Bourdin et al. [30], Dal Maso & Toader [50] and Buliga [40]. The regularized setting of their framework, considered in Bourdin et al. [29, 31], is obtained by Γ-convergence, inspired by the work of image segmentation by Mumford & Shah [166]. The reader is referred to Ambrosio & Tortorelli [2] and the reviews of Dal Maso [49] and Braides [36, 37] for details on Γ-convergent approximations of free discontinuity problems. Recently outlined phase field approaches to brittle fracture based on the classical Ginzburg-Landau type evolution equation as reviewed in Hakim & Karma [101] are conceptually similar, see also Karma et al. [120] and Eastgate

ET AL. [63]. These models may be considered as time dependent viscous regularizations of the above mentioned rate independent theories of energy minimization. In this context, the reader is referred to the work of KUHN & MÜLLER [127] on particular aspects of the numerical implementation by means of the introduction of exponential shape functions. However, these approaches still have a few drawbacks, which limit their application to particular model problems. The model outlined in HAKIM & KARMA [101] is based on a Ginzburg-Landau-type evolution equation of the fracture phase field, which does not differentiate between energy storage and dissipation. These are very strong simplifications of the physical mechanisms of brittle fracture. The formulation of rate independent diffusive fracture proposed by BOURDIN ET AL. [29] models the irreversibility of the process only on a time-discrete level by setting hard Dirichlet-type conditions on the phase field. Furthermore, both existing phase field models consider energy release driven fracture in both tension and compression. Clearly, these fully symmetric formulations are unrealistic for most materials and restricted to the modeling of boundary value problems with tensile stresses in the full solid domain. These approaches are, in general, not thermodynamically consistent and applicable only in particular situations with monotonous loading of arbitrary sub-domains of a fracturing solid. Observe, that most existing phase field approaches to fracture are related to brittle crack propagation in elastic solids. The phase field model, on the other hand, has an enormous potential with respect to the prediction of complex crack phenomena. Energy, stress or strain based criteria for brittle or ductile failure can be included in a modular form. Furthermore, crack growth in multi-physics problems, such as thermo-, electro- or chemo-mechanical problems can be directly modeled with a fracture phase field. The key advantage is that the constitutive formulation of the crack propagation in regularized phase field models is related to the three-dimensional bulk response. The recent works of MIEHE ET AL. [161, 160], MIEHE & SCHÄNZEL [156], BORDEN ET AL. [27, 28], PHAM ET AL. [180] and VERHOOSEL & DE BORST [221] outline a general thermodynamically consistent framework for the phase field modeling of crack propagation at small strains and serve as a basis for the development of phase field fracture approach at large strains.

1.2. Scope and Outline

A central aspect of this work is a comprehensive theoretical study of phase field formulations in fracture mechanics, especially towards the application for polymeric materials. In addition, the development of new algorithms for crack propagation and the investigation of the predictive quality of these new methods are central aspects. Chapter 2 outlines a short introduction to nonlinear continuum mechanics and the notation used in this work. Subsequent to the description of the kinematics of a material body at finite deformations, basic stress measures and heat flux are examined. Finally, some essential balance equations of a solid body undergoing finite, possibly inelastic deformations, are summarized.

The aim of Chapter 3 is to give an introduction to the fundamental features of fracture mechanics representing the basis of the phase field model of fracture. A geometric descriptive motivation is introduced for the one-dimensional setting and then generalized to the multidimensional case, resulting in the definition of a regularized crack surface functional dependent on the crack phase field. This crack functional is considered as the crack surface itself. The surface functional converges to a sharp crack topology when the length scale parameter tends to zero. The proposed model describes a crack discontinuity in a

regularized method, using a crack phase field which is driven by a gradient type balance equation. The theory is embedded into the framework of standard dissipative solids and results in a continuum damage type theory of fracture with specific constitutive functions.

A modular scheme for the coupling of the mechanical material response and the phase field model of fracture is presented in Chapter 4. A purely geometric approach for the description of crack propagation is presented by introducing a balance equation for the regularized crack surface in terms of the regularized crack surface functional. The model bases on the introduction of a set of balance equations, describing the three field problem of finite thermo-viscoelasticity, coupled with fracture. A concept for brittle and ductile crack initiation and propagation, as well as its regularization in space and time is developed. The key aspect is the definition of a criterion for crack initiation and crack growth. Therefore, a summary of energy, stress, strain and inelasticity based criteria is presented. A staggered scheme is introduced for the numerical solution, which bases on a one-pass operator split. Such a solution algorithm is extremely robust, easy to implement and ideally suited for engineering problems. The performance and the vast possibilities of the phase field fracture model at large strains, are demonstrated by means of complex numerical examples in the respective chapters dealing with application.

In Chapter 5, the framework is specified for the description of brittle, rate independent crack propagation in rubbery polymers at large deformations. The approach accounts for micromechanically based features of both the elastic bulk response, as well as the crack toughness of idealized polymer networks. The statistically based fracture toughness of polymer networks is reviewed and an energetically based crack driving force is derived. The crack driving state function is governed by the micromechanically based critical energy release rate. The predictive capability of the modular concept, applied to brittle fracture in elastic rubbery polymers, is successfully demonstrated by comparison of simulation results and experimental data.

Chapter 6 deals with the specification of the general framework towards fully coupled thermomechanical problems at large strains. An important aspect is the constitutive modeling of degrading heat fluxes across cracks. This includes the generation of convective heat exchanges based on additional constitutive functions defined at the crack faces. The introduced maximum principal stress criterion with a critical fracture stress threshold, differentiates between tensile and compression regions. It can be extended towards complex anisotropies in material modeling. The need for such a criterion is demonstrated by means of a classic three point bending test. Various numerical simulations illustrate the developed theory and the coupling in the multifield context.

A model for rate and temperature dependent failure of viscoelastic rubbery polymers is presented in Chapter 7. Viscoelasticity in rubbery polymers is modeled on a micromechanical basis. A hierarchy of superimposed networks related to the ground state network by entanglement mechanisms is associated with the modeling of the overstress response. The rate and temperature dependent crack growth is considered by viscous damping in the fracture phase field evolution equation and by a temperature dependent, stress based fracture criterion. A variety of simulations demonstrates the predictive capability of the modular concept, applied to rate and temperature dependent failure in viscoelastic rubbery polymers.

Chapter 8 describes crazing induced fracture in amorphous glassy polymers. The ductile response is either determined by diffuse shear zones, formed by shear yielding or by crazing. The competition between shear yielding and crazing is controlled in terms of a stress based transition criterion. A scalar state variable is introduced as a measure of accumulated viscoplastic flow due to crazing. From a micromechanical point of view, this models the cumulative distribution of broken fibrils. A ductile fracture criterion based on a critical accumulated viscoplastic flow is introduced. It is devised, such that the crack phase field develops solely under craze flow. Finally, we demonstrate the capability of the phase field model for crazing induced fracture with representative boundary value problems. The model successfully captures the temperature dependent ductile to brittle failure mode transitions.

2. Fundamentals of Continuum Mechanics

This chapter outlines a short introduction to non-linear continuum mechanics and the notation used in this work, based on the lecture notes MIEHE [148, 149]. Subsequent to the description of the kinematics of a material body at finite deformations, basic stress and heat flux measures are presented. Finally, some essential balance equations of a solid body undergoing finite, possibly inelastic, deformations are considered. This is of interest within the forthcoming chapters. For a more comprehensive treatment the reader is referred to the textbooks of TRUESDELL & NOLL [218], MARSDEN & HUGHES [145] or the publications of CHADWICK [44], HOLZAPFEL [110] and HAUPT [103], among others.

2.1. The Motion, Fundamental Geometric Maps and Deformation Measures

A *material body* B is a physical object consisting of specific physical properties, such as stiffness, density, etc. defining its material behavior. B is composed of infinitely many *material points* $P \in B$ which are mapped to a subset of the Euclidean space $\mathbb{R}^3$ by the placement $\boldsymbol{\chi}_t$ defined by

$$\boldsymbol{\chi}_t := \left\{ \begin{array}{rcl} B & \to & \mathcal{B}_t \in \mathbb{R}^3 \, , \\ P \in B & \mapsto & \boldsymbol{x}_t = \boldsymbol{\chi}_t(P) \in \mathcal{B}_t \, , \end{array} \right. \tag{2.1}$$

see Figure 2.1. It is convenient to relate the motion of a material body at the time t_0 to the *reference configuration* that generally possesses an undistorted stress-free state in the absence of physical forces and is henceforth denoted as $\mathcal{B} \equiv \boldsymbol{\chi}_{t_0}(B)$. Likewise, the configuration of the body at current time t is hereafter denoted as $\mathcal{S} \equiv \boldsymbol{\chi}_t(B)$. The reference and the spatial positions occupied by a material point P within the Euclidean space are labeled by the *reference* coordinates $\boldsymbol{X} := \boldsymbol{\chi}_{t_0}(P) \in \mathcal{B}$ and the *spatial* coordinates $\boldsymbol{x} := \boldsymbol{\chi}_t(P) \in \mathcal{S}$, respectively. In order to describe the *motion* of the solid body in the Euclidean space, we introduce a non-linear *deformation map* $\boldsymbol{\varphi}_t(\boldsymbol{X})$ between $\boldsymbol{\chi}_{t_0}(P)$ and $\boldsymbol{\chi}_t(P)$

$$\boldsymbol{\varphi}_t(\boldsymbol{X}) := \left\{ \begin{array}{rcl} \mathcal{B} & \to & \mathcal{S} \, , \\ \boldsymbol{X} & \mapsto & \boldsymbol{x} = \boldsymbol{\varphi}_t(\boldsymbol{X}) := \boldsymbol{\chi}_t \circ \boldsymbol{\chi}_0^{-1}(\boldsymbol{X}) \end{array} \right. \tag{2.2}$$

which maps the material points $\boldsymbol{X} \in \mathcal{B}$ onto their deformed *spatial* positions $\boldsymbol{x} = \boldsymbol{\varphi}_t(\boldsymbol{X}) \in \mathcal{S}$ at time $t \in \mathbb{R}_+$, see Figure 2.2.

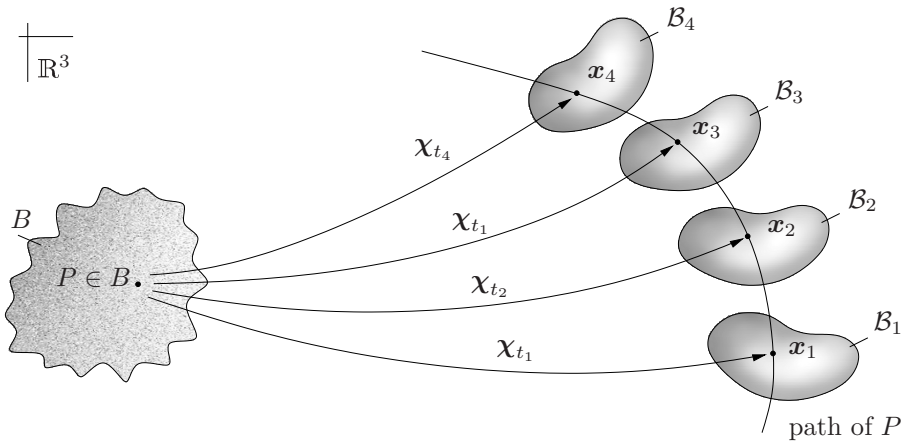

Figure 2.1: The motion of a material body B in the Euclidean space $\mathbb{R}^3$ is a series of placements $\boldsymbol{\chi}_t$ of the physical body B by a family of configurations $\boldsymbol{\chi}_t : B \to \mathcal{B} \in \mathbb{R}^3$.

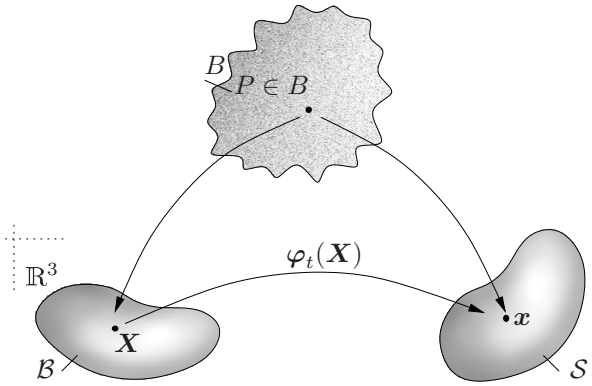

Figure 2.2: Reference configuration $\mathcal{B}$ with positions $\boldsymbol{X}$ and current configuration $\mathcal{S}$ with positions $\boldsymbol{x}$ of the physical body B in the Euclidean space $\mathbb{R}^3$ at time t.

The partial derivative of the deformation of a fixed material point with respect to the time t defines the material velocity. A parametrization by Eulerian coordinates $\boldsymbol{x}$ is obtained by a composition with the inverse deformation map. Hence, material and spatial velocities are defined as

$$\boldsymbol{V}(\boldsymbol{X},t) = \frac{\partial}{\partial t}\boldsymbol{\varphi}(\boldsymbol{X},t) \quad \text{and} \quad \boldsymbol{v}(\boldsymbol{x},t) = \frac{\partial}{\partial t}\boldsymbol{\varphi}(\boldsymbol{X},t) \circ \boldsymbol{\varphi}^{-1}(\boldsymbol{x}). \tag{2.3}$$

They both represent the same quantity but in different parametrizations.

The orthonormal Cartesian reference basis $\{\boldsymbol{E}_A\}_{A=1,2,3}$ and the orthonormal Cartesian spatial basis $\{\boldsymbol{e}_a\}_{a=1,2,3}$ are introduced, to differentiate between reference and spatial quantities also in index notation. The reference positions, spatial positions and the deformation map are represented by $\boldsymbol{X} = X_A\boldsymbol{E}_A$, $\boldsymbol{x} = x_a\boldsymbol{e}_a$ and $\boldsymbol{\varphi}_t = \varphi_a\boldsymbol{e}_a$. According to the summation convention, equal Latin indices imply summation over $\{1, 2, 3\}$. The base vectors are related through the orthogonality relation

$$\delta^A_B = \boldsymbol{E}^A \cdot \boldsymbol{E}_B \quad \text{and} \quad \delta^a_b = \boldsymbol{e}^a \cdot \boldsymbol{e}_b \quad \text{with} \quad \delta^i_j = \begin{cases} 1 \text{ if } a = b \\ 0 \text{ if } a \neq b \end{cases} \tag{2.4}$$

representing the Kronecker-Delta δ. Covariant elements are denoted with superscript indices and contravariant elements with subscript indices. For now, the differentiation is maintained but as curvilinear coordinates are not considered in this work, the base vectors coincide.

Probably the most fundamental deformation measure used in kinematics of finite deformation is the *deformation gradient* defined by the Fréchet derivative as

$$\boldsymbol{F}_t(X) := \nabla_{\boldsymbol{X}}\boldsymbol{\varphi}_t(\boldsymbol{X}) = \mathrm{Grad}(\boldsymbol{\varphi}_t) = \frac{\partial \boldsymbol{\varphi}_a}{\partial X_B}\boldsymbol{e}_a \otimes \boldsymbol{E}_B = \varphi_{a,B}\boldsymbol{e}_a \otimes \boldsymbol{E}_B \ . \tag{2.5}$$

By $\nabla_{\boldsymbol{X}}(\cdot)$ and $\mathrm{Grad}(\cdot)$ we introduced the referential gradient with respect to $\boldsymbol{X}$ of $(\cdot)$ and $\otimes$ defines the dyadic product. The partial derivative of φ_a with respect to X_B is abbreviated by $\varphi_{a,B}$. Because $\boldsymbol{\varphi}_t$ is a one-to-one mapping between reference and current positions without material penetration, we have the constraint that $\det(\boldsymbol{F}_t) \neq 0$ and $\det(\boldsymbol{F}_t) > 0$. The deformation gradient can be considered as a linear map of the referential tangent vectors onto the spatial counterparts. To this end, let $\hat{C}(\Theta) \in \mathcal{B}$ and $\hat{c}(\Theta) \in \mathcal{S}$ be

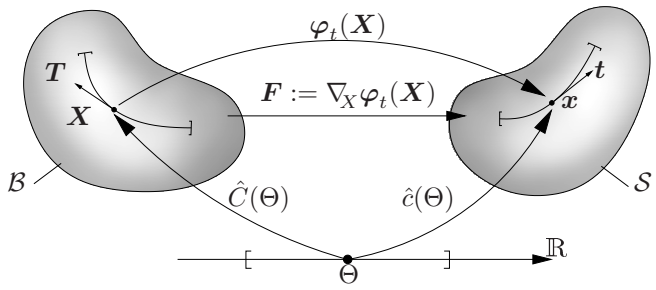

Figure 2.3: The deformation gradient $\boldsymbol{F}$ defined as a *tangent map* linearly transforming the material vector $\boldsymbol{T} \in T_X\mathcal{B}$ tangent to the material curve $\hat{C}(\Theta)$ at $\boldsymbol{X}$ onto the the spatial vector $\boldsymbol{t} \in T_x\mathcal{S}$ tangent to the spatial curve $\hat{c}(\Theta)$ at $\boldsymbol{x}$.

the material and spatial curves parameterized by a common variable $\Theta \in \mathbb{R}$. Furthermore, we consider that the spatial curve is related to the reference curve by the non-linear deformation map $\hat{c}(\Theta) = \boldsymbol{\varphi}_t(\hat{C}(\Theta))$ due to (2.2). Tangents of the curves belonging to the respective tangent spaces, defined as the derivatives $\boldsymbol{T} := d\hat{C}(\Theta)/d\Theta \in T_X\mathcal{B}$ and $\boldsymbol{t} := d\hat{c}(\Theta)/d\Theta \in T_x\mathcal{S}$ are depicted in Figure 2.3. Through the chain rule, the spatial tangent $\boldsymbol{t}$ can be expressed in terms of the material tangent $\boldsymbol{T}$

$$\boldsymbol{t} = \frac{d}{d\Theta}\hat{c}(\Theta) = \nabla_X \boldsymbol{\varphi}_t(\boldsymbol{X})\frac{d}{d\Theta}\hat{C}(\Theta) = \boldsymbol{F}_t\boldsymbol{T} \quad \text{with} \quad t^a = F^a{}_A T^A \,. \tag{2.6}$$

From (2.6) it can be seen that the deformation gradient $\boldsymbol{F}_t$ linearly maps material tangent vectors to associated deformed spatial tangent vectors. It is thus also referred to as the *tangent map*

$$\boldsymbol{F}_t := \left\{ \begin{array}{rcl} T_X\mathcal{B} & \to & T_x\mathcal{S} \,, \\ \boldsymbol{T} & \mapsto & \boldsymbol{t} = \boldsymbol{F}_t\boldsymbol{T} \,, \end{array} \right. \tag{2.7}$$

between the tangent spaces $T_X\mathcal{B}$ and $T_x\mathcal{S}$ of the manifolds $\mathcal{B}$ and $\mathcal{S}$, respectively. Note that (2.6) generally does not preserve the length of $\boldsymbol{T}$. Two further fundamental maps can be expressed through the deformation gradient. In order to derive a definition of volume map, let dV and dv denote the infinitesimal volumes of parallelepipeds

$$dV := d\boldsymbol{X}_1 \cdot (d\boldsymbol{X}_2 \times d\boldsymbol{X}_3) \quad \text{and} \quad dv := d\boldsymbol{x}_1 \cdot (d\boldsymbol{x}_2 \times d\boldsymbol{x}_3) \tag{2.8}$$

defined as the scalar triple product of vectors $d\boldsymbol{X}_{i=1,2,3} \in T_X\mathcal{B}$ and $d\boldsymbol{x}_{i=1,2,3} \in T_x\mathcal{S}$, respectively. Each spatial tangent vector $d\boldsymbol{x}_i$ is defined as a tangential map of its material counterpart, i.e. $d\boldsymbol{x}_i := \boldsymbol{F}d\boldsymbol{X}_i$ for $i = 1, 2, 3$. This then leads to the definition of the *volume map*

$$dv = (\boldsymbol{F}d\boldsymbol{X}_1) \cdot ((\boldsymbol{F}d\boldsymbol{X}_2) \times (\boldsymbol{F}d\boldsymbol{X}_3)) = \det\boldsymbol{F}\; dV =: J\; dV \tag{2.9}$$

following the conventional coordinate-free definition of the determinant of a second order tensor. Then, we say that the volume map, $\det\boldsymbol{F}$, maps the reference volume elements onto their spatial counterparts

$$J = \det\boldsymbol{F} := \left\{ \begin{array}{rcl} \mathbb{R}_+ & \to & \mathbb{R}_+ \,, \\ dV & \mapsto & dv = \det\boldsymbol{F}dV \,. \end{array} \right. \tag{2.10}$$

The *co-factor* of the deformation gradient $\operatorname{cof}\boldsymbol{F}$ is defined as the derivative of the volume map $J := \det\boldsymbol{F}$ with respect to deformation gradient $\boldsymbol{F}$

$$\operatorname{cof}\boldsymbol{F} := \partial_{\boldsymbol{F}}\det\boldsymbol{F} = (\det\boldsymbol{F})\boldsymbol{F}^{-T} \,. \tag{2.11}$$

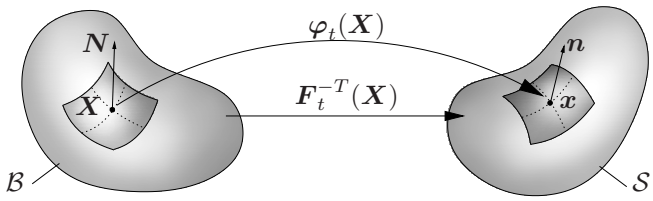

Figure 2.4: The inverse transpose of the deformation gradient $\boldsymbol{F}_t^{-T}$ maps material normal vectors $\boldsymbol{N}$ onto spatial normal vectors $\boldsymbol{n} = \boldsymbol{F}_t^{-T}\boldsymbol{N}$.

In order to make the geometrical meaning of cof $\boldsymbol{F}$ more transparent, let us define the reference and spatial *area co-vectors* $\boldsymbol{N}dA := d\boldsymbol{X}_2 \times d\boldsymbol{X}_3$ and $\boldsymbol{n}da := d\boldsymbol{x}_2 \times d\boldsymbol{x}_3$, respectively. With these definitions at hand, we can recast (2.10) into the following from

$$d\boldsymbol{x}_1 \cdot \boldsymbol{n}da = Jd\boldsymbol{X}_1 \cdot \boldsymbol{N}dA\,. \tag{2.12}$$

If we incorporate the identity $d\boldsymbol{x}_1 = \boldsymbol{F}d\boldsymbol{X}_1$ in (2.12) and solve this equality for $\boldsymbol{n}da$ for an arbitrary tangent vector $d\boldsymbol{X}_1$, we end up with the interpretation of co-factor as the *area map*

$$\boldsymbol{n}da = J\boldsymbol{F}^{-T}\boldsymbol{N}dA = (\operatorname{cof}\boldsymbol{F})\boldsymbol{N}dA\,, \tag{2.13}$$

transforming the co-vectors (one-forms) of the material surfaces onto the normal vectors of spatial surfaces. Furthermore, we observe that the tensorial quantity carrying out the mapping operation in (2.13) is none other than $\boldsymbol{F}^{-T}$. Thus, we consider $\boldsymbol{F}^{-T}$ as the *normal map* transforming the reference co-vectors $\boldsymbol{N}$ onto the spatial co-vectors $\boldsymbol{n}$, belonging to the respective *co-tangent* spaces $T_X^*\mathcal{B}$ and $T_x^*\mathcal{S}$. The *normal map* is then defined as

$$\boldsymbol{F}^{-T} := \left\{ \begin{array}{rcl} T_X^*\mathcal{B} & \to & T_x^*\mathcal{S}\,, \\ \boldsymbol{N} & \mapsto & \boldsymbol{n} = \boldsymbol{F}^{-T}\boldsymbol{N}\,. \end{array} \right. \tag{2.14}$$

We introduce *metric tensors* associated with the Lagrangian and the Eulerian configuration

$$\begin{array}{llll} \boldsymbol{G} & = \delta_{AB}\boldsymbol{E}^A \otimes \boldsymbol{E}^B & \text{and} & \boldsymbol{g} = \delta_{ab}\boldsymbol{e}^a \otimes \boldsymbol{e}^b \\ \boldsymbol{G}^{-1} & = \delta^{AB}\boldsymbol{E}_A \otimes \boldsymbol{E}_B & \text{and} & \boldsymbol{g}^{-1} = \delta^{ab}\boldsymbol{e}_a \otimes \boldsymbol{e}_b \end{array}\,. \tag{2.15}$$

We can interpret the covariant reference $\boldsymbol{G}$ and the spatial $\boldsymbol{g}$ metrics as the mappings from the tangent spaces $T_X\mathcal{B}$ and $T_x\mathcal{S}$ to the co-tangent spaces $T_X^*\mathcal{B}$ and $T_x^*\mathcal{S}$, respectively

$$\boldsymbol{G} : \left\{ \begin{array}{l} T_X\mathcal{B} \to T_X^*\mathcal{B} \\ \boldsymbol{T} \mapsto \boldsymbol{N} = \boldsymbol{G}\boldsymbol{T} \end{array} \right. \quad \text{and} \quad \boldsymbol{g} : \left\{ \begin{array}{l} T_x\mathcal{S} \to T_x^*\mathcal{S} \\ \boldsymbol{t} \mapsto \boldsymbol{n} = \boldsymbol{g}\boldsymbol{t} \end{array} \right. . \tag{2.16}$$

That is, $\boldsymbol{G}$ and $\boldsymbol{g}$ map tangents onto co-vectors by the *index lowering* operation e.g. $\boldsymbol{t}^* = \boldsymbol{g}\boldsymbol{t} = t_a = g_{ab}t^b$. Analogously, the inverse metrics perform the mappings from the co-tangent spaces $T_X^*\mathcal{B}$ and $T_x^*\mathcal{S}$ to the tangent spaces $T_X\mathcal{B}$ and $T_x\mathcal{S}$ through the *index raising* e.g. $\boldsymbol{T} = \boldsymbol{G}^{-1}\boldsymbol{T}^* = T^A = g^{AB}t_B$. With the definitions (2.15), (2.16) at hand, we are ready to construct the commutative diagrams, Figure 2.5, illustrating the *pull-back* and the *push-forward* operations on $\boldsymbol{G}$ and $\boldsymbol{g}$ and their contravariant inverse metrics $\boldsymbol{G}^{-1}$ and $\boldsymbol{g}^{-1}$, separately. As shown in Figure 2.5a, the push-forward of the inverse of the reference metric $\boldsymbol{b} := \boldsymbol{\varphi}_*(\boldsymbol{G}^{-1})$ and the metric itself $\boldsymbol{c} := \boldsymbol{\varphi}_*(\boldsymbol{G})$ are defined by

$$\begin{array}{lll} \boldsymbol{b} := \boldsymbol{\varphi}_*(\boldsymbol{G}^{-1}) = \boldsymbol{F}\boldsymbol{G}^{-1}\boldsymbol{F}^T & , & b^{ab} = F^a{}_A G^{AB} F^b{}_B\,, \\ \boldsymbol{c} := \boldsymbol{\varphi}_*(\boldsymbol{G}) = \boldsymbol{F}^{-T}\boldsymbol{G}\boldsymbol{F}^{-1} & , & c_{ab} = (F^{-1})^A{}_a G_{AB} (F^{-1})^B{}_b \end{array} \tag{2.17}$$

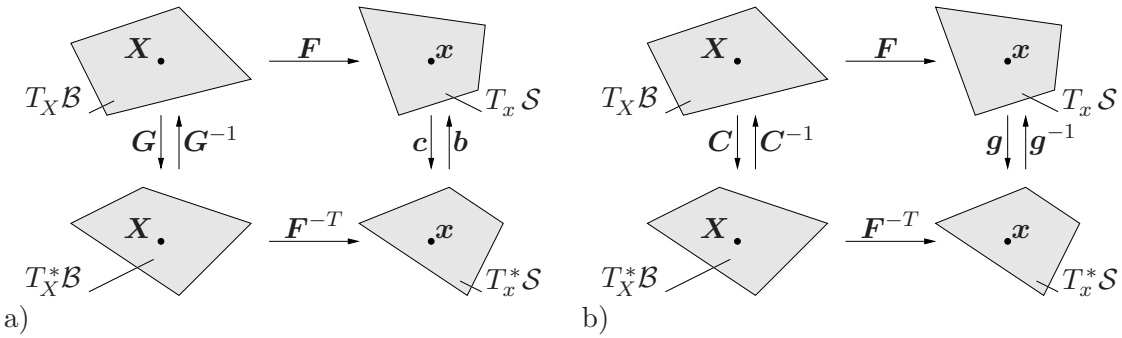

Figure 2.5: The *push-forward* and *pull-back* of the reference $\boldsymbol{G}$ and spatial $\boldsymbol{g}$ metrics and their contravariant inverse forms $\boldsymbol{G}^{-1}$ and $\boldsymbol{g}^{-1}$, separately.

and called the *left Cauchy-Green tensor (Finger deformation tensor)* and the *inverse left Cauchy-Green tensor*, respectively. Similarly, based on the commutative diagram depicted in Figure 2.5b, the pull-back of the spatial metric $\boldsymbol{C} := \boldsymbol{\varphi}^*(\boldsymbol{g})$ and its inverse $\boldsymbol{C}^{-1} := \boldsymbol{\varphi}^*(\boldsymbol{g}^{-1})$ are defined by

$$\begin{aligned} \boldsymbol{C} := \boldsymbol{\varphi}^*(\boldsymbol{g}) &= \boldsymbol{F}^T\boldsymbol{g}\boldsymbol{F} \quad , \quad C_{AB}=F^a{}_A g_{ab} F^b{}_B \,, \\ \boldsymbol{C}^{-1} := \boldsymbol{\varphi}^*(\boldsymbol{g}^{-1}) &= \boldsymbol{F}^{-1}\boldsymbol{g}^{-1}\boldsymbol{F}^{-T} \quad , \quad (C^{-1})^{AB}=(F^{-1})^A{}_a g^{ab}(F^{-1})^B{}_b \end{aligned} \tag{2.18}$$

and denoted as the *right Cauchy-Green tensor (convected spatial metric)* and the *inverse right Cauchy-Green tensor*, respectively. As mentioned above, both metric tensors and their inverse tensors are symmetric and positive definite and therefore so do their respective push-forwards (2.17) and pull-backs (2.18). With the objective of measuring strains locally at a material point, the length of an infinitesimal line element is compared in both its reference as well as its current state

$$\delta := \frac{1}{2}[|d\boldsymbol{x}|^2_{\boldsymbol{g}} - |d\boldsymbol{X}|^2_{\boldsymbol{G}}] = d\boldsymbol{X}\cdot\boldsymbol{E}\cdot d\boldsymbol{X} = d\boldsymbol{x}\cdot\boldsymbol{e}\cdot d\boldsymbol{x}. \tag{2.19}$$

Obviously, this comparison can be carried out either in the Lagrangian or in the Eulerian setting. On the one hand the Lagrangian Green strain tensor $\boldsymbol{E} = \frac{1}{2}[\boldsymbol{C} - \boldsymbol{G}]$ and on the other hand the Eulerian Almansi strain tensor $\boldsymbol{e} = \frac{1}{2}[\boldsymbol{g} - \boldsymbol{c}]$ are obtained. A general representation of strain tensors is given by the Seth-Hill family, cf. Seth [196], Hill [107], of strain measures

$$\boldsymbol{E}^{(m)} = \begin{cases} \frac{1}{m}[\boldsymbol{C}^{m/2} - \boldsymbol{G}] & \text{if } m \neq 0 \\ \frac{1}{2}\ln[\boldsymbol{C}] & \text{if } m = 0 \end{cases} \quad \text{and} \quad \boldsymbol{e}^{(m)} = \begin{cases} \frac{1}{m}[\boldsymbol{g} - \boldsymbol{c}^{m/2}] & \text{if } m \neq 0 \\ \frac{1}{2}\ln[\boldsymbol{c}] & \text{if } m = 0 \end{cases} \tag{2.20}$$

The Green and Almansi strain tensors are obtained for $m = 2$ and the logarithmic strains $m = 0$ are denoted Hencky strains.

2.2. Cauchy's Stress Theorem and the Fundamental Stress Measures

Consider a part $\mathcal{P}_\mathcal{B} \subset \mathcal{B}$ cut off from the reference body $\mathcal{B}$ and its spatial counterpart $\mathcal{P}_\mathcal{S} \subset \mathcal{S}$ closed by the respective boundaries $\partial\mathcal{P}_\mathcal{B}$ and $\partial\mathcal{P}_\mathcal{S}$ as depicted in Figure 2.6. In the deformed configuration, we introduce the *stress vector* $\boldsymbol{t}$ that acts on the surface element da of $\partial\mathcal{P}_\mathcal{S}$ and represents the infinitesimal force vector $d\boldsymbol{f} = \boldsymbol{t}da$, acting of the rest of the body in the vicinity $\mathcal{P}_\mathcal{S} \setminus \mathcal{S}$ on $\partial\mathcal{P}_\mathcal{S}$. The *Cauchy stress theorem* states that the spatial

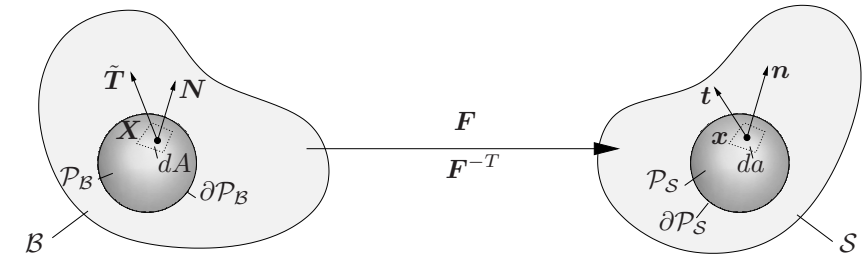

Figure 2.6: The material $\tilde{\boldsymbol{T}}(\boldsymbol{X}, t; \boldsymbol{N}) \in T_X\mathcal{B}$ and spatial $\boldsymbol{t}(\boldsymbol{x}, t; \boldsymbol{n}) \in T_x\,\mathcal{S}$ traction (stress) vectors representing the force action of the rest of the body at the vicinity, on the surfaces of the cut parts $\partial\mathcal{P}_{\mathcal{B}}$ and $\partial\mathcal{P}_{\mathcal{S}}$, respectively.

traction vector $\boldsymbol{t} \in T_x\,\mathcal{S}$ linearly depends on the spatial normal $\boldsymbol{n} \in T_x^*\mathcal{S}$ of the surface $\partial\mathcal{P}_{\mathcal{S}}$, i.e.

$$\boldsymbol{t}(\boldsymbol{x}, t; \boldsymbol{n}) := \boldsymbol{\sigma}(\boldsymbol{x}, t)\ \boldsymbol{n} \tag{2.21}$$

through the *Cauchy (true) stress tensor* $\boldsymbol{\sigma}$. In the geometrical framework outlined so far, the Cauchy stress tensor can be understood as a contravariant mapping transforming normals $\boldsymbol{n} \in T_x^*\mathcal{S}$ onto vectors $\boldsymbol{t} \in T_x\,\mathcal{S}$

$$\boldsymbol{\sigma} := \left\{ \begin{array}{rcl} T_x^*\mathcal{S} & \to & T_x\,\mathcal{S}\,, \\ \boldsymbol{n} & \mapsto & \boldsymbol{t} = \boldsymbol{\sigma}\ \boldsymbol{n}\,. \end{array} \right. \tag{2.22}$$

Another spatial stress measure, the *Kirchhoff stress tensor*, also known as the *weighted Cauchy stress tensor*, is defined as

$$\boldsymbol{\tau} := J\boldsymbol{\sigma} \tag{2.23}$$

and is widely used in the spatial description of stress power terms in the reference volume. Owing to the scalar scaling by the Jacobian J, the Kirchhoff stresses retain the geometrical transformation characteristics of the Cauchy stress, i.e. $\boldsymbol{\tau} : T_x^*\mathcal{S} \to T_x\,\mathcal{S}$. Now let us consider the so called nominal surface traction vector $\boldsymbol{T} \in T_x\,\mathcal{S}$, defined by the force equality $\boldsymbol{T}\ dA := \boldsymbol{t}\ da$ by scaling the spatial force term $(d\boldsymbol{f})$ through the Lagrangian area element dA. Based on this definition, we introduce the *first Piola-Kirchhoff stress tensor* by the reference Cauchy theorem $\boldsymbol{T} := \boldsymbol{P}\boldsymbol{N}$, leading to $\boldsymbol{P}\boldsymbol{N}\ dA = \boldsymbol{\sigma}\boldsymbol{n}\ da$. Using the area map (2.13), we obtain the relation $\boldsymbol{P} = \boldsymbol{\tau}\boldsymbol{F}^{-T} = J\boldsymbol{\sigma}\boldsymbol{F}^{-T}$ between the first Piola-Kirchhoff stress tensor and the spatial stress measures introduced in (2.22) and (2.23). Notice that $\boldsymbol{P}$ is a two-point tensor possessing the geometrical mapping properties

$$\boldsymbol{P} := \left\{ \begin{array}{rcl} T_X^*\mathcal{B} & \to & T_x\,\mathcal{S}\,, \\ \boldsymbol{N} & \mapsto & \boldsymbol{T} = \boldsymbol{P}\ \boldsymbol{N}\,. \end{array} \right. \tag{2.24}$$

The Lagrangian stress vector $\tilde{\boldsymbol{T}} \in T_X\mathcal{B}$ may be defined through the pull-back of the spatial stress vector $\boldsymbol{T} \in T_x\,\mathcal{S}$

$$\tilde{\boldsymbol{T}} = \boldsymbol{\varphi}^*(\boldsymbol{t}) = \boldsymbol{F}^{-1}\boldsymbol{T} \in T_X\mathcal{B} \quad , \quad \tilde{T}^A = (F^{-1})^A{}_a T^a\,,$$

as depicted in Figure 2.6. The third fundamental stress measure, the *second Piola-Kirchhoff stress tensor* $\boldsymbol{S}$, is then defined by $\tilde{\boldsymbol{T}} := \boldsymbol{S}\boldsymbol{N}$ yielding

$$\boldsymbol{S} := \left\{ \begin{array}{rcl} T_X^*\mathcal{B} & \to & T_X\mathcal{B}\,, \\ \boldsymbol{N} & \mapsto & \tilde{\boldsymbol{T}} = \boldsymbol{S}\ \boldsymbol{N}\,. \end{array} \right. \tag{2.25}$$

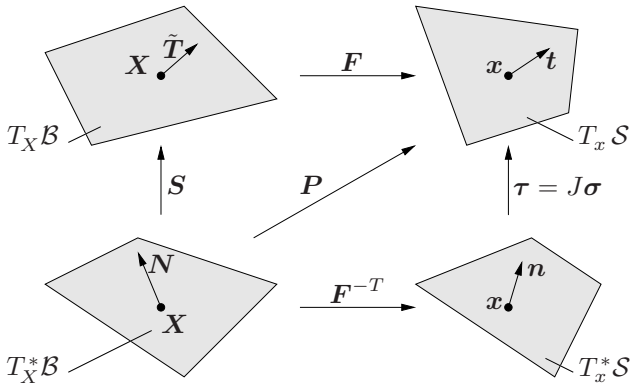

Figure 2.7: Commutative diagram illustrating the *push-forward* and *pull-back* operations among the stress measures.

Incorporating the definitions (2.22)-(2.24) in (2.25), we can express the second Piola-Kirchhoff stress tensor in terms of the other stress tensors

$$\begin{aligned} \boldsymbol{S} := \quad \boldsymbol{\varphi}^*(\boldsymbol{P}) \quad &= \boldsymbol{F}^{-1}\boldsymbol{P} \qquad , \quad S^{AB} \;=\; (F^{-1})^A{}_a P^{aB} \,, \\ \boldsymbol{S} := \quad \boldsymbol{\varphi}^*(\boldsymbol{\tau}) \quad &= \boldsymbol{F}^{-1}\boldsymbol{\tau}\boldsymbol{F}^{-T} \quad , \quad S^{AB} \;=\; (F^{-1})^A{}_a \tau^{ab} (F^{-1})^B{}_b \end{aligned}$$

as the pull-back of the contravariant two-point and spatial objects. Apparently the converse push-forward relations do also hold for the spatial stress tensors

$$\boldsymbol{\tau} = J\boldsymbol{\sigma} = \boldsymbol{\varphi}_*(\boldsymbol{P}) = \boldsymbol{P}\boldsymbol{F}^T \quad \text{and} \quad \boldsymbol{\tau} = \boldsymbol{\varphi}_*(\boldsymbol{S}) = \boldsymbol{F}\boldsymbol{S}\boldsymbol{F}^T \,,$$

as shown in the commutative diagram, Figure 2.7.

Analogous to the definition of the first Piola-Kirchhoff stress tensor, we introduce the *reference heat flux vector* $\mathbb{Q}$. As shown in Figure 2.8, the thermal effects onto the part $\mathcal{P}_\mathcal{S} \in \mathcal{S}$ are described by the scalar heat flux q_n, characterizing the heat flux through the surface in the direction of the normal $\boldsymbol{n}$. Analogously to Cauchys theorem for the stresses, Stokes heat flux theorem

$$q_n(\boldsymbol{x}, t, \boldsymbol{n}) = \mathbb{q}(\boldsymbol{x}, t) \cdot \boldsymbol{n} \tag{2.26}$$

assumes a linear dependence of the heat flux on the normal with $\mathbb{q}$ representing the true heat flux vector defined per unit deformed area. Through $\mathbb{q} \cdot \boldsymbol{n}\; da = \mathbb{Q} \cdot \boldsymbol{N} dA$, the Lagrangian counterpart of $\mathbb{q}$ is introduced which yields with Nansons formula (2.13) the identity

$$\mathbb{Q} = J\boldsymbol{F}^{-1}\mathbb{q} \tag{2.27}$$

in terms of the Lagrangian or nominal heat flux vector $\mathbb{Q}$.

2.3. Balance Principles of Continuum Thermomechanics

The balance laws of continuum mechanics serve as a basic set of equations, required to solve an initial boundary value problem of thermomechanics for the primary variables. This section is devoted to the derivation of the fundamental balance laws of continuum thermomechanics. In what follows, we consider a certain spatial volume $\mathcal{P}_\mathcal{S}$ closed by the boundary $\partial\mathcal{P}_\mathcal{S}$, as shown in Figure 2.6. For this part of the body, we write a balance equation, where we will often have the volumetric source and the surface flux terms contributing a temporal change of the quantity, for which the balance principle is constructed.

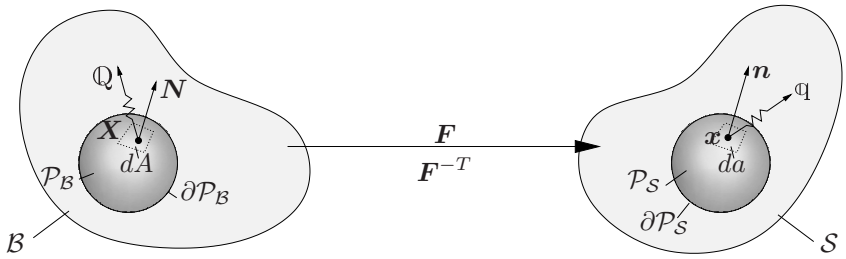

Figure 2.8: The material $\mathbb{Q}(\boldsymbol{X},t) \in T_X\mathcal{B}$ and spatial $\mathbb{q}(\boldsymbol{x},t) \in T_x\mathcal{S}$ heat flux vectors representing the conduction of heat through the rest of the body over the surfaces of the cut parts $\partial\mathcal{P}_\mathcal{B}$ and $\partial\mathcal{P}_\mathcal{S}$, respectively.

In order to derive the local forms of the balance laws, we follow these basic steps. First, we carry the surface flux terms into the body through the Gaussian integral theorem. Once the balance equation is completely recast into a volume integral, the expression can be localized to its local form by stating that integrand must also fulfill the equality for an infinitely small part $\mathcal{P}_\mathcal{S}$, provided that the continuity conditions are met. This spatial balance equation is then recast into its reference form.

Balance of Mass. The balance law demands that the total mass of a closed system, the part of a body $\mathcal{P}_\mathcal{S}$ under consideration, remains constant; that is, the system is free of agencies that produce or destroy mass within the volume $\mathcal{P}_\mathcal{S}$ or is not subjected to flux terms that transfer mass over the surface $\partial\mathcal{P}_\mathcal{S}$. To this end, we define the *spatial mass density* $\rho(\boldsymbol{x},t)$ and its material counterpart the *reference mass density* $\rho_0(\boldsymbol{X})$ and require

$$\frac{d}{dt}\mathcal{M} := \frac{d}{dt}\int_{\mathcal{P}_\mathcal{S}} \rho(\boldsymbol{x},t)dv = \frac{d}{dt}\int_{\mathcal{P}_\mathcal{B}} J\rho(\boldsymbol{x},t)dV = \frac{d}{dt}\int_{\mathcal{P}_\mathcal{B}} \rho_0(\boldsymbol{X})dV = 0\,. \tag{2.28}$$

Making use of the identity $\dot{J} := dJ/dt = \operatorname{cof}\boldsymbol{F} : \dot{\boldsymbol{F}} = J\operatorname{div}(\boldsymbol{v})$ in $(2.28)_3$ and equating the integrands of $(2.28)_2$ and $(2.28)_3$, we end up with the spatial and material forms of the *local mass balance* equations

$$\dot{\rho} + \rho\operatorname{div}(\boldsymbol{v}) = 0 \quad \text{and} \quad J\rho(\boldsymbol{x},t) = \rho_0(\boldsymbol{X})\,. \tag{2.29}$$

Balance of Linear Momentum. Being analogous to classical discrete mechanics, the time rate of linear momentum of the volume $\mathcal{P}_\mathcal{S}$ is equal to the sum of the forces acting on the body. Two types of forces are considered: the mass specific body forces $\boldsymbol{\gamma}(\boldsymbol{x},t)$ due to the action of other bodies at a distance and the surface forces (stress vectors) $\boldsymbol{t}$ due to the action at a vicinity. These can also be regarded as momentum source and momentum flux terms, respectively. The *balance of linear momentum* then requires

$$\frac{d}{dt}\mathcal{L} := \frac{d}{dt}\int_{\mathcal{P}_\mathcal{S}} \rho\boldsymbol{v}(\boldsymbol{x},t)dv = \int_{\mathcal{P}_\mathcal{S}} \rho\boldsymbol{\gamma}(\boldsymbol{x},t)dv + \int_{\partial\mathcal{P}_\mathcal{S}} \boldsymbol{t}(\boldsymbol{x},t;\boldsymbol{n})da\,. \tag{2.30}$$

Incorporation of the mass balance (2.29) in the time derivative and the Cauchy stress theorem (2.21) through the Gaussian surface integral theorem, we obtain the local form of the spatial linear momentum balance

$$\rho\dot{\boldsymbol{v}} = \rho\boldsymbol{\gamma} + \operatorname{div}(\boldsymbol{\sigma})\,. \tag{2.31}$$

Multiplication of the spatial form (2.31) with the Jacobian J and incorporation of the mass balance $(2.29)_1$ and the Piola identity ($\mathrm{Div}[J\boldsymbol{F}^{-T}] = 0$) yields the material form of the local linear momentum balance

$$\rho_0 \dot{\boldsymbol{V}} = \rho_0 \boldsymbol{\Gamma} + \mathrm{Div}(\boldsymbol{P}) \tag{2.32}$$

where $\dot{\boldsymbol{V}}$ denotes the material acceleration and $\boldsymbol{\Gamma}(\boldsymbol{X}, t) := \boldsymbol{\gamma}(\boldsymbol{x}, t) \circ \boldsymbol{\varphi}_t(\boldsymbol{X})$ stands for the material body force defined per unit mass.

Balance of Angular Momentum. The time derivative of the moment of linear momentum of $\mathcal{P}_\mathcal{S}$ is required to be equal to the sum of the moments of the forces acting on the body with respect to the same point. Without loss of generality, taking the moment with respect to the origin yields

$$\frac{d}{dt}\int_{\mathcal{P}_\mathcal{S}} \boldsymbol{x} \times \rho \boldsymbol{v} dv = \int_{\mathcal{P}_\mathcal{S}} \boldsymbol{x} \times \rho \boldsymbol{\gamma}\, dv + \int_{\partial\mathcal{P}_\mathcal{S}} \boldsymbol{x} \times \boldsymbol{t}\, da\,. \tag{2.33}$$

Exploiting the mass balance (2.29), the equality $\boldsymbol{v} \times \boldsymbol{v} = \boldsymbol{0}$ in $(2.33)_1$ and the Cauchy stress theorem (2.21) through the Gaussian integral theorem in the surface integral $(2.33)_3$, we obtain

$$\int_{\mathcal{P}_\mathcal{S}} \boldsymbol{x} \times (\rho \dot{\boldsymbol{v}} - \rho \boldsymbol{\gamma} - \mathrm{div}(\boldsymbol{\sigma}))\, dv = \int_{\mathcal{P}_\mathcal{S}} \boldsymbol{\iota} dv = \boldsymbol{0} \tag{2.34}$$

where we demand $\iota_a := \epsilon_{abc}\sigma^{cb} = 0$. Since the *permutation symbol* ϵ_{abc} is skew symmetric with respect to two indices, e.g. $\epsilon_{abc} = -\epsilon_{acb}$, the equality (2.34) is fulfilled only when the Cauchy stresses is symmetric. Thus, the balance of angular momentum results in

$$\boldsymbol{\sigma} = \boldsymbol{\sigma}^T \quad , \quad \sigma^{ab} = \sigma^{ba}\,. \tag{2.35}$$

Owing to the push-forward and pull-back relations derived in Section 2.2, the other two stress measures $\boldsymbol{\tau}$ and $\boldsymbol{S}$ are required to satisfy the following symmetry relations

$$\boldsymbol{\tau} = \boldsymbol{\tau}^T \quad , \quad \boldsymbol{P}\boldsymbol{F}^T = \boldsymbol{F}\boldsymbol{P}^T \quad , \quad \boldsymbol{S} = \boldsymbol{S}^T \tag{2.36}$$

as well. Observe that the first Piola-Kirchhoff stresses are generally non-symmetric.

Balance of Energy. First Law of Thermodynamics. The balance of energy is often referred to as the *first law of thermodynamics*, a fundamental balance principle describing the evolution of internal energy in a system. Energy is a quantity of deformable bodies measuring the capacity to do work, i.e. a change in energy causes work to be done by mechanical and thermal forces acting on the system. The balance law states the conservation of energy in the sense that the rate of total energy is equilibrated with the sum of the external mechanical and thermal power. The total energy is defined as the sum of kinetic energy $\mathcal{K}$ and internal energy $\mathcal{E}$ given in the specific form

$$\mathcal{K} = \int_{\mathcal{P}_\mathcal{S}} \tfrac{1}{2}\,\rho \boldsymbol{v} \cdot \boldsymbol{v}\, dv \quad \text{and} \quad \mathcal{E} = \int_{\mathcal{P}_\mathcal{S}} \rho e\, dv\,. \tag{2.37}$$

Here, $e(\boldsymbol{x}, t)$ denotes the internal energy density per unit volume which is in the material representation $e_0(\boldsymbol{X}, t) = e(\boldsymbol{x}, t) \circ \boldsymbol{\varphi}(\boldsymbol{x}, t)$. The external mechanical and thermal power is given by

$$\mathcal{P} = \int_{\mathcal{P}_\mathcal{S}} \rho \boldsymbol{\gamma} \cdot \boldsymbol{v}\, dv + \int_{\partial\mathcal{P}_\mathcal{S}} \boldsymbol{t} \cdot \boldsymbol{v}\, da \quad \text{and} \quad \mathcal{Q} = \int_{\mathcal{P}_\mathcal{S}} \rho r\, dv - \int_{\partial\mathcal{P}_\mathcal{S}} \mathfrak{q} \cdot \boldsymbol{n}\, da\,, \tag{2.38}$$

where $q_n(\boldsymbol{x}, t; \boldsymbol{n}) = \mathbb{q}(\boldsymbol{x}, t)\boldsymbol{n}$ is the heat flux entering the body across the surface $\partial\mathcal{P}_\mathcal{S}$ and $r(\boldsymbol{x}, t)$ a given heat source per unit mass generated by internal quantities. The global form of the *balance of internal energy* or *conservation of energy* reads

$$\frac{d}{dt}[\mathcal{K} + \mathcal{E}] = \mathcal{P} + \mathcal{Q} \tag{2.39}$$

stating that the time rate of change in total energy is balanced by the mechanical power and thermal heating of the body. For the surface term in the mechanical power expression $(2.38)_1$ we obtain the form

$$\int_{\partial\mathcal{P}_\mathcal{S}} \boldsymbol{t} \cdot \boldsymbol{v}\, da = \int_{\mathcal{P}_\mathcal{S}} \operatorname{div}[\boldsymbol{\sigma}] \cdot \boldsymbol{v}\, dv + \int_{\mathcal{P}_\mathcal{S}} \boldsymbol{\sigma} : \boldsymbol{l}\, dv \tag{2.40}$$

valid in the domain $\mathcal{P}_\mathcal{S}$, by using Cauchy's theorem and the spatial velocity gradient $\boldsymbol{l} = \nabla_{\boldsymbol{x}}\boldsymbol{v}$. Application of the volume map (2.9) and the Piola identity ($\operatorname{Div}[J\boldsymbol{F}^{-T}] = 0$) gives the Lagrangian representation together with $J\boldsymbol{\sigma} : \boldsymbol{l} = J\boldsymbol{\sigma}\boldsymbol{F}^{-T} : \dot{\boldsymbol{F}} = \boldsymbol{P} : \dot{\boldsymbol{F}} = \boldsymbol{P} : \dot{\boldsymbol{F}}$

$$\int_{\partial\mathcal{P}_\mathcal{S}} \boldsymbol{t} \cdot \boldsymbol{v}\, da = \int_{\mathcal{B}_P} \operatorname{Div}[\boldsymbol{P}] \cdot \boldsymbol{V}\, dV + \int_{\mathcal{B}_P} \boldsymbol{P} : \dot{\boldsymbol{F}}\, dV\ . \tag{2.41}$$

A straightforward transformation of all other quantities to the Lagrangian manifold results in the local Lagrangian form of the balance of energy

$$\rho_0 \dot{e}_0 = \boldsymbol{P} : \dot{\boldsymbol{F}} + \rho_0 R - \operatorname{Div}[\mathbb{Q}] \tag{2.42}$$

with the material representation of the heat source $R(\boldsymbol{X}, t) = r(\boldsymbol{x}, t) \circ \boldsymbol{\varphi}(\boldsymbol{x}, t)$. Push-forward to the current configuration gives the Eulerian form of the balance of energy

$$\rho\dot{e} = \boldsymbol{\sigma} : \boldsymbol{l} + \rho r - \operatorname{div}[\mathbb{q}]\ . \tag{2.43}$$

For the transformation of the heat flux vector from the Eulerian to the Lagrangian manifold the equation $\mathbb{Q} = J\boldsymbol{F}^{-1}\mathbb{q}$ was used.

Entropy Production Inequality. Second Law of Thermodynamics. The second law of thermodynamics serves as a major mathematical restriction on the constitutive equations governing, for instance, heat conduction or evolution of internal variables describing an internal dissipative mechanism. The concept of *entropy* may be conceived as a *measure of disorder*, providing a bridge between thermomechanics with the treatments of statistical mechanics. The global form of the entropy inequality principle states a *positive entropy production*

$$\mathcal{G} = \frac{d}{dt}\mathcal{S} - \mathcal{Q} \geq 0 \tag{2.44}$$

within the part of the body $\mathcal{P}_\mathcal{S}$ under consideration. The *entropy* $\mathcal{S}$ is defined by integrating the *specific entropy* η over the volume

$$\mathcal{S} := \int_{\mathcal{P}_\mathcal{S}} \rho\eta(\boldsymbol{x}, t) dv \tag{2.45}$$

and the *total rate of entropy production* $\mathcal{G}$ is the integration over the volume of the specific rate of entropy production

$$\mathcal{G} := \int_{\mathcal{P}_\mathcal{S}} \rho\gamma(\boldsymbol{x}, t) dv \tag{2.46}$$

based on the local entropy production per unit mass γ. The rate of entropy input $\mathcal{Q}$ is characterized by

$$\mathcal{Q} := \int_{\mathcal{P}_\mathcal{S}} \frac{\rho r}{\theta} dv + \int_{\partial\mathcal{P}_\mathcal{S}} \frac{\mathbb{q} \cdot \boldsymbol{n}}{\theta} da \tag{2.47}$$

in terms of the heat flux (2.26) and the *absolute temperature* $\theta > 0$. Following the conventional steps, we end up with the local spatial entropy balance

$$\rho\gamma \;=\; \rho\dot{\eta} - \rho\frac{r}{\theta} + \operatorname{div}\left(\frac{\mathbb{q}}{\theta}\right) \;=\; \rho\dot{\eta} - \rho\frac{r}{\theta} + \frac{1}{\theta}\operatorname{div}(\mathbb{q}) - \frac{1}{\theta^2}\mathbb{q}\cdot\nabla_x\theta \quad \geq 0\,. \tag{2.48}$$

The inequality $(2.48)_3$ can also be written in the form commonly referred to as the *Clausius-Duhem inequality*

$$\rho\dot{\eta} \;\geq\; \rho\frac{r}{\theta} - \frac{1}{\theta}\operatorname{div}(\mathbb{q}) + \frac{1}{\theta^2}\mathbb{q}\cdot\nabla_x\theta\,. \tag{2.49}$$

The material version of (2.49) then reads

$$\rho_0\dot{\eta} \;\geq\; \rho_0\frac{R}{\theta} - \frac{1}{\theta}\operatorname{Div}(\mathbb{Q}) + \frac{1}{\theta^2}\mathbb{Q}\cdot\nabla_X\theta\,. \tag{2.50}$$

2.4. Dissipation and Thermomechanics with Internal Variables

The *spatial dissipation* is defined as the product of the rate of entropy production in (2.43), with the absolute temperature $\theta(\boldsymbol{x}, t) > 0$, i.e.

$$\mathcal{D} := \rho\gamma\theta \geq 0\,. \tag{2.51}$$

The equation (2.49) can be reformulated by insertion of the local balance of total energy (2.42) in the form

$$\rho_0\mathcal{D}_0 = \boldsymbol{P} : \dot{\boldsymbol{F}} + \rho_0\theta\dot{\eta}_0 - \rho_0\dot{e}_0 - \frac{1}{\theta}\mathbb{q}\cdot\nabla_{\boldsymbol{x}}\theta \geq 0\,. \tag{2.52}$$

In order to use the absolute temperature θ as an independent variable in the material equations, we introduce the free Helmholtz energy Ψ by the Legendre-Fenchel transformation

$$e_0(\boldsymbol{F}, \eta_0, \ldots, \boldsymbol{X}) = \Psi(\boldsymbol{F}, \theta, \ldots, \boldsymbol{X}) - \eta_0\theta\,. \tag{2.53}$$

Insertion into the Clausius-Duhem inequality (2.52) yields

$$\rho_0\mathcal{D}_0 = \boldsymbol{P} : \dot{\boldsymbol{F}} + \rho_0\eta_0\dot{\theta} - \rho_0\dot{\Psi} - \frac{1}{\theta}\mathbb{q}\cdot\nabla_{\boldsymbol{x}}\theta \geq 0\,. \tag{2.54}$$

It makes sense to satisfy this equation separately for the *local* and *conductive* part, i.e. demanding the sharper conditions

$$\rho_0\mathcal{D}_{loc} := \boldsymbol{P} : \dot{\boldsymbol{F}} + \rho_0\eta_0\dot{\theta} - \rho_0\dot{\Psi} \geq 0 \quad \text{and} \quad \rho_0\mathcal{D}_{con} := -\frac{1}{\theta}\mathbb{q}\cdot\nabla_{\boldsymbol{X}}\theta \geq 0 \tag{2.55}$$

known as the *Clausius-Planck inequality* and the *Fourier inequality*. Thermodynamic consistency means that all material equations have to satisfy these two inequalities. In the context of continuum thermomechanics, the material state generally depends on a set of variables which is formed through a mutual combination between the sets $\{\boldsymbol{P}, \boldsymbol{F}\}$ and

$\{\eta, \theta\}$. For inelastic materials, these sets are supplemented by additional *internal variables*, say $\mathbf{q}$, employed for the description of inelastic dissipative processes. The concept of internal variables has widely been used in the constitutive formulation of dissipative materials through the initial value problems, governing their temporal evolution. The set $\mathbf{q}$ may have scalar, tensorial or n-vector character. The internal variables may be observable but generally cannot be externally controlled, see MAUGIN [146] for an excellent review. The *thermodynamical forces*, say $\mathfrak{p}$, conjugate to the set $\mathbf{q}$ on the bases of dissipation, generally are not externally defined. Let us focus on a problem of thermoelasticity for a homogeneous material where the free energy depends on the internal variables. Consistent with the *principle of equipresence*, we assume that the constitutive equations, the free energy Ψ and the heat flux vector $\mathbb{Q}$, depend upon the same set of field variables

$$\Psi = \hat{\Psi}(\boldsymbol{F}, \theta, \mathbf{q}) \quad \text{and} \quad \mathbb{Q} = \hat{\mathbb{Q}}(\boldsymbol{F}, \theta, \mathbf{q}) \ . \tag{2.56}$$

Based on this assumption, we can include the time derivative of the free energy $\dot{\Psi} = \partial_{\boldsymbol{F}}\Psi : \dot{\boldsymbol{F}} + \partial_{\theta}\Psi : \dot{\theta} + \partial_{\mathbf{q}}\Psi : \dot{\mathbf{q}}$ in the Clausius-Planck inequality given in $(2.55)_1$. Gathering the coefficients of the time rates of the common terms, we obtain

$$\rho_0 \mathcal{D}_{loc} := (\boldsymbol{P} - \rho_0 \partial_{\boldsymbol{F}}\Psi) : \dot{\boldsymbol{F}} - \rho_0(\eta + \partial_{\theta}\Psi)\dot{\theta} - \rho_0 \partial_{\mathbf{q}}\Psi \cdot \dot{\mathbf{q}} \geq 0 \ . \tag{2.57}$$

Following the celebrated reasoning of COLEMAN & NOLL [48] and COLEMAN & GURTIN [46] within the framework of thermodynamics with internal variables, we contend that the thermodynamic restriction should be fulfilled for an arbitrary rate of deformation gradient and temperature. Therefore, (2.57) implies a particular form of constitutive equations such that

$$\boldsymbol{P} := \rho_0 \partial_{\boldsymbol{F}}\Psi \quad , \quad \eta := -\partial_{\theta}\Psi \ . \tag{2.58}$$

These two equations state that the free energy acts as a potential for the stresses and the entropy. With the results obtained in (2.58), the Clausius-Planck inequality can be recast into its *reduced* form

$$\rho_0 \mathcal{D}_{loc} := \mathfrak{p} : \dot{\mathbf{q}} \ \geq \ 0 \quad \text{with} \quad \mathfrak{p} := -\rho_0 \partial_{\mathbf{q}}\Psi \ . \tag{2.59}$$

In view to use the absolute temperature θ as an independent variable in the material equations, we derive the heat conduction equation that describes the distribution of heat (or variation in temperature) in a given region over time. Let us rewrite the Clausius-Planck inequality (2.55) by using the time derivative of the Legendre Transformation $\dot{\Psi} = \dot{e} - \dot{\theta}\eta - \theta\dot{\eta}$ and sort for the rate of internal energy:

$$\rho_0 \dot{e}_0 = \boldsymbol{P} : \dot{\boldsymbol{F}} + \rho_0 \theta \dot{\eta} - \rho_0 \mathcal{D}_{loc} \ . \tag{2.60}$$

Along with the balance of internal energy (2.43) we obtain

$$\rho_0 \theta \dot{\eta} = -\operatorname{Div}[\mathbb{Q}] + \rho_0[R + \mathcal{D}_{loc}] \ . \tag{2.61}$$

Exploiting the definition of the entropy $(2.58)_2$, the left hand side of the equation (2.61) can be expressed as

$$\rho_0 \theta \dot{\eta} = \rho_0 c_s \dot{\theta} - \rho_0 H \tag{2.62}$$

with the *heat capacity* per unit mass and the *latent heating*

$$c_s = -\theta \partial^2_{\theta\theta}\Psi \quad \text{and} \quad H = \theta \partial^2_{\theta \boldsymbol{F}}\Psi : \dot{\boldsymbol{F}} + \theta \partial^2_{\theta \mathbf{q}}\Psi : \dot{\mathbf{q}} \ . \tag{2.63}$$

Devising the result (2.62) in (2.61) we end up with the *transient heat conduction* equation

$$\rho_0 c_s \dot{\theta} = -\operatorname{Div}[\mathbb{Q}] + \rho_0 [R + H + \mathcal{D}_{loc}] \ . \tag{2.64}$$

Note that the first bracket vanishes in an adiabatic process, i.e for $\mathbb{Q} \equiv 0$ and $R \equiv 0$. Equation (2.64) is known as the coupled temperature evolution equation of thermo-viscoelasticity. The last two terms on the right-hand side characterize the latent (thermoelastic) and dissipative coupling effects. Similar to applications of metal thermo-viscoelasticity we expect the situation $|H| \ll \mathcal{D}_{loc}$. Investigations of MIEHE [150] for entropic thermoelasticity demonstrated a small amount of latent heating. In our subsequent investigation we neglect the latent heating effect in the temperature evolution equation (2.64) by setting $H \approx 0$.

3. Fundamentals of Fracture Mechanics

3.1. Basic Definitions of Fracture Mechanics

From the macroscopic point of view, a crack is defined as a cut through a three-dimensional body $\mathcal{B}$ yielding two opposite surfaces, the so called *crack surfaces* that intersect in the *crack front*. In a planar description of a body, the crack yields two opposite *crack edges* that meet in the *crack tip*. Regarding the deformation of a crack, one may distinguish between three different relative displacements of the opposite crack surfaces. The so-called crack opening modes depend on the direction of the load in relation to the orientation of the crack surfaces and the crack front. The different opening modes in a local neighborhood are depicted in Figure 3.1. The *Mode I crack* is characterized by

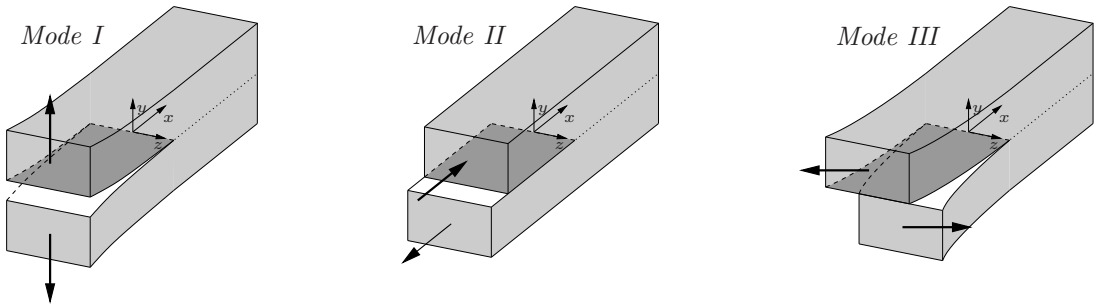

Figure 3.1: The crack opening modes. *Mode I* crack: Opening mode symmetric to the $\{x, z\}$-plane. *Mode II* crack: relative displacement of crack surfaces in x-direction. *Mode III* crack: relative displacement of crack surfaces in z-direction.

a discontinuity in the displacement field in y-direction, i.e. $|u_y(\boldsymbol{x})| \neq 0$, a discontinuous displacement symmetric to the $\{x, z\}$-plane. The *Mode II crack* opening is also called plane shear or sliding mode. The displacement discontinuity appears in x direction normal to the crack front, thus $|u_x(\boldsymbol{x})| \neq 0$. Finally, for the *Mode III crack*, the anti-plane shear or tearing mode, describes a separation in z-direction tangential to the crack tip with $|u_z(\boldsymbol{x})| \neq 0$. The symmetries corresponding to the crack opening modes are in general only local. They are valid for an entire body only in special cases. In general, each crack may be described as a superposition of the three failure modes.

3.1.1. Stress State Near the Crack Tip and Stress Intensity Factors. Linear elastic fracture mechanics considers bodies with linear elastic material behavior. Eventual material or geometrical nonlinearities occurring in the process zone around crack tips, must be negligibly small. Consequently, linear elastic fracture mechanics are suitable for the description of brittle fracture. The crack mechanism of a precracked solid is determined by the stress and strain concentration in the vicinity of the crack tip or the crack front. The singular crack tip field with the intensity K_I describes the intensity of load in a narrow region R around the crack tip. The stress intensity factors are an excellent basis for the formulation of fracture criteria. A criterion states that a crack starts propagating when reaching a critical material state in the process zone, i.e.

$$K_i = K_{ic} \ . \tag{3.1}$$

This critical state is characterized by the so-called fracture toughness K_c. The fracture toughness may be interpreted as the material resistance against crack evolution, while the

stress intensity factor represents the material state induced by the corresponding loading. Considering a general loading of a material body as a combination of the three fracture modes, the stresses may be written in terms of a function B, depending on the three K-factors. The general crack criterion reads

$$B(K_I, K_{II}, K_{III}) = B_c \ . \tag{3.2}$$

The fracture toughness itself is obtained from experimental considerations. For a detailed consideration of the concept of stress intensity factors, the reader is referred to Irwin [112, 113] or regarding a compact overview to Gross & Seelig [98] and Kuna [131].

3.1.2. Griffith Energetic Fracture Approach. The energy release rate was introduced for brittle elastic materials by Griffith [97, 96]. He observed that failure occurs as soon as a critical value of the energy release rate is reached. This critical value is, in contrast to the above described stress intensity factor, independent of the geometry of the body. It depends solely on the material properties, i.e. it is a material parameter. The critical energy release rate may be interpreted as the energy needed for the formation of the two crack surfaces. Griffith's theory is a global approach to fracture mechanics based on the balance of energy. With reference to the work of Gross & Seelig [98] and Kuna [131], this subsection starts with the investigation of a cracked body with elastic material behavior, yielding a typical brittle crack mechanism. Finally, the theory is extended to ductile fracture.

Following the first principle of thermodynamics, the temporal change of total energy $\frac{d}{dt}(\mathcal{E} + \mathcal{K} + \mathcal{D}) = P_{int}$ which coincides with the internal power, equals the power due to external loading $P_{ext} = \mathcal{P} + \mathcal{Q}$

$$\frac{d}{dt}(\mathcal{E} + \mathcal{K} + \mathcal{D}) = \mathcal{P} + \mathcal{Q} \ . \tag{3.3}$$

The rate of the kinetic energy $\dot{\mathcal{K}}$ takes into account dynamic effects. Thermal effects are considered by means of $\mathcal{Q}$. For simplicity, we investigate an isothermal, quasi-static problem with $\mathcal{Q} = 0$, $\dot{\theta} = 0$ and $\dot{\mathcal{K}} = 0$. The external loading $\mathcal{P}$ represents the energy supply due to mechanical power

$$\mathcal{P} = \int_{\mathcal{S}} \rho \boldsymbol{\gamma} \boldsymbol{v} \ dv + \int_{\partial \mathcal{S}_t} \bar{\boldsymbol{t}} \cdot \boldsymbol{v} \ da \tag{3.4}$$

also discussed with (2.38) in terms of the given body force field per unit volume $\boldsymbol{\gamma}$ and the traction forces $\bar{t}$. A detailed discussion of the balance equation is given in (2.39). For isothermal processes, the rate of the internal energy $\dot{\mathcal{E}}$ may be defined in terms of the specific internal energy e, or in terms of the *Helmholtz* free energy Ψ yielding

$$\dot{\mathcal{E}} = \int_{\mathcal{S}} \rho \dot{e} dv = \int_{\mathcal{S}} \rho \dot{\Psi} dv \ . \tag{3.5}$$

Finally, the energy dissipated in the crack zone $\mathcal{D}$ is introduced. It is required for the creation of the crack surfaces and may consequently be related to the surface A and the material constant γ. The factor 2 considers that during crack growth two crack faces are generated

$$\mathcal{D} = 2\gamma A \ . \tag{3.6}$$

Considering a body with elastic material behavior, the internal energy is an internal potential $\mathcal{E} = \Pi_{int}$. Further, it is assumed that external loads are conservative loads, thus it is possible to assign a potential Π_{ext}, which decreases with external power $\dot{\Pi}_{ext} = -\mathcal{P}$. Insertion into (3.3) finally yields

$$\mathcal{P} = \dot{\mathcal{E}} + \dot{\mathcal{D}} \quad , \quad -\dot{\Pi}_{ext} = \dot{\Pi}_{int} + \dot{\mathcal{D}} \tag{3.7}$$

With these assumptions, the quasi-static crack growth between an initial crack state A_1 at time t_1 and the grown crack state $A_2 = A_1 + \Delta A$ at time $t_2 = t_1 + \Delta t$ is analyzed. The difference in total energy between these two states can either be related to the time or crack increment

$$-(\Pi_{ext2} - \Pi_{ext1}) = (\Pi_{int2} - \Pi_{int1}) + 2\gamma(A_2 - A_1) \ . \tag{3.8}$$

Relating this equation to the change of the crack surface $\Delta A = A_2 - A_1$ and summing up the internal and the external potentials to the total potential $\Pi = \Pi_{ext} + \Pi_{int}$ one finally obtains

$$-\frac{\Delta \Pi}{\Delta A} \stackrel{!}{=} \frac{\Delta \mathcal{D}}{\Delta A} = 2\gamma \ . \tag{3.9}$$

The left hand side of (3.9) describes the energy which is available and that may be used for the crack mechanism. It is the so-called energy release rate and is defined for an infinitesimal crack propagation via

$$g = -\frac{\Delta \Pi}{\Delta A} \ . \tag{3.10}$$

The right hand side of (3.9) is the energy needed for the creation of new crack surfaces $2\Delta A$. It depends on the material properties and is defined via the critical energy release rate $g_c = 2\gamma$. With these definitions at hand, one may formulate the crack criterion introduced by Griffith

$$-\frac{\Delta \Pi}{\Delta A} = g = g_c = 2\gamma \ . \tag{3.11}$$

Griffith's energetic fracture criterion postulates that for crack initiation and quasi-static crack growth in a conservative system, the available energy release rate must be equal the critical fracture energy dissipated per surface. The critical energy release rate g_c is a material parameter which corresponds to the energy needed for crack propagation. Thus, a crack may start propagating only if the available energy reaches a critical value. Griffith derived, for a plate under plane stress tension, with a crack of length $2a$, the energy release rate $g = 2\pi\sigma^2 a/E = 4\gamma$, in terms of the Young's modulus E. With this expression at hand, one directly obtains the critical stress which may be related to the K-factor

$$\sigma_c = \sqrt{\frac{2E\gamma}{\pi a}} = \frac{K_{Ic}}{\sqrt{\pi a}} \ . \tag{3.12}$$

The balance of energy during crack propagation formulated in (3.3) is enhanced to incorporate *inelastic material* effects. According to the first law of thermodynamics, the temporal change of total energy equals the power due to external loading, see (3.3). The internal energy $(2.37)_2$, is redefined for the inelastic material response as

$$\mathcal{E} = \mathcal{E}_e + \mathcal{E}_{\mathcal{D}} \tag{3.13}$$

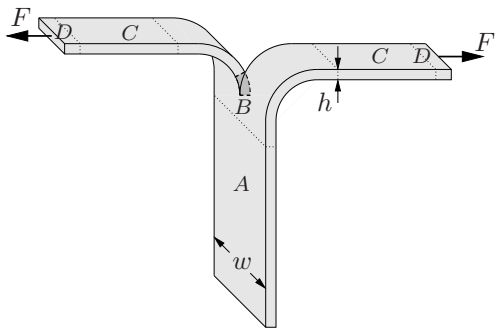

Figure 3.2: Simple extension fracture test correlating a *Mode III* crack opening. An increase Δc in the cut-length increases the region C in simple extension at the expense of the undeformed region A.

with $\mathcal{E}_e$ being the elastic stored internal energy and $\mathcal{E}_\mathcal{D}$ the work dissipated to heat or used for viscous or plastic deformation processes. Insertion of (3.13) into (3.3) yields the global balance of energy for quasi-static, isothermal, ductile crack propagation

$$\frac{d}{dt}(\mathcal{E}_e + \mathcal{E}_\mathcal{D} + \mathcal{D}) = \mathcal{P} \ . \tag{3.14}$$

Consider the elastic internal energy of the type of an internal potential $\mathcal{E} = \Pi_{int}$ and further assume that external loads are governed by the potential Π_{ext}, which decreases with external power $\dot{\Pi}_{ext} = -\mathcal{P}$, (3.14). This yields

$$-\frac{\Delta\Pi}{\Delta A} \stackrel{!}{=} \frac{\Delta\mathcal{D}}{\Delta A} + \frac{\Delta\mathcal{E}_\mathcal{D}}{\Delta A} = g \ . \tag{3.15}$$

The energy released g is not only used for the crack propagation process $\Delta\mathcal{D}/\Delta A = 2\gamma$. The energy release rate includes both the geometry dependent viscous or plastic dissipation of the specimen, the inelastic effects occurring in the process zone and the chemical dissociation energy. Experimentally, it is very difficult to distinguish between these effects. As a result, the entire energy dissipated during crack growth is interpreted as the energy release rate.

3.2. Experimental Identification of Energy Release Rate

Three common testing strategies are presented, which are used to identify the energy release rate as a material characteristic parameter of fracture toughness.

3.2.1. Simple Extension Test. Greensmith & Thomas [91] performed simple extension tests to measure the energy release rates in thin rubber sheets. An initial cut is introduced in a rectangular strip to produce two arms which are clamped in a tension testing machine and pulled apart, see Figure 3.2. The extension ratio in this region is denoted by λ. It is assumed that the thickness h is small enough, such that the couple required to bend the arms is negligible in comparison to the tensile tearing force. The arms are required to be sufficiently long in comparison to the width w, to generate regions of steady strain state. When the specimen is deformed, a simple extension region C develops. The strain distributions in the neighborhood D of the clamps and in the neighborhood B of the tip of the cut are complicated in character. However, provided the uncut portion of the test piece is also sufficiently long, there is a region A which is substantially undeformed. A small increase Δc in the cut length at constant applied

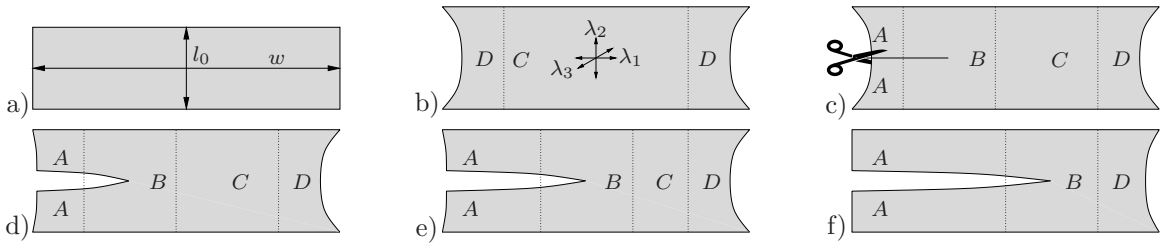

Figure 3.3: a) Specimen geometry. b) Deformation induced strains in the pure shear region C are measured as $\lambda_1 = 1$, λ_2 and $\lambda_3 = -1/\lambda_2$. c) A cut is introduced. The stress free region A and a transition region B develop. d) Crack opens. e) Steady crack growth, region A grows at the expense of C. f) Steady tearing ends when C is consumed.

force F, increases the size of the region C in simple extension. This occurs at the expense of the undeformed region A, while leaving the strain distributions in the neighborhood of the cut tip and of the clamps unaltered. The increase in volume of the regions C, at the expense of the region A, is $\Delta V = wh\Delta c$, referring to the undeformed state. The extension ratio of the material in the region C is unaltered, since it depends only on the applied force F. The increase in stored elastic energy in the test piece is $\Delta E = wh\Delta c\Psi(\lambda)$ in terms of the free energy per unit volume Ψ. The separation Δl of the grips, by which the force is applied, is given by $\Delta l = 2\lambda\Delta c$. The energy release rate is thus computed according to (3.10) with $\Delta A = h\Delta c$ and $\Delta\Pi_{ext} = -2\Delta l F$ as

$$g = \frac{2\lambda\Delta cF + wh\Delta c\Psi(\lambda)}{h\Delta c} = 2\lambda F/h + w\Psi(\lambda) \ . \tag{3.16}$$

It has been shown in Rivlin & Thomas [191] that, if the width w of the test piece is sufficiently large, $\lambda \approx 1$ and $F \gg \Psi hw/2$. Thus (3.16) reduces to

$$g \approx 2F/h \tag{3.17}$$

in terms of the undeformed thickness h of the specimen and the tearing force F.

3.2.2. Pure Shear Test. Measurements of the energy release rate with *pure-shear* test pieces of thin rubber sheets go back to Rivlin & Thomas [191], Thomas [208, 210]. The energy release rate can be calculated from the over-all strain. The shape and dimensions of the specimen are shown in Figure 3.3a. Suitable dimensions are $l_0 \approx 4\,\text{cm}$, $w \approx 30\,\text{cm}$ and $h \approx 1\,\text{mm}$ for the height, width and thickness of the specimen sheets. The specimen is clamped at the long edges and a strain is imposed by separating the clamps in a direction parallel to the short edge l_0. Two strain type regions develop, a region C in pure shear and the regions D, where a slight departure from pure shear takes place close to the force free edge. Two pairs of marks were made on the rubber to measure the strain λ_2 and λ_1 in the region C. The measured $\lambda_1 = 0.994$ was considered to be close enough to $\lambda_1 = 1$, required for pure shear. For a pure shear state, the extension ratios in the three principal directions are thus $\lambda_1 = 1$, $\lambda_2 > 1$ and $\lambda_3 = 1/\lambda_2$, see Figure 3.3b. The incision was then made, Fig. 3.3c. The regions A and B develop in the test piece, where A is substantially undeformed and the region B, lying between A and C, is in a complicated state of strain, Fig. 3.3d. Provided that the overall separation between the clamps is unchanged, the extension ratio λ_2, defining the amount of pure shear in the region C, is unchanged during crack growth. An increase in the cut length of Δc does not alter the state of the strain in the region B but merely shifts this region parallel to

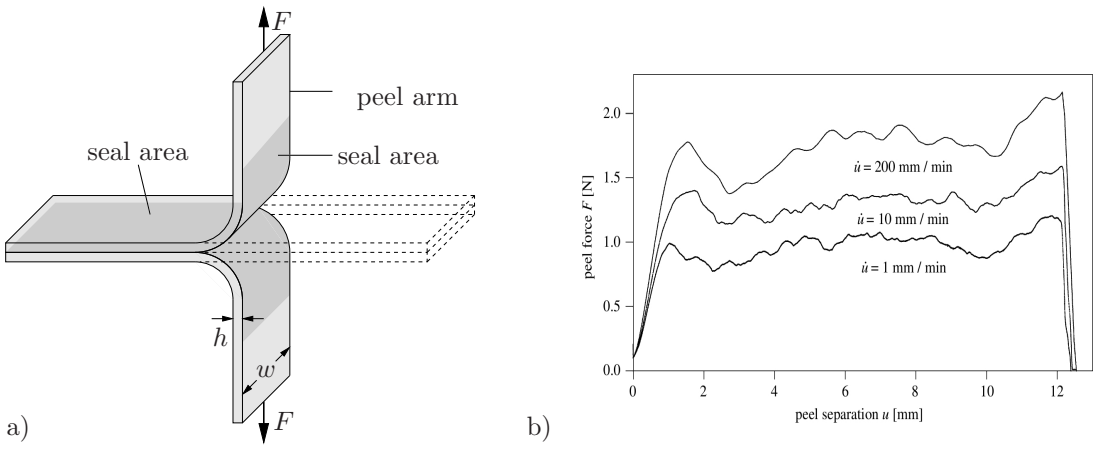

Figure 3.4: a) Peel test geometry. Two layers of flexible polymer are bonded together in the seal area. The peel arms are pulled apart, the angle of separation between the layers is 180°. b) Load-displacement curves from Geissler et al. [78].

the direction of the cut. This causes the regions A to grow at the expense of the region C, Fig. 3.3e. Thus, an increase in crack length Δc transfers a volume $\Delta V = l_0 h \Delta c$ of the rubber from a state of pure shear to the undeformed state until the region C is completely consumed by the growth of A. This marks the end of the steady tearing under pure shear state Fig. 3.3f. As the crack advances a step Δc, the width of the region C decreases by the same amount. The energy in the pure shear state, released during crack growth, must be known in terms of λ_2. Hence the net variation ΔE of stored elastic energy is

$$\Delta E = -\Psi(\lambda_1, \lambda_2, \lambda_3) l_0 h \Delta c \ . \tag{3.18}$$

The quantity Ψ can easily be estimated assuming a material model. To derive the crack speed, equidistant points are marked on the undeformed specimen surface. The passage of the tip past the reference marks is timed, giving the crack speed v. The energy release rate is thus computed according to (3.10) with $\Delta A = \Delta c h$ and $-\Delta\Pi = -\Delta E$ as

$$g = -\Delta E/(\Delta c h) = \Psi(\lambda_1, \lambda_2, \lambda_3) l_0 \tag{3.19}$$

in terms of the undeformed length l_0 of the specimen and the free energy per unit volume.

3.2.3. T-Peel Adhesion Test. The *T-peel test* is used to analyze the adhesion of sealed polymeric films. Gent & Lai [83] analyzed partially crosslinked sheets of elastomer, where the interlinking of two sheets was controlled. Nase et al. [170] analyzed two-component peel systems, consisting of a film and interface component. The interface between two films acts as a predetermined breaking point upon mechanical loading. For testing purposes, the end parts of the layers remain unsealed. These unbonded ends are bent and clamped in the tension testing machine. A constant head speed is applied and the load versus the head movement is recorded. The bent, unbonded ends form a T-shape when pulled apart and the angle of separation between the layers is 180 degrees, see Figure 3.4a. Experiments performed by Geissler et al. [78] are shown in Fig. 3.4b, where the peel force F is plotted over the peel separation u. First, an elastic loading is observed, until the peel force reaches a local maximum at the peel initialization, whereafter the load drops slightly. A plateau like curve progression is followed, in which the force remains constant, except for some fluctuations. An increase of force is observed when

peeling the border region at the end of the test piece. Geissler et al. [78] performed peeling tests at three different constant head speeds, to demonstrate the crack speed dependence of the energy release rate. The peel force F is observed to increase with increasing displacement rate. Transferring the simplification that $\lambda \approx 1$ in the peel arms from the *simple-extension test* to the *T-peel test*, the head movement Δu is equal to the distance peeled Δc. Thus, the crack speed v is equal to the displacement rate of the peel arms $\dot{u}$. According to (3.10) the energy release rate is $g = -\Delta\Pi/\Delta A$. Similar to the simple-extension test shown in Rivlin & Thomas [191], the arms which are in simple extension store comparably little energy, compared to the external power due to loading. By neglecting the increase in stored elastic energy, the energy release rate is computed with $\Delta A = \Delta c w$ and $-\Delta\Pi = 2F\Delta u$ as

$$g \approx \frac{2F\Delta u}{w\Delta c} = \frac{2F}{w} \,. \tag{3.20}$$

The energy release rate may therefore be derived from the tearing force F and is independent of the length Γ of the crack. The rate of propagation of the crack is governed only by the rate of separation of the grips.

3.3. Phase Field Approximation of Crack Topology

This section considers the introduction of a phase field model of crack surface topology. The idea of regularizing a sharp crack by a diffusive crack topology was motivated in Miehe et al. [161]. The introduced *crack phase field* d and the crack functional Γ_l are essential constituents of the phase field model. Based on purely geometrical aspects, a comprehensive understanding of phase field fracture is obtained. In a first step, a one-dimensional bar is investigated, which is then generalized to the two and three dimensional settings.

3.3.1. One-Dimensional Motivation: Bar with a Crack. Imagine an infinitely expanded bar with $L = [-\infty, +\infty]$, with cross-section Γ, occupying the domain $\mathcal{B} = \Gamma \times L$ and the position $x \in L$ defined on the axis. Assume a crack at the axial position $x = 0$ with the crack surface Γ. This sharp crack topology is indicated by an auxiliary field variable $d(x) \in [0, 1]$ with

$$d(x) := \begin{cases} 1 & \text{for } x = 0 \\ 0 & \text{otherwise} \end{cases} \tag{3.21}$$

characterizing the unbroken state for $d = 0$ and the fully broken state of the material for $d = 1$, illustrated in Figure 3.5a. In the following, this auxiliary variable $d(x)$ is termed the *crack phase field*. Obviously, such an approach is related to the continuum theory of damage, where the scalar damage field d describes the development of micro cracks and micro voids in a homogenized macroscopic sense. With this concept in mind, the non-smooth phase field (3.21) is approximated by the exponential function

$$d(x) = \mathrm{e}^{-|x|/l} \,. \tag{3.22}$$

It smears out the crack over the axial domain L of the bar, representing a regularized or diffusive crack topology as depicted in Figure 3.5b. The regularization is governed by the length scale parameter l and gives the discontinuous crack topology (3.21) for $l \to 0$. The exponential function (3.22) has the property

$$d(0) = 1 \quad \text{and} \quad d(\pm\infty) = 0 \tag{3.23}$$

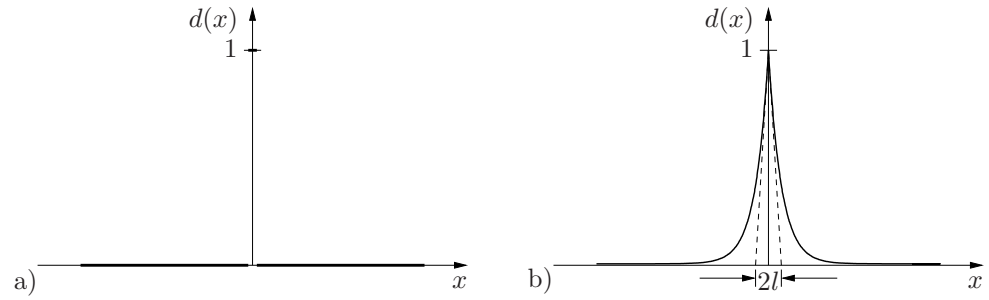

Figure 3.5: Sharp and diffusive crack modeling. a) Sharp crack at $x = 0$ and b) diffusive crack at $x = 0$ modeled with the length scale l.

and is obtained as the solution of the homogeneous differential equation

$$d(x) - l^2 d''(x) = 0 \text{ in } \mathcal{B} \tag{3.24}$$

subject to the Dirichlet-type boundary conditions (3.23). This differential equation is the Euler equation of the variational principle

$$d = \text{Arg}\left\{ \inf_{d \in W} I(d) \right\} \quad \text{with} \quad W = d | d(0) = 1, d(\pm\infty) = 0 \ , \tag{3.25}$$

in terms of the functional

$$I(d) = \frac{1}{2} \int_{\mathcal{B}} \{ d^2 + l^2 d'^2 \} \, dV. \tag{3.26}$$

This functional can easily be constructed by integrating a Galerkin-type weak form of the differential equation (3.24). Insertion of the exponential function (3.22) into (3.26) and evaluation with $dV = \Gamma \, dx$

$$I(d = \mathrm{e}^{-|x|/l}) = l\Gamma \tag{3.27}$$

gives a relation between the functional I and the crack surface Γ. Dividing the functional (3.26) by the length scale parameter l, yields the functional

$$\Gamma_l(d) := \frac{1}{l} I(d) = \frac{1}{2l} \int_{\mathcal{B}} \left\{ d^2 + l^2 d'^2 \right\} \, dV \tag{3.28}$$

alternatively to (3.26). The minimization of this scaled functional also gives the regularized crack topology (3.22) shown in Figure 3.5b. Resulting from the scaling by the length scale parameter l, the functional $\Gamma_l(d)$ may be considered as the crack surface itself. In the one-dimensional problem under consideration, the evaluation of $\Gamma_l(d)$ at the solution point $x = 0$ gives the crack surface Γ for arbitrary length scales l. This property characterizes the functional Γ_l as an important ingredient of the subsequent constitutive modeling of diffusive crack propagation.

3.3.2. Continuous Formulation: Regularized Crack Topology. The idea of regularizing a sharp crack topology by a diffusive crack topology, based on the introduction of a *crack phase field* d, outlined above, can easily be extended to the multi-dimensional context. Let $\mathcal{B} \subset \mathcal{R}^\delta$ be the reference configuration of a material body with dimension $\delta \in [2, 3]$ in space and $\partial\mathcal{B} \subset \mathcal{R}^{\delta-1}$ its surface as shown in Figure 3.6. To study cracks evolving inside the solid within the time range $\mathcal{T} \in \mathcal{R}_+$ we introduce the time dependent crack phase field $d(\boldsymbol{X}, t)$

$$d := \begin{cases} \mathcal{B} \times \mathcal{T} \to [0, 1] \\ (\boldsymbol{x}, t) \mapsto d(\boldsymbol{x}, t) \end{cases} \tag{3.29}$$

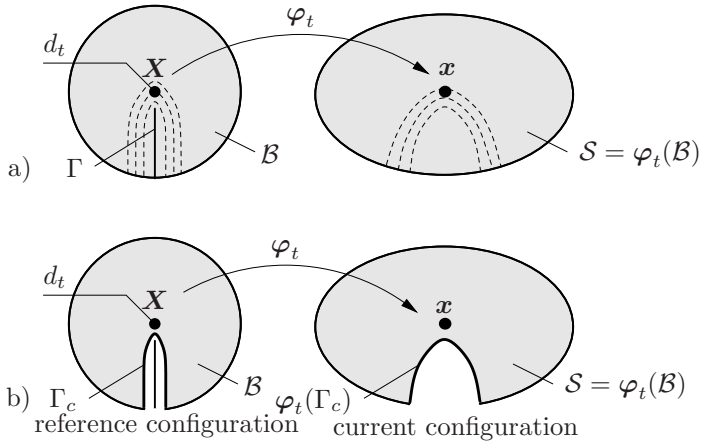

Figure 3.6: Finite deformation of a body with a regularized crack. a) the *crack phase field* d_t defines a regularized crack surface functional $\Gamma_l(d)$ which converges to the sharp crack surface Γ when $l \to 0$. b) the level set $\Gamma_c\{\boldsymbol{X}|d = c\}$ defines for a constant $c \approx 1$ the crack faces in the regularized setting. Parts of the continuum with $d(\boldsymbol{X}, t) > c$ are considered to be free space and are not displayed.

defined on the solid $\mathcal{B}$. Then, a multi-dimensional extension of the regularized crack functional (3.28) reads

$$\Gamma_l(d) = \int_{\mathcal{B}} \gamma(d, \nabla d)\, dV \ , \tag{3.30}$$

where the *crack surface density function* per unit volume of the solid

$$\gamma(d, \nabla d) = \frac{1}{2l} d^2 + \frac{l}{2} |\nabla d|^2 \tag{3.31}$$

has been introduced. This function depends on the crack phase field d and its spatial gradient ∇d. It is governed by the length scale parameter l and plays a critical role in the subsequent modeling of crack propagation. Imagine a given sharp crack surface topology $\Gamma(t) \subset \mathcal{R}^{\delta-1}$ inside the solid $\mathcal{B}$ at time t as depicted in Figure 3.6. In analogy to the one-dimensional variation principle (3.25), the crack phase field $d(\boldsymbol{X}, t)$ on $\mathcal{B}$ is obtained from the *minimization principle of approximated crack topology*

$$d(\boldsymbol{X}, t) = \text{Arg} \left\{ \inf_{d \,\in\, W_{\Gamma(t)}} \Gamma_l(d) \right\} \tag{3.32}$$

proposed in Miehe et al. [161], with the Dirichlet-type boundary constraint $W_{\Gamma(t)} = \{\ d\,|d(\boldsymbol{X}, t) = 1 \text{ at } \boldsymbol{X} \in \Gamma(t)\ \}$. The Euler equations of this variational principle are

$$d - l^2 \Delta d = 0 \ \text{ in } \mathcal{B} \qquad \text{and} \qquad \nabla d \cdot \boldsymbol{n} = 0 \ \text{ on } \partial\mathcal{B} \ , \tag{3.33}$$

where the Laplacian of the phase field is Δd and $\boldsymbol{n}$ is the outward normal on $\partial\mathcal{B}$. Figure 3.7 depicts numerical solutions of the variational problem (3.32) for two dimensional problems, which demonstrate the influence of the length scale l. Note that the limit of the principle (3.32)

$$\lim_{l \to 0} \left\{ \inf_{d \,\in\, W_{\Gamma(t)}} \Gamma_l(d) \right\} = \Gamma(t) \tag{3.34}$$

gives the *sharp crack surface* Γ for vanishing length scale $l \to 0$. A more detailed derivation of the above formulation is outlined in [161]. The crack opening is defined by the *level set of the crack phase field*

$$\Gamma_c = \{\boldsymbol{X} \in \mathcal{B}\,|\, d(\boldsymbol{X}, t) = c\} \ . \tag{3.35}$$

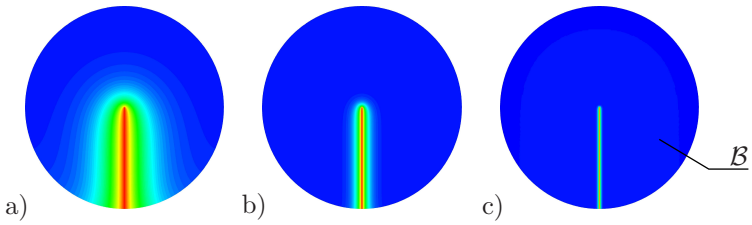

Figure 3.7: Continuum approximations of crack discontinuities with the crack phase field $d \in [0, 1]$ for different length scales $l_a > l_b > l_c$. Solutions of the variational problem (3.32) of diffusive crack topology for a circular specimen with a given sharp crack Γ, prescribed by the Dirichlet condition $d = 1$. The sequence of plots visualizes the limit $\Gamma_l \to \Gamma$ of the regularized crack surface functional (3.30) towards the sharp crack surface for $l \to 0$.

Here, c is a constant, for example $c = 0.98$. Parts of the continuum with a crack phase field $d(\boldsymbol{X}, t) > c$ above the level set, are considered to be free space and are not displayed. In the current configuration, we recognize the opening of the crack by a separation of the crack faces defined by the level set, see Figure 3.6.

4. Phase Field Modeling of Fracture

In this chapter, a model for phase field fracture in *multi-physics problems* is introduced. The overall goal is to design a continuum theory of crack propagation applicable in a modular format, to a large spectrum of coupled multi-field problems, where focus is put on the model problem of finite thermo-viscoelasticity that covers dissipation and thermomechanics with internal variables. A mainly geometric approach to the diffusive crack modeling is introduced. It is based on the introduction of a balance of diffusive crack surfaces and defined in terms of the crack functional and the crack phase field, introduced in Chapter 3. In order to obtain a model for irreversible crack evolution, a restriction on the phase field evolution is introduced to ensure local crack growth. Along with a positive crack driving force, this induces a representation of the crack driving force in terms of a crack driving state function. This constitutive function, which depends on a set of state variables of the multi-physics bulk response, provides the key impact from the bulk response to the crack evolution. Rate independent and rate dependent evolution equations are outlined for the phase field. A key aspect is the definition of a criterion for crack initiation and crack growth. Therefore, a summary of energy, stress, strain and inelasticity based criteria is presented. The energetic approach to brittle fracture introduced in Miehe et al. [161] is briefly reviewed. Furthermore, a maximum stress criterion is introduced, which makes a differentiation between tensile and compression regions simple and is open for complex anisotropies in the constitutive modeling. The qualitative features of the different driving forces are demonstrated with one-dimensional studies. For the three field coupled problem, consisting of the mechanical deformation field, the temperature field and the phase field, a staggered solution scheme is outlined. Practical investigations use an operator splitting technique with fracture phase field predictor, followed by a mechanical subproblem and a heat conduction corrector in line with treatments in Miehe [150], Miehe et al. [161]. Such a tool offers a simple algorithm for crack updates, that can be linked for any crack driving state function to any multi-physics problem via one-pass operator splits or Gauss-Seidel-type iterations between crack and bulk response.

4.1. Primary Fields and Functionals

In the large strain context, the response of the fracturing solid is characterized by the deformation field, the absolute temperature field and the crack phase field

$$\boldsymbol{\varphi} : \begin{cases} \mathcal{B} \times \mathcal{T} \to \mathcal{R}^\delta \\ (\boldsymbol{X}, t) \mapsto \boldsymbol{\varphi}(\boldsymbol{X}, t) \end{cases} , \quad \theta : \begin{cases} \mathcal{B} \times \mathcal{T} \to \mathcal{R}_+ \\ (\boldsymbol{X}, t) \mapsto \theta(\boldsymbol{X}, t) \end{cases} \text{ and } \quad d : \begin{cases} \mathcal{B} \times \mathcal{T} \to [0, 1] \\ (\boldsymbol{X}, t) \mapsto d(\boldsymbol{X}, t) \end{cases} . \tag{4.1}$$

$\boldsymbol{\varphi}$ (2.2) maps material points $\boldsymbol{X} \in \mathcal{B}$ onto spatial points $\boldsymbol{x} = \boldsymbol{\varphi}(\boldsymbol{X}, t)$ at time $t \in \mathcal{T}$. d (3.29) determines locally the fractured state of the material point $\boldsymbol{X} \in \mathcal{B}$ at time $t \in \mathcal{T}$, that is for $d = 0$ unbroken and for $d = 1$ fully broken. The gradients of the deformation and the temperature field are

$$\boldsymbol{F} := \nabla \boldsymbol{\varphi}_t \quad \text{and} \quad \mathbb{F} := \nabla \theta \ . \tag{4.2}$$

The *spatial temperature gradient* is obtained by a parametrization of the temperature by the spatial coordinates $\boldsymbol{x} = \boldsymbol{\varphi}(\boldsymbol{X}, t)$, yielding the relationship

$$\mathbb{f} := \nabla_{\boldsymbol{x}} \theta(\boldsymbol{x}, t) = \boldsymbol{F}^{-T} \mathbb{F} \ . \tag{4.3}$$

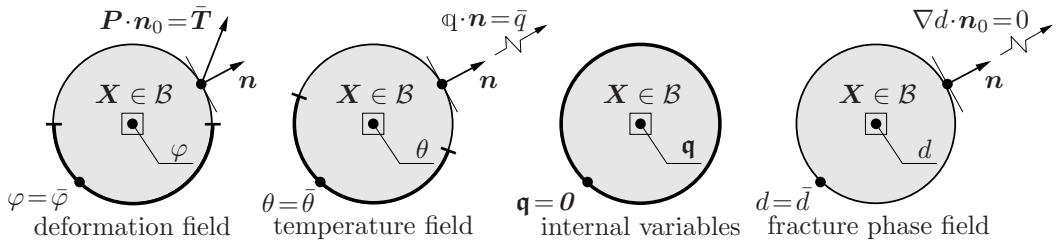

Figure 4.1: Primary fields of thermo-viscoelasticity coupled with phase field fracture. The deformation field $\boldsymbol{\varphi}$, temperature field θ, internal variables $\mathfrak{q}$ and phase field d are defined on the solid domain $\mathcal{B}$. The boundary $\partial\mathcal{B}$ of the solid is decomposed for Dirichlet- and Neumann-type boundary conditions associated with the mechanical and thermal problem. The diffusive fracture problem has zero Neumann conditions on the full boundary.

Let $\boldsymbol{\sigma}$ denote the Eulerian (true) Cauchy stress tensor (2.22). Then, the Kirchhoff (2.23), the first Piola (2.24) and the symmetric Piola stress tensor (2.25) are

$$\boldsymbol{\tau} := J\boldsymbol{\sigma} \quad , \quad \boldsymbol{P} := J\boldsymbol{\sigma}\boldsymbol{F}^{-T} \quad \text{and} \quad \boldsymbol{S} := \boldsymbol{F}^{-1}J\boldsymbol{\sigma}\boldsymbol{F}^{-T} \, , \tag{4.4}$$

respectively. Furthermore, let $\mathbb{q}$ (2.26) denote the Eulerian (true) heat flux vector and $\mathbb{h} := J\mathbb{q}$ the Kirchhoff-type heat flux. Then

$$\mathbb{Q} := J\boldsymbol{F}^{-1}\mathbb{q} \tag{4.5}$$

is the Lagrangian heat flux vector (2.27). The regularized crack surface Γ_l (3.30) is defined

$$\Gamma_l(d) = \int_{\mathcal{B}} \gamma(d, \nabla d)\, dV \quad \text{with} \quad \gamma(d, \nabla d) = \frac{1}{2l}d^2 + \frac{l}{2}|\nabla d|^2 \tag{4.6}$$

in terms of the crack surface density function (3.31). This function, which depends on the crack phase field d and its spatial gradient, ∇d, plays a central role in the modeling of crack propagation.

4.2. Boundary Conditions of the Coupled Problems

In order to solve the set of balance equations defined in Section 2.3 for finite thermo-viscoelasticity coupled with the fracture phase field equation, we have to postulate boundary conditions for the coupled problem. To this end, the surface $\partial\mathcal{B}$ of the reference configuration is decomposed into mechanical and thermal parts

$$\partial\mathcal{B} = \partial\mathcal{B}^{\varphi} \cup \partial\mathcal{B}^{t} \quad \text{and} \quad \partial\mathcal{B}^{\theta} \cup \partial\mathcal{B}^{q} \tag{4.7}$$

with $\partial\mathcal{B}^{\varphi} \cap \partial\mathcal{B}^{t} = \emptyset$ and $\partial\mathcal{B}^{\theta} \cap \partial\mathcal{B}^{q} = \emptyset$. We postulate Dirichlet- and Neumann-type boundary conditions for the mechanical problem

$$\boldsymbol{\varphi} = \bar{\boldsymbol{\varphi}}(\boldsymbol{X}, t) \text{ on } \partial\mathcal{B}^{\varphi} \quad \text{and} \quad \boldsymbol{\sigma}\boldsymbol{n} = \bar{t}(\boldsymbol{x}, t) \text{ on } \partial\mathcal{S}^{t} \tag{4.8}$$

and for the thermal problem

$$\theta = \bar{\theta}(\boldsymbol{X}, t) \text{ on } \partial\mathcal{B}^{\theta} \quad \text{and} \quad \mathbb{q}\boldsymbol{n} = \bar{q}(\boldsymbol{x}, t) \text{ on } \partial\mathcal{S}^{q} \tag{4.9}$$

with prescribed deformation $\bar{\boldsymbol{\varphi}}$, traction $\bar{\boldsymbol{t}}$, temperature $\bar{\theta}$ and heat outflux $\bar{q}$, see Figure 4.1. The *convective heat exchange* is of particular importance. It is governed by the constitutive equation

$$\bar{q} = h_c(\theta - \theta_\infty) \text{ on } \partial\mathcal{S}^{q} \tag{4.10}$$

defined on the exterior boundary, where h_c is the convective heat exchange coefficient and θ_∞ a given ambient temperature. In addition, the homogeneous Neumann-type boundary conditions

$$\partial_{\nabla d}\gamma \cdot \boldsymbol{n}_0 = 0 \quad \text{on} \quad \partial\mathcal{B} \tag{4.11}$$

are applied for the fracture phase field d, see Figure 4.1.

4.3. General Equations of Finite Thermo-Viscoelasticity

The state of a local material point is assumed to be described by the deformation gradient $\boldsymbol{F}$, the temperature θ and the phase field d. For inelastic materials, this set is extended by additional internal variables, say $\mathbf{q}$, employed for the description of inelastic dissipative processes. The *Helmholtz free energy per unit mass* is then formulated in terms of these state variables

$$\Psi = \hat{\Psi}(\boldsymbol{F}, \theta, \mathbf{q}, d) \ . \tag{4.12}$$

The specific constitutive function will be presented in detail in each chapter. With this functional dependency at hand, we get the intrinsic (local) *dissipation* from the Clausius-Planck inequality (2.55)

$$\rho_0 \mathcal{D}_{loc} := \boldsymbol{P} : \dot{\boldsymbol{F}} - \rho_0 \dot{\Psi} - \rho_0 \eta \dot{\theta} \ \geq \ 0 \ , \tag{4.13}$$

defined per unit reference volume. Here, $\boldsymbol{P}$ is the *nominal stress* tensor introduced in (2.24) and η is the *specific entropy* per unit mass. Incorporation of the time derivative of the free energy function gives the expression

$$\rho_0 \mathcal{D}_{loc} = (\boldsymbol{P} - \rho_0 \partial_{\boldsymbol{F}} \Psi) : \dot{\boldsymbol{F}} - (\rho_0 \eta + \rho_0 \partial_\theta \Psi)\, \dot{\theta} - \rho_0 \partial_{\mathbf{q}} \Psi : \dot{\mathbf{q}} \ - \rho_0 \partial_d \Psi \dot{d} \geq \ 0 \ . \tag{4.14}$$

The constitutive expressions for the nominal stress tensor $\boldsymbol{P}$ and the entropy η are then determined by the free energy. Following a standard argument, we obtain

$$\boldsymbol{P} = \rho_0 \partial_{\boldsymbol{F}} \Psi(\boldsymbol{F}, \theta, \mathbf{q}, d) \qquad \text{and} \qquad \eta = -\partial_\theta \Psi(\boldsymbol{F}, \theta, \mathbf{q}, d) \ . \tag{4.15}$$

These assumptions reduce the Clausius-Planck inequality (4.14) to the form

$$\rho_0 \mathcal{D}_{loc} = \mathfrak{p} : \dot{\mathbf{q}} + \beta \dot{d} \geq \ 0 \quad \text{with} \quad \left\{ \begin{array}{l} \mathfrak{p} := -\rho_0 \partial_{\mathbf{q}} \Psi(\boldsymbol{F}, \theta, \mathbf{q}, d) \\ \beta := -\rho_0 \partial_d \Psi(\boldsymbol{F}, \theta, \mathbf{q}, d) \end{array} \right. , \tag{4.16}$$

where we introduced, per definition, the thermodynamic driving forces $\mathfrak{p}$, conjugated to the internal variables $\mathbf{q}$. β is the energetic dual variable to the fracture phase field d. A typical form of the evolution system of internal variables is provided by the constitutive initial-value problem

$$\partial_{\mathbf{q}} \Psi(\boldsymbol{F}, \theta, \mathbf{q}, d) + \partial_{\dot{\mathbf{q}}} \Phi(\dot{\mathbf{q}}) = \mathbf{0} \quad \text{with} \quad \mathbf{q}(0) = \mathbf{q}_0 \tag{4.17}$$

in terms of a dissipation function Φ that depends smoothly on the temporal evolution $\dot{\mathbf{q}}$ of the internal variables with normalization condition $\Phi(\mathbf{0}) = 0$. Assuming local crack growth $\dot{d} \geq 0$, Φ to be convex and Ψ to be convex and monotonically decreasing with d, we observe that (4.16) is automatically satisfied. An alternative form of the evolution system of internal variables is provided by the constitutive initial-value problem

$$\dot{\mathbf{q}} = \mathcal{F}(\boldsymbol{F}, \theta, \mathbf{q}, d) \quad \text{with} \quad \dot{\mathbf{q}}(0) = \dot{\mathbf{q}}_0 \ . \tag{4.18}$$

Note, that the overall constitutive model of thermo-viscoelasticity is governed by the constitutive functions Ψ for the free energy and Φ or $\mathcal{F}$ for the dissipation.

The heat flux in the interior of the body is assumed to be governed by an isotropic Eulerian Fourier-type law for the Kirchhoff heat flux $\mathbb{h}$. This gives the constitutive formulation

$$\mathbb{Q} = -k\, \boldsymbol{C}^{-1}\mathbb{F} \tag{4.19}$$

for the Lagrangian heat flux defined in (4.5), in terms of the material temperature gradient $(4.2)_2$. This provides a positive dissipation

$$\mathcal{D}_{con} := -\frac{1}{\theta}\mathbb{Q}\cdot\mathbb{F} \geq 0 \tag{4.20}$$

for a positive heat conductivity parameter $k > 0$. The coupling of the heat flux with the deformation is governed by its dependence on the right Cauchy Green tensor $\boldsymbol{C} = \boldsymbol{F}^T\boldsymbol{F}$, which is a positive definite tensor.

We now embed the above outlined general constitutive functions into the global balance equations. These govern the initial boundary value problem of coupled thermo-viscoelasticity at finite strains. The first set of equations covers the balances of linear (2.32) and angular momentum (2.34)

$$\boxed{\rho_0\ddot{\boldsymbol{\varphi}} = \mathrm{Div}[\boldsymbol{P}] + \rho_0\boldsymbol{\gamma} \quad \text{and} \quad \boldsymbol{F}\boldsymbol{P}^T = \boldsymbol{P}\boldsymbol{F}^T\ .} \tag{4.21}$$

Here, $\boldsymbol{\gamma}$ is a prescribed body-force field, $\boldsymbol{P}$ is the nominal stress tensor introduced in (2.24) and $\mathrm{Div}(\cdot)$ is the divergence operator with respect to the Lagrangian coordinates $\boldsymbol{X}$. The second essential global equation is the balance of internal energy (2.43)

$$\rho_0\dot{e}_0 = \boldsymbol{P} : \dot{\boldsymbol{F}} - \mathrm{Div}[\mathbb{Q}] + \rho_0 R\ . \tag{4.22}$$

The internal energy density is e_0, with respect to the volume of the reference configuration. R denotes a predefined heat source with respect to the unit of the reference volume and $\boldsymbol{P}:\dot{\boldsymbol{F}}$ is the stress power with respect to the unit of the reference volume. Based on the Legendre transformation $e_0 = \Psi + \theta\eta$, we insert the constitutive equations (4.15) and (4.16) to obtain the evolution $\rho_0\dot{e}_0 = \boldsymbol{P} : \dot{\boldsymbol{F}} + \rho_0\theta\dot{\eta} - \rho_0\mathcal{D}_{loc}$. Insertion into (4.22) gives the evolution equation for the entropy

$$\rho_0\theta\dot{\eta} = \mathrm{Div}[-\mathbb{Q}] + \rho_0 R + \rho_0\mathcal{D}_{loc} \tag{4.23}$$

in terms of the dissipation $\mathcal{D}_{loc} \geq 0$, defined in (4.16). Starting from $(4.15)_2$, we obtain the constitutive rate equation

$$\rho_0\theta\dot{\eta} = \rho_0 c_s\,\dot{\theta} - \rho_0 H\ , \tag{4.24}$$

with the *heat capacity*

$$c_s := -\theta\partial^2_{\theta\theta}\Psi(\boldsymbol{F}, \mathfrak{q}, \theta, d) \tag{4.25}$$

and the *latent heating*

$$H := \theta\partial_\theta\,[\,\boldsymbol{P} : \dot{\boldsymbol{F}} - \mathcal{D}_{loc}\,] = (\theta\partial_\theta\boldsymbol{P}) : \dot{\boldsymbol{F}} - (\theta\partial_\theta\mathfrak{p}) : \dot{\mathfrak{q}} - (\theta\partial_\theta\beta)\dot{d}\ . \tag{4.26}$$

Insertion into (4.23) finally gives an evolution equation for the temperature

$$\boxed{\rho_0 c_s \dot{\theta} = \mathrm{Div}[-\mathbb{Q}] + \rho_0(R + H + \mathcal{D}_{loc}) \ .} \tag{4.27}$$

Note that the first bracket vanishes in an adiabatic process, i.e for $\mathbb{Q} \equiv 0$ and $R \equiv 0$. Equation (4.27) is known as the coupled temperature evolution equation of thermo-viscoelasticity. The last two terms on the right-hand side, characterize the latent (thermoelastic) and dissipative coupling effects. Similar to applications of metal thermo-viscoelasticity, we expect the situation $|H| \ll \mathcal{D}_{loc}$. Investigations of MIEHE [150] for entropic thermoelasticity demonstrated the small amount of latent heating. In our subsequent investigation we neglect the latent heating effect in the temperature evolution equation (4.27) by setting $H \approx 0$.

4.4. Balance Equation of Phase Field Fracture

We consider a generalized formulation for the evolution of the phase field $d(\boldsymbol{X}, t)$ that is open for different constitutive models of energetic and non-energetic driving forces. Keeping in mind a purely geometric picture, we introduce a balance of the regularized *crack surface functional* Γ_l defined in (3.30)

$$\dot{\Gamma}_l(d) = S_l - R_l \ . \tag{4.28}$$

$\dot{\Gamma}_l$ is the evolution of regularized crack surface, S_l is a local crack source and R_l is a local viscous crack resistance term. The evolution of regularized crack surface can be recast into the form

$$\dot{\Gamma}_l(d) = \int_{\mathcal{B}} \delta_d\gamma \cdot \dot{d} \, dV + \int_{\partial\mathcal{B}} (\partial_{\nabla d}\gamma \boldsymbol{n}) \cdot \dot{d} \, dA \tag{4.29}$$

where we have introduced the variational or functional derivative of the crack surface density function

$$\delta_d\gamma := \partial_d\gamma - \mathrm{Div}[\partial_{\nabla d}\gamma] = \frac{1}{l}[d - l^2\Delta d] \ . \tag{4.30}$$

In (4.29), $\boldsymbol{n}$ is the outward normal on $\mathcal{B}$. In what follows, we assume homogeneous Neumann-type boundary conditions on the surface $\partial\mathcal{B}$ of the reference configuration $\mathcal{B}$

$$\nabla d \cdot \boldsymbol{n} = 0 \quad \text{on } \partial\mathcal{B} \ . \tag{4.31}$$

As a consequence $\partial_{\nabla d}\gamma \boldsymbol{n} = l\nabla d \cdot \boldsymbol{n} = 0$ and the right hand side of (4.29) vanishes. We obtain the evolution of the regularized crack surface

$$\dot{\Gamma} = \frac{1}{l}\int_{\mathcal{B}} D_c \cdot \dot{d} \, dV \quad \text{with} \quad D_c := l\delta_d\gamma = d - l^2\Delta d \tag{4.32}$$

the dimensionless *geometric crack resistance*, defined by the variational derivative of the crack density function $\boldsymbol{\gamma}_l$ introduced in (3.31). The local crack source S_l and the local viscous crack resistance R_l are introduced as power type expressions, in terms of a crack driving force $\mathcal{H}$ and a crack evolution time η

$$S_l = \frac{1}{l}\int_{\mathcal{B}} (1-d)\mathcal{H} \cdot \dot{d} \, dV \geq 0 \quad \text{and} \quad R_l = \frac{1}{l}\int_{\mathcal{B}} (\eta\dot{d})\dot{d} \, dV \tag{4.33}$$

Thus, the global balance of the regularized crack surface reads

$$\int_{\mathcal{B}} D_c \dot{d} \; dV = \int_{\mathcal{B}} (1-d)\mathcal{H} \cdot \dot{d} \; dV - \int_{\mathcal{B}} (\eta \dot{d}) \dot{d} \, dV \; . \tag{4.34}$$

Reformulating the balance equation (4.34) into a local constraint, we obtain the local balance equation

$$\boxed{[d - l^2 \Delta d] = (1-d)\mathcal{H} - \eta \dot{d}} \tag{4.35}$$

that governs the nonlocal evolution of crack phase field d, in the case of loading and unloading and is defined in terms of a *local effective driving force* $\mathcal{H}$. The term $\Delta(\cdot) = \mathrm{Div}(\nabla_{\boldsymbol{X}}(\cdot))$ denotes the Laplace operator. We focus on an *irreversibility* of the crack evolution, governed by the constraint

$$\frac{d}{dt} \Gamma_l(d) \geq 0 \tag{4.36}$$

on the evolution of the regularized crack surface. Hence, the constitutive crack driving power must be positive. Taking into account the constitutive representation (4.33), this is achieved for the physically based restrictions

$$d \in [0,1] \; , \quad \dot{d} \geq 0 \quad \text{and} \quad \mathcal{H} \geq 0 \; . \tag{4.37}$$

These conditions ensure a growth of the fracture phase field up to the fully broken state. The condition $(4.37)_1$ demands locally, that the phase field d, which starts from the initial condition $d = 0$ for the unbroken state, is bounded by $d \to 1$ when cracks accumulate. In order to obtain further insight to the constitutive definition of the driving force $\mathcal{H}$, consider a rate-independent crack growth with $\eta = 0$ for a homogeneous problem with $\nabla d = 0$. Then (4.35) gives a one-to-one relationship between the crack phase field d and the crack driving force $\mathcal{H}$. As a consequence, conditions $(4.37)_{1,2}$ can be recast into the constraints

$$d = \frac{\mathcal{H}}{1+\mathcal{H}} \in [0,1] \quad \text{and} \quad \dot{d} = \frac{\dot{\mathcal{H}}}{(1+\mathcal{H})^2} \geq 0 \tag{4.38}$$

in terms of the driving force $\mathcal{H}$ and its evolution $\dot{\mathcal{H}}$, which must be satisfied by the constitutive expression (4.37). Clearly, as indicated by $(4.38)_1$, locally unbroken and fully broken states are associated with

$$d = 0 \Leftrightarrow \mathcal{H} = 0 \quad \text{and} \quad d \to 1 \Leftrightarrow \mathcal{H} \to \infty \; . \tag{4.39}$$

Taking into account these relationships, the driving force $\mathcal{H}$ must satisfy the constraint

$$\frac{d}{dt} \mathcal{H} \geq 0 \; . \tag{4.40}$$

Hence, the constitutive driving force $\mathcal{H}$ must be a positive, monotonously growing function. This is realized by expressing the local crack driving force $\mathcal{H}$ by the maximum value of the associated crack driving state function $\widetilde{D}$

$$\mathcal{H}(\boldsymbol{X}, t) = \max_{s \in [0,t]} \widetilde{D}(\boldsymbol{X}, s) \quad \text{with} \quad \widetilde{D}(\boldsymbol{X}, s) \geq 0 \tag{4.41}$$

obtained in the full process history $s \in [0,t]$. $\widetilde{D}$ is independent of the crack phase field d. It is assumed to be a positive constitutive function of physical state variables, responsible for the accumulation of the phase field. Combining the evolution equation (4.35) with (4.41) is consistent with the structure

$$\eta \dot{d} = \langle (1-d)\widetilde{D} - D_c \rangle \geq 0 \ . \tag{4.42}$$

Hence, a non-smooth evolution of the crack phase field takes place, when the nominal state function $(1-d)\widetilde{D}$ exceeds the geometric crack resistance D_c. For the rate-independent limit $\eta \to 0$, the associated local evolution system is

$$\dot{d} \geq 0 \ , \quad [(1-d)\widetilde{D} - D_c] \leq 0 \ , \quad \dot{d}[(1-d)\widetilde{D} - D_c] = 0 \ . \tag{4.43}$$

Observe again, that the dimensionless crack state function $\widetilde{D}$ is the key constitutive input on the driving side, while the dimensionless geometric crack resistance $D_c = l\delta_d\gamma_l$ is related to the variational derivative of the crack surface density function γ_l.

4.5. Crack Driving State Functions for Different Fracture Criteria

The definition of the effective crack driving state function $\widetilde{D}$ allows a strong flexibility, with regard to alternative crack driving criteria. In the following, some examples are presented to complete specific definitions of the phase field equation (4.35).

4.5.1. Evolution Equations in Gradient Damage Mechanics. A class of gradient damage approaches to the modeling of brittle fracture assumes a total pseudo-energetic density W per unit volume, which consists of the sum

$$W(\boldsymbol{\varepsilon}, d, \nabla d) = W_{bulk}(\boldsymbol{\varepsilon}; d) + W_{frac}(d, \nabla d) \tag{4.44}$$

of a degrading elastic bulk energy W_{bulk} and a contribution due to fracture W_{frac}, which contains the accumulated dissipative energy. The bulk contribution is assumed to have the simple form

$$W_{bulk}(\boldsymbol{\varepsilon}; d) = g(d)\widetilde{\Psi}(\boldsymbol{\varepsilon}) \ , \tag{4.45}$$

where $\widetilde{\Psi}(\boldsymbol{\varepsilon})$ is the effective energy stored in the undamaged material and $g(d) = (1-d)^2$ is a degradation function that satisfies the properties $W_{bulk}(\boldsymbol{\varepsilon}; 0) = \widetilde{\Psi}(\boldsymbol{\varepsilon}), W_{bulk}(\boldsymbol{\varepsilon}; 1) = 0$, $\partial_d W_{bulk}(\boldsymbol{\varepsilon}; d) < 0$ and $\partial_d W_{bulk}(\boldsymbol{\varepsilon}; 1) = 0$. In the finite deformation context, $\boldsymbol{\varepsilon}$ is Almansi's tensor as defined in (2.20). The above introduction of competing bulk and surface energy densities is in line with treatment of gradient damage theories outlined in the works Frémond & Nedjar [74], Frémond [73], Marigo and collaborators Benallal & Marigo [21] and Pham et al. [180]. See also Miehe [164] for an embedding into variational principles. The evolution of the damage variable d is then determined by the variational derivative of this potential density. In a rate independent setting, this is provided by the Kuhn-Tucker-type equations

$$\dot{d} \geq 0 \ ; \quad -\delta_d W \leq 0 \ , \quad \dot{d}[-\delta_d W] = 0 \ . \tag{4.46}$$

This equation is shown in Miehe [164] to be the Euler equation of a rate-type variational principle for the evolution problem of gradient damage mechanics. It provided the basis for the phase field modeling of brittle fracture proposed by Miehe et al. [161].

4.5.2. Strain Criterion Without Threshold. An energetic criterion without threshold used by MIEHE ET AL. [161] is based on the fracture contribution to the total pseudo-energy (4.44)

$$W_{frac}(d, \nabla d) = g_c \gamma_l(d, \nabla d) = \frac{g_c}{l}[d^2 + l^2 |\nabla d|^2] \ . \tag{4.47}$$

It is directly related to the crack surface density function γ_l defined in (3.31). Here, g_c is Griffith's critical energy release rate. Hence, a fracture surface energy per unit volume is obtained by multiplying g_c with the crack surface density function. The total pseudo-energy potential takes the form

$$W(\boldsymbol{\varepsilon}, d, \nabla d) = (1-d)^2 \widetilde{\Psi}(\boldsymbol{\varepsilon}) + g_c \gamma_l(d, \nabla d) \tag{4.48}$$

in terms of the two functions $\widetilde{\Psi}$ and γ_l. Then, the loading criterion (4.46) for the phase field includes the loading function

$$-\delta_d W = 2(1-d)\widetilde{\Psi} + g_c \delta_d \gamma_l(d, \nabla d) \tag{4.49}$$

and can be recast into the form

$$\frac{g_c}{l}[d - l^2 \Delta d] = 2(1-d) \max_{s \in [0,t]} \widetilde{\Psi}(\boldsymbol{\varepsilon}(\boldsymbol{X}, s)) \ , \tag{4.50}$$

see MIEHE ET AL. [161]. The comparison with (4.35) identifies the effective crack driving state function

$$\widetilde{D} = \frac{2\widetilde{\Psi}(\boldsymbol{\varepsilon})}{g_c / l} \ . \tag{4.51}$$

Note that this driving state function depends on the ratio of the locally stored effective elastic energy $\widetilde{\Psi}$ to the critical energy release rate g_c, that can be considered to be smeared out over the length scale l. The function $\widetilde{\Psi}(\boldsymbol{\varepsilon})$ is monotonously growing and may be considered to be a norm of the strain $\boldsymbol{\varepsilon}$. Hence, the driving state function is related to the amount of local distortion. A formulation based on a decomposition of the free energy into tensile and compression parts was considered in MIEHE ET AL. [161]

4.5.3. Strain Criterion With Threshold. The criterion (4.51) is a monotonous increasing function of the strains $\boldsymbol{\varepsilon}$, as shown in Figures 4.2a and 4.3a. As a consequence, a damage-type degradation already occurs at low stress and strain levels. In order to avoid this effect, an energetic criterion with threshold can be constructed based on the fracture contribution to the total pseudo-energy (4.44)

$$W_{frac}(d, \nabla d) = 2\Psi_c [d + l^2 |\nabla d|^2] \ . \tag{4.52}$$

Here, Ψ_c is the specific fracture energy per unit volume. Note that, in contrast to the definition (4.47), the phase field d enters the formulation by a linear term. Such formulations of gradient damage mechanics are discussed in FRÉMOND [73], FRÉMOND & NEDJAR [74], PHAM ET AL. [180], MIEHE [164]. After some algebraic manipulation, the total energy potential (4.44) reads

$$W(\boldsymbol{\varepsilon}, d, \nabla d) = (1-d)^2 [\widetilde{\Psi}(\boldsymbol{\varepsilon}) - \Psi_c] + 2\Psi_c l \gamma_l(d, \nabla d) \tag{4.53}$$

in terms of the crack surface density function γ_l defined in (3.31). Then, the loading criterion (4.46) for the phase field includes the loading function

$$-\delta_d W = 2(1-d)[\widetilde{\Psi}(\boldsymbol{\varepsilon}) - \Psi_c] - 2\Psi_c l \delta_d \gamma_l(d, \nabla d) \tag{4.54}$$

and can be recast into the form

$$2\Psi_c[d - l^2\Delta d] = 2(1-d)\max_{s\in[0,t]}\langle\widetilde{\Psi}(\boldsymbol{\varepsilon}(\boldsymbol{X},s)) - \Psi_c\rangle \ . \tag{4.55}$$

The comparison with (4.35) identifies the crack driving state function

$$\widetilde{D} = \Big\langle \frac{\widetilde{\Psi}(\boldsymbol{\varepsilon})}{\Psi_c} - 1 \Big\rangle \tag{4.56}$$

in terms of the ramp function $\langle\cdot\rangle := (\cdot + |\cdot|)/2$ determined by the McAuley bracket. Note that this criterion is independent of the length scale l, because the material parameter Ψ_c for the specific fracture energy refers to the unit volume.

4.5.4. Stress Criteria With and Without Threshold. In order to obtain a simple approach to brittle fracture that takes into account a decomposition into tension and compression, a stress criterion is developed. To this end, consider the Legendre-Fenchel transformation of the effective energy $\widetilde{\Psi}$ to its dual $\widetilde{\Psi}^*$

$$\widetilde{\Psi}^*(\widetilde{\boldsymbol{\sigma}}) = \sup_{\boldsymbol{\varepsilon}}[\widetilde{\boldsymbol{\sigma}} : \boldsymbol{\varepsilon} - \widetilde{\Psi}(\boldsymbol{\varepsilon})] \tag{4.57}$$

in terms of the effective Cauchy stress $\widetilde{\boldsymbol{\sigma}}$. Insertion into (4.51) and (4.56) gives the alternative representations

$$\widetilde{D} = \frac{2}{g_c/l}[\widetilde{\boldsymbol{\sigma}} : \boldsymbol{\varepsilon} - \widetilde{\Psi}^*(\widetilde{\boldsymbol{\sigma}})] \quad \text{and} \quad \widetilde{D} = \Big\langle \frac{1}{\Psi_c}[\widetilde{\boldsymbol{\sigma}} : \boldsymbol{\varepsilon} - \widetilde{\Psi}^*(\widetilde{\boldsymbol{\sigma}})] - 1 \Big\rangle \tag{4.58}$$

of the fracture driving state functions in terms of the stress function $\widetilde{\Psi}^*$. Inspired by the linear theory of elasticity, based on quadratic functions with identical images $\widetilde{\Psi}^*(\widetilde{\boldsymbol{\sigma}}) = \widetilde{\Psi}(\boldsymbol{\varepsilon}) = \frac{1}{2}\widetilde{\boldsymbol{\sigma}} : \boldsymbol{\varepsilon}$, we postulate the criteria

$$\widetilde{D} = \frac{2\widetilde{\Psi}^*(\widetilde{\boldsymbol{\sigma}})}{g_c/l} \quad \text{and} \quad \widetilde{D} = \Big\langle \frac{\widetilde{\Psi}^*(\widetilde{\boldsymbol{\sigma}})}{\Psi_c} - 1 \Big\rangle \tag{4.59}$$

dual to (4.51) and (4.56) and apply it to nonlinear elasticity.

4.5.5. Principal Tensile Stress Criterion With Threshold. In order to obtain a simple criterion for mixed tensile compression stress modes applicable to general nonlinear and possibly anisotropic elasticity, consider first the decomposition of the effective stresses into tensile and compressive parts

$$\widetilde{\boldsymbol{\sigma}} = \widetilde{\boldsymbol{\sigma}}^+ + \widetilde{\boldsymbol{\sigma}}^- \quad \text{with} \quad \widetilde{\boldsymbol{\sigma}}^+ = \sum_{a=1}^{3}\langle\widetilde{\sigma}_a\rangle \boldsymbol{n}_a \otimes \boldsymbol{n}_a \tag{4.60}$$

in terms of the ramp function $\langle\cdot\rangle := (\cdot + |\cdot|)/2$. In a second step, a quadratic effective stress function is introduced for the definition of the fracture driving force

$$\widetilde{\Psi}^*_{frac}(\widetilde{\boldsymbol{\sigma}}^+) = \frac{1}{2E}|\widetilde{\boldsymbol{\sigma}}^+|^2 = \frac{1}{2E}\sum_{a=1}^{3}\langle\widetilde{\sigma}_a\rangle^2 \,, \tag{4.61}$$

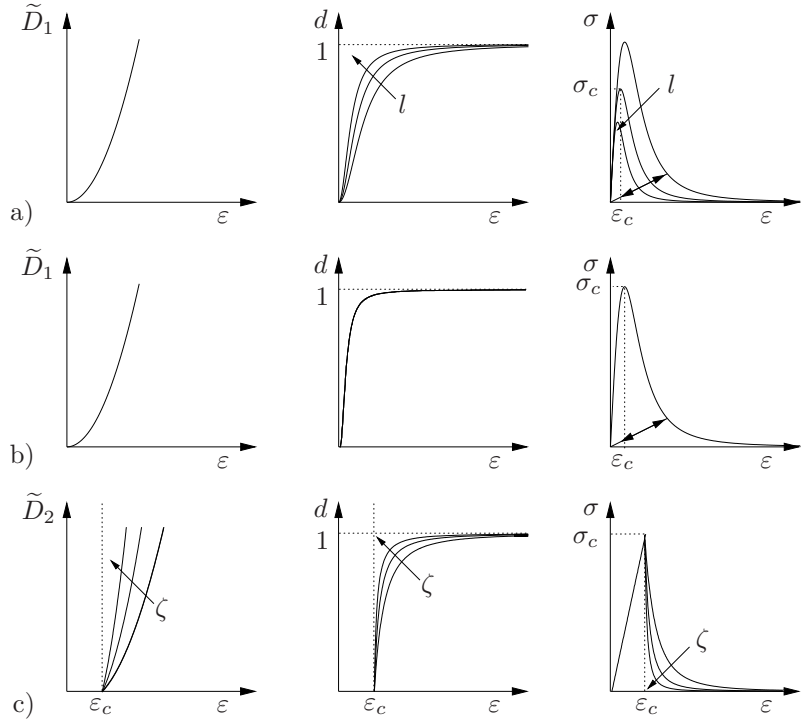

Figure 4.2: Qualitative features of different driving forces in homogeneous test. Performance of a) energetic criterion $\widetilde{D}_1 = E\varepsilon^2/(g_c/l)$ for different length scale parameters l, b) energetic criterion $\widetilde{D}_1 = E\varepsilon^2/(g_c/l)$ with g_c in terms of critical stress σ_c and length scale l $g_c = \frac{\sigma_c l}{E}\frac{4\cdot\sqrt{2}}{3}$ and c) maximum stress criterion $\widetilde{D}_2 = \zeta \cdot \langle(\widetilde{\sigma}/\widetilde{\sigma_c})^2 - 1\rangle$.

independent of the bulk response, where E is a parameter related to Young's modulus. Next, assume the critical fracture energy Ψ_c per unit volume, to be related to a critical fracture stress σ_c via

$$\Psi_c := \frac{\sigma_c^2}{2E} \ . \tag{4.62}$$

Then, insertion of (4.61) and (4.62) into $(4.59)_2$ gives the simple *principal tensile stress criterion*

$$\boxed{\widetilde{D} = \zeta\Big\langle \sum_{a=1}^{3} \langle\widetilde{\sigma}_a/\sigma_c\rangle^2 - 1\Big\rangle \ ,} \tag{4.63}$$

where an additional dimensionless parameter $\zeta > 0$ was introduced that influences the growth of the crack phase field for $\zeta \neq 1$, in the post-critical range. The driving state function provides a quadratically increasing barrier function for stress levels above a failure surface in the principal stress space. It is determined by the critical tensile stress σ_c as depicted in Figure 4.4, whose slope can be influenced by the parameter ζ. Such a criterion is extremely simple to implement and applicable to brittle fracture in nonlinear possibly anisotropic finite elasticity. It generalizes the classical maximum principle stress criterion, which can be traced back to Rankine, Lamé and Navier, to the phase field modeling of fracture. A pure Rankine-type criterion would be related to the phase field driving state function

$$\widetilde{D} = \zeta\big\langle \max(\langle\widetilde{\sigma}_1\rangle^2, \langle\widetilde{\sigma}_2\rangle^2, \langle\widetilde{\sigma}_3\rangle^2)/\sigma_c^2 - 1\big\rangle \ . \tag{4.64}$$

It is related to the simple scenario of decohesion of surfaces perpendicular to the maximum principle stress. Figures 4.2c and 4.3c demonstrate qualitative features of the criterion

(4.63). In particular, Figure 4.3c characterizes the force (4.63) as being physically meaningful. It preserves the elastic properties in uncracked zones.

4.5.6. Ductile Strain Criterion with Threshold. Simple criteria for ductile fracture, occurring after large plastic deformations, can be related to a critical amount of the plastic strains. Let $\mathfrak{q}$ denote a tensorial internal variable that measures the plastic strain, e.g. the Lagrangian logarithmic plastic strain. A simple, non-energetic criterion for ductile fracture may be based on the accumulated plastic strain

$$\epsilon(\boldsymbol{X},t) := \int_{s=0}^{t} |\dot{\mathfrak{q}}(\boldsymbol{X},s)|\, ds \ . \tag{4.65}$$

In formal analogy to the criteria (4.56) and (4.63) of brittle fracture, a crack driving state function can be defined as a barrier function of the equivalent state variable ϵ, as

$$\widetilde{D} = \zeta\langle \frac{\epsilon^2}{\epsilon_{crit}^2} - 1\rangle \ , \tag{4.66}$$

where ϵ_{crit} is a critical equivalent plastic strain at which ductile fracture occurs. This function can be considered as the regularization of an indicator function

$$\widetilde{D} = \begin{cases} 0 & \text{for } \epsilon < \epsilon_{crit} \\ \infty & \text{otherwise} \end{cases} \tag{4.67}$$

that triggers the fracture at $\epsilon = \epsilon_{crit}$. Conceptually, this type of barrier function can be applied to any other plastic state variable, such as the void fraction f in the Gurson-Tvergaard-Needleman models of ductile damage, see Gurson [100] and Tvergaard & Needleman [219]. Chapter 8 uses this state function (4.66) in the analysis of fracture in glassy polymers, related to a critical value of crazes.

4.6. Qualitative Features of Different Driving Forces

Though crack propagation is a highly inhomogeneous phenomenon and should be only considered in the multi-dimensional context, a look at homogeneous and one-dimensional states in Figures 4.2 and 4.3 may illustrate the modeling capabilities. For homogeneous states with $\eta = 0$ and zero Laplacian $\Delta d = 0$, equation (4.35) has the closed-form solution

$$d(t) = \frac{\mathcal{H}(t)}{1+\mathcal{H}(t)} \quad \text{with} \quad \mathcal{H}(t) := \max_{s\in[0,t]} \widetilde{D}(s) \tag{4.68}$$

with starting value $d(0) = 0$ for a virgin state $\widetilde{D}(0) = 0$. Note the limit $d \to 1$ for $\mathcal{H} \to \infty$. As depicted in Figure 4.2, the length scale l controls the shape of the fracture phase field d that turns out to be jump-like for $l \to \infty$. Assuming for the qualitative description in Figures 4.2 and 4.3, the quadratic effective energy functions

$$\widetilde{\Psi} = \frac{E}{2}\varepsilon^2 \quad \text{and} \quad \widetilde{\Psi}^* = \frac{1}{2E}\widetilde{\sigma}^2 \tag{4.69}$$

in the small strain context, the stress function is postulated to have the form

$$\sigma = (1-d)^2\widetilde{\sigma} \quad \text{with} \quad \widetilde{\sigma} = E\varepsilon \ . \tag{4.70}$$

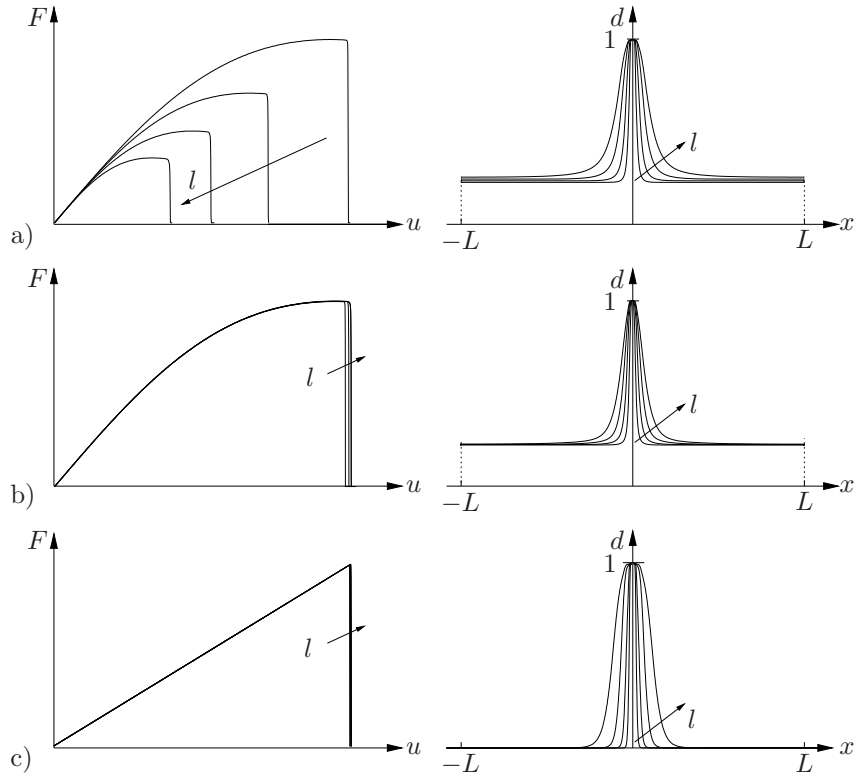

Figure 4.3: Qualitative features of different driving forces in a one-dimensional finite element simulation. Performance of a) energetic criterion $\widetilde{D}_1 = E\varepsilon^2/g_c$, b) energetic criterion $\widetilde{D}_1 = E\varepsilon^2/g_c(\sigma_c)$ with g_c in terms of critical stress σ_c and length scale l $g_c = \frac{\sigma_c^2 l}{E}\frac{4\sqrt{2}}{3}$ and c) maximum stress criterion $\widetilde{D}_2 = \langle(\widetilde{\sigma}/\widetilde{\sigma}_c)^2 - 1\rangle$ for different length scale parameters l with $l/L = \{0.004, 0.008, 0.016, 0.032\}$.

The phase field is computed by the closed-form result (4.68). The energetic criterion without threshold (4.51) takes the form

$$\widetilde{D}_1 = \frac{2\widetilde{\Psi}}{g_c/l} = \frac{E\varepsilon^2}{g_c/l} \quad \text{or} \quad \widetilde{D}_1 = \frac{2\widetilde{\Psi}^*}{g_c/l} = \frac{\sigma^2/E}{g_c/l} \ , \tag{4.71}$$

alternatively, in terms of the strains ε or the effective stresses $\widetilde{\sigma}$. As shown in Figure 4.2a the stress σ defined in (4.70) has different peak values for a given critical energy release rate g_c

$$\sigma_c = \frac{9}{16} E\varepsilon_c \quad \text{with} \quad \varepsilon_c = \sqrt{\frac{g_c/l}{3E}} \ , \tag{4.72}$$

which depend on the length scale l. This has been pointed out by Borden et al. [27]. A modification of (4.70), that uses the critical fracture stress σ_c as a material parameter, resolves $(4.72)_1$ for a length scale dependent g_c

$$\hat{g}_c(l) = \frac{256}{27}\frac{\sigma_c^2 l}{E} \ , \tag{4.73}$$

yielding driving state functions which do not depend on the length scale l

$$\widetilde{D}_1 = \frac{27}{256}(\frac{E\varepsilon}{\sigma_c})^2 \quad \text{or} \quad \widetilde{D}_1 = \frac{27}{256}(\frac{\widetilde{\sigma}}{\sigma_c})^2 \ . \tag{4.74}$$

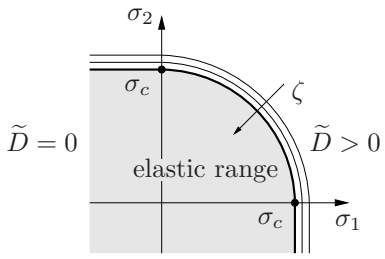

Figure 4.4: Failure surface for the principle stress criterion (4.63). Stress states above the failure surface, determined by the critical fracture stress σ_c, rise the driving force function $\widetilde{D}$ in (4.63), whose slope can be pronounced by the additional parameter $\zeta \geq 1$.

Figure 4.2b shows that such a setting gives a homogeneous stress response σ, independent of the length scale l. This is also the case for the energetic criterion with threshold, (4.56) that takes the form

$$\widetilde{D}_2 = \zeta\big\langle \widetilde{\Psi}/\Psi_c - 1\big\rangle = \zeta\big\langle (\varepsilon/\varepsilon_c)^2 - 1\big\rangle \quad \text{or} \quad \widetilde{D}_2 = \zeta\big\langle \widetilde{\Psi}^*/\Psi_c^* - 1\big\rangle = \zeta\big\langle (\widetilde{\sigma}/\sigma_c)^2 - 1\big\rangle \tag{4.75}$$

alternatively, in terms of tensile strains ε or the tensile effective stresses $\widetilde{\sigma}$. Here, the energetic threshold was expressed by $\Psi_c := E\varepsilon_c^2/2$ or $\Psi_c^* := \widetilde{\sigma}_c^2/2E$ and by strain and stress thresholds ε_c and σ_c, respectively. Note that the response of $\widetilde{D}_2$ shown in Figure 4.2c, is independent of the length scale l. Figure 4.3 depicts the simulation of cracking in a one-dimensional bar, with a slight perturbation of the fracture toughness in its center. In contrast to the energetic criterion $\widetilde{D}_1$ in Figures 4.3a-b, the maximum stress criterion $\widetilde{D}_2$ in Figure 4.3c does not affect zones in a far distance of the crack. This is a strong argument for the criterion (4.63) with threshold.

4.7. Time-Space Discretization and Solution Algorithms

We now construct a robust solution procedure of the multifield problem, built of the three equations (4.21), (4.27) and (4.35), associated with the fields visualized in Figure 4.1. It is based on convenient algorithmic operator splits, in line with the small-strain treatment. The algorithm extends the formulation proposed in Miehe et al. [160], from the small-strain setting, to finite deformation problems. The one-pass split provides three sub-problems for the evolution of the deformation field, the temperature and the phase field, respectively.

4.7.1. Time-Discrete Field Variables in Incremental Setting. We now consider field variables at the discrete times $0, t_1, t_2, \dots, t_n, t_{n+1}, \dots, T$ of the process interval $[0, T]$. In order to advance the solution within a typical time step, we focus on the finite time increment $[t_n, t_{n+1}]$, where

$$\tau_{n+1} := t_{n+1} - t_n > 0 \tag{4.76}$$

denotes the step length. In the subsequent treatment, all field variables at time t_n are assumed to be known. The goal is then to determine the fields at time t_{n+1}. In order to keep the notation compact, subsequently all variables without subscript are evaluated at time t_{n+1}. As a consequence, the rates of the deformation, temperature and phase field are considered to be constant in the time increment (4.76) under consideration, defined by

$$\dot{\boldsymbol{\varphi}}^\tau := (\boldsymbol{\varphi} - \boldsymbol{\varphi}_n)/\tau \ , \quad \dot{d}^\tau := (d - d_n)/\tau \quad \text{and} \quad \dot{\theta}^\tau := (\theta - \theta_n)\tau \ . \tag{4.77}$$

Note that, due to the given fields at time t_n, the above rates associated with the time increment (4.76), are linear functions of the variables at the current time t_{n+1}. An algorithmic expression

$$(\cdot)_\alpha := (1-\alpha)(\cdot)_n + \alpha(\cdot) \tag{4.78}$$

is introduced in terms of an algorithmic parameter $\alpha \in [0,1]$, which gives the backward Euler scheme for $\alpha = 1$, the trapezoidal rule and for $\alpha = 1/2$ and the forward Euler scheme for $\alpha = 0$. A robust, algorithmically decoupled system is obtained for staggered one-pass operations using explicit updates, which is in line with the treatment of Miehe et al. [160] or Miehe [150, 151].

Update of Fracture Phase Field. A robust algorithm for the update of the phase field is obtained by explicit update of the driving state function as $\mathcal{H} = \mathcal{H}_{\alpha=0} = \mathcal{H}_n$. This induces an algorithmic decoupling of updates for the phase field and the bulk response in the time interval under consideration and is the key ingredient of a modular implementation of phase field fracture. We introduce the algorithmic representation of the Euler-Lagrange equation of phase field fracture

$$[d - l^2\Delta d] + \eta \dot{d}^\tau - (1-d)\mathcal{H} = 0 \ . \tag{4.79}$$

The weak form is constructed by a standard Galerkin procedure. Let $\boldsymbol{X} \mapsto \delta d \in \mathcal{W}^d := \{\delta d | \delta d = 0 \text{ on } \partial\mathcal{B}^d\}$ be the test function for the fracture phase field, then

$$G_d(d,\delta d) = \int_{\mathcal{B}} [l^2 \nabla_X d \cdot \nabla_X \delta d + (\eta \dot{d}^\tau + (1+\mathcal{H})d - \mathcal{H})\delta d]\, dV = 0 \tag{4.80}$$

is the weak form of the phase field equation. The linearization of the weak form of the fracture phase field (4.80) is the following

$$G_d^{lin}(\delta d, \Delta d, d) := G_d(\delta d, d) + \Delta G_d(\delta d, \Delta d, d) = 0 \tag{4.81}$$

in terms of the increment ΔG_d reading

$$\Delta G_d(\delta d, \Delta d, d) := \int_{\mathcal{B}} \nabla_X \Delta d \ (\boldsymbol{1} l^2) \ \nabla_X \delta d + \Delta d \ (\eta/\tau + 1 + \mathcal{H}) \ \delta d \, dV \ . \tag{4.82}$$

Update of Deformation Field. For a known fracture phase field d at time t_{n+1}, we compute the current deformation field $\boldsymbol{\varphi}$ from the algorithmic Euler-Lagrange equation (4.21) for the quasistatic case

$$\mathrm{Div}[\boldsymbol{P}] + \rho_0 \boldsymbol{\gamma} = 0 \ , \tag{4.83}$$

using a decoupling from the temperature evolution by an explicit update of the temperature field $\theta = \theta_{\alpha=0} = \theta_n$, together with the boundary condition $(4.8)_2$. The weak form is constructed by a standard Galerkin procedure. Let $\boldsymbol{X} \mapsto \delta\boldsymbol{\varphi} \in \mathcal{W}^{\boldsymbol{\varphi}} := \{\delta\boldsymbol{\varphi} | \delta\boldsymbol{\varphi} = 0 \text{ on } \partial\mathcal{B}^{\boldsymbol{\varphi}}\}$ be the test function for the deformation, then

$$G_\varphi^\tau(\boldsymbol{\varphi}, \delta\boldsymbol{\varphi}) = \int_{\mathcal{B}} [\boldsymbol{P} : \delta\boldsymbol{F} - \rho_0 \boldsymbol{\gamma} \delta\boldsymbol{\varphi}]\, dV - \int_{\partial\mathcal{B}^t} \bar{\boldsymbol{T}} \delta\boldsymbol{\varphi}\, dA = 0 \tag{4.84}$$

is the weak form of the balance of momentum, when inertia effects are neglected. The linearization of the weak form of the balance of momentum (4.84) reads

$$G_\varphi^{lin}(\delta\boldsymbol{\varphi}, \Delta\boldsymbol{\varphi}, \boldsymbol{\varphi}) := G_\varphi(\delta\boldsymbol{\varphi}, \boldsymbol{\varphi}) + \Delta G_\varphi(\delta\boldsymbol{\varphi}, \Delta\boldsymbol{\varphi}, \boldsymbol{\varphi}) = 0 \ , \tag{4.85}$$

with the linear increment of the weak form

$$\Delta G_\varphi(\delta\boldsymbol{\varphi}, \Delta\boldsymbol{\varphi}, \boldsymbol{\varphi}) := \int_{\mathcal{B}} \Delta\boldsymbol{F} : \mathbb{C} : \delta\boldsymbol{F}\, dV \ . \tag{4.86}$$

Here, the linear increment of the first Piola stresses is replaced by the expression $\Delta\boldsymbol{P} = \Delta\boldsymbol{F} : \mathbb{C}$. For updated fracture phase field d and deformation field $\boldsymbol{\varphi}$ of bulk response, the crack driving state function is updated based on the constitutive crack driving state function

$$\mathcal{H}(\boldsymbol{X}, t) = \max_{s\in[0,t]} \widetilde{D}(\boldsymbol{X}, s) \quad \text{with} \quad \widetilde{D}(\boldsymbol{X}, s) \geq 0 \ . \tag{4.87}$$

Update of Temperature Field. An algorithm for the update of the temperature field θ in the increment $[t_n, t_{n+1}]$ at time t_{n+1}, can be based on the time-discrete form of the evolution equation (4.27)

$$\rho_0 c\dot{\theta}^\tau = -\operatorname{Div}[\mathbb{Q}^\alpha] + \rho s^\alpha \quad \text{with} \quad s^\alpha := R^\alpha + H^\alpha + \mathcal{D}^\alpha_{loc} \ . \tag{4.88}$$

An implicit update of the already updated phase field d and deformation map $\boldsymbol{\varphi}$ at time t_{n+1}, is obtained by setting $\alpha = 1$. Let $\boldsymbol{X} \mapsto \delta\theta \in \mathcal{W}^\theta := \{\delta\theta | \delta\theta = 0 \text{ on } \partial\mathcal{B}^\theta\}$ be the test function for the temperature, then

$$G^\tau_\theta(\boldsymbol{\varphi}, \theta, d; \delta\theta) = \int_{\mathcal{B}} [\mathbb{Q}^\alpha \cdot \delta\nabla\theta + \rho_0\{s^\alpha - c\dot{\theta}^\tau\} \cdot \delta\theta]\, dV - \int_{\partial\mathcal{S}^h} \bar{q}^\alpha \delta\theta da = 0 \tag{4.89}$$

is the weak form of the temperature evolution equation. The linearization of (4.89) reads

$$G^{lin}_\theta(\delta\theta, \Delta\theta, \theta) := G_\theta(\delta\theta, \theta) + \Delta G_\theta(\delta\theta, \Delta\theta, \theta) = 0 \ , \tag{4.90}$$

with the linear increment of the weak form

$$\Delta G_\theta(\delta\theta, \Delta\theta, \theta) := \int_{\mathcal{B}} [\Delta\mathbb{F} \cdot (-k\boldsymbol{C}^{-1})\delta\mathbb{F} - \Delta\theta\rho_0 c\delta\theta]\, dV \ . \tag{4.91}$$

4.7.2. Space-Time-Discrete Finite Element Formulation. Now consider a standard finite element discretization of the spatial domain $\mathcal{B}$ of the reference configuration and Neumann surfaces $\partial\mathcal{S}^t$ and $\partial\mathcal{S}^q$ of the *current configuration*. We write

$$\mathcal{B} = \bigcup_{e=1}^{N_e} \mathcal{B}^e \,, \quad \partial\mathcal{S}^t = \bigcup_{s^t=1}^{N_s^t} \partial\mathcal{S}^{t\,s^t} \quad \text{and} \quad \partial\mathcal{S}^q = \bigcup_{s^q=1}^{N_s^q} \partial\mathcal{S}^{q\,s^q} \tag{4.92}$$

where N_e is the number of *bulk finite elements*, N_s^t and N_s^q are the numbers of *surface finite elements* for the mechanical traction and the heat flow, respectively. The discretization by *bulk elements* $\mathcal{B}^e \subset \mathcal{B}$ in the reference configuration is based on the finite element shapes

$$\left.\begin{array}{rcl} \boldsymbol{\varphi}^h(\boldsymbol{X}) &=& \boldsymbol{N}^e_\varphi(\boldsymbol{X})\boldsymbol{d}^e_\varphi \\ \theta^h(\boldsymbol{X}) &=& \boldsymbol{N}^e_\theta(\boldsymbol{X})\boldsymbol{d}^e_\theta \\ d^h(\boldsymbol{X}) &=& \boldsymbol{N}^e_d(\boldsymbol{X})\boldsymbol{d}^e_d \end{array}\right\} \quad \text{and} \quad \left.\begin{array}{rcl} \nabla\boldsymbol{\varphi}^h(\boldsymbol{X}) &=& \boldsymbol{B}^e_\varphi(\boldsymbol{X})\boldsymbol{d}^e_\varphi \\ \nabla\theta^h(\boldsymbol{X}) &=& \boldsymbol{B}^e_\theta(\boldsymbol{X})\boldsymbol{d}^e_\theta \\ \nabla d^h(\boldsymbol{X}) &=& \boldsymbol{B}^e_d(\boldsymbol{X})\boldsymbol{d}^e_d \end{array}\right\} \tag{4.93}$$

in terms of the matrices $\boldsymbol{N}^e_\varphi$, $\boldsymbol{N}^e_\theta$ and $\boldsymbol{N}^e_d$ of bulk shape functions and their derivatives $\boldsymbol{B}^e_\varphi$, $\boldsymbol{B}^e_\theta$ and $\boldsymbol{B}^e_d$. Here, $\boldsymbol{d}^e_\varphi$, $\boldsymbol{d}^e_\theta$ and $\boldsymbol{d}^e_d$ are the space-time-discrete values of the deformation, as well as the temperature and phase field at typical nodal points of the finite element mesh. The discretization of the Neumann surfaces by *surface elements* $\partial\mathcal{S}^{t\,s^t} \subset \partial\mathcal{S}^t$ and $\partial\mathcal{S}^{q\,s^q} \subset \partial\mathcal{S}^q$ is based on the finite element shapes

$$\left.\begin{array}{rcl} \boldsymbol{\varphi}^h(\boldsymbol{x}) & = & \boldsymbol{N}^s_\varphi(\boldsymbol{x})\boldsymbol{d}^e_\varphi \\ \theta^h(\boldsymbol{x}) & = & \boldsymbol{N}^s_\theta(\boldsymbol{x})\boldsymbol{d}^e_\theta \end{array}\right\} \tag{4.94}$$

in terms of the matrices $\boldsymbol{N}^s_\varphi$ and $\boldsymbol{N}^s_\theta$ of surface shape functions. Insertion of shapes (4.93) and (4.94) into the time-discrete weak forms (4.84), (4.89) and (4.80) gives the decoupled system of equations, for the presented, staggered update scheme

$$\begin{aligned} \boldsymbol{R}_d &= \mathop{\mathsf{A}}_{e=1}^{N_e} \int_{\mathcal{B}^e} [\boldsymbol{B}^{eT}_d l^2 \nabla d^h + \boldsymbol{N}^{eT}_d(\eta \dot{d}^\tau + (1+\mathcal{H})d^h - \mathcal{H})]\, dV && = \boldsymbol{0}\ , \\ \boldsymbol{R}_{\boldsymbol{\varphi}} &= \mathop{\mathsf{A}}_{e=1}^{N_e} \int_{\mathcal{B}^e} [\boldsymbol{B}^{eT}_\varphi \boldsymbol{P} - \boldsymbol{N}^{eT}_\varphi \rho_0 \boldsymbol{\gamma}]\, dV - \mathop{\mathsf{A}}_{s^t=1}^{N^t_s} \int_{\partial\mathcal{S}^{t\,s^t}} \boldsymbol{N}^{sT}_\varphi \bar{\boldsymbol{t}}\, da && = \boldsymbol{0} \text{ and} \\ \boldsymbol{R}_\theta &= \mathop{\mathsf{A}}_{e=1}^{N_e} \int_{\mathcal{B}^e} [\boldsymbol{B}^{eT}_\theta \mathbb{Q}^\alpha - \boldsymbol{N}^{eT}_\theta \rho_0 (s^\alpha - c\dot{\theta}^\tau)]\, dV - \mathop{\mathsf{A}}_{s^q=1}^{N^q_s} \int_{\partial\mathcal{S}^{q\,s^q}} \boldsymbol{N}^{sT}_\theta \bar{q}^\alpha\, da = \boldsymbol{0}\ . \end{aligned} \tag{4.95}$$

For the staggered update scheme, according to the choice of update α presented above, this is a decoupled system for the determination of the nodal values for the deformation, the temperature and the phase field $\boldsymbol{d}^e_\varphi$, $\boldsymbol{d}^e_\theta$ and $\boldsymbol{d}^e_d$ at the current time t_{n+1}.

4.7.3. Solution of the Coupled Algebraic Finite Element System. The algebraic system (4.95) can be solved by standard methods for the solution of nonlinear equations. Introducing the compact notation for the global degrees of freedom and the residual of the finite element mesh

$$\boldsymbol{R} := [\ \boldsymbol{R}_\varphi\ \boldsymbol{R}_\theta\ \boldsymbol{R}_d\ ]^T \quad \text{and} \quad \boldsymbol{d} := [\boldsymbol{d}_\varphi\ \boldsymbol{d}_\theta\ \boldsymbol{d}_d\ ]^T\ , \tag{4.96}$$

we write the algebraic problem (4.95)

$$\boldsymbol{R}(\boldsymbol{d}) = \boldsymbol{0}\ . \tag{4.97}$$

A canonical solver is the Newton-Raphson scheme, with iterations based on the updates

$$\boldsymbol{d} \Leftarrow \boldsymbol{d} - [D\boldsymbol{R}(\boldsymbol{d})]^{-1}\boldsymbol{R} \tag{4.98}$$

until convergence is achieved in the sense $||\boldsymbol{R}|| < tol$. In general, it is based on a full linearization of the nonlinear algebraic system, based on the monolithic tangent $D\boldsymbol{R}(\boldsymbol{d})$. However, for the staggered update scheme presented above, we obtain three decoupled residual, expressions that are solved stepwise, using Newton-Raphson schemes. The tangent $D\boldsymbol{R}(\boldsymbol{d})$ is obtained from discretization of the increments introduced above.

5. Brittle Crack Propagation in Rubbery Polymers

In this chapter, a phase field model for the analysis of fracture in polymer materials undergoing finite strains is presented. The goal is to design a continuum theory of crack propagation in rubber-like materials for the rate independent limit, which accounts for the micromechanical roots of the bulk response and the fracture toughness. We show that the two basic macroscopic parameters, namely the *elastic bulk stiffness* μ, as well as the *critical energy release rate* g_c, are linked by concepts of statistical mechanics to the microstructure of the polymer network. Embedded in the framework presented in Chapter 4, we specify the constitutive equations for the crack propagation in elastic rubbery polymers under isothermal conditions, where we make use of the statistically derived material parameters. We start our investigation in Section 5.1, with a review of the micromechanical basis of modeling bulk elasticity. This concerns the outline of models for the *elastic bulk stiffness*, with expressions for entropic elasticity. Fundamental theories on polymer elasticity base on Gaussian statistics, whereas more advanced theories, applicable to large deformation problems, replace the Gaussian by Langevin statistics. *Network models* provide a link between the response of a single polymer chain and the macroscopic deformation of a continuum. The nominal energy is governed by the micromechanical network model for the bulk response and a specific crack degradation function. In Section 5.2 the statistically based *critical energy release rate* of polymer networks is reviewed and Section 5.3 an energetically based crack driving force is derived. The crack driving state function is governed by the micromechanically based critical energy release. Finally, Section 5.4 outlines representative numerical examples, which demonstrate the capability of the proposed phase field model of fracture in rubbery polymers. The general framework of coupled problems presented in Chapter 4, is specified to isothermal elastic problems in this chapter. Therefore the internal variables $\mathbf{q}$ (4.12) are dropped, as well as the temperature evolution $\dot{\theta} = 0$ (4.27). A two field coupled problem is obtained, governed by the balance equations (4.21) and (4.35)

$$\begin{array}{ll} \rho_0 \ddot{\boldsymbol{\varphi}} & = \mathrm{Div}[\boldsymbol{P}] + \rho_0 \boldsymbol{\gamma} \\ (d - l^2 \Delta d) & = (1-d)\mathcal{H} - \eta \dot{d} \ . \end{array} \tag{5.1}$$

The crack evolution time η is treated as a numerical regularization and the sensitivity of the structural response with respect to this parameter is studied in the following. For the modeling of brittle crack propagation the, crack evolution time is chosen very small, $\eta \to 0\,\mathrm{s}$. Within the modular treatment summarized in Chapter 4, the impact from the bulk response on the crack propagation is governed by the crack driving state function $\widetilde{D}$. Vice versa, the crack phase field enters the bulk state response function Ψ, by modeling degradation from the initial unbroken, to the fully broken state.

5.1. Micromechanical Modeling of Bulk Elasticity

The degradation of the solid response needs to be constructed, depending on the phase field $d \in [0,1]$. We consider isothermal elastic problems and assume the constitutive structure

$$\Psi(\boldsymbol{F}; d) = g(d) \widetilde{\Psi}(\boldsymbol{F}) \ , \tag{5.2}$$

where the volume specific effective energy function $\widetilde{\Psi}$ is associated with the intact solid. The monotonically decreasing *degradation function* $g(d)$ describes the softening of the

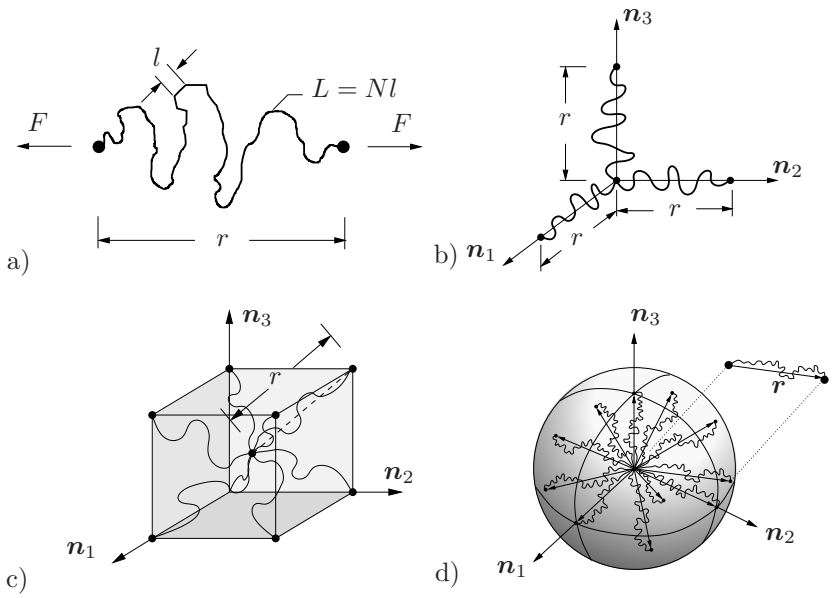

Figure 5.1: Network models for rubbery polymers. a) Single chain with N segments of length l, end-to-end distance r and contour length $L = Nl$. b) Three chain model: chains in principal stretch directions $\boldsymbol{n}_i$. c) Eight-chain model: chains placed along the space-diagonals of a cube, all undergoing the same stretch. d) Microsphere model: chain orientation continuum with directors $\boldsymbol{r}$, stretch fluctuation determined by a principle of minimum averaged energy.

material with evolving damage. It is assumed to have the properties

$$g(0) = 1 \quad , \quad g(1) = 0 \quad \text{and} \quad g'(1) = 0 \ . \tag{5.3}$$

The first two conditions include the limits for the intact and the fully broken case. As shown below, the latter constraint ensures that the fracture force converges to a finite value, if the damage converges to the fully broken state $d = 1$. A simple example of a function that fulfills the above properties, is $g(d) = (1 - d)^m$, whereas $g(d)$ recovers the classical damage theory for $m = 1$. The variational theory of brittle fracture in elastic solids, outlined in Miehe et al. [161], is obtained for $m = 2$.

In classical entropic elasticity of polymer networks, the entropy η of a single polymer chain is governed by the Boltzmann equation. Hence, the free energy of a chain is

$$\psi = -\theta\eta \quad \text{with} \quad \eta = k \ln p \ , \tag{5.4}$$

where p is the probability density that describes the free chain response. k is the Boltzmann constant and θ is the absolute temperature. Now consider a single polymer consisting of N segments of equal length l, as depicted in Figure 5.1a. The classical Gaussian statistics derived by Kuhn [128, 129] considers the unconstrained chain with end-to-end distance $r := |\boldsymbol{r}| \ll L := Nl$ much smaller than the contour length L, i.e. moderate deformations of the chain. Here, the probability density per unit volume of a randomly jointed chain, characterized by the end-to-end vector $\boldsymbol{r}$, has the form

$$p(\boldsymbol{r}) = p_0 \exp[-\frac{3}{2}\lambda^2] \quad \text{with} \quad p_0 := (3/2Nl^2\pi)^{3/2} \ , \tag{5.5}$$

see Treloar [216] in terms of the stretch $\lambda := r/r_0 \in [0, \sqrt{N})$. Here, $r_0 := \sqrt{N}l$ is the random-walk mean-square distance of a chain. Insertion of (5.5) into (5.4) gives the *free*

energy of the chain

$$\psi(\lambda) = \frac{3}{2} k\theta \lambda^2 \tag{5.6}$$

as a function of the stretch λ. The simplest *network model* that links the response of a single polymer chain to the macroscopic deformation of a continuum is the *three-chain model*, which can be traced back to Kuhn & Grün [130] and James & Guth [115]. It considers a network of n chains per unit volume and links, by an *affine deformation assumption*, the microscopic stretch λ of a single chain to the three macroscopic principal stretches $\{\lambda_i\}_{i=1,3}$ of the continuum, obtained by the singular value decomposition of the (isochoric) deformation gradient

$$\boldsymbol{F} := \nabla \boldsymbol{\varphi}(\boldsymbol{X}) = \sum_{i=1}^{3} \lambda_i \boldsymbol{n}_i \otimes \boldsymbol{N}_i \quad \text{with} \quad \det[\boldsymbol{F}] = 1 \tag{5.7}$$

at a typical point $\boldsymbol{X} \in \mathcal{B}$ of the continuum $\mathcal{B} \subset \mathcal{R}^3$. The macroscopic free energy of the continuum is constructed by taking the arithmetic average of *three representative chain energies*, aligned with the macroscopic principal stretch directions, as depicted in Figure 5.1b, i.e.

$$\Psi = n\langle \psi \rangle \quad \text{with} \quad \langle \psi \rangle := \frac{1}{3}[\psi(\lambda_1) + \psi(\lambda_2) + \psi(\lambda_3)] \ . \tag{5.8}$$

Insertion of (5.6) into (5.8) and taking into account $\mathrm{tr}\,[\boldsymbol{F}^T\boldsymbol{F}] = \lambda_1^2 + \lambda_2^2 + \lambda_3^2$, finally gives the classical closed-form *macroscopic free energy function* of the polymer network

$$\Psi(\boldsymbol{F}) = \frac{\mu}{2}\,\mathrm{tr}\,[\boldsymbol{F}^T\boldsymbol{F}] \quad \text{with} \quad \mu := nk\theta \ . \tag{5.9}$$

The macroscopic elastic response of the rubber-like material is then governed by the principle of minimum potential energy

$$\boldsymbol{\varphi} = \mathrm{Arg}\Big\{ \inf_{\boldsymbol{\varphi}} \int_{\mathcal{B}} \Psi(\nabla \boldsymbol{\varphi}) dV \Big\} \ , \tag{5.10}$$

that determines the deformation map $\boldsymbol{\varphi} : \boldsymbol{X} \mapsto \boldsymbol{x}$ of the continuum. In continuum mechanics, this energy function is known as the Neo-Hookean free energy. It has a well-defined micromechanically motivated *network stiffness* μ. More advanced network theories of rubbery polymers, applicable to large deformations, replace the Gaussian statistics by the *inverse Langevin statistics*, developed by Kuhn & Grün [130] and James & Guth [115], which take account of the finite extensibility of the chain. It results in the free energy of a single chain

$$\psi(\lambda) = Nk\theta\Big(\lambda_r \mathcal{L}^{-1}(\lambda_r) + \ln \frac{\mathcal{L}^{-1}(\lambda_r)}{\sinh \mathcal{L}^{-1}(\lambda_r)}\Big) \ , \tag{5.11}$$

which advances (5.6) for end-to-end distances $\boldsymbol{r}$ up to the limiting value L. Here, $\mathcal{L}(x) = \coth x - 1/x$ is the well-known Langevin function, see Treloar [216] and the relative stretch is $\lambda_r := r/L = \lambda/\sqrt{N} \in [0, 1)$. Furthermore, the restrictive affine deformation assumption can be relaxed by more advanced network models, such as the *non-affine microsphere network model* developed in Miehe et al. [158].

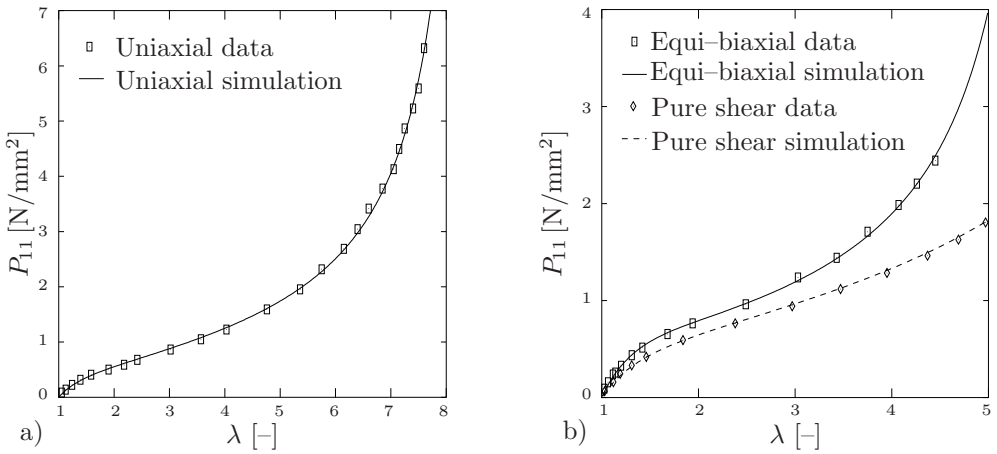

Figure 5.2: Performance of the non-affine micro-sphere model developed in MIEHE ET AL. [158]. Fit of multi–dimensional test data from TRELOAR [214] with five micromechanically motivated material parameters $\mu = 0.292\,MPa, N = 22.01, p = 1.472, U = 0.744, q = 0.1086$. a) uniaxial deformation b) equi-biaxial and pure shear deformation.

It links the micro-stretch λ of the single chain to the macroscopic deformation gradient (5.7) by a particular homogenization method on the unit sphere $\mathcal{S} \subset \mathcal{R}^2$ with the p-root average of the macroscopic stretch.

$$\langle \bar{\lambda} \rangle_p := \Big[|\mathcal{S}|^{-1} \int_{\mathcal{S}} \bar{\lambda}^p \, dA \Big]^{1/p} \quad \text{with} \quad \bar{\lambda} := |\boldsymbol{F}\boldsymbol{r}| \; , \tag{5.12}$$

where $\boldsymbol{r}$ is the unit director to the surface of the sphere. The macroscopic free energy of the non-affine network model is derived as

$$\Psi(\boldsymbol{F}) = n\psi(\langle \bar{\lambda} \rangle_p) \; . \tag{5.13}$$

This function describes the idealized network with free fluctuation of the chains between the crosslinks of the network. An additional free energy, representing the energy due to interaction of the chains, is added. The model is based on five, physically motivated, material parameters and shows excellent fits to multi-dimensional experimental results, as demonstrated in Figure 5.2. The eight chain model proposed by ARRUDA & BOYCE [12], see Figure 5.1c, is obtained from the microsphere model by the specific choice of $p = 2$. The macroscopic free energy is

$$\Psi(\boldsymbol{F}) = n\psi(\langle \bar{\lambda} \rangle_2) \quad \text{with} \quad \langle \bar{\lambda} \rangle_2 = \sqrt{\text{tr}[\boldsymbol{F}^T\boldsymbol{F}]/3} \; , \tag{5.14}$$

which is attractive due to its closed-form relationship to the invariant $\text{tr}[\boldsymbol{F}^T\boldsymbol{F}]$ of $\boldsymbol{F}$. This summarizes our overview about physically motivated network models of rubbery polymers. Further details can be found in the textbooks TRELOAR [216], FLORY [70] and DOI & EDWARDS [56], as well as in the papers BOYCE & ARRUDA [33] and MIEHE ET AL. [158]. For the subsequent development, we consider the weakly volumetric compressible Neo-Hookean function as a model problem

$$\rho_0 \Psi_0(\boldsymbol{F}) = \frac{\mu}{2}[\text{tr}[\boldsymbol{F}^T\boldsymbol{F}] - 3] + \frac{\mu}{\beta}[(\det \boldsymbol{F})^{-\beta} - 1] \; , \tag{5.15}$$

with the shear modulus $\mu > 0$ defined by the Gaussian network model in (5.9). The parameter $\beta > 0$ can be linked to the classical Poisson number of linear elasticity via

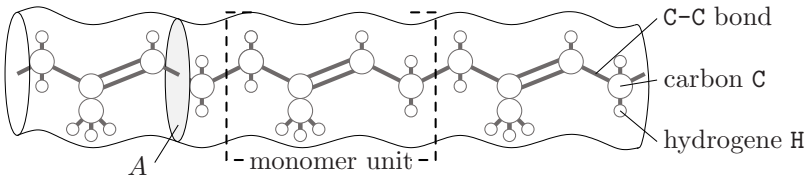

Figure 5.3: Molecular structure of natural rubber. The polymer molecule consists of N monomer units (isoprene) with cross-sectional area A. The breaking of a C-C bond gives a first estimate of the energy release rate and the fracture toughness.

$\beta = 2\nu/1-2\nu$. The constitutive function (4.15) is evaluated for the effective stress tensor

$$\widetilde{\boldsymbol{P}} := \partial_{\boldsymbol{F}}\Psi(\boldsymbol{F}) = \mu[\boldsymbol{F} - J^{-\beta}\boldsymbol{F}^{-T}] \ . \tag{5.16}$$

The consistent tangent modulus necessary for the numerical solution is $\mathbb{C} = \mu\mathbb{I} + \mu\beta\boldsymbol{F}^{-T}\otimes\boldsymbol{F}^{-T} + \mu J^{-\beta}\boldsymbol{F}^{-T}\odot\boldsymbol{F}^{-T} = \mathbb{C}_{ijkl} = \mu\delta_{ij}\delta_{kl} + \mu\beta F^{-1}_{ji}F^{-T}_{kl} + \mu J^{-\beta}F^{-1}_{li}F^{-1}_{jk}$.

5.2. Micromechanically Motivated Fracture Toughness

Not only the elastic response of rubbery polymers but also basic characteristics of the rupture of rubbers at finite strains, can be micromechanically motivated by a network theory. Rivlin & Thomas [191] examined how the stored energy can be used to describe a criterion for tearing in rubbery polymers. Their approach is based on the classical brittle fracture criterion suggested by Griffith [97]. This criterion predicts crack propagation, if the change in elastic strain energy per unit area of crack growth, also denoted as *energy release rate*

$$g := -\frac{\delta}{\delta\Gamma}E(\boldsymbol{\varphi}) \quad \text{with} \quad E(\boldsymbol{\varphi}) = \inf_{\boldsymbol{\varphi}}\int_{\mathcal{B}_\Gamma}\Psi(\nabla\boldsymbol{\varphi})dV \ , \tag{5.17}$$

reaches a *critical value* g_c. In this context, Γ is the crack surface generated inside of the body $\mathcal{B}_\Gamma$ and $\delta(\cdot)/\delta\Gamma$ is the variational or functional derivative of the stored bulk energy E_Γ. Ψ is the stored energy function obtained by the micromechanical network models outlined above, see (5.9), (5.13) or (5.14) and (5.15). Rivlin & Thomas [191] studied the tearing energy, which they called the energy release rate, experimentally. Different test specimens were loaded slowly, up to a point of sudden rupture. The load-displacement relations were recorded and analyzed. The work required until rupture was evaluated and related to the initial cut length, to get a relation between increase in cut length and work required. From the slope of these curves, they identified experimental values of the critical energy release rate g_c. They concluded that g_c is a characteristic material constant. Some years later, Lake & Thomas [133] proposed a simple micromechanical model, which determines the critical energy release rate g_c, explaining the experimental observations. They derived g_c by analyzing the rupture of a polymer molecule, as schematically depicted in Figure 5.3. A first estimate of fracture toughness is achieved by the considering the energy necessary to rupture a molecule, in particular the chemical binding energy between the carbon atoms and the average cross-sectional area. The monomer unit (isoprene) of the natural rubber depicted in Figure 5.3 has a cross-sectional area A and an average dissociation energy U [1] of the C-C bonds. Thus, the surface energy for rupture of a

[1] The dissociation of a chemical substance is usually expressed in [kJ/mol]. For a single monomer, we obtain U by dividing the molar dissociation energy with Avogadro's constant.

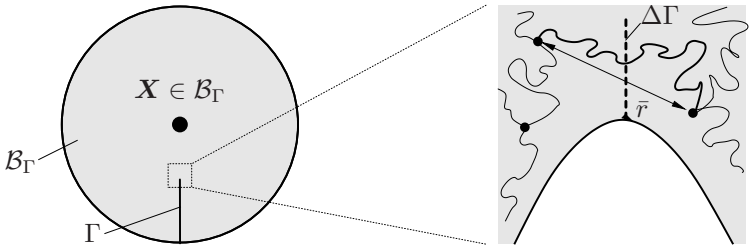

Figure 5.4: Macro-continuum $\mathcal{B}_\Gamma$ with a crack Γ and zoom out of the deformed crack tip. Chains whose crosslinks lie on opposite sides of a possible extension $\Delta\Gamma$ of the crack surface Γ must break if crack propagation takes place. This microscopic failure governs the macroscopic critical energy release rate g_c.

monomer is

$$g_{monomer} = U/A \ . \tag{5.18}$$

This simple analysis of monomer rupture does not take into account the real microstructure, consisting of flexible long-chain molecules that form a network via crosslinks. Thus, it dramatically underestimates experimental results for rubbers. As a consequence, Lake & Thomas [133] analyzed a chain as depicted in Figure 5.4, as the part of a molecule lying in between two crosslinks. Assume the molecule intersects the plane of crack propagation and that the crosslinks lie on opposite sides of the plane. The chain consists of N monomer units, with end-to-end distance between the two crosslinks $r := |\boldsymbol{r}|$. To break a particular bond within the chain, it is necessary to subject all other bonds in the same chain, to the same breaking force. Each unit in the chain must be strained until rupture before the chain will break. If the surface energy required to rupture a monomer unit is $g_{monomer}$, defined in (5.18), the *energy required to rupture a single chain* consisting of N monomers is

$$g_{chain} = N g_{monomer} \ . \tag{5.19}$$

In order to calculate the energy required to rupture a network, we apply the Gaussian statistics for the probability density $p(\boldsymbol{r})$ per unit volume of a randomly jointed chain already defined in (5.5). Then, the probability density per unit of the radius r of a sphere, is obtained by multiplying $p(\boldsymbol{r})$ with the surface area $S := 4\pi r^2$

$$P(r) = p(\boldsymbol{r})S = 4\pi r^2 p_0 \exp[-\frac{3}{2}\lambda^2] \ , \tag{5.20}$$

see Treloar [216]. The mean end-to-end distance of the chains is thus

$$\bar{r} = \int_0^\infty r \cdot P(r) dL = \int_0^\infty 4\pi r^3 p_0 \exp[-\frac{3}{2} r^2/Nl^2]\, dr = \sqrt{\frac{8N}{3\pi}} l \ . \tag{5.21}$$

When a macroscopic crack growth occurs, a number n_Γ of chains, that cross a unit area, have to be broken to create the new surface $\Delta\Gamma$. For a perfectly uniform network, where all chains have the same mean end-to-end distance $\bar{r}$ and contain the same number of monomer units N, the number of chains crossing a unit area is

$$n_\Gamma = \tfrac{1}{2}\, \bar{r} n \ , \tag{5.22}$$

where n is again the number of chains per unit volume. For these assumptions of perfectly uniform networks, the micromechanically motivated expression for the macroscopic critical

energy release rate is

$$g_c = n_\Gamma g_{chain} \ . \tag{5.23}$$

This defines a criterion for crack propagation in rubbery polymer networks. Finally, a micromechanically motivated Griffith-type criterion reads

$$-\frac{\delta}{\delta\Gamma}E(\boldsymbol{\varphi}) = g_c \quad \text{with} \quad g_c := \sqrt{\frac{2}{3\pi}} nlN^{3/2}U/A \ . \tag{5.24}$$

Based on this micromechanically motivated approach to the fracture toughness of rubbers at large strains, the following subsection develops a macroscopic crack driving force for the phase field fracture model.

5.3. Energetic Crack Driving Force

This section develops a macroscopic crack driving force for the Griffith-type phase field fracture model in rubbers at large strains, which can be linked to the micromechanical approaches of the fracture toughness, outlined above. In particular, it accounts for the micromechanical parameter for the *fracture toughness* g_c, outlined in (5.24). The Griffith criterion predicts crack propagation, if the change in elastic strain energy per unit area of crack growth, also denoted as the *energy release rate*

$$g_c = -\frac{\delta\mathcal{E}(state)}{\delta\Gamma} \quad \text{with} \quad \mathcal{E}(state) = \int_{\mathcal{B}} \Psi(state) dV \ , \tag{5.25}$$

reaches a *critical value* g_c. In this context, Γ is the crack surface generated inside of the body $\mathcal{B}_\Gamma$ and $\delta\mathcal{E}/\delta\Gamma$ is the variational or functional derivative of the stored bulk energy $\mathcal{E}$. Multiplication of (5.25) with $\delta\Gamma/\delta d$, shifts the variational derivative and yields the expression

$$g_c\delta_d\Gamma = -\delta_d\mathcal{E} \ . \tag{5.26}$$

On the left side we introduce the variation of the crack surface functional with respect to the phase field d and obtain

$$g_c\delta_d\Gamma = g_c \int_{\mathcal{B}} \delta_d\gamma(d, \nabla d)\, dV = \frac{g_c}{l}\int_{\mathcal{B}} D_c\, dV \tag{5.27}$$

in terms of the crack resistance D_c, defined in (4.32). The right hand side is expressed with $(5.25)_2$

$$-\delta_d\mathcal{E} = -\frac{\delta}{\delta d}\int_{\mathcal{B}} (1-d)^2\widetilde{\Psi}(\boldsymbol{X}, t)\, dV = \int_{\mathcal{B}} 2(1-d)\widetilde{\Psi}(\boldsymbol{X}, t)\, dV \ , \tag{5.28}$$

where use was made of the isotropic degradation defined in (5.2). Dividing (5.27) and (5.28) by g_c/l, we obtain the expression

$$\int_{\mathcal{B}} D_c\, dV = \int_{\mathcal{B}} 2(1-d)\widetilde{\Psi}(\boldsymbol{X}, t) l/g_c\, dV \ , \tag{5.29}$$

which is in the form of the global balance equation of crack surface (4.34). We can identify the driving state function

$$\widetilde{D} = 2\widetilde{\Psi}(\boldsymbol{X}, t) l/g_c \tag{5.30}$$

as a ratio of effective elastic energy and energy release rate of the material. According to (4.41) the maximum of the local effective crack driving state function $\widetilde{D}$, obtained in terms of time, enters the evolution equation for phase field fracture as the crack driving force $\mathcal{H}$.

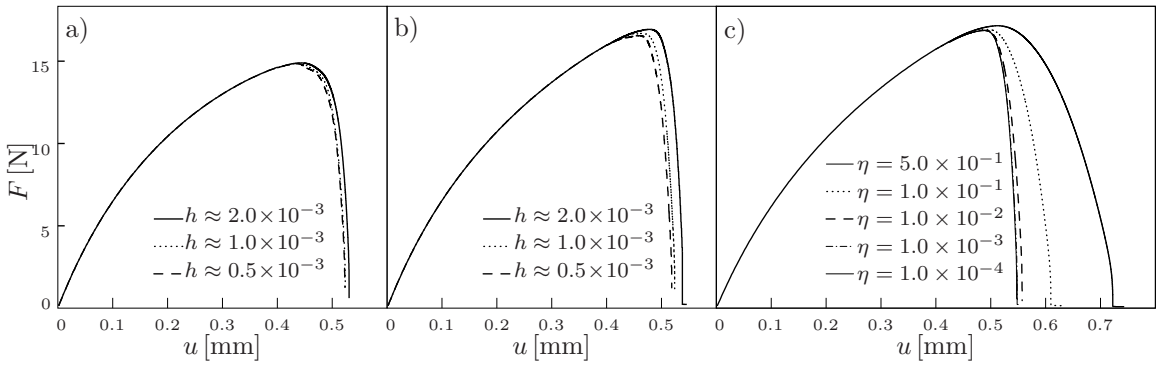

Figure 5.5: Penny shape tension test. Load-displacement curves for simulations with 5 000, 15 000 and 45 000 elements carried out with the same viscosity and with the length scales a) l= 0.02 mm and b) l=0.01 mm. Different crack evolution times η at length scale $l = 0.01$ mm c). For vanishing η the graphs converge to the rate–independent limit.

5.4. Numerical Examples

We now demonstrate the modeling capability of the proposed approach to crack propagation in rubbery polymers at large strains, by means of two representative examples. As a first benchmark problem, we consider a penny shape precracked test specimen, subjected to tensile loading. Furthermore, we investigate different geometries of a double edge notched specimen under tension, which allow to validate the model prediction by comparison with experimental data.

5.4.1. Penny Shaped Precracked Test Specimen. We investigate a rectangular plate of 2 mm width and 0.4 mm height, with a horizontal notch of 0.2 mm in length, placed in the center of the specimen. The geometric setup is depicted in Figure 5.6a. In order to capture the crack pattern properly, the mesh is refined where the crack is expected to propagate. Three finite element discretizations are generated with $N_{ele} = \{5, 14, 45\} \times 10^3$ finite elements, with an effective element size in the critical zone of $h \approx 2, 1, 0.5 \times 10^{-3}$ mm, respectively. The macroscopic shear modulus, that had been micromechanically motivated in (5.9), is chosen to $\mu = 5\,\mathrm{N/mm^2}$. We consider a weakly compressible response with Poisson's ratio $\nu = 0.45$. The critical fracture energy, which was micromechanically motivated in (5.24), is set to $g_c = 2.4\,\mathrm{N/mm}$. The computation is performed in a monotonic, displacement-driven context, with constant displacement increments $\Delta u = 1 \times 10^{-5}$ mm. In order to point out the effects that arise due to the length scale parameter l and the crack evolution time η, different simulations are performed. The subsequent study analyzes the influence of the discretization on the global response. For the three mesh densities mentioned before, the load-displacement curves are compared in Figures 5.5a,b for the length scale $l = 0.02$ mm and $l = 0.01$ mm. Obviously, the structural responses show minor differences and the results converge to a solution of finest mesh density.

To analyze the effect of the regularizing crack evolution time η on the global response, five simulations are performed with varying damping parameter $\eta = \{0.001, 0.01, 0.5\}$ [s]. We observe that the curves obtained with the two lowest viscosities almost coincide and a rate independent limit is obtained for vanishing crack evolution time $\eta \to 0$. For the simulation, using an effective element size of $h = 2.0 \times 10^{-3}$ mm at a length scale of $l = 0.01$ mm, the deformed configuration of the specimen at different time steps is depicted in Figure 5.6. It shows the crack evolution until final rupture. The corresponding load-

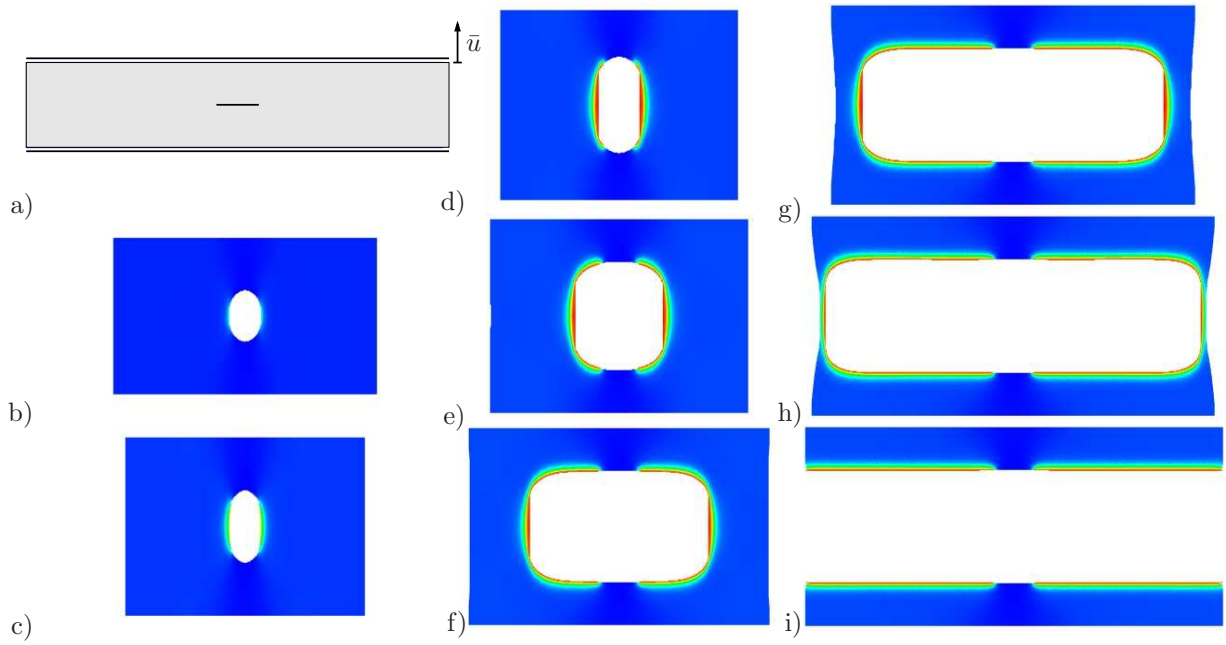

Figure 5.6: Penny shape tension test. a) Boundary conditions. Crack pattern at a displacement of b) $\bar{u} = 0.334\,\text{mm}$ c) $\bar{u} = 44\,\text{mm}$ d) $\bar{u} = 494\,\text{mm}$ e) $\bar{u} = 0.512\,\text{mm}$, f) $\bar{u} = 0.526\,\text{mm}$, g) $\bar{u} = 0.536\,\text{mm}$, h) $\bar{u} = 0.538\,\text{mm}$ and finally i) $\bar{u} = 0.5382\,\text{mm}$ for a length scale of $l = 0.01\,\text{mm}$ and an effective element size $h = 2 \times 10^{-3}\,\text{mm}$.

displacement curve is plotted in Figure 5.5c. We see the contour of the fracture phase field, where the blue color characterizes the undamaged state of the solid. If the fracture phase field is fully developed, the field-variable d has the value $d = 1$, which corresponds to the red color. Figure 5.6b shows the large deformation of a rubbery polymer. Up to this deformation, the fracture phase field is virtually undeveloped, which can be clearly seen from the overall blue color. The applied deformation is $\bar{u} = 0.334\,\text{mm}$ in 5.6b. Figure 5.6c shows the deformed configuration of the system and the contour of the phase field after an overall deformation of $\bar{u} = 0.44\,\text{mm}$. Based on the changing color in the phase field contour plot, it can be seen that the phase field begins to develop in the area near the initial notch. For an applied deformation of $\bar{u} = 0.494\,\text{mm}$, the fracture phase field is fully developed in the vicinity of the horizontal notch, see Fig.5.6d. Once the fracture phase field has reached a value representing fully damaged material, a drastic increase in crack growth occurs. Figures 5.6e-i report the system at prescribed boundary displacements of $\bar{u} = \{0.512, 0.526, 0.536, 0.538, 0.5382\}\,\text{mm}$. The crack propagates continuously until the body has fractured into two parts.

The technique for the visualization of crack opening, already used in Figure 5.6, is explained in Figure 5.7, where the contour of the fracture phase field and the contour of the normal stresses are depicted. It is constructed such that the left sides of the specimen are displayed without graphic manipulation. In Figure 5.7a, on the left side, we observe an area in which the contour plot shows red for $d = 1$. A crack has propagated from the initial notch towards the edges. The stresses in 5.7b, on the left side, have the value $P_{22} = 0$, in the areas where $d = 1$. On the right sides, the crack opening is visualized. Since this is only post processing for graphic output, the real boundary of the continuum is shown by the black lines. To visualize the crack opening and the crack growth we exploit the level set function Γ_c introduced in (3.35). For the visualization of crack opening,

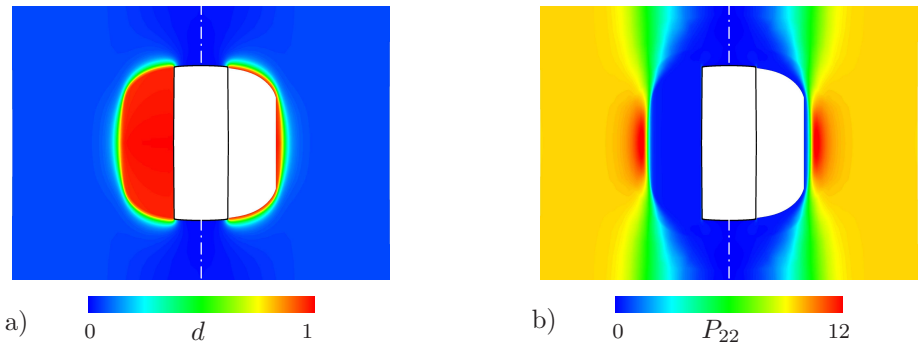

Figure 5.7: Penny shape tension test. The fully developed fracture phase field, depicted in a) causes the degradation of material stiffness which is clearly visible through the zero P_{22} stress in the center of the specimen, depicted in b). Left sides without graphic manipulation, right sides uses blanking to visualize crack opening for d beyond the level set $c \geq 0.98$.

the delimitation for continua, which have negligible stiffness, contribution is chosen at a level set of $c \geq 0.98$. Based on this, the contour plots of the fracture phase field are adapted, such that the finite elements with a level set of $c \geq 0.98$ are not displayed. In Figure 5.7a, on the right side, we see the boundary layer between undamaged state and the cracked state where $0 > d > c$. This represents the diffusive crack surface which has developed. In Figure 5.7b, on the right side, the initial cut and the crack surface can only be distinguished with the help of the continuum outline. The edges are traction free and in front of the crack tip, stresses concentrate, as was expected.

5.4.2. Double Edge Notched Specimen in Tension. The next benchmark applies the model to five boundary value problems, which are related to experimental data available in Hocine et al. [108]. They performed experiments on double edge notched tension specimens to estimate the critical fracture energy. The geometric setup, which all the specimen have in common, is depicted in Figure 5.8a. All dimensions are given in [mm]. The initial crack length a varies and has the values a_i=$\{12, 16, 20, 24, 28\}$ mm. In our simulation we exploited the symmetry of the specimen and discretized one quar-

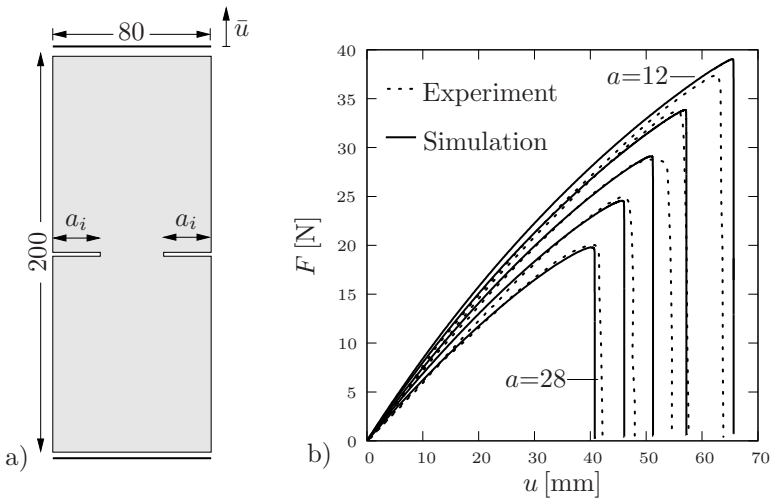

Figure 5.8: Double edge notched specimen in tension. a) Boundary conditions and geometry in [mm], discretized with quadrilateral elements. Varying initial notch length $a_i = \{12, 16, 20, 24, 28\}$[mm]. b) Comparison of experimental load-deflection curves from Hocine et al. [108] with the simulations.

ter of the specimen with approximately $7000 - 15000$ elements. In order to capture the crack pattern properly, the mesh is refined where the crack is expected to propagate. In the critical zone, an effective element size of $h = 0.05\,\mathrm{mm}$ is chosen. The length scale parameter applied in the simulations is $l = 1\,\mathrm{mm}$, resembling 10 elements. The computations are performed in a monotonic, displacement driven context, with refinement of the displacement increments Δu as soon as the fracture has initiated due to the rapid crack propagation. The elastic constants are $\mu = 0.203\,\mathrm{N/mm^2}$ and $\nu = 0.45$. The critical fracture energy is $g_c = 2.67\,\mathrm{N/mm}$. Note, that μ and g_c can be derived from micromechanical quantities of the polymer network, according to (5.9) and (5.24). The artificial crack evolution time parameter is chosen to $\eta = 10^{-3}$ for all simulations of the five boundary value problems. Figure 5.8b shows the load-displacement curves of the experiments and those obtained from the simulations of the five specimen geometries. The dotted lines are the load-displacement curves experimentally determined by Hocine et al. [108]. The solid curves are the results of the simulations. The geometric setup with the largest initial notch $a_i = 28\,\mathrm{mm}$, yields the load-displacement curve with the lowest fracture force level. The smaller the initial notch, the higher the strength of the entire system. When comparing the experimental and the numerical results in Figure 5.8b, we observe that the

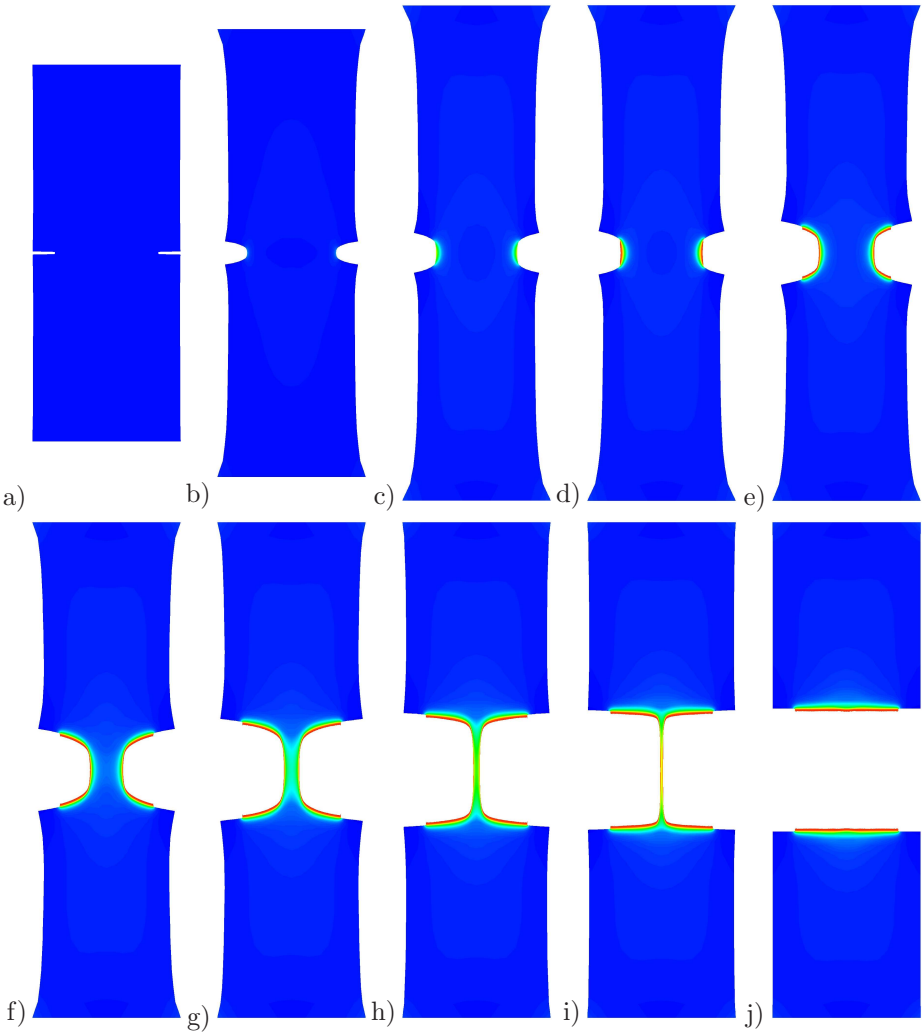

Figure 5.9: Crack pattern of the double edge notched tension specimen with smallest initial notch of 12 mm width.

softening effect of the varying initial notch on the overall system response is captured for all cases in an excellent way. The maximum load that is reached until the rapid crack propagation occurs, is predicted by the model in all cases in a very satisfying way. This validates the capabilities of the presented model for the prediction of fracture in rubbery polymers. Finally, Figure 5.9 shows the resulting crack pattern with the smallest initial crack $a = 12\,\text{mm}$. Again, blue and red colors correspond to the virgin and fully cracked state, respectively. The visualization of the crack opening and the crack growth, exploits the level set function Γ_c introduced in (3.35). The delimitation of continua which have negligible stiffness contribution, is chosen at a level set of $c \geq 0.98$. The contour plots of the fracture phase field are adapted, such that these areas are not displayed. Figures 5.9a-c show the elastic deformation of the specimen until an overall deformation of $\bar{u} = 65.44\,\text{mm}$ at which the maximum load is almost reached. The contour plot shows that the phase field is developed to some amount around the initial notch tip. Figure 5.9d represents the onset of fracture, as the phase field exceeds the level set the first time, at an overall deformation of $\bar{u} = 65.608\,\text{mm}$. Beyond this point the load drastically decreases. Figures e-j depict the subsequent propagation of the crack, until the body has separated into two parts.

6. Brittle Crack Propagation in Thermoelastic Solids

The overall goal of this chapter is to design a continuum theory of crack propagation applicable to the model problem of thermoelasticity at finite strains, according to the recent publication MIEHE ET AL. [163]. Therefore, the deformations are decomposed into elastic stress producing and volumetric thermal expansion parts. A concept of transition rules is proposed, which describes the degradation of the intact solid state and the rise of crack state response, governed by the fracture phase field. In particular, all constitutive functions of the bulk response are assumed to degrade with an evolving phase field. Hence, the modeling of the bulk response is essentially restricted to the modeling of the nominal response of the undamaged material. A *maximum stress criterion* based on a critical fracture stress is introduced, that makes a differentiation between tensile and compression region simple and is open for complex anisotropies in the constitutive modeling. A main aspect is to outline a concept for the constitutive definition of non-mechanical fluxes at the crack phases. This is achieved by approximating sharp crack surface integrals by distinct volume integrals. As a consequence, a *conduction across a crack* is modeled by a degrading heat flux function for the solid-freespace mixture. A *convective heat exchange* is described by an extra contribution to the bulk heat source. The constitutive expressions enter the governing Euler equations of the coupled problem, presented in Chapter 4. Finally, numerical examples demonstrate fundamental geometric and physical coupling effects in thermoelastic solids at fracture. These are the generation of heat due to cracking, inducing an increase of temperature, the degradation of non-mechanical fluxes at crack surfaces and the appearance of new fluxes at the generated crack surfaces. Furthermore, the generation of cracks due to thermally induced stress states is investigated.

The general framework of coupled problems presented in Chapter 4 is specified to the modeling of crack propagation in thermoelastic solids. Therefore, the internal variables $\mathbf{q}$ are dropped. A three field coupled problem is obtained, governed by the balance equations (4.21), (4.27) and (4.35)

$$\begin{array}{ll} \rho_0 \ddot{\boldsymbol{\varphi}} & = \mathrm{Div}[\boldsymbol{P}] + \rho_0 \boldsymbol{\gamma} \\ \rho_0 c \dot{\theta} & = \mathrm{Div}[-\mathbb{Q}] + \rho_0 (R + H + \mathcal{D}_{loc}) \\ (d - l^2 \Delta d) & = (1-d)\mathcal{H} - \eta \dot{d} \ . \end{array} \tag{6.1}$$

The crack evolution time η is treated as a numerical regularization and for the modeling of brittle crack propagation, $\eta \to 0$ is used. Within the modular treatment of crack propagation and bulk response, summarized in Chapter 4, the impact of the bulk response on the crack propagation is governed by the crack driving state function $\widetilde{D}$. Vice versa, the crack phase field enters the bulk state response function Ψ, by modeling degradation from the initial unbroken to the fully broken state.

6.1. Constitutive Energy Storage Function

6.1.1. Phase Transition from Unbroken to Broken Response. For the specific multi-physics scenario under consideration, constitutive functions for the degrading elastic solid response as well as the rise of new non-mechanical effects in damaged zones need to be constructed, depending on the crack phase field $d \in [0, 1]$. The first set of functions considers the degradation of elastic stored energy, stresses and non-mechanical fluxes in the solid with increasing phase field d. The second set of functions concerns a new constitutive response in the damaged domain, that increases with increasing phase

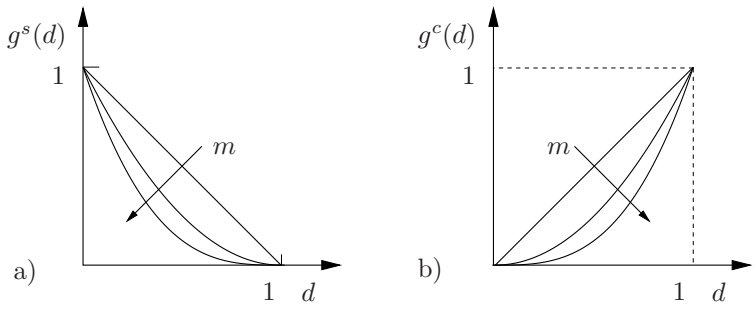

Figure 6.1: a) Fracture degradation function for solid response $g^s(d) = (1-d)^m$ with $m = \{1, 2, 3\}$, b) Build up function for diffusive crack phase $g^c(d) = d^m$ with $m = \{1, 2, 3\}$.

field d. With this approach, the rise of non-mechanical fluxes such as heat flow, diffusion, electric displacement or magnetic induction across diffusive crack faces can be modeled. A general structure for the phase transition from the intact to the fully broken response, is introduced by the generic constitutive function

$$\boldsymbol{f} = \hat{\boldsymbol{f}}(\cdot; d) \ , \tag{6.2}$$

where $(\cdot)$ stands for a set of constitutive state variables, e.g. those for the treated case of thermoelasticity. The above mentioned degrading and rising response in the range $d \in [0, 1]$ of the crack phase field, may be described by a *rule of mixture*, which assumes the constitutive structure

$$\hat{\boldsymbol{f}}(\cdot; d) = \hat{\boldsymbol{f}}^s(\cdot; d) + \hat{\boldsymbol{f}}^c(\cdot; d) \tag{6.3}$$

with degrading functions $\hat{\boldsymbol{f}}^s$ for the solid response and growing functions $\hat{\boldsymbol{f}}^c$ in diffusive crack zones. These functions are related to effective functions

$$\widetilde{\boldsymbol{f}}^s(\cdot) := \hat{\boldsymbol{f}}(\cdot; 0) \quad \text{and} \quad \widetilde{\boldsymbol{f}}^c(\cdot) := \hat{\boldsymbol{f}}(\cdot; 1) \ , \tag{6.4}$$

which describe the responses at intact and fully broken states. The decreasing and increasing functions must show the characteristic properties

$$\partial_d \hat{\boldsymbol{f}}^s(\cdot; d) \leq 0 \wedge \hat{\boldsymbol{f}}^s(\cdot; 1) = \boldsymbol{0} \quad \text{and} \quad \partial_d \hat{\boldsymbol{f}}^c(\cdot; d) \geq 0 \wedge \hat{\boldsymbol{f}}^c(\cdot; 0) = \boldsymbol{0} \ . \tag{6.5}$$

A simple constitutive function for the rule of mixture (6.3) is

$$\hat{\boldsymbol{f}}^s(\cdot; d) = g^s(d)\widetilde{\boldsymbol{f}}^s(\cdot) + g^c(d)\widetilde{\boldsymbol{f}}^c(\cdot) \ , \tag{6.6}$$

where $g^s(d)$ and $g^c(d)$ are weight functions. Continuous functions are assumed for these weight functions that fulfill the conditions

$$\begin{cases} g^{s\prime}(d) \leq 0 \\ g^{c\prime}(d) \geq 0 \end{cases} \quad \text{with} \quad \begin{cases} g^{s\prime}(0) = 1 \\ g^{c\prime}(0) = 0 \end{cases} \quad \text{and} \quad \begin{cases} g^{s\prime}(1) = 0 \\ g^{c\prime}(1) = 1 \ . \end{cases} \tag{6.7}$$

A choice, for instance, are the functions $g^s(d) = (1-d)^m$ with dual $g^c(d) = d^m$ depicted in Figure 6.3. For the mixture parameter $m = 1$, the classical $(1-d)$-theory of damage is recovered. The variational theory of brittle fracture in elastic solids outlined in Miehe et al. [161] is obtained for $m = 2$. A quadratically increasing function $g^c(d) = d^2$ for the diffusive crack zones can be motivated for a heat transfer across crack faces based on geometric arguments, i.e. consistent with the crack surface functional γ_l defined in (3.31). A more detailed description is given below.

6.1.2. Nominal Constitutive Energy Storage Function. For the thermodynamic model under consideration, the free energy storage in the bulk is assumed to be additively split up into a part due to *elastic distortions* and a purely *thermal part*

$$\hat{\Psi}(\cdot; d) = g^s(d)\widetilde{\Psi}^s_e(\boldsymbol{F}, \theta) + \widetilde{\Psi}^s_\theta(\theta) \ , \tag{6.8}$$

where the nominal constitutive function for the solid-freespace mixture results from the specific mixture rule (6.3), with $g^s(d) = (1-d)^2$. A full degradation of $\widetilde{\Psi}^s_e$, the effective elastic stored energy (6.11) but no degradation of the stored thermal energy $\widetilde{\Psi}^s_\theta$ (6.13) is assumed.

Effective Elastic and Thermal Energy Storage Functions. In order to describe the thermal expansion, we decompose the deformation gradient into a thermal expansion part $\boldsymbol{F}_\theta$ and a stress producing part $\boldsymbol{F}_e$, defined by

$$\boldsymbol{F}_e := \boldsymbol{F}\boldsymbol{F}_\theta^{-1} \quad \text{with} \quad \boldsymbol{F}_\theta := (J_\theta(\theta))^{1/3}\boldsymbol{1} \ . \tag{6.9}$$

$\boldsymbol{F}_\theta$ is defined, such that isotropic expansions are assumed, governed by the scalar constitutive function

$$J_\theta(\theta) = \exp[3\alpha_s(\theta - \theta_0)] \ , \tag{6.10}$$

with the linear thermal expansion coefficient α_s, see for example Lu & Pister [142]. We consider for the model problem a compressible Neo-Hookean function of the form

$$\rho_0\widetilde{\Psi}^s_e(\boldsymbol{F}_e) = \frac{\mu}{2}[\mathrm{tr}[\boldsymbol{F}^{eT}\boldsymbol{F}^e] - 3] + \frac{\mu}{\beta}[J_e^{-\beta} - 1] \ , \tag{6.11}$$

with the shear modulus μ and a parameter β, related to the Poisson's ratio of the linear theory of elasticity via $\beta = 2\nu/(1-2\nu)$. With the elastic energy $\widetilde{\Psi}^s_e$ at hand, we may evaluate the constitutive function (4.15) for the effective stresses

$$\widetilde{\boldsymbol{P}} = \mu J_\theta^{-1/3}[\boldsymbol{F}^e - J_e^{-\beta}\boldsymbol{F}^{e-T}] \ . \tag{6.12}$$

The purely thermal part of the free energy $(6.8)_2$ is assumed to have the convenient form

$$\rho_0\Psi^s_\theta(\theta) = \rho_0\Psi_0 - \rho_0\eta_0(\theta - \theta_0) - \rho_0 c_s[\theta \ln\frac{\theta}{\theta_0} - \theta + \theta_0] \ , \tag{6.13}$$

where c_s is a heat capacity parameter that is assumed to be a constant. With this function (6.13) for the thermal energy at hand, we may evaluate the constitutive function (4.15) for the entropy

$$\eta = \eta_0 + c_s \ln\frac{\theta}{\theta_0} + 3\alpha_s p/\rho_0 \quad \text{with} \quad p := \tfrac{1}{3}\,\mathrm{tr}[\boldsymbol{P}\boldsymbol{F}^T] \ . \tag{6.14}$$

6.2. Nominal Constitutive Heat Flux and Heat Source Function

Besides the constitutive equations for the mechanical variables, a constitutive equation with regard to the heat flux is needed. We apply the rule of mixture (6.3), which assumes the constitutive structure

$$\hat{\mathbb{Q}}(\boldsymbol{F}, \theta; d) = g^s(d)\widetilde{\mathbb{Q}}^s(\boldsymbol{F}, \theta) + g^c(d)\widetilde{\mathbb{Q}}^c(\boldsymbol{F}, \theta) \ , \tag{6.15}$$

with the effective functions $\widetilde{\mathbb{Q}}^s$ and $\widetilde{\mathbb{Q}}^c$, which describe the solid response at intact and fully broken state and the corresponding degradation function $g^s(d) = (1-d)^2$ as well as the rise function $g^c(d) = d^2$. The Kirchhoff heat flux $J_{\mathbb{q}}$ in the interior will be treated by an isotropic Eulerian Fourier-Type law. For the Lagrangian heat flux defined in (2.27) this gives the constitutive form

$$\widetilde{\mathbb{Q}}^s = -k_s \boldsymbol{C}^{-1} \nabla\theta \ , \tag{6.16}$$

where the heat conductivity k_s is introduced. The Fourier inequality is only satisfied for positive values of the heat conductivity

$$k_s \geq 0 \ . \tag{6.17}$$

New surfaces produced by a crack extend the surface of the body and undergo interchanges with the surrounding medium.

6.2.1. Heat Conduction Across Crack Faces. The appearance of *heat conduction* through the new crack surface of the body requires the construction of a constitutive function in the damaged zone, as already considered in (6.3). In order to motivate a constitutive equation for the heat flux across crack surfaces, consider a transition from the sharp crack surface modeling to the diffusive phase field modeling. Let Γ denote the sharp crack surface and $\gamma^{\pm} = \boldsymbol{\varphi}_t^{\pm}(\Gamma)$ the deformed crack faces. Assume that the deformed crack surfaces $\gamma^{\pm}$ stay close to each other, as shown in Figure 6.2a and consider the simple constitutive equation for the heat transport across the crack surfaces

$$q_T = -h_T [\![\theta]\!] \quad \text{on} \quad \boldsymbol{\varphi}^{\pm}(\Gamma) \ , \tag{6.18}$$

where $[\![\theta]\!] := \theta^+ - \theta^-$ is the temperature jump. The heat transition parameter h_T is introduced and the temperatures at the opposite crack faces $\gamma^{\pm}$ are denoted with $\theta^{\pm}$. Consequently, the transport of heat across a sharp crack surface is

$$T^c := \int_{\boldsymbol{\varphi}_t}^{-} (\Gamma) q_t da = -\int_{\Gamma} l_{\boldsymbol{x}} h_T \frac{[\![\theta]\!]}{l_{\boldsymbol{x}}} da \ , \tag{6.19}$$

where $l_{\boldsymbol{x}}$ is a characteristic length. A transition of this sharp crack setting to the regularized phase field formulation is obtained by the transition of the material crack surface element $dA \to \gamma_l(d, \nabla d)\, dV$ towards the volume element, governed by the crack surface density function $\gamma_l(d, \nabla d)\, dV$ defined in (3.31). Additionally, the spatial gradient in (6.19) may be replaced by the continuum gradient normal to the crack, i.e. $[[\theta]]/l_{\boldsymbol{x}} \to \nabla_{\boldsymbol{x}}\theta \cdot \boldsymbol{n}$, where $\boldsymbol{n}$ is the normal of the crack surface $\boldsymbol{\varphi}(\Gamma)$. Considering the geometric relationship $\nabla_{\boldsymbol{x}}\theta = \boldsymbol{F}^{-T}\nabla\theta$, the volume and area map $dv = \det[\boldsymbol{F}]\, dV$ and $\boldsymbol{n}da = \det[\boldsymbol{F}]\boldsymbol{F}^{-T}\boldsymbol{N}dA$, introduced in (2.10) and (2.13), we obtain the continuum approximation

$$T^c \approx T_l^c := -\int_{\mathcal{B}} l_{\boldsymbol{x}} h_T (\boldsymbol{C}^{-1}\nabla\theta \cdot \boldsymbol{N}) \gamma_l(d; \nabla d) dv = \int_{\mathcal{B}} \mathfrak{Q}^c \cdot \boldsymbol{N} dv \tag{6.20}$$

of the transport (6.19), where

$$\mathfrak{Q}^c := -l_{\boldsymbol{x}} h_T (\boldsymbol{C}^{-1}\nabla\theta \cdot \boldsymbol{N}) \gamma_l(d; \nabla d) = l_{\boldsymbol{x}} h_T (\boldsymbol{C}^{-1}\nabla\theta \frac{1}{2l}[d^2 + l^2 |\nabla d|^2] \tag{6.21}$$

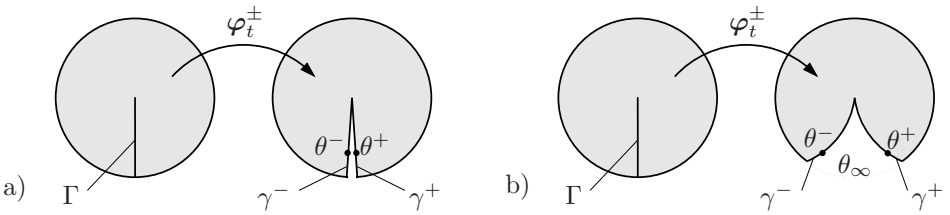

Figure 6.2: Thermal boundary conditions on sharp crack faces, which are treated in the continuum phase field formulation in a regularized manner. a) Conduction across gap for moderate crack opening with heat transport $q_T = -h_T(\theta^+ - \theta^-)$. b) Convective heat exchange for large crack opening with heat source $h_c(\theta^\pm - \theta_\infty)$.

is a heat flux per unit volume across the damaged zone. Assuming both terms in the bracket are of the same order, which is true for a damage profile of the form $d(x) = \exp[-|x|/l]$ in terms of a scalar coordinate x perpendicular to the crack, a *material heat flux per area* is estimated to have the constitutive form

$$\mathbb{Q}^c \approx l\mathfrak{Q}^c = -l_{\boldsymbol{x}} h_T d^2 \boldsymbol{C}^{-1}\nabla\theta = d^2\widetilde{\mathbb{Q}}^c \ . \tag{6.22}$$

Note that the function d^2 models a quadratic increase of the heat transport across a regularized crack in the range $d \in [0,1]$. This corresponds to the rise of crack state in $(6.15)_2$. It is furthermore clear, that $l_{\boldsymbol{x}} h_T$ is a reduced Fourier-Type heat conduction coefficient in the damaged zone in the continuum phase field model. The effective heat flux per unit volume in the damaged zone is expressed as

$$\widetilde{\mathbb{Q}}^c = -k_c \boldsymbol{C}^{-1}\nabla\theta \quad \text{with} \quad k_c \approx l_{\boldsymbol{x}} h_T \ . \tag{6.23}$$

Hence, in the phase field modeling of fracture, a reduced heat conductivity in the damaged zone, models a heat transfer across nearby crack faces as visualized in Figure 6.2a.

6.2.2. Heat Source Function for Solid-Freespace Mixture. The appearance of a possible convective heat exchange at a free crack surface can be described in the continuum phase field model by an additional heat source. In order to motivate this, assume that the deformed crack surfaces $\gamma^\pm = \boldsymbol{\varphi}_t^\pm(\Gamma)$ are in contact with a medium of ambient temperature θ_∞ inside of the free space generated by the crack opening, see Fig. 6.2b. The heat exchange is incorporated by the simple constitutive equations

$$q_c^\pm(\theta^\pm) = h_c(\theta^\pm - \theta_\infty) \text{ on } \boldsymbol{\varphi}_t^\pm(\Gamma) \ , \tag{6.24}$$

as already considered for the exterior surfaces defined in (4.10). Here, $\theta^\pm$ are the temperatures at the deformed crack faces $\gamma^\pm$ and h_c is the convective heat exchange parameter. Hence, the total influx of heat through the crack faces is

$$Q^c := -\int_\Gamma (q^+ + q^-)dA = -\int_\Gamma 2h_c(\theta_m - \theta_\infty)dA \ , \tag{6.25}$$

in terms of the mean temperature $\theta_m := (\theta +^- \theta^-)/2$ defined on the sharp crack surface Γ. A transition of this sharp crack setting to the regularized phase field formulation is achieved by the transition of the crack surface element $dA \to \gamma(d;\nabla d)dV$ towards the volume element, governed by the crack surface density function $\gamma_l(d,\nabla d)$ defined in (3.31). It yields the approximation

$$\boldsymbol{Q}^c \approx \boldsymbol{Q}_l^c := -\int_{\mathcal{B}_0} 2h_c(\theta - \theta_\infty)\gamma_l(d,\nabla d)dV \ . \tag{6.26}$$

As a consequence of the spatial regularization, a convective heat exchange at crack faces can be described by an *additional heat source per unit volume*

$$r^c \approx -2h_c(\theta-\theta_\infty)\gamma_l(d,\nabla d) = -2h_c(\theta-\theta_\infty)\frac{1}{2l}[d^2+l^2|\nabla d|^2]\ . \tag{6.27}$$

Assuming both terms in the bracket are of the same order, which is true for a damage profile of the form $d(x)=\exp[-|x|/l]$ in terms of a scalar coordinate x perpendicular to the crack we may approximate (6.27) by

$$r^c := -2\frac{h_c}{l}(\theta-\theta_\infty)d^2\ . \tag{6.28}$$

Note that the function d^2 models a quadratic increase of the action of a convective heat exchange on the crack in the range $d\in[0,1]$.

6.3. Principal Tensile Stress Crack Driving Force

In order to obtain a simple criterion for mixed tensile-compression stress modes, applicable to general non-linear and possibly anisotropic elasticity, consider first the decomposition of the effective stresses into tensile and compressive parts

$$\widetilde{\boldsymbol{\sigma}} = \widetilde{\boldsymbol{\sigma}}^+ + \widetilde{\boldsymbol{\sigma}}^- \quad \text{with} \quad \widetilde{\boldsymbol{\sigma}}^+ = \sum_{a=1}^{3}\langle\widetilde{\sigma}_a\rangle \boldsymbol{n}_a\otimes\boldsymbol{n}_a\ , \tag{6.29}$$

in terms of the ramp function $\langle\cdot\rangle := (\,\cdot\,+|\,\cdot\,|)/2$. In a second step, specify a quadratic effective stress function for the definition of the fracture driving force

$$\widetilde{\psi}^*_{frac}(\widetilde{\boldsymbol{\sigma}}^+) = \frac{1}{2E}|\widetilde{\boldsymbol{\sigma}}^+|^2 = \frac{1}{2E}\sum_{a=1}^{3}\langle\widetilde{\sigma}_a\rangle^2\,, \tag{6.30}$$

independent from the bulk response, where E is a parameter related to Young's modulus. Next, assume the critical fracture energy ψ_c per unit volume to be related to a critical fracture stress σ_c via

$$\psi_c := \frac{\sigma_c^2}{2E}\ . \tag{6.31}$$

Then, insertion of (6.30) and (6.31) into $(4.59)_2$ gives the simple *principal tensile stress criterion*

$$\widetilde{D} = \zeta\Big\langle\sum_{a=1}^{3}\langle\widetilde{\sigma}_a/\sigma_c\rangle^2 - 1\Big\rangle\ , \tag{6.32}$$

where an additional dimensionless parameter $\zeta>0$ was introduced, which influences the growth of the crack phase field in the postcritical range for $\zeta\neq 1$. The crack driving state function provides a quadratically increasing barrier function for stress levels above a *failure surface in the principal stress space*, determined by the critical tensile stress σ_c as depicted in Figure 4.4, whose slope can be influenced by the parameter ζ. Such a criterion is extremely simple to implement and applicable to brittle fracture in nonlinear, possibly anisotropic, finite elasticity. It generalizes the classical maximum principle stress criterion, which can be traced back to Rankine, Lamé and Navier, to the phase field

Table 6.1: Material Parameters

No.	Parameter	Name	Eq.	Value	Unit
1	μ	shear modulus	(6.11)	1.0	$\mathrm{N/mm^2}$
2	ν	Poisson's ratio	(6.11)	0.45	[-]
3	α_s	linear thermal expansion	(6.10)	1×10^{-3}	$\mathrm{K^{-1}}$
4	k	thermal conductivity	(6.16)	0.1	N/(Ks)
5	$\rho_o c_s$	heat capacity	(6.13)	10	$\mathrm{N/(mm^2 K)}$
6	h_C	surface convection	(4.10)	5	N/(s mm K)
7	θ_∞	ambient temperature	(4.10)	273	K
8	σ_c	critical stress	(6.32)	2.0	$\mathrm{N/mm^2}$
9	ζ	driving force slope	(6.32)	1	-
10	l/h	length scale / mesh ratio	(3.31)	≈ 2	-

modeling of fracture. A pure Rankine-type criterion would be related to the phase field driving force

$$\widetilde{D} = \zeta \big\langle \max(\langle\widetilde{\sigma}_1\rangle^2, \langle\widetilde{\sigma}_2\rangle^2, \langle\widetilde{\sigma}_3\rangle^2)/\sigma_c^2 - 1 \big\rangle \ . \tag{6.33}$$

It is related to the simple scenario of decohesion of surfaces, perpendicular to the maximum principle stress. Figures 4.2c and 4.3c demonstrate qualitative features of the criterion (6.32). In particular, Figure 4.3c characterizes the force (6.32) as being physically meaningful. It preserves the elastic properties in uncracked zones.

6.4. Numerical Examples

This section demonstrates the performance of the continuum phase field model for fracture in thermoelastic solids by means of representative numerical examples. The simulations are conceptual in nature and designed, such that the modeling capacity of fundamental coupling phenomena of fracturing thermoelastic solids at finite strains are highlighted. In particular, the subsequent simulations demonstrate

- the performance of phase field fracture with the *stress criterion* $\widetilde{D}$ defined in (6.32),
- the temperature increase at crack faces due to the *dissipative heating* $\mathcal{D}_{loc}$ in (4.27),
- the generation of a *convective heat exchange* via the source r^c defined in (6.28),
- the *cracking* due to inhomogeneous stress fields *induced by thermal expansion* (6.10).

The material parameters used in the subsequent simulations are related to rubber-like polymers which show thermoelastic behavior at finite strains, see for example Miehe [150]. A basic set of parameters is given in Table 6.1. Some of these values are modified on demand, in order to emphasize particular effects. This is commented in the description of the examples.

6.4.1. Fracture and Dissipative Heat Generation in Bending Test. This example demonstrates the performance of the phase field model for fracture at large strains and the thermomechanical coupling effect, namely temperature increase due to the dissipative crack propagation. We perform a bending test on a simply supported notched beam, under plane strain conditions, shown in Figure 6.3a. The dimensions are 40 mm in width and 10 mm in height. The supports are located 4 mm inwards from the outer

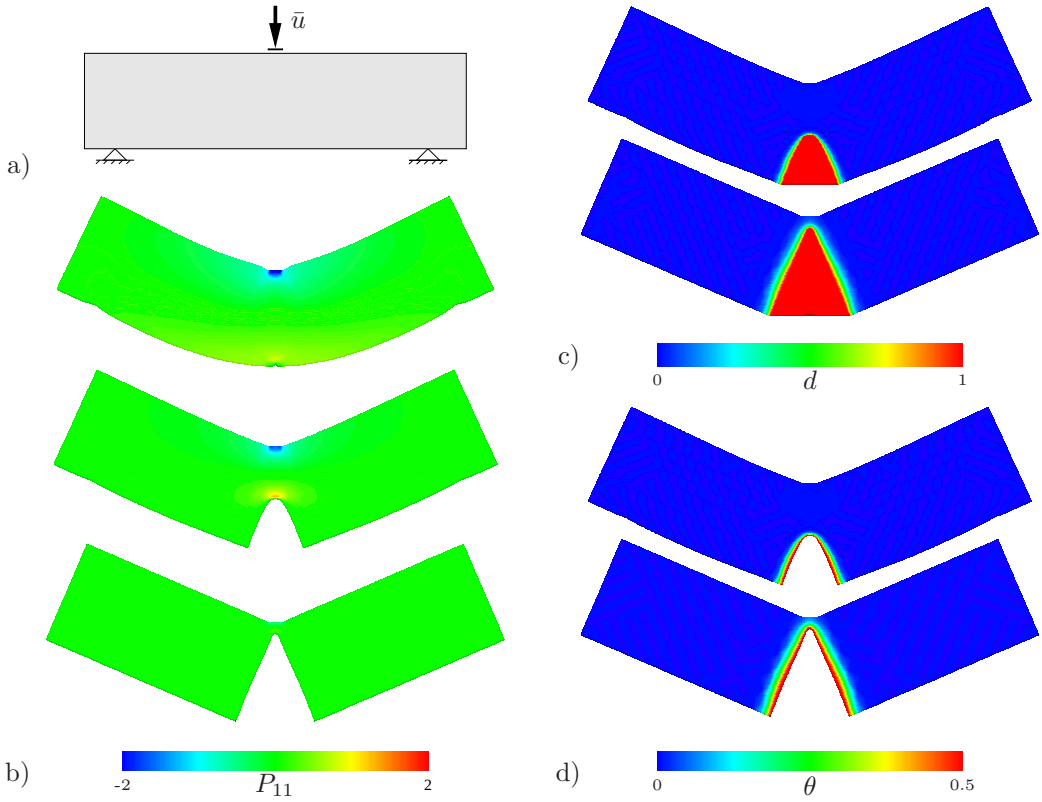

Figure 6.3: Three point bending test. a) Geometry, b) stress contour, c) phase field contour and d) temperature increase due to dissipation for several displacements.

edge, the load is applied in the middle of the upper edge by a predefined deformation. A tiny initial notch of length 0.125 mm is introduced in the middle of the lower edge. The mesh is refined in the areas where the crack is expected to propagate. Exploiting symmetry, a discretization of half the specimen, with 1550 elements and an effective element size in the refined region of $h = 0.0625$ mm is used. The computation is performed in a displacement-driven context. As expected, the material in the top region of the beam is compressed while the material at the bottom is stretched. Figure 6.3b shows the nominal stress distribution P_{11} in axial direction. The stress-based crack driving state function $\widetilde{D}$ defined in (6.32) starts to evolve once the threshold σ_c is reached. Then the crack phase field evolves and the crack grows from the initial notch towards the top region of the beam. At two stages during crack propagation the phase field is depicted in Figure 6.3c. The blue color corresponds to virgin, undamaged material, whereas fully damaged continuum (or free space continuum) is represented by red. The dissipation $\mathcal{D}_{loc}$ due to phase field evolution defined in (4.16) enters the temperature evolution equation (4.27) and causes an increase of temperature in regions close to the crack faces, shown in Fig. 6.3d. This temperature increase is small, with a maximum value of 0.5 K. Here, the level set function (3.35) $\Gamma_c = \{\boldsymbol{X} \,|\, d = c\}$ introduced in Figure 3.6b is used to visualize the crack opening for the contour plots of the stresses and the temperature state.

Figure 6.4 investigates effects due to the length scale l and the driving force slope parameter ζ introduced in (6.32). For a fixed ratio of length scale to element size $l_1/h = 2$, the influence of ζ is analyzed. Load-deflection curves for different values $\zeta = \{40, 50, 60, 100\}$ are depicted in Figure 6.4a. Note the convergence towards a limit associated with the failure surface determined by the ideal local stress limit σ_c. For increasing ζ, the curves $\zeta = \{60, 100\}$ almost coincide. This is a structural counterpart to

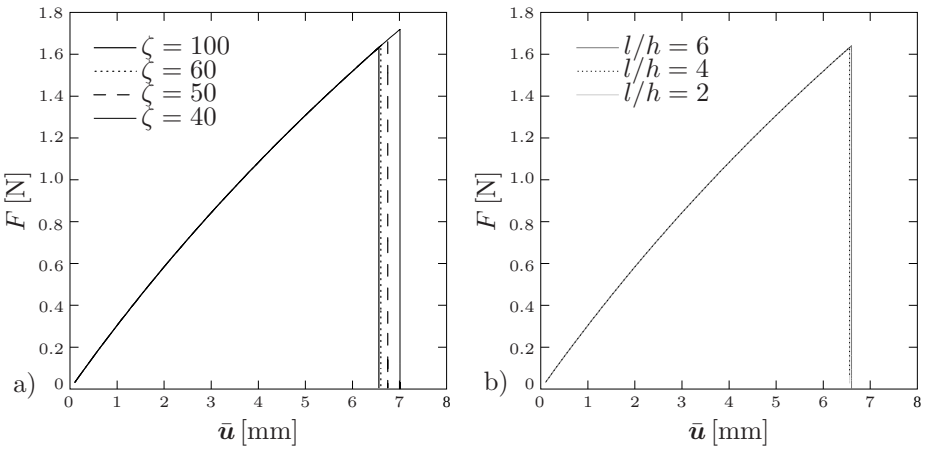

Figure 6.4: Three point bending test. a) Sensitivity of structural response on driving force slope factor ζ introduced in (4.63). Curves for $\zeta = 60$ and 100 almost coincide. b) Influence of length scale l at fixed $\zeta = 60$. Curves for $l/h = \{2, 4, 6\}$ almost coincide.

the homogeneous problem investigated in Figure 4.2c. The influence of the length scale l is analyzed at fixed $\zeta = 60$ for three simulations with $l_1/h = 2$, $l_2/h = 4$ and $l_3/h = 6$. As shown in Figure 6.4b, the overall structural response is not very sensitive to the length scale l. The curves nearly coincide.

6.4.2. Inhomogeneous Strip under Tension. This example shows a boundary value problem in which curvilinear cracks develop. A rectangular strip of 60 mm width and 30 mm height with two excentrical holes of diameter 10 mm is analyzed for tensile loading. The geometry is depicted in Figure 6.5a. Notice that no initial crack is introduced. The elastic constants in Table 6.1 are modified for this example to $\mu = 0.19\,\mathrm{N/mm^2}$, $\nu = 0.45$. When the specimen is loaded, an inhomogeneous stress distribution in the strip develops, with maximum values at the top and bottom positions of the holes. Once these values exceed the threshold σ_c, the stress based crack driving state function evolves and thus, the fracture phase field d evolves. A crack initiates and grows quickly through the narrow strip towards the edge. The crack growth takes place in the direction of maximum stress. After the fracture of the narrow strip, stresses develop towards a maximum at the opposite side of the holes. There, new cracks initiate, growing through the specimen in the direction of maximum principal tensile stress. Figure 6.6 displays the stress P_{11} on the deformed configuration and shows different stages of failure of the deformation controlled problem. As shown in the last plot, the specimen breaks into three parts. The phase field variable d is shown in Figure 6.5b for the fractured state, on the undeformed configuration, to highlight the curvilinear crack path that has developed.

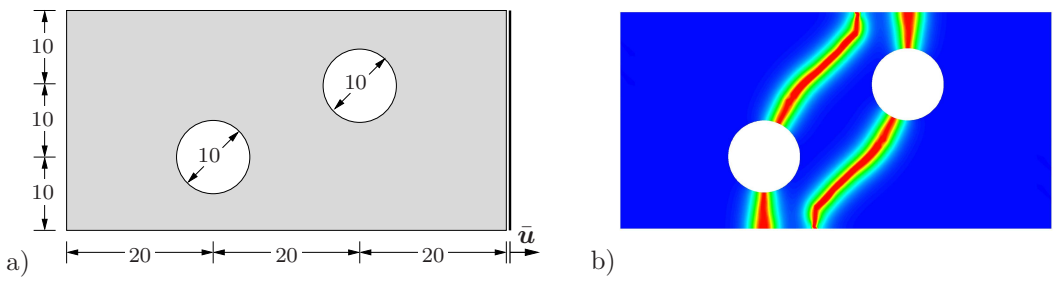

Figure 6.5: Inhomogeneous strip under tension. a) Geometry with all dimensions in [mm], b) contour of fracture phase field d at the fractured state, on the reference configuration.

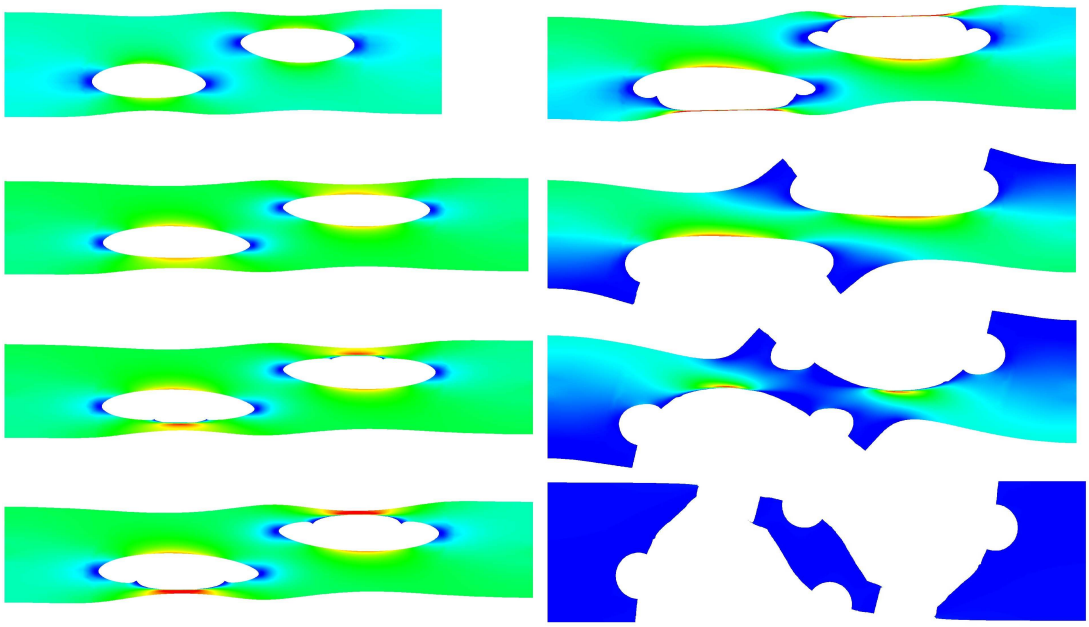

Figure 6.6: Inhomogeneous strip under tension. Stress distribution P_{11} for different stages of the deformation controlled loading process. Depicted are states at the onset of crack evolution and crack growth towards a fully fractured state.

6.4.3. Heat Flux Response at Evolving Cracks in Notched Tension Test. This example demonstrates alternative constraints for the heat flux at evolving crack faces under large strains. A rectangular specimen of width 40 mm and height 10 mm, with a horizontal centered notch of 10 mm width, is loaded by a controlled displacement at its top. In addition, a steady-state heat flux from the top to the bottom region is enforced by prescribed temperatures at the surfaces. The geometry, including the mechanical and thermal boundary conditions is depicted in Figure 6.7a. The mesh is refined in areas where the crack is expected to propagate, i.e. in a centered horizontal strip of the specimen. Exploiting symmetry, a discretization of half the specimen with 5300 elements with an effective element size of $h \approx 0.05\,\mathrm{mm}$ in the refined zone is applied. For this simulation, we modify some parameters of Table 6.1 towards $\mu = 0.19\,\mathrm{N/mm^2}$, $\sigma_c = 50\,\mathrm{N/mm^2}$, $c_s = 0$, $k_s = 10$ and $\alpha_s = 0$, in order to focus on basic effects associated with the heat flux. The computation is performed in a monotonous, displacement-driven context. The temperature field is increased by $\theta^+ = 10\,\mathrm{K}$ at the top and decreased by $\theta^- = -10\,\mathrm{K}$ at the bottom, in relation to the ambient temperature θ_∞.

Three simulations are performed, which show alternative treatments of heat flux $\mathbb{Q}^c$ across the crack, modeled by the phase transition of the heat flux defined in (6.15). In the first case, *no degradation of the heat flux* is considered, i.e. $k_c = k_s$ in (6.23). The temperature of the deformed specimen is shown in Figure 6.8a for two crack states, including the final fracture of the specimen into two parts. An intermediate state is depicted in Figure 6.7b, where the phase field d and the temperature change θ are plotted, respectively. The plot of the phase field shows the undamaged material in blue and in the fully broken continuum in red, where a crack has developed at large strains. For non-degraded conductivity, the generated *free space part* still conducts heat, as if it were undamaged. The arrows in the picture symbolize the spatial heat flux $\mathbb{q}^c$ and visualize the conduction through the free space. Obviously, this result is unphysical.

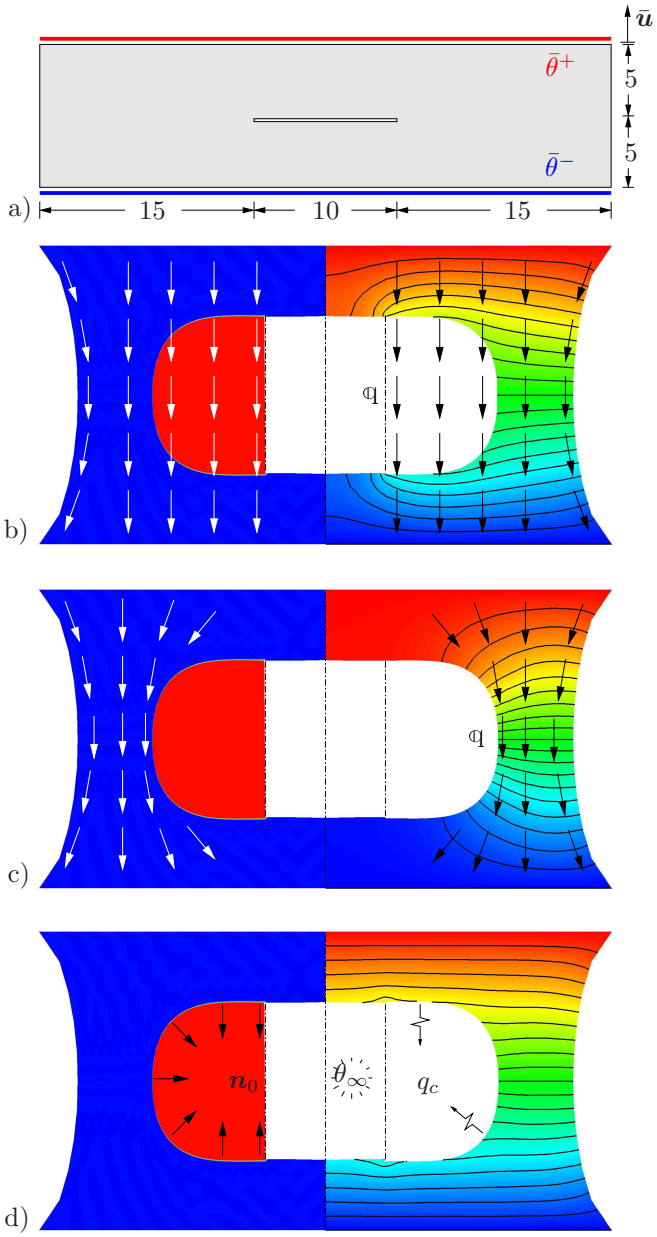

Figure 6.7: Notched tension test with prescribed temperature at boundaries. a) Geometry [mm], discretized with quadrilateral elements, and boundary conditions. In the subsequent plots: on the left, the phase field d and on the right, the temperature θ. b) Heat flux $\mathbb{q}$, indicated by arrows, with nonphysical conduction $k_c = k_s$ through crack. c) Heat flux $\mathbb{q}$ for impermeable crack $k_c = 0$ that surrounds the crack tip. d) Convective heat exchange q_c with ambient temperature θ_∞, modeled by the heat source r^c defined in (6.28).

The second case study considers a *fully degrading bulk conductivity*, i.e. $k_c = 0$ in (6.23). The temperature field during crack growth is depicted for two deformation states in 6.8b. For an intermediate state, Figure 6.7c shows the contours of the fracture phase field d and the temperature change θ. Again, red represents the fully broken continuum, i.e. the generated free space. Due to the vanishing conductivity in the free space, the spatial heat flux $\mathbb{q}^c$ becomes deformation-dependent and the heat flow surrounds the crack, which is indicated by the arrows. Because the conductivity of the free space is assumed to be zero, a thermally impermeable solution is obtained. Consequently, the

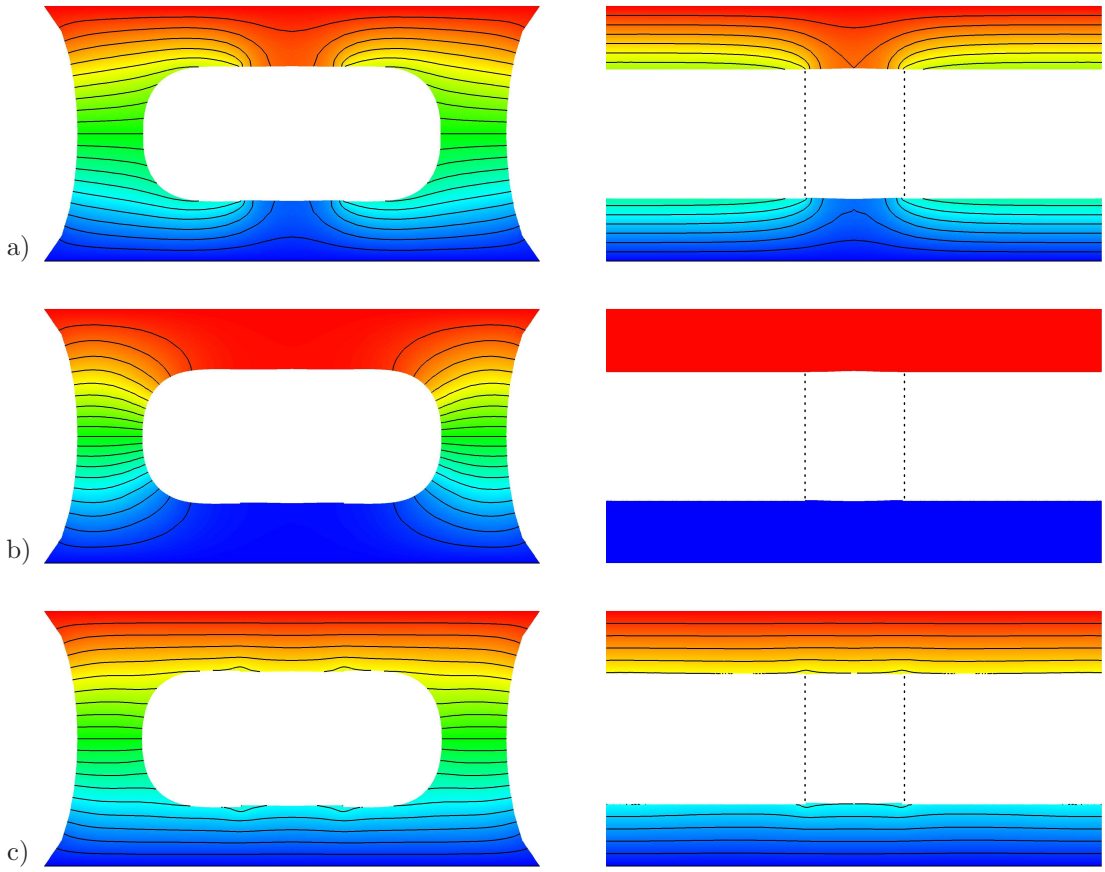

Figure 6.8: Notched tension test with prescribed temperature at boundaries. Temperature field on deformed configuration at crack growth and for fully fractured specimen. a) Non-degraded conductivity $k_c = k_s$ yielding nonphysical conduction through crack. b) Fully degraded conductivity $k_c = 0$ forms impermeable crack and two thermally decoupled fractured pieces. c) Convective heat exchange on notch and created crack surface to surrounding medium. The dotted lines indicate the position of the initial notch.

temperature contour lines are perpendicular to the newly created crack surfaces. Figure 6.8b shows that the continuing crack evolution, finally divides the specimen into two parts with homogeneous distributions of temperature. The temperature changes of these two parts are prescribed by the corresponding boundary conditions at the top and bottom surfaces.

The third simulation represents a realistic scenario. Besides the *fully degrading bulk conductivity*, it additionally takes into account *convective heat exchange on generated crack surfaces*, i.e. convection to a surrounding medium in the free space. This is realized in the context of the phase field description of fracture by the additional heat source r^c defined in (6.27). In addition to the prescribed temperature changes $\theta^+ = 10\,\mathrm{K}$ and $\theta^- = -10\,\mathrm{K}$ at the top and bottom surfaces, a convective heat exchange q_c is applied on the full surface of the specimen, according to (4.10) and modeled on crack faces by the heat source r^c, defined in (6.27). The exchange coefficient is set to $h_c = 1\,\mathrm{N}/(\mathrm{s\,mm\,K})$. Figure 6.8c depicts the temperature changes at two deformation states. As shown in the pictures, the temperatures of the initial notch surface and the newly created crack surface are equal. Especially in the final state, when the specimen is split into two parts, the influence of surface convection on the temperature is significant, see Figure 6.8c. Here, in

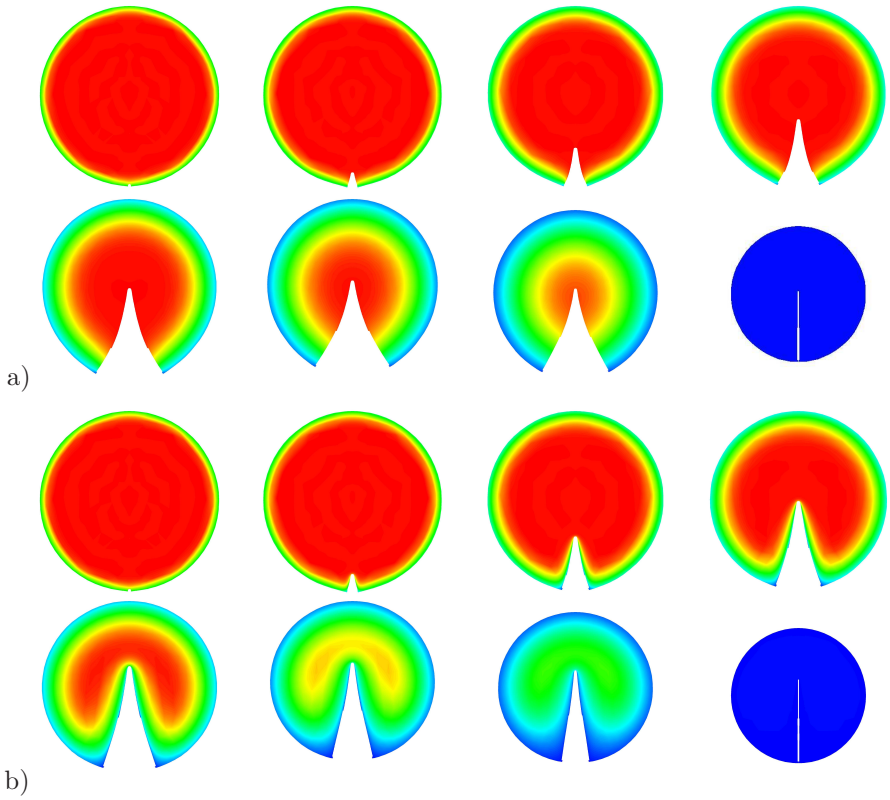

Figure 6.9: Circular body with initial notch and prescribed temperature decrease at the boundary. Transient temperature field due to surface convection to medium with linearly decreasing ambient temperature. Due to the inhomogeneous temperature gradient, the boundary contracts, leading to tensile stresses which create cracks. Temperature distribution a) without and b) with convection on crack faces, modeled by the heat source r^c in (6.28) at the times t=$\{4.85, 6.5, 15.3, 25.3, 50, 90, 140\ 1000\}$ s.

order to the separate the initial horizontal notch from the newly generated crack surface we introduce dotted lines. In the zone where convection influences the temperature on the body, the temperature field shows a uniform distribution in the zone of the initial notch as well as on the crack faces.

6.4.4. Temperature Induced Crack Propagation in a Circular Plate. The aim of this example is to predict crack propagation in solids, induced by inhomogeneous stress fields triggered by thermal expansion. To this end, a circular plate with radius $r = 1\,\text{mm}$, with a tiny initial notch of $0.025\,r$, is subjected to thermal loading. Exploiting symmetry, half of the specimen is discretized with 4200 elements, the mesh is refined to $h \approx 0.00625\,\text{mm}$ in the zone of expected crack propagation. A convective heat exchange q_c defined in (4.10) is applied to the entire surface of the specimen and modeled on crack faces by the heat source r^c defined in (6.27). The initial body temperature is $\theta(t = 0) = 300°\text{C}$, whereas the ambient temperature is set to $\theta_\infty = 0°\text{C}$. The convection coefficient is set to $h = 0.1\,\text{N}/(\text{s}\,\text{mm}\,\text{K})$. A transient temperature field in the bulk of the specimen results from the boundary condition. It causes a thin layer with a high temperature gradient and a core with almost no temperature change. The thermally induced contraction of the boundary layer induces tension tangential to the surface of the specimen. At the tip of the notch, the stresses concentrate and exceed the critical value σ_c in the driving force $\widetilde{D}$ defined in (6.32) and thus fracture is induced. At first, the crack speed is very high,

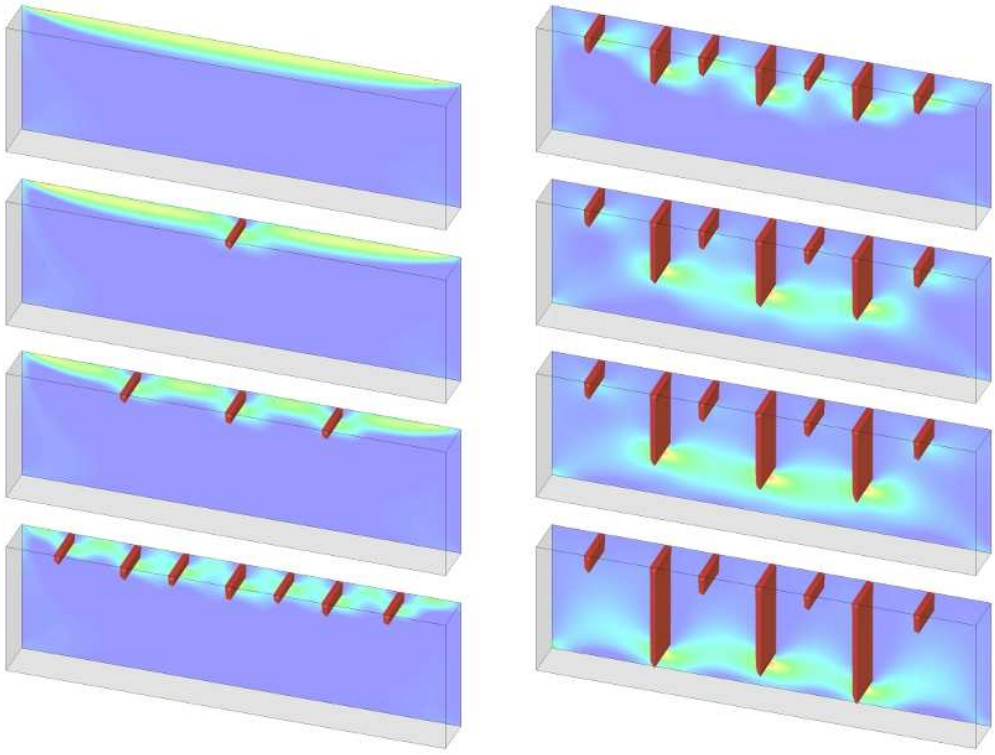

Figure 6.10: Thin Glass Plate, clamped at the bottom. Prescribed temperature drop of $-100°C$ on the upper surface leads to contraction and to natural tensile transversal stress with maximum in the middle of the upper edge. Cracks open up, partitioning the upper surface in regular segments. Stress plots and evolving cracks at $t = \{6.1, 6.78, 7.36, 9.33, 24.2, 60, 84, 1550\}$ s.

so the crack evolves instantaneously. Then, the crack speed decreases and at some stage the crack stops growing. While the crack opens, the contraction of the boundary layer bends the body open. The crack surfaces obtain a convex, curved shape. The surface convection cools down the specimen until, after a long period of time, the entire body has adapted to the ambient temperature and returned to its circular form. Figure 6.9a shows the temperature change with the thin layer of high gradients, when only the degrading bulk conductivity is considered at the times t=$\{4.85, 6.5, 15.3, 25.3, 50, 90, 140\ 1000\}$ s. The test is repeated by considering not only the convection on the outer surface, but also a *convective heat exchange at the generated crack surfaces*, modeled by the additional heat source r^c defined in (6.27). The resulting temperature changes are depicted in Figure 6.9b. As long as the crack propagates with high speed, the results resemble the ones of the previous example. When the crack speed slows down and the crack arrests, the surface convection on the crack surface becomes visible. The surface convection cools down the specimen until, after ≈ 1000 s, the entire body has adapted to the ambient temperature and recovered its circular shape.

6.4.5. Thermal Shock Induced Crack in a Brittle Solid. This example demonstrates the evolution of thermally induced complex crack patterns. An experimental study of Geyer & Nemat-Nasser [85] on thermally induced cracks in brittle solids is simulated. An analysis of this problem was recently outlined in Sicsic et al. [197]. In the experiment, a glass slab with uniform temperature is brought into contact with dry

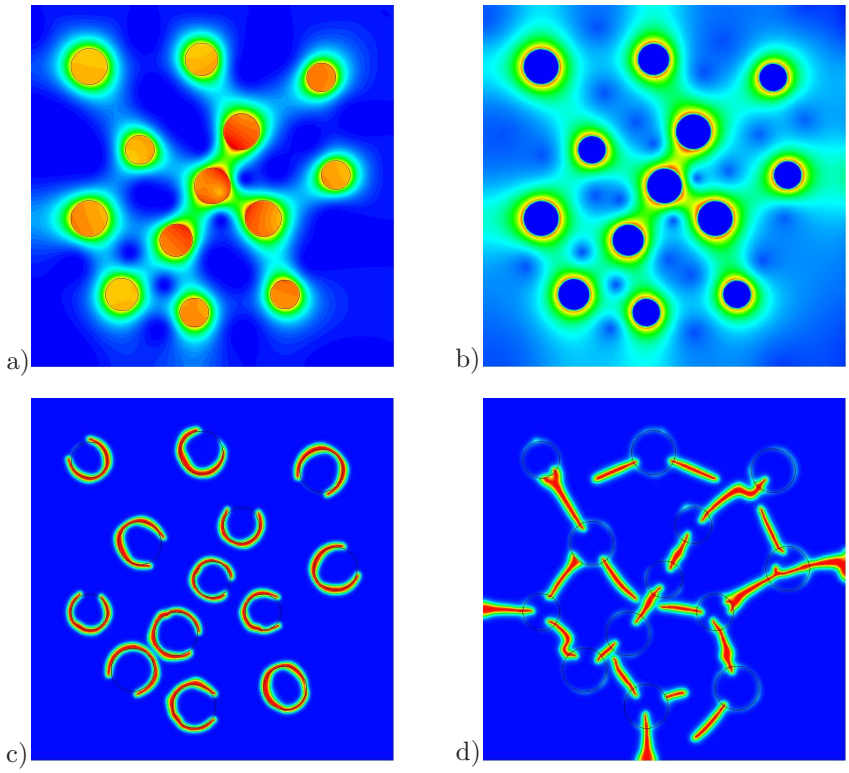

Figure 6.11: Stresses induced by cooling from manufacturing temperature of $\approx 700°C$ to room temperature. *Composite 1* develops positive stresses in the spheres, see a), whereas *composite 2* shows maximum positive stresses around the particles, see b). Further cooling induces spontaneous microcracks. In *composite 1*, circumferential cracks grow, see c), in *composite 2* radial cracks grow between the spheres in the matrix, see d).

ice. Because of the cooling of the contacting edge, a thermal boundary layer develops in the solid within a transient process, yielding thermally induced cracks. In order to simulate this effect, a rectangular plate of width 100 mm and height 30 mm is discretized. The bottom surface is fixed in all directions and the temperature is held constant at $\theta = 22°C$. The thermal loading through contact is modeled by a Dirichlet-type control of the temperature field at the upper surface. In a period of 10 s, the temperature is linearly decreased from $\bar{\theta} = 22°C$ to a minimum of $\bar{\theta} = -78°C$, which is then held constant. The shock-like thermal stimulation leads to contraction and a natural tensile transversal stress in a thin layer. Through the natural stress state, a maximum in the middle of the upper surface evolves, leading to a first crack there. In Figure 6.10, the stress P_{11} and the evolving cracks are shown at the times $t = \{6.1, 6.78, 7.36, 9.33, 24.2, 60, 84, 1550\}$ s. With ongoing cooling, the stress on the upper surface again reaches its maximum in the middle of the partitions, producing secondary cracks. This process repeats once more. Because of the ongoing conduction process the cracks grow perpendicular to the cooled edge. However, alternate cracks stop at critical points, while the remaining ones continue to grow. When a homogeneous temperature gradient between upper and lower surface is reached, all cracks end. The results are in good qualitative agreement with the experiments reported in Geyer & Nemat-Nasser [85].

6.4.6. Fracture of a Two Phase Composite Material. This example treats the crack evolution in different types of two-phase materials. Numerous commercial ceramic materials consist of a crystalline phase embedded in a glass matrix. The strength control-

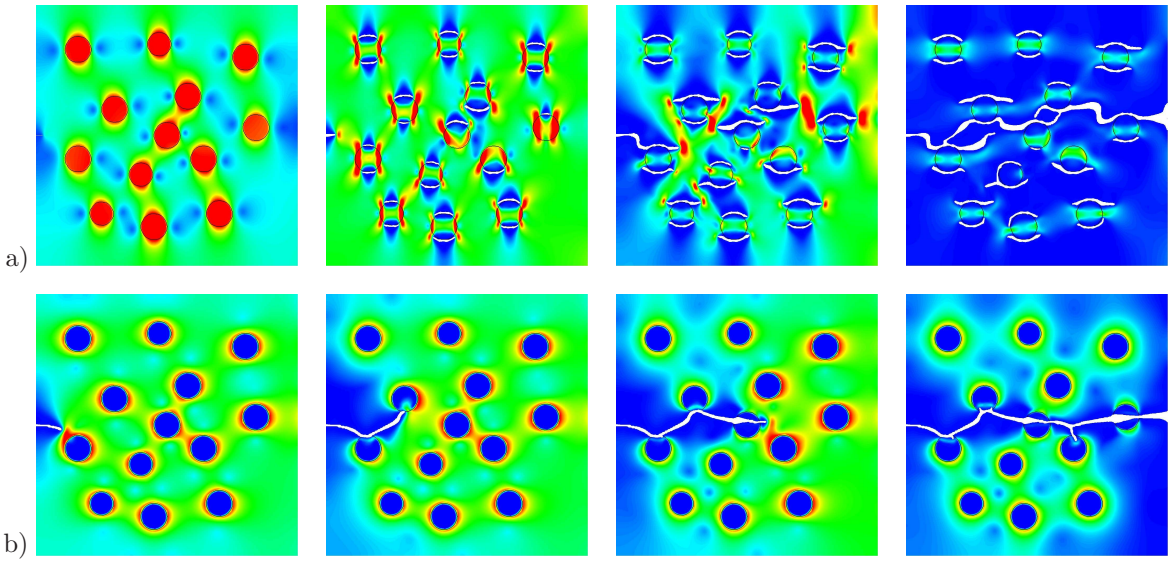

Figure 6.12: Plate under tensile loading. a) *Composite 1* with high internal residual stresses inside the spheres. Cracks propagate around the spheres inside the matrix. b) *Composite 2* with tensile tangential stresses in the matrix-sphere interface. The crack is directed towards the spheres and eventually cracking of the spheres is observed.

ling factors are the expansion coefficients of the two phases, the volume fraction, particle size and the elastic properties. Davidge & Green [52] studied the effect of these mechanical properties on the stresses around particles. Different types of glass containing 10 % thoria spheres were prepared and tested. On this basis, we investigate two different composites, with $\mu_M = 29166\,\mathrm{N/mm^2}$, $\nu_M = 0.2$ and $\mu_S = 97847\,\mathrm{N/mm^2}$, $\nu_s = 0.275$ for the matrix and the spheres, respectively. The expansion coefficient of the spheres is $\alpha_S = 8.7 \times 10^{-6}$. In *Composite 1* with $\alpha_S > \alpha_{M1}$, the matrix expansion coefficient is $\alpha_{M1} = 6.8 \times 10^{-6}$, whereas in *Composite 2* the matrix expands more than the spheres $\alpha_S < \alpha_{M2} = 10.5 \times 10^{-6}$. Fracture induced by sphere-matrix interaction occurs either after fabrication due to the differences in thermal expansion, or due to the influence of an externally applied load. For the simulation, a sample is created with the dimensions $1 \times 1\,\mathrm{mm}$, containing 13 circular inclusions of diameter 0.09 or 0.1 mm which yields a fraction of $\approx 10\,\%$. The sample is meshed with ≈ 117000 quadrilateral elements having an edge length of $h \approx 0.003\,\mathrm{mm}$. The length scale is $l = 0.012\,\mathrm{mm}$, $\zeta = 10$. The critical stress parameters for the matrix and the spheres are set to $\sigma_{c,M} = 110\,\mathrm{N/mm^2}$and $\sigma_{c,S} = 200\,\mathrm{N/mm^2}$, respectively.

Stresses around the spheres originate from production processes, where the material is first vacuum hot-pressed at around 700°C and cooled down afterwards. In *Composite 1*, where the particles contract more than the matrix, positive stresses develop in the spheres, see Figure 6.11a. *Composite 2* shows maximum positive stresses around the particles, see Figure 6.11b. Further cooling induces spontaneous microcracks at the interfaces. At a very low temperature, the stresses around the spheres exceed the critical stresses σ_c, initiating cracks. The nature of cracking depends on the type of composite. In *Composite 1*, cracks occur on the phase boundaries in a circumferential manner, separating the spheres from the matrix, see Figure 6.11c. In *Composite 2*, cracks initiate on the boundaries and grow radially between the spheres into the matrix, breaking the body into fragments, see Figure 6.11d. These failure mechanisms occur solely due to thermal contraction.

The influence of sphere matrix interaction on the fracture of an *externally loaded* plate at room temperature is also studied. Therefore, cooling from the production process to room temperature is simulated first, followed by a simple tensile loading in vertical direction. The internal residual stress state occurring from particle and matrix contraction is already shown in Figure 6.11a,b. The stresses which arise from the deformation controlled loading are superimposed on the internal residual stresses. Since the inclusions are stiffer than the matrix, the inclusions reach higher stresses. *Composite 1* shows high stresses inside the spheres and on the interfaces. Tangential cracks develop at all sphere boundaries in the brittle matrix. Cracks in higher stressed regions in the matrix propagate around the spheres and approach each other. Finally the plate is separated into two pieces. The internal residual stresses in the spheres are almost relieved. *Composite 2* shows tensile tangential stresses in the matrix-sphere interface. A single crack grows from the boundary inside the matrix. It is directed towards the spheres and either grows along the interfaces or passes through the spheres. The Internal residual stresses around the uncracked spheres remain in the fragments.

7. Rate and Temperature Dependent Viscoelasticity and Failure

A phase field model for rate-independent crack propagation in rubbery polymers at large strains was discussed in Chapter 5. In this chapter, the brittle fracture model for finite elasticity is extended, towards the description of *rate and temperature dependent failure of viscoelastic rubbery polymers*. Rubbery polymers may exhibit very complicated inelastic effects, such as rate and temperature dependent bulk response. The micromechanical model of elasticity, presented in Chapter 5, is extended towards the modeling of viscoelasticity by a time dependent motion of superimposed entangled chains, visualized in Figure 7.1. The latter effect is micromechanically motivated by motion of the superimposed chains relative to the ground state network. Upon deformation, as shown in Figure 7.1b,c, the dangling ends of the chains retract by Brownian motion, yielding the relaxation of the non-equilibrium stresses. According to the molecular dynamics theory of reptation, outlined in de Gennes [53] and Doi & Edwards [56], the rate of the relaxation process differs with the elapsed time in the relaxation process. This result of the theory of molecular dynamics is taken into account by a *discrete spectrum of relaxation times*. Conceptually following the work of Bergström & Boyce [23] or Miehe & Göktepe [152], we now consider a hierarchy of superimposed chains, as schematically indicated in Figure 7.1b. These superimposed chains are related to the ground state network by entanglement mechanisms. We associate the ground state network with the macroscopically observed equilibrium curve and the superimposed chains with the viscous overstress response of Figure 7.1a, respectively.

Crack propagation in non-crystallizing polymers is observed to be rate and temperature dependent, with an energy release rate varying over decades with changing crack speed. Fracture of rubber is initiated from imperfections in the body of the material or on its surface. When a crack grows, irreversible processes occur in the vicinity of the moving crack tip, leading to energy losses that must be made up for by the available elastic energy. Thus, the energy necessary to propagate a crack at a particular rate may greatly exceed the thermodynamic surface free energy. Elastomers that do not crystallize on stretching

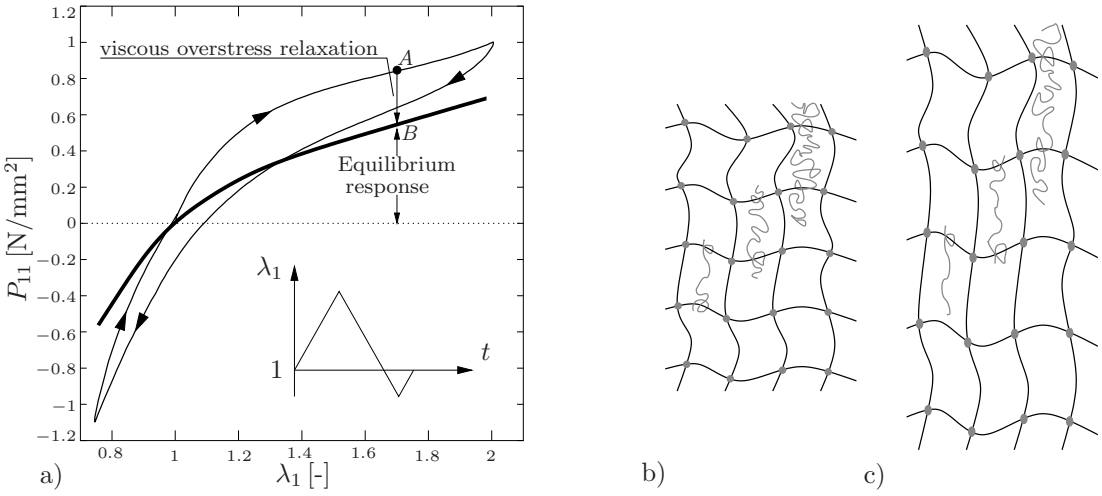

Figure 7.1: a) Non-equilibrium cyclic and elastic equilibrium curve without hysteresis (thick line). A spectrum of non-equilibrium networks is superimposed via entanglements to the equilibrium network. At a deformation b) to c), the dangling ends of the chains retract by Brownian motion. Different lengths of the gray chains motivate the utilization of the relaxation spectrum.

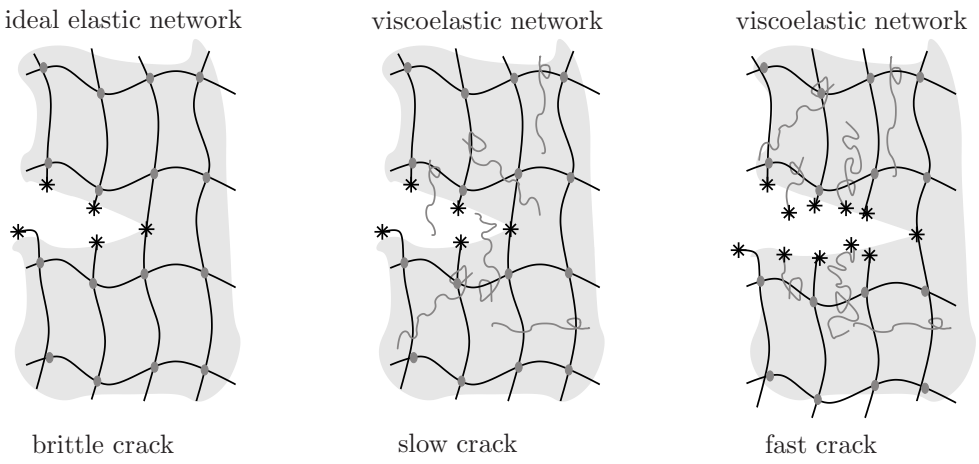

Figure 7.2: Chains crossing the fracture plane are broken during fracture. In an ideal elastic network, a brittle crack occurs for $g = g_c$. During slow crack growth in a viscoelastic network, superimposed chains relax and the crack grows for $g \gtrapprox g_c$. During fast crack growth, crosslinked and entangled chains are broken, since relaxation is retarded. The fracture toughness is increased and crack grows for $g \gg g_c$.

are often found to tear in a steady, time dependent manner. In Figure 1.3 and 7.12, the experimental results from Gent & Lai [83] show the variation of energy release rate g with crack speed v. The energy release rate increases for increasing crack speed. Gent [82] pointed out that the strength properties are greatly enhanced by viscous resistance to internal motion or, more generally, by internal losses. We exploit the concept of a hierarchy of chains superimposed to a three-dimensional ground state network for the motivation of rate dependent fracture processes. In Figure 7.2, ideal and viscoelastic networks are sketched. The viscoelastic network consists of an ideal elastic ground state network, with a hierarchy of superimposed chains. The behavior of the brittle crack in an ideal elastic network reconfirms the ideas of Chapter 5. Chains, whose crosslinks lie on opposite sides of the plane of crack propagation, need to be broken to create the new crack surface. At low crack tip velocity, the tensile loading is very slow and the polymer chain segments between the cross links rearrange themselves. The superimposed chains disentangle and relax. Much of the external load will be distributed on the cross link bonds and a low fracture energy is observed. On the other hand, at a fast crack growth, the polymer chains do not have enough time to rearrange themselves and large stress is necessary to break the chemical bonds in the block. Additional to the chains in the ground elastic network, superimposed chains need to be broken as well, to create crack surface. The superimposed chains raise the resistance to fracture and damp the crack speed. Since the mobility of the polymer chains is strongly affected by temperature, the resistance to fracture increases with decreasing temperature, as does the material stiffness.

The remainder of this chapter is organized as follows. First, the constitutive model for the thermo-viscoelastic bulk response is derived, then a maximum stress criterion based on a critical fracture stress is introduced, which makes a differentiation between tensile and compression region simple. A constitutive assumption on the decrease of fracture toughness with increasing temperature is motivated and introduced in the crack driving force. The constitutive expressions enter the governing Euler equations of the coupled problem, presented in Chapter 4. The increase in crack resistance is modeled by a viscous crack resistance. Finally, we demonstrate the performance of the phase field model of rate and temperature dependent fracture at large strains, by means of representative

numerical examples. They successfully demonstrate the ability of the model to predict the experimentally observed relation between crack-speed, temperature and energy release rate.

7.1. Specific Constitutive Functions for Rubbery Polymers

The general framework of coupled problems presented in Chapter 4 is specified towards the modeling of crack propagation in thermo-visco-elastic rubbery polymers. A three field coupled problem is obtained, governed by the balance equations (4.21), (4.27) and (4.35)

$$\begin{array}{ll} \rho_0 \ddot{\boldsymbol{\varphi}} & = \mathrm{Div}[\boldsymbol{P}] + \rho_0 \boldsymbol{\gamma} \\ \rho_0 c \dot{\theta} & = \mathrm{Div}[-\mathbb{Q}] + \rho_0 (R + H + \mathcal{D}_{loc}) \\ (d - l^2 \Delta d) & = (1-d)\mathcal{H} - \eta \dot{d} \ . \end{array} \tag{7.1}$$

The *crack evolution time* η is a decisive parameter for the modeling of rate dependent crack propagation. The parameter η is adapted to experimental results to model the increase in crack resistance with increasing crack speed. Within the phase field model of fracture at large strains, summarized in Chapter 4, the impact of the bulk response on crack propagation is governed by the crack driving state function $\widetilde{D}$. Vice versa, the crack phase field enters the bulk state response function Ψ, by modeling degradation from the initially unbroken, to the fully broken state. The dissipation potential (4.17) governs the evolution of the internal variables $\mathfrak{q}$.

7.1.1. Nominal Constitutive Energy Storage Function. The degradation of the solid response needs to be constructed, depending on the phase field $d \in [0,1]$. We assume the constitutive structure for the nominal free energy

$$\Psi(\boldsymbol{F}, \mathfrak{q}, \theta; d) = g(d) \widetilde{\Psi}(\boldsymbol{F}, \theta, \mathfrak{q}) + \Psi_\theta(\theta) \tag{7.2}$$

where the volume specific effective energy function $\widetilde{\Psi}$ is associated with the intact solid. The purely thermal part of the free energy is assumed to have the convenient form

$$\rho_0 \Psi^s_\theta(\theta) = \rho_0 \Psi_0 - \rho_0 \eta_0 (\theta - \theta_0) - \rho_0 c_s [\theta \ln \frac{\theta}{\theta_0} - \theta + \theta_0] \ , \tag{7.3}$$

where c_s is a heat capacity parameter that is assumed to be a constant. The monotonically decreasing *degradation function* $g(d)$ describes the softening of the material with evolving damage. It is assumed to have the properties

$$g(0) = 1 \quad , \quad g(1) = 0 \quad , \quad g'(1) = 0 \ . \tag{7.4}$$

The first two conditions include the limits for the intact and the fully-broken case. As shown below, the latter constraint ensures that the fracture force converges to a finite value, if the damage converges to the fully-broken state $d = 1$. A simple example of a function that fulfills the above properties is $g(d) = (1-d)^m$, whereas $g(d)$ recovers the classical damage theory for $m = 1$. The variational theory of brittle fracture in elastic solids outlined in Miehe et al. [161], is obtained for $m = 2$.

7.1.2. Decoupled Volumetric and Isochoric Stress Response. We consider a class of weakly compressible polymers, where the bulk response is assumed to be elastic and viscosity effects are exclusively restricted to the isochoric part of the deformation. A

decoupling of the stress response into volumetric and isochoric contributions is based on the decomposition

$$\boldsymbol{F} = \bar{\boldsymbol{F}}\boldsymbol{F}_{vol} \quad \text{with} \quad \boldsymbol{F}_{vol} := J^{1/3}\boldsymbol{1} \ . \tag{7.5}$$

The unimodular part of the deformation gradient $\bar{\boldsymbol{F}} = J^{-1/3}\boldsymbol{F}$ is assumed to govern the deviatoric stresses. In order to describe the thermal expansion, we decompose the volumetric deformation $\boldsymbol{F}_{vol}$

$$\boldsymbol{F}_{vol} := \boldsymbol{F}_e\boldsymbol{F}_\theta \quad \text{with} \quad \boldsymbol{F}_\theta = J_\theta^{1/3}\boldsymbol{1} \quad \text{and} \quad \boldsymbol{F}_e := J_e^{1/3}\boldsymbol{1} \tag{7.6}$$

into a stress producing part $\boldsymbol{F}_e$ and a part $\boldsymbol{F}_\theta$ due to the thermal expansion. J_θ is defined such that isotropic expansions are assumed, governed by the scalar constitutive function

$$J_\theta(\theta) = \exp[3\alpha_s(\theta - \theta_0)] \ , \tag{7.7}$$

with the linear thermal expansion coefficient α_s, see Lu & Pister [142]. The volumetric stress producing invariant J_e can be determined explicitly in terms of the total Jacobian

$$J_e(J,\theta) = J\, J_\theta^{-1}. \tag{7.8}$$

A decoupled volumetric-isochoric structure of finite viscoelasticity is obtained by considering the specific form

$$\widetilde{\Psi} = U(J_e) + \bar{\Psi}(\bar{\boldsymbol{F}}, \mathfrak{q}, \theta) \tag{7.9}$$

of the effective stored energy of intact solid. Then, the effective stresses $\widetilde{\boldsymbol{P}} = \rho_0\partial_{\boldsymbol{F}}\widetilde{\Psi}(\bar{\boldsymbol{F}}, \mathfrak{q}, \theta)$ additively decompose into spherical and deviatoric contributions

$$\widetilde{\boldsymbol{P}} = p(J_\theta^{-1}J\boldsymbol{F}^{-T}) + \mathbb{P}_F : \bar{\boldsymbol{P}} \quad \text{with} \quad p := U'(J_e) \quad \text{and} \quad \bar{\boldsymbol{P}} := \rho_0\partial_{\bar{\boldsymbol{F}}}\bar{\Psi}(\bar{\boldsymbol{F}}, \mathfrak{q}, \theta) \ , \tag{7.10}$$

where $\mathbb{P}_F := \partial_{\boldsymbol{F}}\bar{\boldsymbol{F}} = J^{-1/3}[\mathbb{I} - \frac{1}{3}\boldsymbol{F} \otimes \boldsymbol{F}^{-T}]$ with $\mathbb{I}_{ijkl} = \delta_{ik}\delta_{jl}$ is the fourth-order deviatoric projection tensor. For an almost incompressible response of the polymer network, the potential U can be considered as a penalty function, which approximately enforces the incompressibility constraint. Appendix (B) presents a *Q1-P0* element formulation including phase field fracture aspects.

7.2. Decoupled Isochoric Equilibrium and Overstress Response

Based on the network model approach of rubber viscoelasticity, we decompose the isochoric free energy into an elastic equilibrium and a viscoelastic overstress response, by the additive split of the isochoric stress potential

$$\bar{\Psi} = \bar{\Psi}^0(\bar{\boldsymbol{F}}, \theta) + \bar{\Psi}^v(\bar{\boldsymbol{F}}, \theta, \mathfrak{q}) \ . \tag{7.11}$$

This induces a further split of the stresses $\bar{\boldsymbol{P}}$ defined in $(7.10)_3$ according to

$$\bar{\boldsymbol{P}} = \bar{\boldsymbol{P}}^0 + \bar{\boldsymbol{P}}^v \quad \text{with} \quad \bar{\boldsymbol{P}}^0 := \rho_0\partial_{\bar{\boldsymbol{F}}}\bar{\Psi}^0(\bar{\boldsymbol{F}}, \theta) \quad \text{and} \quad \bar{\boldsymbol{P}}^v := \rho_0\partial_{\bar{\boldsymbol{F}}}\bar{\Psi}^v(\bar{\boldsymbol{F}}, \theta, \mathfrak{q}) \ . \tag{7.12}$$

The elastic equilibrium stress response $\bar{\boldsymbol{P}}^0$ of the polymer network is assumed to be *isotropic*. The dissipative viscoelastic overstresses $\bar{\boldsymbol{P}}^v$ of the superimposed networks provide a *deformation-induced anisotropy* in the non-equilibrium state, which is described by the evolution of the internal variables $\mathfrak{q}$ over time.

7.2.1. Free Energy of the Ground State Response. A constitutive model is introduced for the description of the ground state network elasticity. A micromechanically motivated network model is applied, based on the energy storage of a single chain in terms of the inverse Langevin statistics and a homogenization scheme is applied for the network structure. The advanced *non-affine microsphere network model*, developed in MIEHE ET AL. [158], links the micro-stretch of the single chain to the macroscopic deformation gradient by an average of the macroscopic stretch, using a particular homogenization method on the unit sphere. The *eight chain model* proposed by ARRUDA & BOYCE [12] obtains a closed-form relationship to the invariant $\mathrm{tr}[\boldsymbol{F}^T\boldsymbol{F}]$ and is applied for the model. The stretches are defined as $\lambda := [\mathrm{tr}(\bar{\boldsymbol{F}}^T\bar{\boldsymbol{F}})/3]^{1/2}$. With the definition of λ at hand, we define the relative stretch $\lambda_r := \lambda/\sqrt{N}$, with the number of segments N in the fictitious prototype chain. For a typical Langevin function, we then are able to define the free energy to

$$\rho_0\hat{\Psi}^0(\lambda_r) = \mu_0(\theta)N\left(\lambda_r\mathcal{L}^{-1}(\lambda_r) + \ln\frac{\mathcal{L}^{-1}(\lambda_r)}{\sinh\mathcal{L}^{-1}(\lambda_r)}\right) , \tag{7.13}$$

where μ_0 is the shear modulus and $\mathcal{L}^{-1}$ the inverse of the Langevin function, defined by $\mathcal{L}(\cdot) := \coth(\cdot) - 1/(\cdot)$. The shear modulus μ_0 depends on the temperature through the standard expression

$$\mu_0(\theta) = nk_B\theta \tag{7.14}$$

of the entropic polymer network theory, see TRELOAR [216]. Here, n is the chain density and k_B is the Boltzmann constant. Note that no exact formulation, but different approximations of the inverse Langevin function exist. A possible approximation is the Padé function $\mathcal{L}^{-1}(\lambda_r) \approx \frac{1}{\sqrt{N}}\lambda\ (3N-\lambda^2)/(N-\lambda^2)$, proposed by COHEN [45]. It is attractive for modeling the bulk response because of its compact form and good approximating quality. However, it is unsuitable because of the discontinuity at $\lambda = \sqrt{N}$. Alternatively, $\mathcal{L}^{-1}$ can be approximated by a Taylor series $\mathcal{L}^{-1}(\lambda_r) \approx \sum_{i=1}^{\infty} C_i(\lambda/\sqrt{N})^{2i-1}$, where C_i are the Taylor coefficients. A list of the first relevant coefficients are documented in ITSKOV ET AL. [114]. The Stress $\bar{\boldsymbol{P}}^0$ is computed as

$$\bar{\boldsymbol{P}}^0 = \partial_{\bar{\boldsymbol{F}}}\ \rho_0\Psi^0 = \frac{\mu_0(\theta)}{3\lambda_r}\ \mathcal{L}^{-1}\ \bar{\boldsymbol{F}}\ . \tag{7.15}$$

7.2.2. Free Energy and Dissipation of Viscoelastic Overstress Response. The formulation of inelasticity in the logarithmic strain space is a special, metric-based approach to finite inelasticity. The modular structure of the formulation of finite viscoelasticity in the logarithmic strain space consists of three basic steps: geometric pre-processor, material modeling and geometric post-processor. The geometric pre-processor step defines the logarithmic isochoric strain measure of Hencky-type $\boldsymbol{\varepsilon} := \frac{1}{2}\ln\bar{\boldsymbol{C}}$ which enters the constitutive framework. The energy storage of the superimposed chain spectrum is defined in terms of a Lagrangian elastic strain variable, depending on the isochoric right Cauchy Green tensor $\bar{\boldsymbol{C}} = \bar{\boldsymbol{F}}^T\bar{\boldsymbol{F}}$ and the internal variables $\mathfrak{q}$. The elastic strains are provided by the *additive decomposition* $\boldsymbol{\varepsilon}^e := \boldsymbol{\varepsilon} - \sum_{i=1}^{n}\boldsymbol{\varepsilon}^v$. Here, we introduced tensorial, strain-like internal variables $[\boldsymbol{\varepsilon}_i^v, \ldots, \boldsymbol{\varepsilon}_n^v] = \mathfrak{q}$. The phenomenological modeling is assumed to be governed by a spectrum of $i = 1...n$ subnetworks, superimposed onto the ground state that produces strains. We denote this discrete spectrum as a *hierarchy of non-equilibrium* strains, described by the internal strain-tensor variables $\boldsymbol{\varepsilon}_i^v$. These variables are assumed to govern the viscoelastic overstress. The energy storage of the entire

spectrum of subnetworks is obtained by the summation

$$\hat{\Psi}^v = \sum_{i=1}^{n} \hat{\Psi}_i^v \quad \text{with} \quad \rho_0 \hat{\Psi}_i^v(\boldsymbol{\varepsilon}, \boldsymbol{\varepsilon}^v, \theta) = \mu_i |\boldsymbol{\varepsilon} - \boldsymbol{\varepsilon}_i^v|^2 \tag{7.16}$$

for each discrete superimposed network, where μ_i is the shear modulus of the $i-$th subnetwork, with temperature dependence according to (7.14). The viscous over-stresses can be calculated from (7.16) as

$$\boldsymbol{s}_i^v = \partial_{\boldsymbol{\varepsilon}_i} \rho_0 \Psi_i^v = 2\mu(\boldsymbol{\varepsilon} - \boldsymbol{\varepsilon}_i^v) \ . \tag{7.17}$$

For the evolution system provided in (4.17), we assume the dissipation functions of the form

$$\hat{\Phi}^v = \sum_{i=1}^{n} \hat{\Phi}_i^v \quad \text{with} \quad \rho_0 \hat{\Phi}_i^v(\boldsymbol{\varepsilon}_i^v) = \mu_i \tau_i(\theta) |\dot{\boldsymbol{\varepsilon}}_i^v|^2 \ , \tag{7.18}$$

where τ is the relaxation time of the i-th subnetwork, that is shifted by time-temperature shift. With the specific functions for the viscous free energy and the dissipation potential of each subnetwork i at hand, we can now derive the specific flow rule of the specific viscous strain tensor. From the dissipation potential (7.18), we obtain

$$\partial_{\dot{\boldsymbol{\varepsilon}}_i^v} \rho_0 \hat{\Phi}_i^v(\boldsymbol{\varepsilon}_i^v) = 2\mu_i \tau_i \dot{\boldsymbol{\varepsilon}}_i^v \ . \tag{7.19}$$

With the additive decomposition of logarithmic strains and the definition of the evolution system (4.17), we derive the definition of the flow rule of the i-th viscous strain tensor

$$\dot{\boldsymbol{\varepsilon}}_i^v = \boldsymbol{s}_i^v / (2\mu_i \tau_i) \ . \tag{7.20}$$

In total, n equations (7.20) govern the evolution of the overstresses of the superimposed networks, in terms of $2 \cdot n$ material parameters in addition to the elastic equilibrium response. The final step, the *geometric post-processor*, is concerned with the mapping of the algorithmic stresses (7.17), obtained in the logarithmic strain space onto their nominal counterparts $\bar{\boldsymbol{P}}^v = \boldsymbol{s}^v : \mathbb{L}$ with $\mathbb{L} = \partial_{\bar{\boldsymbol{F}}} \boldsymbol{\varepsilon}$. These transformation operations are nothing more than chain rule exploitations. For more detailed discussion the reader is referred to the works of Miehe & Lambrecht [155], Miehe et al. [157].

In order to model the temperature dependent material response, the mechanical relaxation times are expressed as the product of a shift factor a_T and the known relaxation time at reference temperature θ_{ref}

$$\tau_i(\theta) = \tau_i(\theta_{ref}) \cdot a_T \ . \tag{7.21}$$

Generally, the shift factor allows a simple modeling of temperature dependent material response. For the determination of the shift factor, we adapt the simple, empirical function presented by Williams et al. [224]

$$\log a_T = -C_1 \cdot (\theta - \theta_{ref}) / (C_2 + \theta - \theta_{ref}) \ , \tag{7.22}$$

depending on the current and the reference temperature. This equation includes the empirical constants C_1 and C_2, that are found to be of general validity for most thermorheologically simple elastomers. By selecting the glass transition temperature as the reference value $\theta_{ref} = \theta_g$, the parameters are $C_1 = 17.44$ [-] and $C_2 = 51.6°$K, as proposed by Williams et al. [224]. To transform the constants from those obtained at the reference temperature θ_{ref} to a reference temperature $\theta'_{ref} = \theta_{ref} + \delta$, the only changes in (7.22) are the replacement of C_1 by C'_1 with $C'_1 = C_1 C_2 / (C_2 + \delta)$ and of C_1 by $C'_2 = C_2 + \delta$. For $\delta = 50°$K, the parameters are $C_1 = 8.86$ [-] and $C_2 = 101.6°$K. The range of definition of (7.22) is restricted to $\theta_g < \theta < \theta_g + 100°$C.

7.2.3. Internal Variable Update. Using a backward Euler scheme for the time increment $\Delta t := t - t_n$, the evolution of the specific viscous strain for each subnetwork can be written as

$$\dot{\boldsymbol{\varepsilon}}_i^v = (\boldsymbol{\varepsilon}_i^v - \boldsymbol{\varepsilon}_{in}^v)/\Delta t \ . \tag{7.23}$$

With the specific flow rule (7.20) and the function for the driving stress tensor (7.17), we obtain $\boldsymbol{\varepsilon}_i^v = \boldsymbol{\varepsilon}_{in}^v + \Delta t/\tau_i(\mathrm{dev}[\boldsymbol{\varepsilon}] - \boldsymbol{\varepsilon}_i^v)$. The algorithmic value of the viscous strains is

$$\boldsymbol{\varepsilon}_i^v = \frac{\boldsymbol{\varepsilon}_{in}^v + \mathrm{dev}[\boldsymbol{\varepsilon}]\ \Delta t/\tau_i}{1 + \Delta t/\tau_i} \ . \tag{7.24}$$

Resulting from the additive split of the isochoric free energy, the moduli can be split into a ground state and a viscous part $\bar{\mathbb{C}}^{algo} = \bar{\mathbb{C}}^0 + \bar{\mathbb{C}}^v$. The ground state moduli read

$$\bar{\mathbb{C}}^0 = \partial^2_{\bar{\boldsymbol{F}}\bar{\boldsymbol{F}}}\ \rho_0\Psi^0 = \frac{\mu_0\mathcal{L}^{-1}}{3\lambda_r}\mathbb{I} + \frac{\mu_0}{9\lambda_r^2}\ \boldsymbol{F}\otimes\boldsymbol{F}\left(\partial_\lambda\mathcal{L}^{-1} - \frac{\mathcal{L}^{-1}}{\lambda}\right) . \tag{7.25}$$

For the numerical approximation of the inverse Langevin function, the Taylor approximation is used. Finally, the moduli of the subnetworks are derived as the sum of the total derivation of the $i-$th viscous stresses (7.17) by the strain

$$\mathbb{E}^v = \textstyle\sum_{i=1}^n \mathbb{E}_i^v \quad \text{with} \quad \mathbb{E}_i^v = \dfrac{d\boldsymbol{s}_i^v}{d\boldsymbol{\varepsilon}} = 2\mu_i\left(1 - \dfrac{\Delta t/\tau_i}{1+\Delta t/\tau_i}\right) , \tag{7.26}$$

in terms of the $i-$th shear modulus and relaxation time. The isochoric logarithmic moduli $\mathbb{E}^v$ have to be projected to the Lagrangian moduli $\bar{\mathbb{C}}^v$. The projection of $\bar{\mathbb{C}}^{algo}$ to the isochoric contribution to the moduli $\mathbb{C}^{algo}$ follows by chain rule exploitation, see Miehe & Lambrecht [155].

7.3. Principal Tensile Stress Crack Driving Force

In order to obtain a simple criterion for mixed tensile-compression stress modes applicable to general non-linear and possibly anisotropic elasticity, consider first the decomposition of the effective Cauchy stresses into tensile and compressive parts

$$\widetilde{\boldsymbol{\sigma}}^+ + \widetilde{\boldsymbol{\sigma}}^- \quad \text{with} \quad \widetilde{\boldsymbol{\sigma}}^+ := \sum_{a=1}^3 \langle\widetilde{\sigma}_a\rangle \boldsymbol{n}_a\otimes\boldsymbol{n}_a \ , \tag{7.27}$$

in terms of the ramp function $\langle\cdot\rangle := \frac{1}{2}(\ \cdot\ + |\cdot|)$. In a second step, we introduced the simple principal tensile stress criterion

$$\widetilde{D} = \zeta\big\langle \sum_{a=1}^3 (\langle\widetilde{\sigma}_a\rangle/\sigma_c)^2 - 1\big\rangle \ , \tag{7.28}$$

where an additional dimensionless parameter $\zeta > 0$ is introduced, which influences the growth of the crack phase field in the post-critical range for $\zeta \neq 1$. The driving force provides a quadratically increasing barrier function for stress levels, above a failure surface in the principal stress space, determined by the critical tensile stress σ_c. From Figure 1.3 taken from Gent & Lai [83], one can see that the fracture toughness increases with decreasing temperature. Gent [82] shows that the energy release rate values are superposable by horizontal shifts using a shift factor. In order to model the temperature

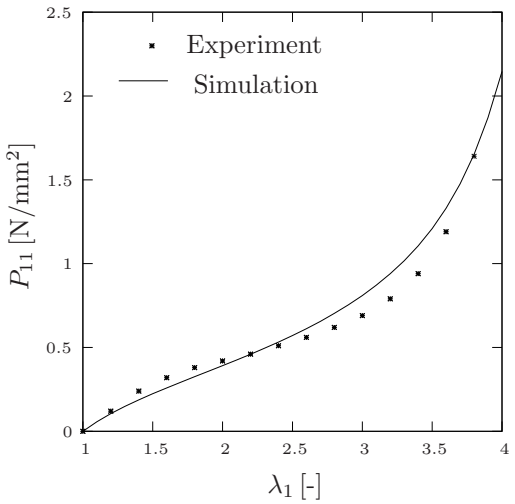

Figure 7.3: Uniaxial tension test at reference temperature $\theta_0 = 20°$C. Simulation and experimental data for getting the mechanical material parameter of the ground elasticity.

dependent shift in energy release rate, we assume a shift in critical tensile stress. Inspired by Gent [82], Gent & Lai [83], Persson et al. [179], Persson & Brener [178] or D'Amico et al. [51], we propose the critical tensile stress as

$$\sigma_c(\theta) = \sigma_c(\theta_{ref})(1 + a_T^s) \ . \tag{7.29}$$

It is decomposed into a known constant low limit $\sigma_c(\theta_{ref})$ at reference temperature and a variable part $\sigma_c(\theta_{ref})a_T^s$ as the product of the known critical tensile stress and the shift factor a_T^s with the exponent s. Such a criterion is extremely simple to implement.

7.4. Numerical Examples

We now assess the modeling capability of the proposed formulation, by comparing its simulations to experimental data. The experimental data includes monotonous and cyclic processes, at different loading rates and temperatures.

7.4.1. Simulation of Homogeneous Experiments. The model is first evaluated by comparing the simulations with experimental data of the elastic equilibrium response. The data from experiments with pre-damaged hydrogenated nitrile butadiene rubber HNBR50 are reported in Miehe & Göktepe [152]. The parameters introduced for the elastic equilibrium were identified as shear modulus $\mu = 0.24$ N/mm^2 and number of segments $N = 8.0$. As can be seen in Figure 7.3, the elastic equilibrium response of the material in uniaxial tension test fits very well, considering that only two parameters determine the material response. In order to investigate the dependence of the stress response on the loading rate, the cyclic uniaxial loading of pre-conditioned cylindrical specimens, between the stretch values $\lambda_1 = 2$ and $\lambda_1 = 0.75$, is simulated at three different absolute loading rates $|\dot{\lambda}_1| = \{0.05,\ 0.5,\ 5\}\,\text{min}^{-1}$. The stress-stretch relation from the simulations is compared to the experimental results from Miehe & Göktepe [152]. Figure 7.4a shows the uniaxial stress-stretch responses of the three test conditions to the first two loading cycles. When the loading rate increases, the material response becomes stiffer. Furthermore, the area in the hysteresis, which is proportional to the integrated dissipation, becomes larger as the loading rate increases. An additional conclusion which might be derived from the cyclic experiments, is that the difference between the first

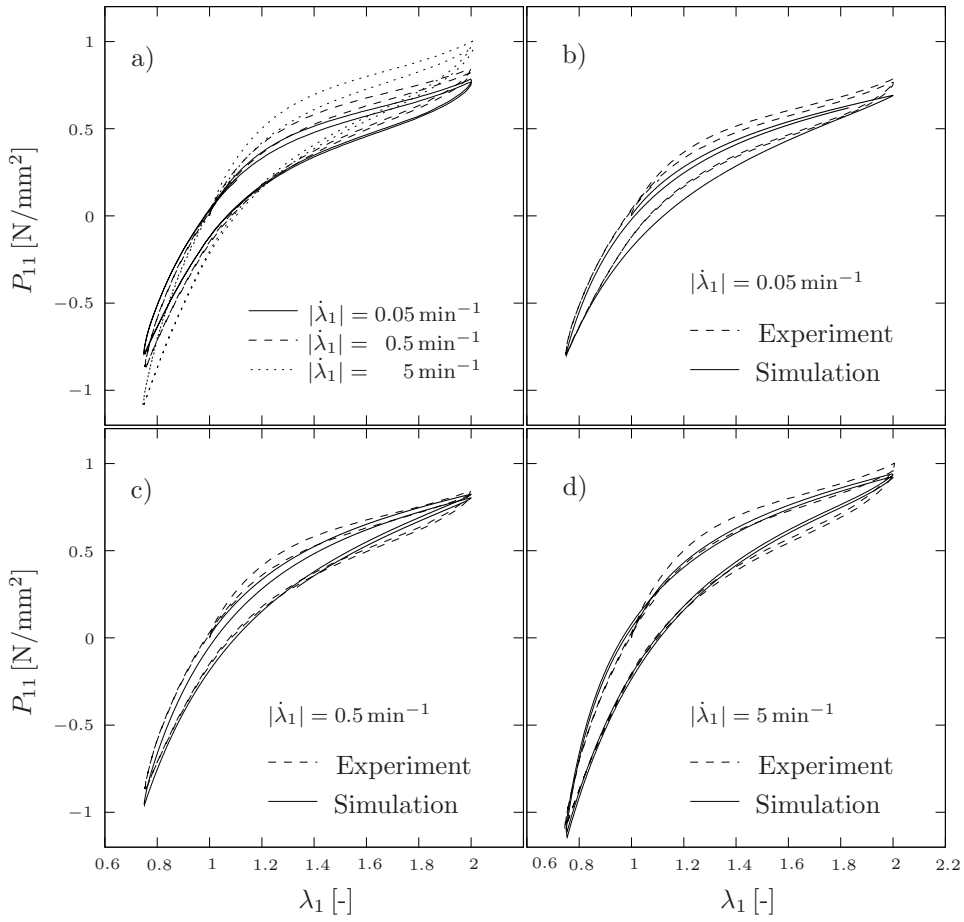

Figure 7.4: Cyclic uniaxial loading experiments and their simulations for three different loading rates: a) experimental data of all three loading rates, b) $|\dot{\lambda}_1| = 0.05\,\mathrm{min}^{-1}$ c) $|\dot{\lambda}_1| = 0.5\,\mathrm{min}^{-1}$ and d) $|\dot{\lambda}_1| = 5\,\mathrm{min}^{-1}$.

and the second stress-stretch curves becomes more apparent when the loading rate is increased. The viscous overstress part of the network model is set to be modeled by a spectrum of $n = 7$ subnetworks. The experimental results are utilized to determine the material parameters of the viscous overstress part of the network model. During the identification process, the 7 relaxation times are a priori assigned to the values $\tau_i = 10^a\,\mathrm{s}$ with $a = \{-1, 0, 1, 2, 3, 4, 5\}$ and kept frozen during the identification process. Identified values of the remaining 7 material parameters are $\mu_i = \{0.1,\ 0.13,\ 0.15,\ 0.15,\ 0.15,\ 0.07,\ 0.05\}$. The simulations with the proposed model successfully capture the material behavior observed in experiments. Therefore, the presented approach is very suitable to model finite viscoelasticity of rubbery polymers.

7.4.2. Temperature Dependent Material Response. To assess the modeling of the temperature dependent material response, three cyclic uniaxial simulations are performed at room temperature 20°C, at 10°C and at 35°C, at an intermediate strain rate $|\dot{\lambda}_1| = 0.5\,\mathrm{min}^{-1}$. The reference temperature in (7.22) is 20°C, which is approximately 50°C above the glass transition temperature. Thus, the utilized coefficients in (7.22) are the suggested common values $C_1 = 8.86$ and $C_2 = 101.6$. The change in of the relaxation times with the shift factor, results in a softer material response at a high temperature and a stiffer response at a low temperature, see Figure 7.5a. The validity is proven by comparing the simulation at low and high temperatures with the results from slow and

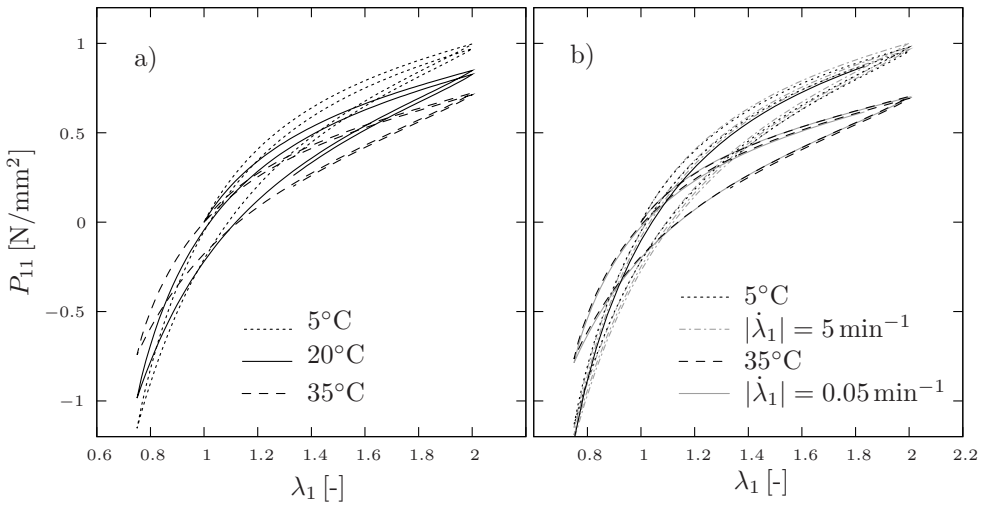

Figure 7.5: Temperature dependent material response: a) Cyclic uniaxial loading at loading rate $|\dot{\lambda}_1| = 0.5\,\mathrm{min}^{-1}$ at three temperatures $\{5,\ 20,\ 35\}$°C. Decreasing stiffness with increasing temperature. Time–Temperature Shift: b) Cyclic uniaxial curves from Figure 7.4 for fast loading resembles cold temperature and slow loading resembles high temperature.

fast cyclic tests. In Figure 7.5b, the results of cyclic uniaxial tests at strain rates of $|\dot{\lambda}_1| = \{0.05, 5\}\,\mathrm{min}^{-1}$ are compared with the simulation at $\{5,\ 35\}$°C, at an intermediate strain rate $|\dot{\lambda}_1| = 0.5\,\mathrm{min}^{-1}$. The curve of the fast loading resembles the curve at low temperature and the curve of the slow loading resembles the curve obtained at high temperature.

7.4.3. Dissipative Heating of a Conical Spring. Conical springs, used for example in trains, are associations of two materials. The discretized conical spring consists of four layers of steel (light gray) and three layers of rubber (dark gray) between them. For the geometry and dimensions of the spring see Figure 7.6a. The spring has a full height

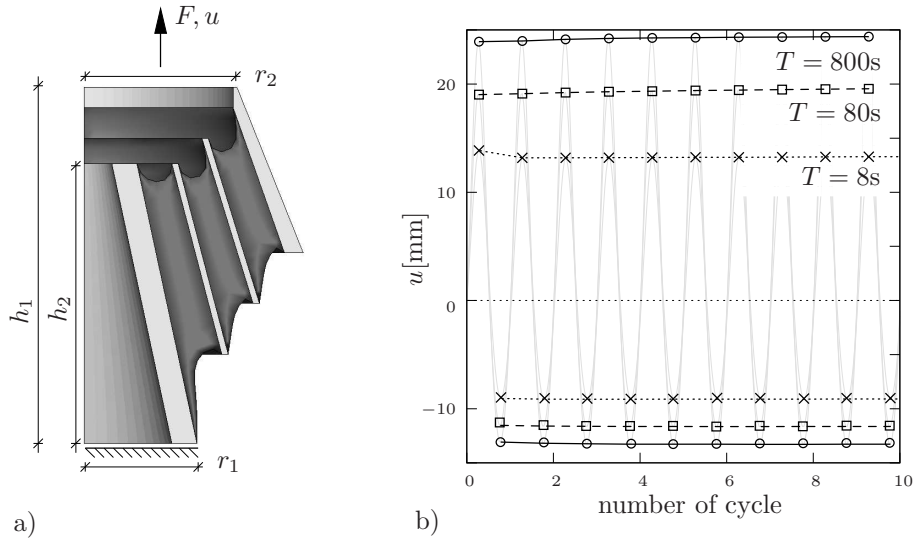

Figure 7.6: a) Geometry of a fourth conical spring with the two materials rubber (dark) and steel (light), dimensions $h_1 = 110\,\mathrm{mm}$, $h_2 = 140\,\mathrm{mm}$, $r_1 = 45\,\mathrm{mm}$ and $r_2 = 61\,\mathrm{mm}$. b) Displacement u versus number of cycle for the periods $T = \{8{,}80{,}800\}\,\mathrm{s}$. The maximum amplitude increases with increasing period time.

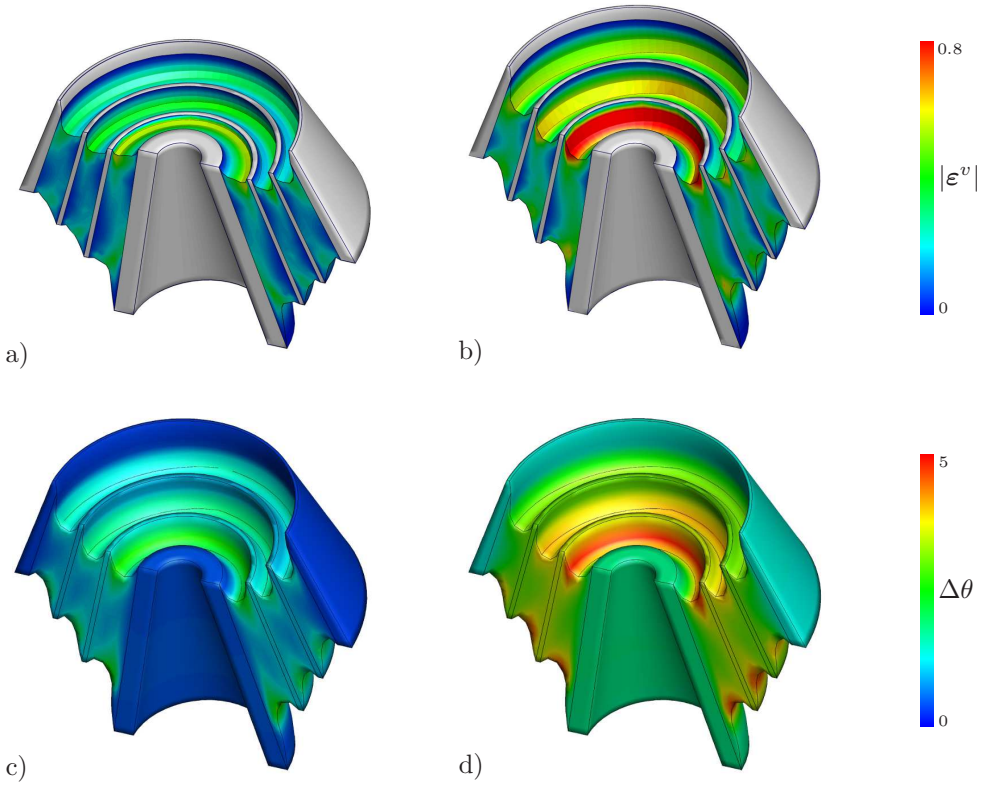

Figure 7.7: Conical spring under cyclic loading with $T = 8\,\text{s}$. Norm of viscous strains $|\boldsymbol{\varepsilon}^v|$ at maximum extension in a) and compression in b). The maximum of viscous strain occurs in the inner rubber layer. Temperature rise $\Delta\theta\,[°\text{C}]$ after 50 and 150 cycles in c) and d).

of $h_2 = 140\,\text{mm}$ and an outer radius of $r_2 = 61\,\text{mm}$. Because of the symmetry, only a quarter of the spring is discretized with 6430 elements. The spring is fixed at the bottom in all directions, at the top only in the two horizontal directions. At the top, the spring is loaded with a sinusoidal force $F = F_0 \sin(2\pi t/T)$ for different periods T=$\{8,\ 80,\ 800\}\,\text{s}$, $F_0 = 2960\,\text{N}$. The displacement of the conical spring depends on the frequency $f = 1/T$ of loading, as can be seen in Figure 7.6b, where the deformation during cyclic loading is given. A low frequency results in a high deformation. By a frequency of $f = 1/8\,\text{Hz}$, the maximum vertical displacement is $u_z \approx 14\,\text{mm}$, by $f = 1/80\,\text{Hz}$, the maximum vertical displacement is $u_z \approx 19\,\text{mm}$ and by a frequency of $f = 1/800\,\text{Hz}$ we obtain a value of $u_z \approx 25\,\text{mm}$. It can also be seen that the deformation during tension is greater than during compression. The amount of the viscous stretches differs within the rubber layers. Figures 7.7a and 7.7b show the norm of the viscous strains $|\boldsymbol{\varepsilon}^v| = \sum_{i=1}^{n} |\boldsymbol{\varepsilon}_i^v|$ after 150 cycles with a frequency $f = 1/8\,\text{Hz}$ of the loading. One can see that the inner layer of rubber shows the largest amount of viscous strain, while only little viscous strains occur in the outer layer. The amount of viscous strains is more pronounced under tension, Fig. 7.7b, than under compression, see Fig. 7.7a. The amount of dissipative heating of the material is related to the viscous strains. In Figures 7.7c and 7.7d, the temperature rise in the conical spring, loaded at frequency of $f = 1/8\text{Hz}$, is plotted after 50 and 150 cycles. In the beginning, only the rubber layers are heated by about $\Delta\theta = 2.0°\text{C}$, see Figure 7.7c. With increasing number of cycles, the temperature of the steel layers between the rubber layers also increases, due to heat conduction. The outer steel layer undergoes only a minimal temperature rise. Similar to the norm $|\boldsymbol{\varepsilon}^v|$, the highest temperatures can

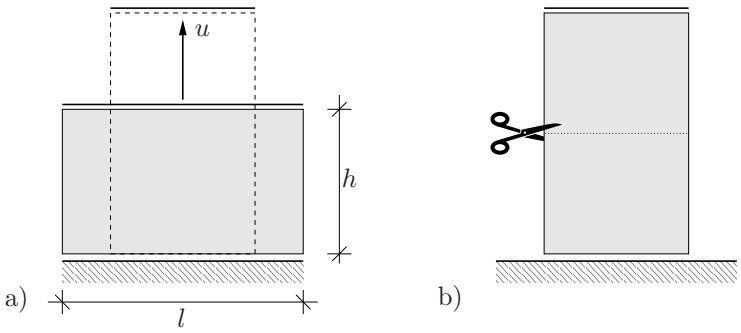

Figure 7.8: Boundary value problem. Rectangular specimen with varying height and length and varying deformation u. After deforming, a initial cut is introduced.

be found on the top and bottom of the innermost rubber layer. Here the temperature increases about $\Delta\theta = 5.5°\text{C}$ after 150 cycles, see Figure 7.7d.

7.4.4. Steady Crack Growth in Simple Extension Test. In 1920, Griffith introduced the so-called energy release rate for brittle elastic materials, see Griffith [97, 96]. This theory is a global approach to fracture mechanics, based on the balance of energy. According to (3.10) the energy release rate is

$$g = -\frac{\Delta\Pi}{\Delta A} \,, \tag{7.30}$$

provided that the internal energy is an internal potential $\mathcal{E} = \Pi_{int}$ and the external loads are conservative governed by a potential Π_{ext}, already discussed in Section 3.1.2. If inelastic material effects are considered, the internal energy $(2.37)_2$ is redefined for the inelastic material response as $\mathcal{E} = \mathcal{E}_e + \mathcal{E}_\mathcal{D}$, with $\mathcal{E}_e$ being the stored elastic internal energy of the type of an internal potential $\mathcal{E} = \Pi_{int}$ and $\mathcal{E}_\mathcal{D}$, the work dissipated to heat or used for viscous or plastic deformation processes. As discussed in Section 3.1.2, the energy released g is

$$g = \frac{\Delta\mathcal{D}}{\Delta A} + \frac{\Delta\mathcal{E}_\mathcal{D}}{\Delta A} = -\frac{\Delta\Pi}{\Delta A} \,. \tag{7.31}$$

The energy released during crack growth includes both the geometry dependent viscous or plastic dissipation of the specimen, the inelastic effects occurring in the process zone and the chemical dissociation energy $\mathcal{D} = 2\gamma A$. Experimental energy release rate values from Gent [82], Greensmith & Thomas [91] and Thomas [210] are extracted and displayed together in Figure 7.12. The experimental data shows a linear correlation between g and the crack speed v in double logarithmic scale.

Five simulations on steady crack growth in rectangular test pieces under simple extension are performed, see Figure 7.8. The lower edge is fixed against vertical displacement but displacements parallel to the edge are allowed. The specimen is stretched by displacing the upper edge by u. The loading is linearly applied in $10^6\,\text{s}$ to the ultimate extension, which is then held constant. This guarantees a fully relaxed material state without viscous overstress. To initiate the crack process, the incision is introduced as an initial crack by Dirichlet boundary conditions with $d = 1$ at $t_1 = 0\,\text{s}$. The test geometries have the particular dimensions and loadings ($l\,[\text{mm}]\times h\,[\text{mm}]\times u\,[\text{mm}]$) `a`: $100\times40\times40$, `b`: $40\times20\times11$, `c`: $40\times20\times15$, `d`: $100\times40\times30$ and `e`: $100\times40\times60$. Due to symmetry, only half the specimen is discretized. The mesh is refined to a size of 0.5 mm in areas where the crack is expected to propagate, the phase field length scale is set to $l = 1\,\text{mm}$.

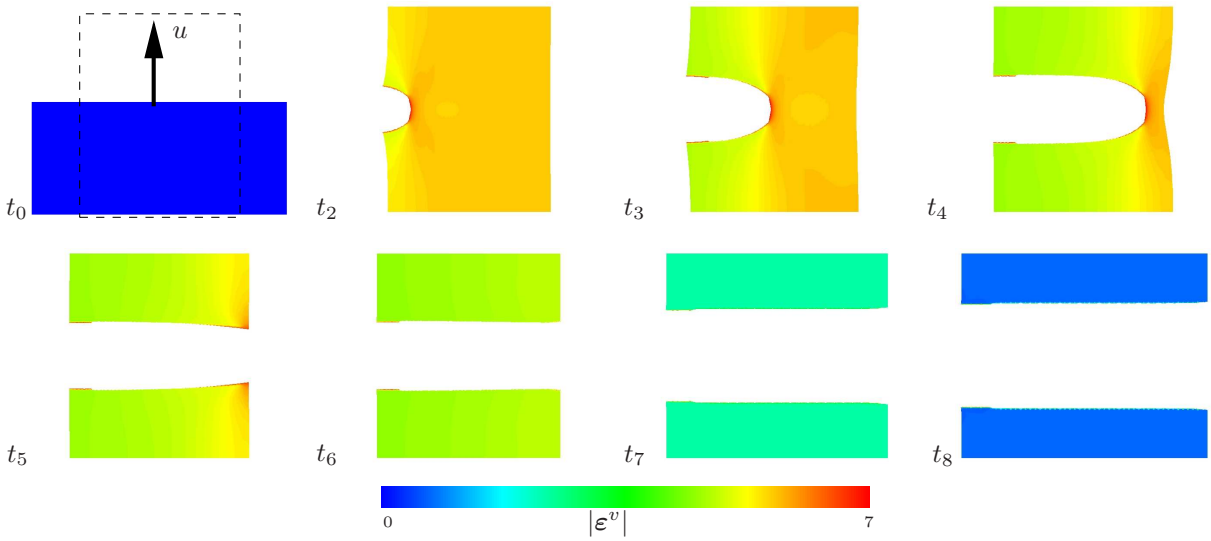

Figure 7.9: Rectangular specimen of 100×40 mm is stretched by u =40 mm. Norm of viscous strains $|\varepsilon^v|$ at times $t_1 = 0$, $t_2 = 6.4$, $t_3 = 15.2$, $t_4 = 25.3$, $t_5 = 26.7$, $t_6 = 34.8$, $t_7 = 9940$, $t_8 = 110000$ s. Crack is faster than the relaxation time, the relaxation takes place after fracture.

Test a. A rectangular test piece of 100 mm×40 mm is stretched with $u = 40$ mm under simple extension. A crack of length 12 mm is introduced at $t_1 = 0$ s, hereafter the deformation and the stress state become inhomogeneous, with stresses concentrating at the crack tip. Crack growth is initiated and the crack accelerates, until a steady crack growth takes place. When the crack tip approaches the end of the test piece, the crack accelerates again until the piece is fractured into two parts. During crack growth, the material is unloaded. However, the viscous strains from the initial loading process, stored in the material, balance the total strains in the ground network and the elastic strains in the subnetworks, which slowly relax with time. The crack is faster than the relaxation time, thus the parts of the body relax after the crack has splitted the body, until the fragments return to their original shape. Figure 7.9 shows the contour plot of the norm of viscous strains $|\varepsilon^v|$ at several times. At t_0, the undeformed specimen is shown and the deformed configuration after uniaxial extension is sketched. The cut is introduced at $t_1 = 0$ s and at $t_2 = 6.4$ s, the crack has opened and starts to grow. At times $t_3 = 15.2$ s and $t_4 = 25.3$ s the crack grows steadily, at $t_5 = 26.7$ s the specimen is completely fractured.

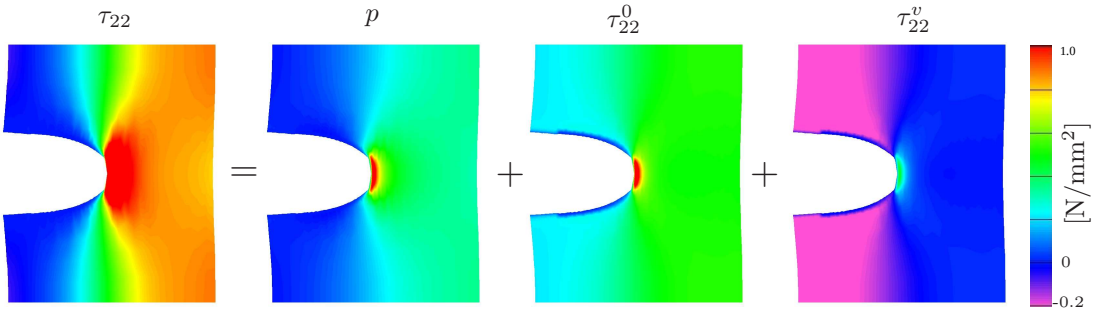

Figure 7.10: Stress decomposition $\tau_{22} = p + \tau^0_{22} + \tau^v_{22}$. Parts which are unloaded by crack are macroscopically stress free, i.e. $\tau_{22} = 0$ however, due to unrelaxed viscous strains, positive residual stresses in the ground network and compressive over stresses in the subnetworks exist which relax in time.

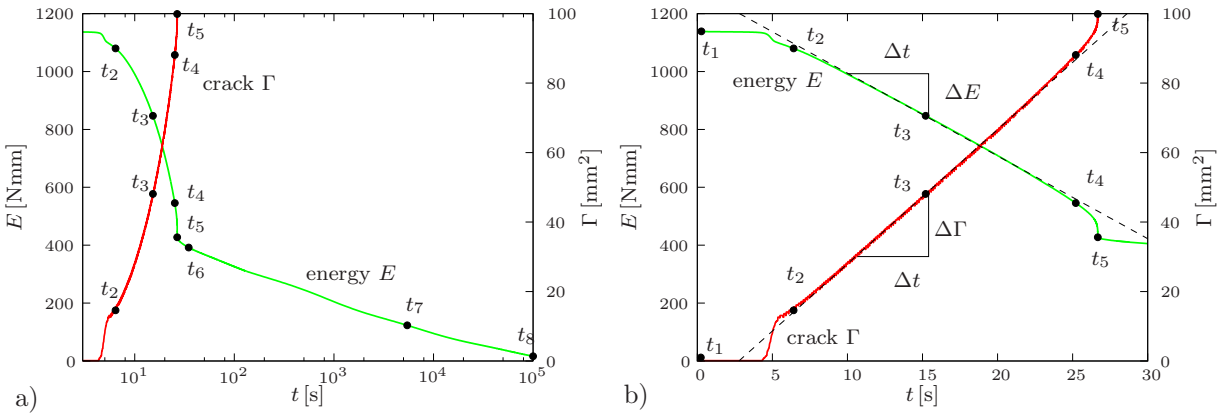

Figure 7.11: Energy and crack length obtained from the simulation `a` are plotted over time in a) in logarithmic scale to overview the full process and in b) in the time range $t \in [0, 30]$ s to focus on the crack growth process. The time points $t_1 - t_8$ correspond with the contour plots in Figure 7.9. The constant crack growth is described by linear functions.

Relaxation of viscous strains occurs in the following, at $t_6 = 34.8$ s and $t_7 = 9940$ s, until at $t_8 = 110000$ s the fragments recover their original shape see Figure 7.9. The effect of the residual viscous strains in the material after unloading is explained in Figure 7.10. The first contour shows the total Kirchhoff stress in vertical direction, τ_{22}, which is decomposed into pressure p, ground state τ^0_{22} and viscous overstress τ^v_{22}. Unloaded by the crack, the total stresses in the cracked parts are zero, however the network is not instantaneously relaxed. The viscous strains from the initial loading process stored in the material, are balanced by total strains in the ground network and elastic strains in the subnetworks. The ground network is stretched, whereas the subnetworks are compressed. Thus, the ground state stresses have small positive values whereas the viscous overstresses have small negative values. These intrinsic stresses reduce with the strain relaxation over time.

Energy Release Rate Computation. For the steady tearing of this body, we derive the energy release rate and the crack speed. The crack length and the elastically stored energy in the test piece are obtained from volume integrals. In each time step, the crack length and the stored energy in the body are obtained as

$$\Gamma = \int_{\mathcal{B}} \gamma(\boldsymbol{X}, t) dV \quad \text{and} \quad E = \int_{\mathcal{B}} \Psi(\boldsymbol{X}, t) dV \ . \tag{7.32}$$

The energy and the crack length obtained from the simulation `a` are plotted over time, in Figure 7.11a, in logarithmic scale to overview the entire process and in 7.11b in the time range $t \in [0, 30]$ s to focus on the crack growth process. At $t_1 = 0$ s the crack is introduced into the stretched body, thus the crack opens and accelerates. The crack curve (red) is nonlinear. After t_2 the crack grows linearly with time until t_4, where the crack approaches the end of the specimen. Finally, the crack accelerates until the body fractures into two pieces at t_5. The energy curve (green) shows the same nonlinear initialization, the steady part and the nonlinear split characteristic, see Figure 7.11. At crack initialization, the elastically stored energy is maximum. During crack growth the material is unloaded and the viscous strains stored in the material relax slowly over time. At the time t_5, when the body is fractured, a relevant amount of energy is still stored in the body. After fracture, viscous strains relax and thus the elastic stored energy in the ground state and

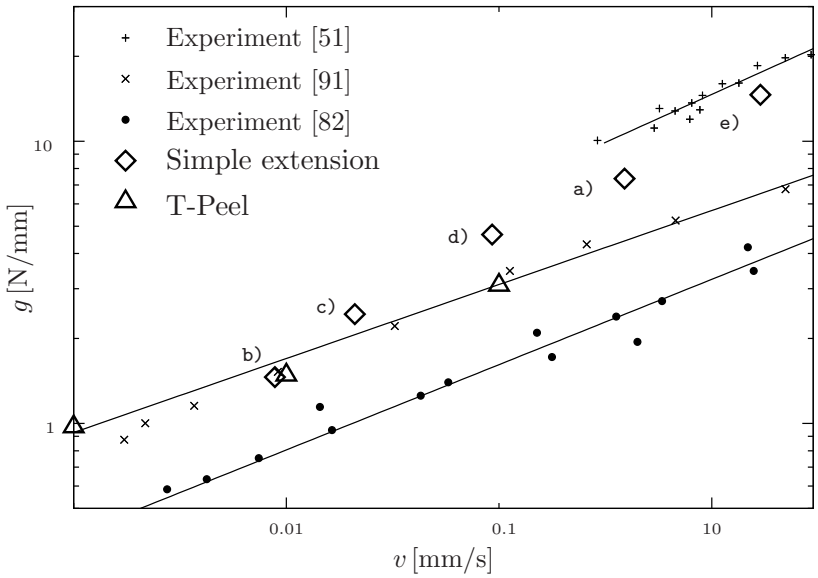

Figure 7.12: Energy release rate g increases with increasing crack speed. Simple extension and peel test simulations are compared with experimental data from D'Amico et al. [51], Greensmith & Thomas [91] and Gent [82] with auxiliary lines as guides for the eye.

the subnetwork relaxes. The relaxation process takes some time until at t_8 the material is undeformed and stress free again. From the energy and crack length plot, the crack speed and energy release rate of the steady crack growth are determined. In the regime of steady crack growth, the energy and crack length can be described by linear functions $f_{e,c} = m_{e,c} \cdot t + b_{e,c}$, where the slope m is the change of energy or the change in the crack length per unit time, see Figure 7.11b. We can derive $m_c = \frac{\partial \Gamma}{\partial t} = v$ as the crack speed and $m_e = \frac{\partial E}{\partial t}$ as the rate of energy. We further obtain

$$g = -\frac{\partial E}{\partial \Gamma} = -\frac{\dot{E}}{v} = -\frac{m_e}{m_c} \,. \tag{7.33}$$

From the simulation, the slopes are read as $\frac{\partial \Gamma}{\partial t} = v = 3.89$ and $\frac{\partial E}{\partial t} = \dot{E} = -28.67$. The energy release rate is thus $g = 28.67/3.89 = 7.37\,\mathrm{N/mm}$. This value for the energy release rate is plotted in relation to the crack speed $\dot{\Gamma} = v$ in Figure 7.12.

Tests `b` – `e`. Further simulations using the test geometries `b`–`e` also show the linear range of stored elastic energy and crack length values over time with steady crack growth. The resulting energy release rates are plotted against the respective crack speeds, see Figure 7.12 in double logarithmic plot. Note that, despite some small fluctuations, the energy release rate shows linear dependence on the crack speed. This precisely resembles the various experimental data. For the slowest test `b`, the threshold σ_c was adapted to the experimental data. The quasi-static crack growth (at a speed of $\approx 0.1\,\mathrm{mm/s}$) shows little rate dependence of crack growth $\dot{d}$. Thus the critical stress parameter is obtained as $\sigma_c = 2\,\mathrm{N/mm^2}$, $\zeta = 100$. The other simulations were adapted to the experimental data and the damping parameter $\eta = 200$ was identified.

7.4.5. Steady Crack Growth in T-Peel Test. The *T-peel test* is used to analyze the adhesion of sealed polymeric films. Gent & Lai [83] analyzed partially crosslinked sheets of elastomers, where the interlinking of two sheets was controlled. Nase et al.

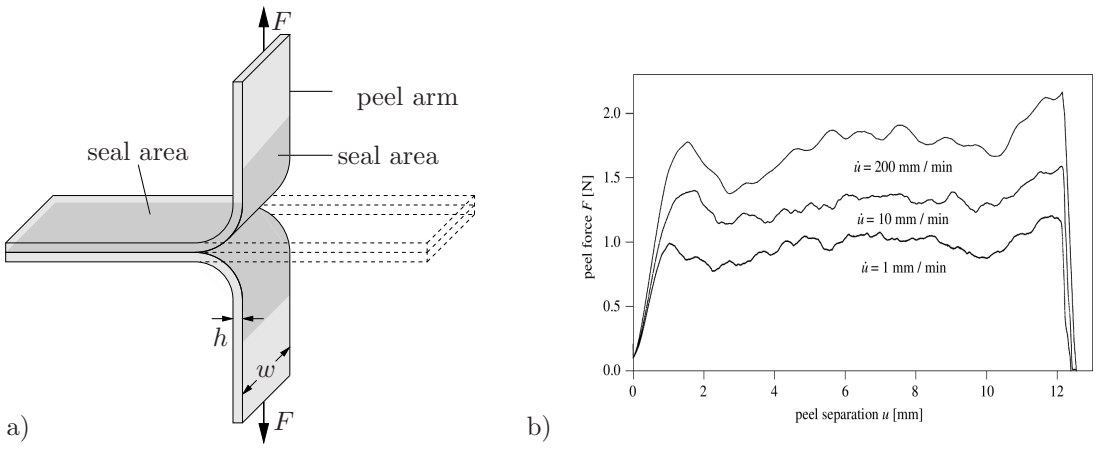

Figure 7.13: a) Peel test geometry. Two layers of flexible polymer are bonded together in the seal area. The peel arms are pulled apart, the angle of separation between the layers is 180°. b) Load-displacement curves from GEISSLER ET AL. [78].

[170] analyzed two-component peel systems, consisting of a film and an interface component. The interface between two films acts as a predetermined breaking point upon mechanical loading. For testing purposes, the end parts of the layers remain unsealed. These unbonded ends are bent and clamped in a tension testing machine. A constant head speed is applied and the load versus the head movement is recorded. The bent, unbonded ends form a T-shape when pulled apart and the angle of separation between the layers is 180 degrees, see Figure 7.13a. Experiments performed by GEISSLER ET AL. [78] are shown in Fig. 7.13b, where the peel force F is plotted over the peel separation u. First, an elastic loading is observed, until the peel force reaches a local maximum at the peel initialization, whereafter the load drops slightly. A plateau like curve progression is followed, in which the force remains constant, except for some fluctuations. An increase of force is observed when peeling the border region at the end of the test piece. GEISSLER ET AL. [78] performed peeling tests at three different constant head speeds, to

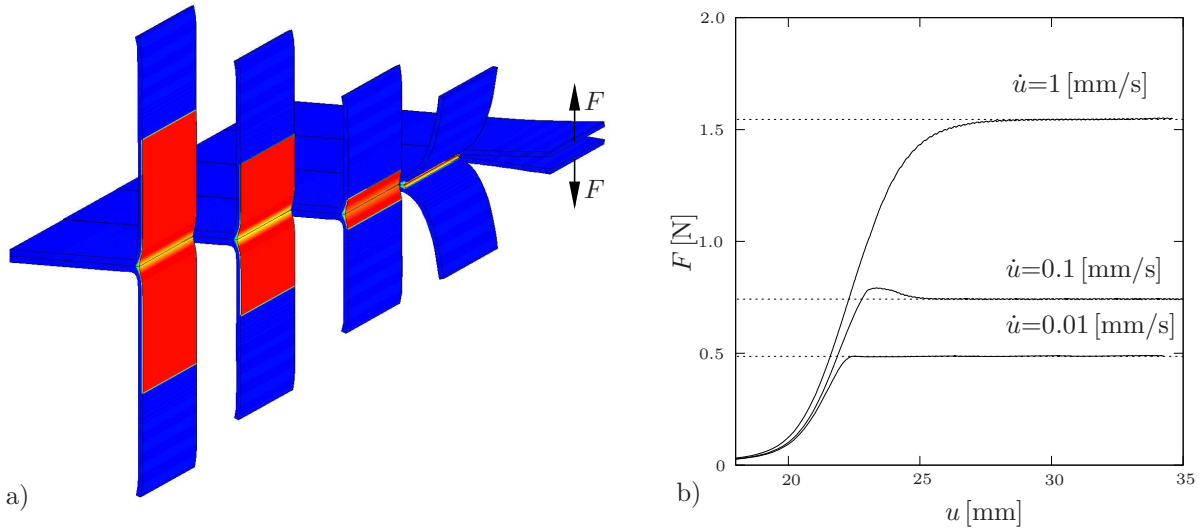

Figure 7.14: a) Peel test at $\dot{u} = 0.01$ mm/s at crack initialization and during steady crack grow. b) Peel force - displacement curves obtained from simulations at $\dot{u}$ ={0.01, 0.1, 1} mm/s. Constant peel forces read F={0.487, 0.743, 1.54} N per unit width.

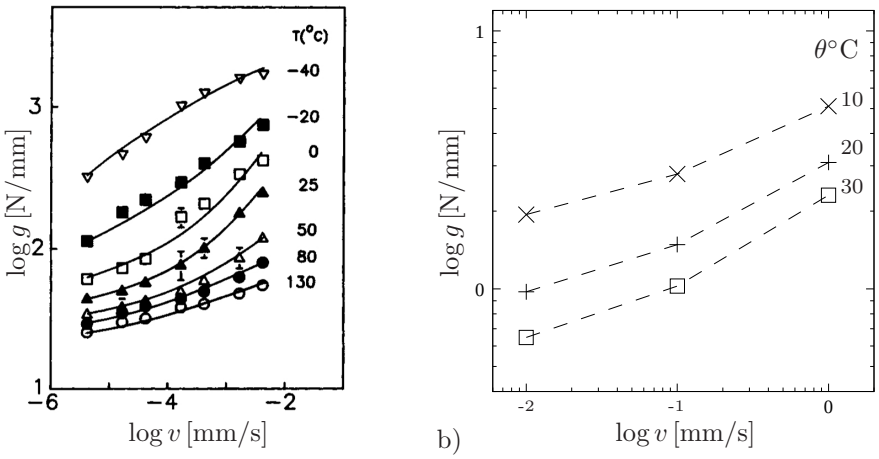

Figure 7.15: Peel test showing the dependence of energy release rate g on crack speed v and temperature θ from Gent & Lai [83] in a) and simulation results in b).

demonstrate the crack speed dependence of the energy release rate. The peel force F is observed to increase with increasing displacement rate.

Peel simulations are performed on specimens with layer thickness $h = 1\,\text{mm}$ and length 70 mm, using two-dimensional plane strain elements. The unsealed end parts are 20 mm in length. Due to the symmetry, only half of the specimen is discretized. The layer is modeled only with the elastic ground state network, using $\mu = 4.0$, $N = 8$ and $\sigma_c \approx \infty$. The interface component has a thickness of 0.3 mm and is the rubber material used for the previous simulations. The elements in the interface layer have a size of 0.15 mm, the length scale is $l = 0.3\,\text{mm}$. The peel arm end is displaced at a constant rate $\dot{u}$ and the reaction Force F, per unit width of 1 mm of the peel arm is recorded. Peeling simulations are performed at increasing rates $\dot{u} = 0.01$ mm/s, 0.1 mm/s and 1 mm/s. The load versus head movement curves are given in Figure 7.14b. At $u \approx 25\,\text{mm}$, the peel force reaches its plateau value. Further constant loading results in a constant peeling force. The peeling is performed until a head displacement of $u = 35\,\text{mm}$, where approximately 10 mm constant peeling occurred. The deformation and phase field d during peeling are shown in Figure 7.14. The rate dependence of the peel force F is recovered by the model. An increasing peel force for increasing loading rate is observed, which is in good qualitative agreement with the experiments of Geissler et al. [78]. Transferring the simplification, that $\lambda \approx 1$ in the peel arms, from the *simple-extension test* to the *T-peel test*, the head movement Δu is equal to the distance peeled Δc. Thus, the crack speed v is equal to the displacement rate of the peel arms $\dot{u}$. According to (3.10), the energy release rate is $g = -\Delta\Pi/\Delta A$. Similar to the simple-extension test shown in Rivlin & Thomas [191], the arms which are in simple extension store comparably little energy, compared to the external power due to loading. By neglecting the increase in stored elastic energy, the energy release rate is computed with $\Delta A = \Delta c w$ and $-\Delta\Pi = 2F\Delta u$ as

$$g \approx \frac{2F\Delta u}{w\Delta c} = \frac{2F}{w}\,. \tag{7.34}$$

According to the measured force, the energy release rates are evaluated as g=$\{0.974, 1.468, 3.08\}$ N/mm. The values of the energy release rate are plotted against the crack speed, with square symbols in Figure 7.12. The results of the simulations are consistent with the experiments. Since the values of peel toughness correspond to the simple tension

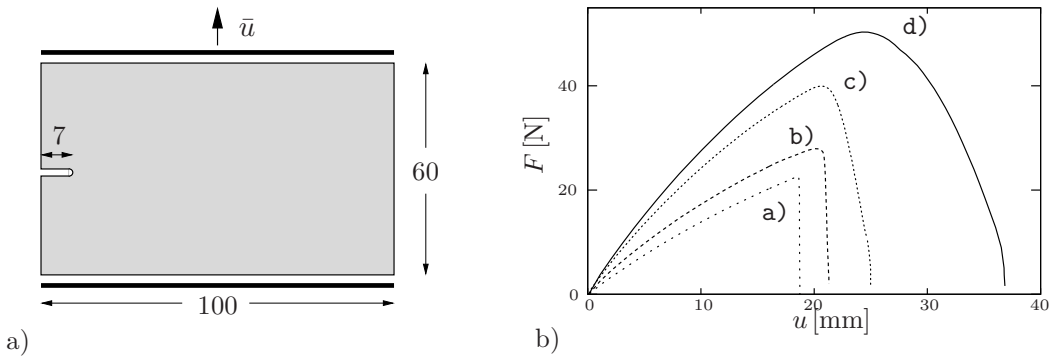

Figure 7.16: Single edge notch tension specimen. a) Geometry and boundary conditions in [mm]. b) Load displacement curves obtained for monotonous loading $\dot{u}_{\mathtt{a-d}} = \{10^{-6}, 10^{-3}, 0.1, 1\}$ mm/s.

values, the objectivity of the model is demonstrated. The presented approach is well suited for modeling rate dependent crack growth in non-crystallizing viscoelastic solids.

7.4.6. Temperature Dependent T-Peel Test. The T-peel test is used to analyze the temperature dependent adhesion of sealed polymeric films. Results for g, obtained at different temperatures from Gent & Lai [83] on partially crosslinked sheets of elastomer, are shown in Figure 7.15a. In order to show that the model also captures this temperature dependent effect, 9 simulations are performed. The temperature is set to θ=10°C, 20°C and 30°C and peel tests at the rates $\dot{u} = 0.01$ mm/s, 0.1 mm/s and 1 mm/s are simulated. 20 °C is taken as a reference temperature for known material parameters. The shift factors a_T for 10°C and 30°C are computed and the relaxation times, as well as the critical stress values, are shifted. The energy release rate values are derived according to (7.34) and plotted against the crack speed in Figure 7.15. Since the parameters of the model are not fitted to the material used in Gent & Lai [83], only a qualitative fitting is possible. The energy release rate increases with increasing crack speed and decreasing temperature. The resulting values for g are given in 7.15b, which show very good qualitative agreement with the experimental values. The experimental data is captured very well by the proposed model.

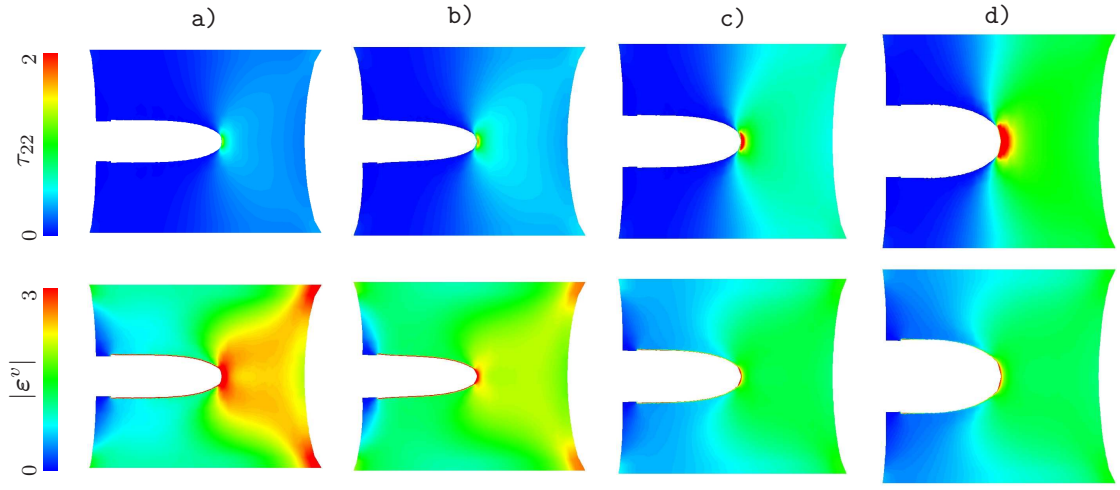

Figure 7.17: Influence of loading rates $\dot{u}_{\mathtt{a-d}} = \{10^{-6}, 10^{-3}, 0.1, 1\}$ mm/s on the stress τ_{22} [N/mm^2] and viscous strain norm $|\boldsymbol{\varepsilon}^v|$ of pre-notched rectangular plates.

7.4.7. Loading Rate Dependent Single Edge Notch Tension Test. A series of simulations is performed, to show the effect of loading rate on the fracture process of a pre-notched specimen. Therefore, a rectangular plate of 100 mm×60 mm having an initial notch of 7 mm, is stretched at various rates. The bottom of the specimen is fixed and the top is displaced with constant speed $\dot{u}_{\mathtt{a-d}} = \{10^{-6}, 10^{-3}, 10^{-1}, 1\}$ mm/s. The geometry and the load displacement curves obtained from the simulations are shown in Figures 7.16a and 7.16b. The stresses and viscous strains during fracture are pictured in Figure 7.17. Generally, one observes an increase of load and deformation before fracture with increasing loading rate. Simulation `a`, with an extension rate of $\dot{u} = 10^{-6}$, is a quasi elastic loading process followed by brittle fracture. During loading, only elastic stresses evolve, viscous over-stresses are nearly zero and viscous strains are high. A relatively low load level at the onset of fracture is observed. The unloading path drops steeply with growing crack. With increasing rate of deformation, we observe an increasing amount of viscous over-stresses and a decreasing amount of viscous strains in the material, see the contour plots Figure 7.17. The stiffness contribution of the subnetwork can be seen from the increased slope of the loading path. The viscous damping of crack evolution increases the crack resistance, see simulations `b, c` and `d`, which leads to an increase of fracture load and displacement.

8. Crazing Induced Fracture in Glassy Polymers

High fracture toughness, light weight, optical properties and easy processability make the use of amorphous glassy polymers very attractive in applications ranging from microelectronics over housewares to aerospace components. It is therefore of utmost interest to investigate the durability and failure of glassy polymers due to mechanical loading. The brittle behavior has been generally considered to be favored by high loading rates, low temperature levels, tension dominated straining and the existence of flaws or grooves in the material. This response is distinguished by very small inelastically deformed zones, the so-called *crazes*, having the thickness of micrometers and spanning fractions of a millimeter, see KRAMER [124]. The ductile response of amorphous polymers, on the other hand, is typically characterized by diffuse shear zones involving much greater amounts of material than the former. The diffuse shear zones are formed by *shear yielding* mechanisms, preceding substantial volume-preserving plastic deformation. Most glassy polymers, except thermosets, exhibit crazing prior to fracture. Although the crazes dissipate considerable amounts of energy, the highly localized nature of the crazes leads to brittle macroscopic fracture. The tailoring of glassy polymers in terms of various fillers, promotes multiple, concurrent craze nucleation sites and enhances the fracture toughness considerably, see for example SEELIG & VAN DER GIESSEN [194, 195]. In order to enable the tailored design of such materials, in the context of modern computational material design tools, a continuum-based description of craze nucleation, propagation and crazing induced fracture in a unified setting is of high interest.

Despite tremendous contributions on the particular aspects of glassy polymers, only a few approaches exist, describing the initiation, elongation-widening and breakdown of crazes, leading to a macroscopic failure in a unified continuum mechanics setting. VAN DER GIESSEN and co-workers [67, 211, 212] proposed a cohesive zone formulation for the craze initiation, widening and breakdown. The competition between crazing and shear yielding is incorporated through craze opening rate and craze initiation sensitivity of the material. The shortcomings of this approach are the a priori existing crack and the lack of information on the location and orientation of the cohesive elements within the continuum. GEARING & ANAND [76] have developed a stress based craze initiation criterion and a continuum based viscous evolution equation for craze-growth. The model accounts for the concurrent shear yielding and crazing, the latter initiating according to a switch function based on the craze initiation criteria. The final breakdown of the material is modeled by element deletion, according to a failure criteria depending on the accumulated crazing strain. The advantage of this approach over the theories of ESTEVEZ ET AL. [67] and TIJSSENS ET AL. [211, 212], is the independence of the model from an existing crack tip. However, the theory is not mesh objective and the element deletion, based on accumulated crazing strain, lacks physical basis.

As a novel aspect, we specify the general model for phase field fracture, introduced in Chapter 4, towards the objective continuum formulation for concurrent shear yielding, crazing and final breakdown of material. To this end, the specific forms of the constitutive functions governing the finite inelasticity of glassy polymer are outlined. A continuum model of glassy polymers of Argon type flow rule [7] is adopted, in the sense of BOYCE ET AL. [34] and MIEHE ET AL. [159]. The nonlinear viscous flow rule of GEARING & ANAND [76] is used for the initiation and growth of the crazes. The competition between shear yielding and crazing is controlled in terms of a stress based switch function in the

sense of Gearing & Anand [76]. Once the crazes initiate, the fiber directions are frozen, according to the eigenvector corresponding to the maximum principal stress direction. A scalar state variable is introduced as a measure of accumulated viscoplastic flow due to crazing. From a micromechanical point of view, this models the cumulative distribution of broken fibrils. A ductile fracture criterion, based on a critical accumulated viscoplastic flow is introduced, which is devised such that the crack phase field develops solely under craze flow. Finally, we demonstrate the capability of the phase field model for crazing induced fracture with representative boundary value problems.

8.1. Constitutive Model in the Logarithmic Strain Space

Within the treatment of phase field fracture presented in Chapter 4, a three field coupled problem is obtained, governed by the balance equations (4.21), (4.27) and (4.35)

$$\begin{aligned} \rho_0 \ddot{\boldsymbol{\varphi}} &= \mathrm{Div}[\boldsymbol{P}] + \rho_0 \boldsymbol{\gamma} \\ \rho_0 c \dot{\theta} &= \mathrm{Div}[-\mathbb{Q}] + \rho_0 (R + H + \mathcal{D}_{loc}) \\ (d - l^2 \Delta d) &= (1-d)\mathcal{H} - \eta \dot{d} \ . \end{aligned} \tag{8.1}$$

The crack evolution time η is treated as a numerical regularization and $\eta \to 0$ is used for the modeling of brittle crack propagation. The impact from the bulk response on the crack propagation is governed by the crack driving state function $\widetilde{D}$. Vice versa, the crack phase field enters the bulk state response function Ψ, by modeling degradation from the initially unbroken, to the fully broken state. The flow rule function $\mathcal{F}$ in (4.18) governs the evolution of the internal variables $\mathfrak{q}$. Constitutive formulation in the logarithmic strain space is a special case of metric-based approaches to finite inelasticity. The modular structure of the formulation of finite elastoplasticity in the logarithmic strain space, consists of three basic steps: geometric pre-processor, material modeling and geometric post-processor. The geometric pre-processor step defines the total logarithmic strain measure of Hencky-type

$$\boldsymbol{\varepsilon} := \tfrac{1}{2} \ln \boldsymbol{C} \quad \text{with} \quad \boldsymbol{C} := \boldsymbol{F}^T \boldsymbol{F} \ , \tag{8.2}$$

that enters the constitutive framework. The plastic energy storage is defined in terms of the logarithmic elastic strain variable and the internal variables $\mathfrak{q}$. The generalized internal variables are composed of Hencky-type *plastic* and *crazing* strain variables

$$\mathfrak{q} = \{\boldsymbol{\varepsilon}^p, \boldsymbol{\varepsilon}^c\} \ , \tag{8.3}$$

associated with *shear yielding* and *crazing*, with initial conditions $\boldsymbol{\varepsilon}^{p,c}(t=0) = \boldsymbol{0}$. The elastic strains are provided by the *additive decomposition*

$$\boldsymbol{\varepsilon}^e := \boldsymbol{\varepsilon} - \boldsymbol{\varepsilon}^p - \boldsymbol{\varepsilon}^c \ . \tag{8.4}$$

The logarithmic strain measures serve as primary kinematic variables in the following material model. The free energy is assumed to be additively decomposed into *elastic*, *plastic* and *purely thermal* contributions such as

$$\Psi(\boldsymbol{\varepsilon}, \boldsymbol{\varepsilon}^p, \boldsymbol{\varepsilon}^c, \theta, d) := \Psi^e(\boldsymbol{\varepsilon}^e, \theta, d) + \Psi^p(\boldsymbol{\varepsilon}^p, \theta) + \Psi^\theta(\theta) \ . \tag{8.5}$$

In the logarithmic strain space, the stress tensors are

$$\boldsymbol{s} := \partial_{\boldsymbol{\varepsilon}} \rho_0 \Psi^e(\boldsymbol{\varepsilon}^e, d) \quad \text{and} \quad \boldsymbol{s}^p := \partial_{\boldsymbol{\varepsilon}^p} \rho_0 \Psi^p(\boldsymbol{\varepsilon}^p) \ . \tag{8.6}$$

The generalized driving force in (4.16) decomposes to $\mathfrak{p} := \{\mathfrak{p}^p, \mathfrak{p}^c\}$ with

$$\begin{array}{lll} \mathfrak{p}^p & = -\partial_{\varepsilon^p}\rho_0\Psi^e(\boldsymbol{\varepsilon}^e,\theta,d) - \partial_{\varepsilon^p}\rho_0\Psi^p(\boldsymbol{\varepsilon}^p,\theta) & = \boldsymbol{s} - \boldsymbol{s}^p \\ \mathfrak{p}^c & = -\partial_{\varepsilon^c}\rho_0\Psi^e(\boldsymbol{\varepsilon}^e,\theta,d) & = \boldsymbol{s} \ . \end{array} \tag{8.7}$$

For the evolution of the two inelastic strain variables, we define two constitutive functions

$$\dot{\boldsymbol{\varepsilon}}^{p,c} = \mathcal{F}^{p,c}(\boldsymbol{\varepsilon},\boldsymbol{\varepsilon}^p,\boldsymbol{\varepsilon}^c,\theta,d) \quad \text{with} \quad \dot{\boldsymbol{\varepsilon}}^{p,c}(0) = \dot{\boldsymbol{\varepsilon}}_0^{p,c} \ . \tag{8.8}$$

At craze initiation, the evolution of inelastic strains changes from shear yielding to crazing. We postulate a function of stress state, which allows to identify whether the plastic shear yielding strains or crazing strains grow

$$f_c(\boldsymbol{s}) : \begin{cases} \leq 0 & \text{shear yielding} \\ > 0 & \text{crazing} \ , \end{cases} \tag{8.9}$$

where $\boldsymbol{s}$ is the stress tensor which is attributed to the logarithmic strain tensor. The geometric post processing gives

$$\boldsymbol{P} = \mathbb{P} : \boldsymbol{s} \quad \text{with} \quad \mathbb{P} = \partial_{\boldsymbol{F}}\boldsymbol{\varepsilon} \ . \tag{8.10}$$

Observe the analogy between the proposed model in logarithmic strain space and the geometrically linear theory of plasticity, which makes this constitutive framework very attractive with regard to its numerical formulation.

8.2. Free Energy Storage Function

The degradation of the solid response needs to be constructed, depending on the phase field $d \in [0,1]$. We assume the constitutive structure

$$\Psi(\boldsymbol{\varepsilon},\boldsymbol{\varepsilon}^p,\boldsymbol{\varepsilon}^c,\theta,d) = g(d)\widetilde{\Psi}^e(\boldsymbol{\varepsilon}^e,\theta) + \Psi^p(\boldsymbol{\varepsilon}^p,\theta) + \Psi^\theta(\theta) \ , \tag{8.11}$$

where the volume specific effective elastic energy storage function $\widetilde{\Psi}^e$ is associated with the intact solid. The logarithmic stresses can be expressed in terms of the effective stress tensor and the degradation function

$$\boldsymbol{s} = g(d)\widetilde{\boldsymbol{s}} \quad \text{with} \quad \widetilde{\boldsymbol{s}} = \partial_{\boldsymbol{\varepsilon}}\rho_0\widetilde{\Psi}^e(\boldsymbol{\varepsilon},\boldsymbol{\varepsilon}^p,\boldsymbol{\varepsilon}^c,\theta) \ . \tag{8.12}$$

The monotonically decreasing *degradation function* $g(d)$ describes the softening of the material with evolving damage. It is assumed to have the properties

$$g(0) = 1 \quad , \quad g(1) = 0 \quad \text{and} \quad g'(1) = 0 \ . \tag{8.13}$$

The first two conditions include the limits for the intact and the fully-broken case. As shown below, the latter constraint ensures that the fracture force converges to a finite value, if the damage converges to the fully-broken state $d = 1$. A simple example of a function that fulfills the above properties is $g(d) = (1-d)^m$, whereas $g(d)$ recovers the classical damage theory for $m = 1$. The variational theory of brittle fracture in elastic solids, outlined in Miehe et al. [161], is obtained for $m = 2$.

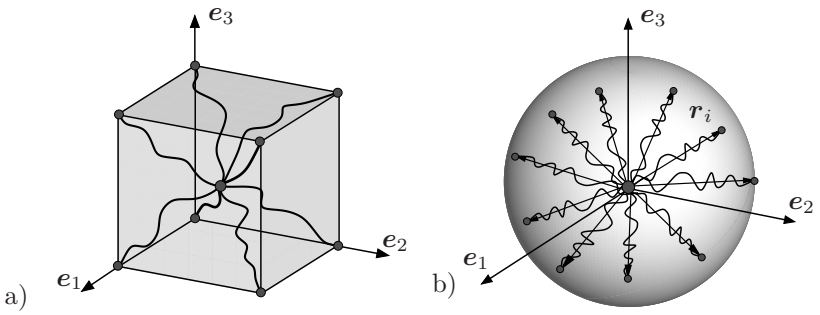

Figure 8.1: Polymer network models employed for modeling the post-yield kinematic hardening. a) The eight chain model of Arruda & Boyce [13] and b) the non-affine microsphere model of Miehe et al. [158].

8.2.1. Thermal Contribution. The purely thermal contribution to the stored energy (8.11) is assumed to have the simple form

$$\rho_0 \Psi^s_\theta(\theta) = \rho_0 \Psi_0 - \rho_0 \eta_0 (\theta - \theta_0) - \rho_0 c_s [\theta \ln \frac{\theta}{\theta_0} - \theta + \theta_0] \ , \tag{8.14}$$

where c_s is a heat capacity parameter, that is assumed to be a constant.

8.2.2. Elastic Contribution. Experimental observations indicate that the deformations in the pre-yield branch are limited to small values, compared to the plastic strains attained. For this reason, linear elasticity in the logarithmic strain space is considered to be sufficient for the current scope. For the isotropic elastic response, we adopt the constitutive function

$$\rho_0 \widetilde{\Psi}^e(\boldsymbol{\varepsilon}^e, \theta) = \frac{\kappa}{2} \operatorname{tr}^2[\boldsymbol{\varepsilon}^e] - \kappa \alpha_T \operatorname{tr}[\boldsymbol{\varepsilon}^e](\theta - \theta_0) + \mu \big| \operatorname{dev}[\boldsymbol{\varepsilon}^e] \big|^2, \tag{8.15}$$

where κ is the bulk modulus. The shear modulus $\mu = \mu(\theta)$ is assumed to be dependent on the temperature, as suggested by Boyce et al. [35], through the empirical relation

$$\mu(\theta) = \exp[\ \log(\mu_0) - b(\theta - \theta_0)\ ] \ , \tag{8.16}$$

in terms of the modulus μ_0 at the reference temperature θ_0 and a sensitivity parameter b. Exploitation of (8.12) gives the logarithmic stress tensor

$$\widetilde{\boldsymbol{s}} := \kappa[\operatorname{tr}[\boldsymbol{\varepsilon}^e]\, \mathbf{1} - \alpha_T(\theta - \theta_0)] + 2\mu \operatorname{dev}[\boldsymbol{\varepsilon}^e] \ . \tag{8.17}$$

8.2.3. Plastic Contribution. This contribution to the free energy describes the characteristic kinematic hardening effect due to the back stress $\boldsymbol{s}^p$, introduced in $(8.6)_2$. This back stress models the intramolecular resistance to the plastic flow, due to the alignment of the chains in the principal deformation direction. For this reason, it is common practice to model the post-yield strain hardening by polymer network models. These models provide a bridge between microscopic and macroscopic deformations, through particular kinematic assumptions. Typical examples are the *three chain model* of James & Guth [115] and Wang & Guth [222], the affine *full network model* of Treloar [215], Treloar & Riding [217], the non-affine *eight chain model* of Arruda & Boyce [12] and the non-affine *microsphere model* of Miehe et al. [158]. The stored free energy due to the distorted polymer network in plastically deformed glassy polymers is assumed

to be isotropic and formulated in terms of the principal strains. Therefore, we perform a spectral decomposition $\boldsymbol{\varepsilon}^p = \sum_{A=1}^{3} \epsilon_A^p \, \boldsymbol{n}_A^p \otimes \boldsymbol{n}_A^p$ where $\{\boldsymbol{n}_A^p\}_{A=1,2,3}$ are the plastic principal directions and ϵ_A^p are the principal stretches in the logarithmic strain space. For the eight chain model of ARRUDA & BOYCE [12], we define the *network stretch* λ^p from

$$(\lambda^p)^2 = \frac{1}{3} \sum_{A=1}^{3} \exp[2\epsilon_A^p] \; . \tag{8.18}$$

Here, the plastic stretch of a chain extending from the center of a plastically deformed rectangular prism, having the edges oriented in the principal plastic directions $\boldsymbol{n}_A^p$, is assumed to be representative for the whole polymer network, see Figure 8.1a. A more complicated relationship gives the microsphere model. We refer to the recent isothermal approach to glassy polymers by MIEHE ET AL. [159]. With the above network stretch at hand, one expresses the energetic state of the full network by the energy of a fictitious prototype chain. The limited extensibility range of a chain is controlled through the relative plastic network stretch $\lambda_r^p := \lambda^p / \sqrt{N_p}$. N_p stands for the number of segments in the fictitious prototype chain. Using the typical Langevin function approach, we are able to define the plastic part of the free energy to

$$\rho_0 \widetilde{\Psi}^p(\lambda_r, \theta) = \mu_p N_p \left(\lambda_r^p \mathcal{L}^{-1}(\lambda_r^p) + \ln \frac{\mathcal{L}^{-1}(\lambda_r^p)}{\sinh \mathcal{L}^{-1}(\lambda_r^p)} \right) \; . \tag{8.19}$$

The plastic shear modulus μ_p depends on the temperature through the standard expression

$$\mu_p(\theta) = n_p(\theta) k_B \theta \tag{8.20}$$

of the entropic polymer network theory, see TRELOAR [216]. Here, $n_p(\theta)$ is the chain density and k_B the Boltzmann constant. However, experiments on glassy polymers show that the strain hardening decreases with increasing temperature. RAHA & BOWDEN [183] and ARRUDA ET AL. [14] proposed the dependence

$$n_p(\theta) = B - D \exp[\, -E_a / R\theta \,] \tag{8.21}$$

of the chain density on the temperature, where B and D are material parameters. E_a is the dissociation energy per mole and R the universal gas constant. Equation (8.21) describes thermal dissociations of entanglements in the molecular network. Introducing the constraint that the molecular network breaks down when the glass transition temperature is reached, i.e. $n_p(\theta_g) = 0$, one gets the relationship $B/D = \exp[\, -E_a / R\theta_g \,]$ between the two constants B and D as suggested in BASU & VAN DER GIESSEN [19]. A mass-type balance assumes the number of molecular links to be constant, i.e. $n_p(\theta) N_p(\theta) = n_p(\theta_0) N_p(\theta_0) = const.$, see ARRUDA ET AL. [14] and references therein. This equation determines the current number of chain segments in terms of the current chain density (8.21) via

$$N_p(\theta) = N_p(\theta_0) \; n_p(\theta_0) / n_p(\theta) \; . \tag{8.22}$$

The function $\mathcal{L}^{-1}$ in (8.19) denotes the inverse of the well-known Langevin function defined by $\mathcal{L}(\cdot) := \coth(\cdot) - 1/(\cdot)$. It can be approximated by the Padè approximation $\mathcal{L}^{-1}(\lambda_r^p) \approx \lambda_r^p \, (3 - \lambda_r^{p2}) / (1 - \lambda_r^{p2})$ as proposed by COHEN [45]. The parameter N_p controls the limited extensibility range of chains through the relative plastic network stretch $\lambda_r^p := \lambda^p / \sqrt{N_p}$.

The back stress in the logarithmic space defined in $(8.6)_2$, is obtained by the chain rule operation

$$\boldsymbol{s}^p := \partial_{\lambda^p}\rho_0\Psi_0^p(\lambda^p)\,\partial_{\boldsymbol{\varepsilon}^p}\lambda^p(\boldsymbol{\varepsilon}^p)\ . \tag{8.23}$$

The first part is directly obtained from (8.19), the second part from (8.18), yielding

$$\partial_{\lambda^p}\rho_0\Psi^p = \mu_p\lambda^p\frac{3-\lambda_r^{p2}}{1-\lambda_r^{p2}} \quad \text{and} \quad \partial_{\boldsymbol{\varepsilon}^p}\lambda^p = \sum_{A=1}^{3}\frac{\exp[2\epsilon_A^p]}{3\lambda^p}\boldsymbol{n}_A^p\otimes\boldsymbol{n}_A^p\ , \tag{8.24}$$

where use was made of the result $\partial_{\boldsymbol{\varepsilon}^p}\epsilon_A^p = \boldsymbol{n}_A^p\otimes\boldsymbol{n}_A^p$. Finally, insertion into (8.23) gives the representation of the back stress tensor

$$\boldsymbol{s}^p := \frac{\mu_p}{3}\frac{3-\lambda_r^{p2}}{1-\lambda_r^{p2}}\sum_{A=1}^{3}\exp[2\epsilon_A^p]\boldsymbol{n}_A^p\otimes\boldsymbol{n}_A^p\ . \tag{8.25}$$

8.3. Transition from Shear Yielding to Crazing

A variety of craze nucleation criteria exist, including some based on principal stresses or principal strains. Alternative criteria base on linear elastic fracture mechanics, or the lowering of the glass transition temperature due to local negative pressure at craze nucleation sites. Sternstein & Myers [201], Sternstein & Ongchin [202] suggested a principal stress based criterion. Therefore, they carried out combined torsion and tension loading tests on various specimens, revealing four distinct regions of loading in the principal stress planes. They defined a *stress bias* between two in-plane stresses and suggested a craze nucleation criterion

$$\sigma_b = |\sigma_1 - \sigma_2| \geq A(\theta) + \frac{B(\theta)}{\sigma_{vol}}\ , \tag{8.26}$$

based on two temperature dependent functions $A(\theta)$ and $B(\theta)$, the mean normal stress $3\sigma_{vol} = \operatorname{tr}\boldsymbol{\sigma}$ and the principal stresses $\sigma_1 > \sigma_2 > \sigma_3$. They stated that the stress bias loosens the tight molecular structure, permitting the mean normal stress σ_{vol} to initiate a craze in terms of plastic dilatation. A craze initiation criterion based on principal strains was derived by Oxborough & Bowden [176]. They formulated an alternative criterion for craze initiation in terms of principal strains

$$\epsilon_c = \frac{X'}{\sigma_{vol}} + Y'\ , \tag{8.27}$$

where ϵ_c is the critical strain for craze formation and X' and Y' are time- and temperature-dependent parameters. Equation (8.27) can equivalently be obtained from a principal stress criterion, based on two linear elastic constants. Further initiation criteria base on linear elastic fracture mechanics (LEFM), see for example Andrews & Bevan [4] and Bucknall [39], or on the lowering of the glass transition temperature due to local negative pressure at craze nucleation sites, see Gent [81]. The microscopic scenarios proposed by Kramer [124] and Argon [8], Argon & Hannoosh [5] explain craze nucleation as a cavitation, triggered by triaxial stresses. Without loss of generality, we adopt a simple stress based approach for crack initiation. Regarding the difficulties associated with the interpretation of the stress bias term (8.26) in a three-dimensional continuum, we use the

slightly modified version of this criterion in the sense of Gearing & Anand [76]. We consider the spectral decomposition

$$\boldsymbol{s} = \sum_{A=1}^{3} s_A \boldsymbol{n}_A \otimes \boldsymbol{n}_A \ , \tag{8.28}$$

with principal stresses $\{s_A\}$ and principal stress directions $\{\boldsymbol{n}_A\}$ and identify the label of maximum principal stress

$$M = \{A| \max_{A\in(1,2,3)} \{s_A\}\} \ . \tag{8.29}$$

The maximum principle stress is s_M, the corresponding eigenvector is $\boldsymbol{n}_M$, which is kept frozen upon craze initiation. We introduce a function describing a critical stress state[2]

$$f_c(\boldsymbol{s}) = s_M - (c_1 + \frac{c_2}{p} + c_3 s_{vol}) \tag{8.30}$$

in terms of the mean normal stress $s_{vol} = \mathrm{tr}[\boldsymbol{s}]/3$. We assume that crazing initiates, when the maximum principal stress, the mean normal stress and the stress state functional (8.30) are positive

$$f_c(\boldsymbol{s}) : \begin{cases} \leq 0 \quad \text{or} \quad s_M \leq 0, \text{ or } s_{vol} \leq 0 & \text{shear yielding} \\ > 0 \quad \text{and} \quad s_M > 0, \ s_{vol} > 0 & \text{crazing} \ . \end{cases} \tag{8.31}$$

The temperature dependence of the parameters c_1 and c_2 was proposed in Tijssens et al. [211] as

$$c_{1,2}(\theta) = c_{1,2}(0) \ \exp[Q_{1,2}/k_B\theta] \ . \tag{8.32}$$

Here, k_B is the Boltzmann constant, $c_1(0)$, $c_2(0)$, Q_1 and Q_2 must be determined from experimental data.

8.4. Viscoplastic Flow Rules for Shear Yielding and Crazing

We introduce two constitutive flow rules for the two internal variables $\boldsymbol{\varepsilon}^p$ and $\boldsymbol{\varepsilon}^c$. The material is initially viscoplastic where the crazing strains are frozen $\dot{\boldsymbol{\varepsilon}}^c = \boldsymbol{0}$. Once the stress state of the material reaches the criterion stated in (8.31), crazing initiates and the plastic strains due to shear yielding are frozen $\dot{\boldsymbol{\varepsilon}}^p = \boldsymbol{0}$.

8.4.1. Flow Rule for Shear Yielding. For the description of shear yielding, we consider an isotropic, volume preserving, viscoplastic flow in the direction of the thermodynamic driving force, in the sense of Boyce et al. [34]. This gives the structure

$$\dot{\boldsymbol{\varepsilon}}^p = \begin{cases} \boldsymbol{0} & \text{if } f_c(\boldsymbol{s}) > 0 \text{ and } s_{vol} > 0 \text{ and } s_M > 0 \\ \dot{\gamma}^p \dfrac{\mathrm{dev}[\mathbf{p}^p]}{|\,\mathrm{dev}[\mathbf{p}^p]|} & \text{otherwise} \end{cases} \ , \tag{8.33}$$

with $\mathbf{p}^p = \boldsymbol{s} - \boldsymbol{s}^p$ in terms of the scalar flow functions $\dot{\gamma}^p$ for viscoplastic shear yielding. In the present model, we use the flow rule

$$\dot{\gamma}^p := \dot{\gamma}_0^p \exp\left[-\frac{As}{\theta}\left(1 - \left\{\frac{\tau}{\hat{s}}\right\}^{\frac{5}{6}}\right)\right] \tag{8.34}$$

[2]Since the kinematic structure of the whole model is constructed in the logarithmic strain space, the craze initiation criterion is established in terms of the logarithmic stresses $\boldsymbol{s}$ for the sake of convenience. It can equivalently be constructed in terms of the principal Cauchy stresses without loss of generality.

in terms of the stress norm $\tau := \sqrt{\mathrm{dev}[\boldsymbol{s}^p] : \mathrm{dev}[\boldsymbol{s}^p]/2}$ and the material parameters $\dot{\gamma}_0^p$ and A. It is derived from the *double-kink theory* of ARGON [7], based on the wedge disclinations. In (8.34), the athermal shear strength is taken to be different from s_0 in the original theory [7]. In order to account for the pressure dependency of yielding, as well as the succeeding true stress softening, we replace the original athermal shear strength s_0 with $\hat{s} := s + \alpha p$, where α is a new material parameter controlling the pressure sensitivity of the yield stress. Its value ranges from 0.1 to 0.2 for most glassy polymers, see e.g. RABINOWITZ ET AL. [182], BOWDEN & JUKES [32]. The stress softening is incorporated by employing the phenomenological evolution rule for s, proposed by BOYCE ET AL. [34]

$$\dot{s} = h\,(1 - s/s_{ss})\,\dot{\gamma}^p \quad \text{with} \quad s(0) = s_0 \;, \tag{8.35}$$

where h, s_0 and s_{ss} denote the additional material parameters describing the slope of the softening, initial and steady state values of the athermal shear strength s, respectively. Inserting (8.34) into (8.33), the restriction dictated by the second law of thermodynamics on shear yielding (4.16) finally reads

$$\mathcal{D}_{loc} = |\,\mathrm{dev}[\mathbf{p}^p]|\dot{\gamma}^p \geq 0 \;. \tag{8.36}$$

As a consequence, the model is said to be thermodynamically consistent for a *positive amount of viscoplastic flow* $\dot{\gamma}^p \geq 0$.

8.4.2. Flow Rule for Crazing. To model the plastic flow accounting for crazing, we introduce a flow rule in the direction of the maximum principle tensile stress as proposed in GEARING & ANAND [76]. Reconsider the spectral decomposition (8.28) $\mathbf{p}^c = \boldsymbol{s} = \sum_{A=1}^{3} s_A \boldsymbol{n}_A \otimes \boldsymbol{n}_A$, the label M of maximum principle stress s_M, see (8.29) and the corresponding eigenvector $\boldsymbol{n}_M$, which is kept frozen upon craze initiation. The phenomenological flow rule, which describes the inelastic flow due to crazing in the continuum, is defined as

$$\dot{\boldsymbol{\varepsilon}}^c = \begin{cases} \dot{\gamma}^c \boldsymbol{n}_M \otimes \boldsymbol{n}_M & \text{if } f_c(\boldsymbol{s}) > 0 \text{ and } s_{vol} > 0 \text{ and } s_M > 0 \\ \boldsymbol{0} & \text{otherwise} \end{cases} \tag{8.37}$$

in terms of the scalar flow function $\dot{\gamma}^c$ in the direction of the maximum principal stress $\boldsymbol{n}_M$. The amount of flow is determined from the constitutive function

$$\dot{\gamma}^c = \dot{\gamma}_0^c \left[\frac{\widetilde{s}_M}{s_{cr}}\right]^{\frac{1}{m}} \;, \tag{8.38}$$

with a reference craze strain rate $\dot{\gamma}_0^c$, dependent on the amount of plastic strain at the instant of crazing initiation. The driving stress is the effective stress $\widetilde{s}_M = s_M/(1-d)^2$, considering local increase in fibril stress when local failure occurs and $d > 0$. The resistance to craze-flow is incorporated by the parameter s_{cr}, the strain rate sensitivity by the parameter m. Inserting (8.38) into (8.37), the restriction dictated by the second law of thermodynamics on crazing (4.16) finally reads

$$\mathcal{D}_{loc} = s_M \dot{\gamma}^c \geq 0 \;. \tag{8.39}$$

As a consequence, the model is said to be thermodynamically consistent for a *positive amount of crazing flow* $\dot{\gamma}^c \geq 0$.

8.4.3. Internal Variable Update. According to the numerical solution algorithm, presented in Section 4.7, the plastic or crazing strains are updated by means of a deformation driven update algorithm. This algorithm computes the change of the internal variables within the time increment $[\,t_n,\, t_{n+1}\,]$, for a prescribed deformation.

Algorithm for Shear Yielding. Within the mechanical subproblem of Section 4.7, we update the viscoplastic flow by means of a deformation-driven update algorithm. This algorithm computes the change of the internal variables within the time increment $[\,t_n,\, t_{n+1}\,]$, for a prescribed deformation. These updates follow from the coupled system of local equations

$$\boldsymbol{r} := \begin{bmatrix} \partial_{\boldsymbol{\varepsilon}^p}\Psi(\boldsymbol{\varepsilon},\boldsymbol{\varepsilon}^p,\boldsymbol{\varepsilon}^c,d_n) + \mathfrak{p}^p \\ \boldsymbol{\varepsilon}^p - \boldsymbol{\varepsilon}^p_n - \Delta\gamma^p\,\mathrm{dev}[\mathfrak{p}^p]/|\,\mathrm{dev}[\mathfrak{p}^p]| \\ \Delta\gamma^p - \Delta t\dot{\gamma}^p_0 \exp\left[-\frac{As}{\theta}\left(1-\frac{\tau}{s}\right)^{\frac{5}{6}}\right] \\ s - s_n + h\,\Delta\gamma^p(1-\frac{s}{s_{ss}}) \end{bmatrix} = \mathbf{0}\ . \tag{8.40}$$

The first equation defines the driving force (8.7) at the current time. The sequent equation states a fully implicit backward Euler-type integration of the flow rule (8.33). The third equation contains the increment of the viscoplastic flow (8.34) in the time increment $[\,t_n,\, t_{n+1}\,]$. The following equation contains the implicit update of the athermal shear strength. The system (8.40) determines the dissipative variables $\mathbf{u}$ at the current time t_{n+1} for a deformation driven scenario, i.e. for prescribed total logarithmic strain $\boldsymbol{\varepsilon}$,

$$\mathbf{u} := \{\ \mathfrak{p}^p, \boldsymbol{\varepsilon}^p, \Delta\gamma^p, s\ \}\ . \tag{8.41}$$

Algorithm for Crazing. Within the mechanical subproblem of Section 4.7, we update the crazing flow by means of a deformation-driven update algorithm. This algorithm computes the change of the internal variables within the time increment $[\,t_n,\, t_{n+1}\,]$ under consideration, for a prescribed deformation. These updates follow from the coupled system of local equations

$$\boldsymbol{r} := \begin{bmatrix} \partial_{\boldsymbol{\varepsilon}^c}\Psi(\boldsymbol{\varepsilon},\boldsymbol{\varepsilon}^p,\boldsymbol{\varepsilon}^c,d_n) + \mathfrak{p}^c \\ \boldsymbol{\varepsilon}^c - \boldsymbol{\varepsilon}^c_n - \Delta\gamma^c \boldsymbol{n}_M \otimes \boldsymbol{n}_M \\ \Delta\gamma^c - \Delta t\dot{\gamma}^c_0 \left[\frac{\widetilde{s}_M}{s_{cr}}\right]^{\frac{1}{m}} \end{bmatrix} = \mathbf{0}\ . \tag{8.42}$$

The first equation defines the driving force $(8.7)_2$ at the current time. The second equation states a fully implicit backward Euler-type integration of the flow rule (8.37). The third equation contains the increment of the crazing flow (8.38) in the time increment $[\,t_n,\, t_{n+1}\,]$. The system (8.42) determines the dissipative variables $\mathbf{u}$ at the current time t_{n+1}, for a deformation-driven scenario, i.e. for prescribed total logarithmic strain $\boldsymbol{\varepsilon}$,

$$\mathbf{u} := \{\ \mathfrak{p}^c, \boldsymbol{\varepsilon}^c, \Delta\gamma^c\ \}\ . \tag{8.43}$$

The nonlinear systems (8.40,8.42) are linearized and solved by a local Newton algorithm

$$\mathbf{u} \Leftarrow \mathbf{u} - [\boldsymbol{A}(\mathbf{u})]^{-1}\boldsymbol{r}(\mathbf{u}) \quad \text{with} \quad \boldsymbol{A} := \partial_{\mathbf{u}}\boldsymbol{r}(\mathbf{u})\ , \tag{8.44}$$

until convergence is achieved in the sense $|\boldsymbol{r}(\mathbf{u})| \leq tol$. For given dissipative variables, the evaluation of the potential equation (8.12) gives the current stresses in the logarithmic strain space

$$\boldsymbol{s}^{algo} = \partial_{\boldsymbol{\varepsilon}} \rho_0 \Psi(\boldsymbol{\varepsilon}, \boldsymbol{\varepsilon}^p, \boldsymbol{\varepsilon}^c, \theta, d) \ . \tag{8.45}$$

The sensitivity of these stresses with respect to increments of the total logarithmic strains

$$\Delta \boldsymbol{s}^{algo} = \mathbb{E}_c^{algo} : \Delta \boldsymbol{\varepsilon} \ , \tag{8.46}$$

defines the tangent moduli, consistent with the algorithm (8.42) in the logarithmic space. With the above outlined linearization of the constitutive algorithm at hand, this tangent operator assumes the closed form representation

$$\mathbb{E}_c^{algo} \ = \ \partial^2_{\boldsymbol{\varepsilon}\boldsymbol{\varepsilon}} \Psi \ - \ \begin{bmatrix} \partial^2_{\boldsymbol{\varepsilon}\boldsymbol{\varepsilon}^c} \Psi \\ \boldsymbol{0} \\ 0 \end{bmatrix}^T \ \boldsymbol{A}^{-1} \ \begin{bmatrix} \partial^2_{\boldsymbol{\varepsilon}^c\boldsymbol{\varepsilon}} \Psi \\ \boldsymbol{0} \\ 0 \end{bmatrix} \ . \tag{8.47}$$

Details on a compact update scheme for the evolution of the shear yielding internal variables and for the consistent algorithmic tangent expressions can be found in Miehe et al. [159]. In Appendix A, a compact update scheme for the evolution of the crazing internal variables and for the consistent algorithmic tangent expressions is introduced, as an alternative to the representation introduced above.

8.5. Crazing Based Crack Driving Force

To give an introduction to the craze break down mechanisms, we comment on the works of Kramer & Berger [125] and Yang et al. [231]. They performed experiments to study breakdown statistics. After loading film specimen, the first event they observed was craze initiation. Upon further loading, crazes grow both in width and length, until somewhere within one craze the fibrils break down. This results in a void, which is observed as a growing spot within the craze, see Figures 8.2a and 8.2c. The last event monitored is catastrophic fracture, see Figure 8.2b. Due to imperfections in the material, the three events appear at different stages of the overall loading. As depicted in Figure 8.2d, craze initiation is a rather instantaneous process, whereas fibril break and fracture deviate considerably, due to the unequal distribution of imperfections. In the diagram, the fracture curve always follows the shape of the fibril break curve but is displaced to higher strain levels. Conceptually in line with these observations, the fibril breakdown process is incorporated in terms of cumulative crazing strain as a growth function for the crack phase field. We define the accumulated viscoplastic flow due to crazing

$$\epsilon^c(\boldsymbol{X}, t) = \int_0^t \dot{\gamma}^c(\boldsymbol{X}, \tau) d\tau \ . \tag{8.48}$$

With this state variable, we define the *crack driving state function* (4.41), which drives the phase field d as

$$\widetilde{D}(\boldsymbol{X}, t) := \zeta \langle \epsilon^c - \epsilon_c^\star \rangle^2 \ . \tag{8.49}$$

Here, $\epsilon_c^\star$ is the critical accumulated viscoplastic flow in the craze, representing the onset of fibril breakdown, which initiates the crazing induced fracture. The critical flow $\epsilon_c^\star$ is closely

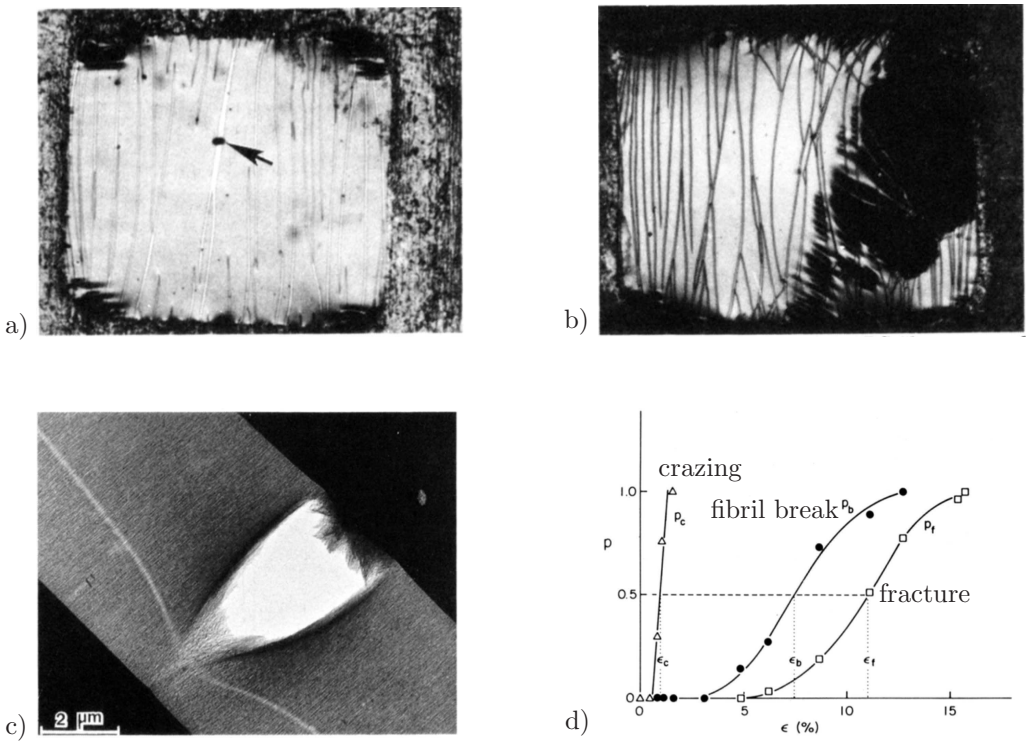

Figure 8.2: Statistical analysis of around 40 squares of polymer sheets. a) Local fibril break is observed as a spot under a light microscope. b) Catastrophic fracture. c) TEM micrograph of fibril breakdown. d) Cumulative number fraction of film squares, where crazing, fibril break down or fracture occurred. Pictures are taken from YANG ET AL. [231].

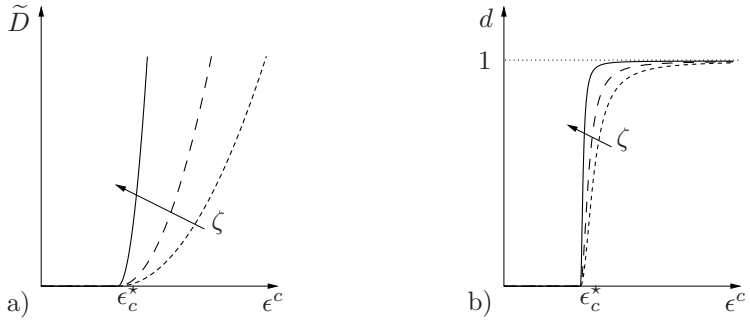

Figure 8.3: a) effective crack driving force $\widetilde{D}$ and b) local evolution of phase field d with respect to the accumulated flow $\hat{\epsilon}^c$ for various values of ζ.

related to the ability of the bulk material, around each individual craze, to supply new polymer chains into the craze, in order to elongate[3] [58], [134]. ζ is a material parameter associated with the growth process for the crack phase field. $\langle\cdot\rangle = \frac{1}{2}(\cdot + |\cdot|)$ is the ramp function, expressed by McAuley brackets. The growth function is plotted against the accumulated crazing flow for different values of ζ in Figure 8.3a. The effective driving force (8.49) is incorporated into the balance equation governing the nonlocal evolution of crack phase field (4.35). For very small values of the length scale parameter l, the

[3]This parameter is closely related to accumulated plastic strain history $\epsilon_p^\star := \boldsymbol{\varepsilon}^p : \boldsymbol{n}_M \otimes \boldsymbol{n}_M$ around the craze. The smaller the accumulated plastic strain history in the craze direction, the higher is the ability of the bulk material to supply material or transform into crazes. Hence, the parameter $\epsilon_c^\star$ can be physically considered as the degree of ductility of the craze. For the sake of simplicity, $\epsilon_c^\star$ is kept constant throughout the investigations carried out in this work.

Box 1: Finite viscoplasticity in the logarithmic strain space.

1. *Kinematics*	$\boldsymbol{\varepsilon} := \frac{1}{2}\ln \boldsymbol{C}\ , \quad \mathfrak{q} = \{\boldsymbol{\varepsilon}^p, \boldsymbol{\varepsilon}^c\}\ , \quad \boldsymbol{\varepsilon}^e = \boldsymbol{\varepsilon} - \boldsymbol{\varepsilon}^p - \boldsymbol{\varepsilon}^c$
2. *Free energy*	$\Psi = (1-d)^2\widetilde{\Psi}^e(\boldsymbol{\varepsilon}^e) + \widetilde{\Psi}^p(\boldsymbol{\varepsilon}^p)$
3. *Stresses*	$\boldsymbol{s} := (1-d)^2\partial_{\boldsymbol{\varepsilon}^e}\rho_0\widetilde{\Psi}^e(\boldsymbol{\varepsilon}^e)\ , \quad \boldsymbol{s}^p = \partial_{\boldsymbol{\varepsilon}^p}\rho_0\widetilde{\Psi}^p(\boldsymbol{\varepsilon}^p)$
4. *Driving force*	$\mathfrak{p}^p = \boldsymbol{s} - \boldsymbol{s}^p\ , \quad \mathfrak{p}^c = \boldsymbol{s}$
5. *Transition*	$\{f_c(\boldsymbol{s}), s_M, s_{vol}\} = \begin{cases} < 0 & \text{Shear yielding} \\ \geq 0 & \text{Crazing} \end{cases}$
6. *Shear flow rule*	$\dot{\boldsymbol{\varepsilon}}^p = \begin{cases} \dot{\gamma}_0^p \exp\left[-\frac{As}{\theta}(1-(\frac{\tau}{\hat{s}})^{\frac{5}{6}})\right]\dfrac{\operatorname{dev}\mathfrak{p}^p}{\lvert\operatorname{dev}\mathfrak{p}^p\rvert} & \text{if } f_c(\boldsymbol{s}) < 0 \\ \boldsymbol{0} & \text{otherwise} \end{cases}$
7. *Crazing flow rule*	$\dot{\boldsymbol{\varepsilon}}^c = \begin{cases} \dot{\gamma}_0^c\left[\widetilde{s}_M/s_{cr}\right]^{\frac{1}{m}}\boldsymbol{n}_M \otimes \boldsymbol{n}_M & \text{if } f_c(\boldsymbol{s}) \geq 0 \\ \boldsymbol{0} & \text{otherwise} \end{cases}$
8. *Crack driving force*	$\widetilde{D} = \zeta\langle\epsilon^c - \epsilon_c^\star\rangle^2 \quad \text{with} \quad \epsilon^c = \int_0^t \lvert\dot{\boldsymbol{\varepsilon}}^c\rvert d\tau$

Laplacian term $l^2\Delta d$ can be omitted, and a closed form solution for the local evolution of the phase field $d = \mathcal{H}/(1+\mathcal{H})$ can be obtained, in terms of the maximum value of local driving function $\mathcal{H} = \max_{s\in[0,t]}\widetilde{D}$. In terms of the local driving function (8.49), we are able to study the sensitivity of the closed form of the phase field evolution equation with respect to the parameter ζ, see Figure 8.3b. The constitutive equations for the phase field model of fracture in glassy polymers, showing transition from shear yielding to crazing is, summarized in Box 1.

8.6. Numerical Examples

In this section, the proposed phase field model for crazing induced fracture will be applied to two representative boundary value problems. At first, craze initiation, propagation and crazing induced fracture of a square sheet with a circular hole are investigated. The temperature dependent brittle to ductile transition is demonstrated through inhomogeneous tension tests of a dumbbell-shaped specimen, under isothermal conditions. We start with the identification of the material parameters, which are depicted in Table 8.1. The first parameters (1–9), governing the shear yielding, are obtained from the compression experiments of Arruda et al. [14] for PMMA, where crazing is suppressed. The material parameters (10–14), governing the initiation of crazing and the crazing flow, are taken identical to those identified by Gearing & Anand [76], except for the strain rate sensitivity m, which is chosen rather viscous. The parameters (15–17) describe the growth conditions of the crack phase field and the length scale parameter. By modification of some material parameters, a second parameter set is obtained, in order to demonstrate a hypothetical ductile response, see Table 8.1.

8.6.1. Tension of a Square Plate with a Circular Hole. A tension test is performed on a micro-structure plate with a hole in the center, depicted in Figure 8.4a. The radius of the hole is chosen as $r = 0.5\,\text{mm}$, with this the specimen has the width and

Table 8.1: Material parameters for PMMA.

No.	Par.	Set 1	Set 2	Unit	No.	Par.	Set 1	Set 2	Unit
1	κ	2500	2500	N/mm^2	10	s_{cr}	200	310	N/mm^2
2	μ	1005	1005	N/mm^2	11	m	0.5	0.5	-
3	μ_p	15	15	N/mm^2	12	c_1	45.60	200	N/mm^2
4	N_p	2.7	2.7	-	13	c_2	400	200	N^2/mm^4
5	$\dot{\gamma}_0^p$	2.8×10^8	2.8×10^8	s^{-1}	14	$\dot{\gamma}_0^c$	10	3	s^{-1}
6	A	100.6	100.6	N/(mmK)	15	l	0.01	0.01	mm
7	h	315	315	N/mm^2	16	$\epsilon_c^\star$	0.01	0.01	-
8	s_0	138	138	nmm	17	ζ	1×10^8	1×10^5	-
9	s_{ss}	114.45	114.45	N/mm^2	18	θ	296	296	K

height of $4r = 2\,\mathrm{mm}$. The lower edge is fixed horizontally and vertically, while the upper edge is fixed in the horizontal direction and the specimen is loaded monotonically in the vertical direction.

Brittle Fracture. The load-displacement curve follows a linear path until the crack is fully developed in the initial position. Subsequently, the load drops almost vertically to zero, see the solid line in Figure 8.4b. Figure 8.5a depicts the contour plots of the effective stresses s_M within the crazes and the maximum principal stresses in the uncrazed bulk material. Figure 8.5b depicts the crazing strain ϵ^c. Upon loading, the stresses develop and concentrate at the midplane of the specimen, where the cross-section of the specimen is thinnest. Once the stress threshold of the switching function is met, crazing initiates as shown in Figure 8.5(i). Plastic strains due to crazing accumulate and as ϵ^c exceeds the threshold $\epsilon_c^\star$, the crack phase field develops. The phase field increases until the fully broken state in the material is reached. Figure 8.5(ii) shows the stress and crazing distribution at the onset of the crack. As the crack propagates, stresses concentrate in the crack front, driving the craze. Subsequently, the crack phase field develops as a result of the accumulated plastic strain due to crazing, see Figure 8.5(iii). Finally, the specimen fractures into two pieces in a stress free state, see Figure 8.5(iv). The pieces return to their initial unloaded shape.

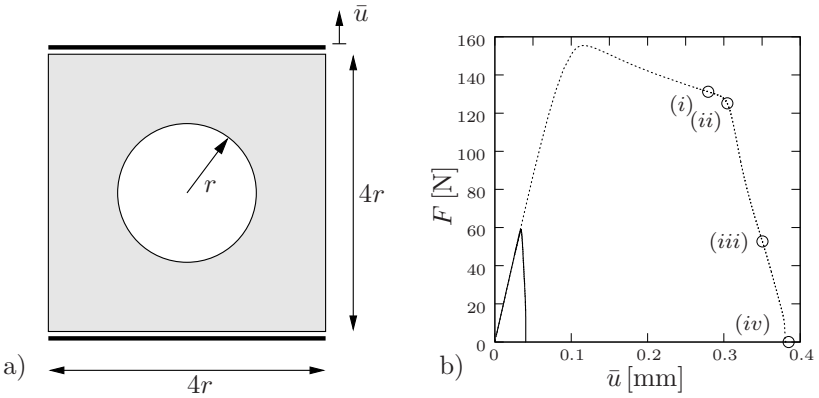

Figure 8.4: a) Micro-structure specimen with $r = 0.5\,\mathrm{mm}$. b) Load-displacement curves resulting from the simulation, applying parameter set 1 of Table 8.1 with solid line. Usage of the parameter values 2 result in ductile behavior until failure, see dashed curve. The circles correspond to stages in Figure 8.6.

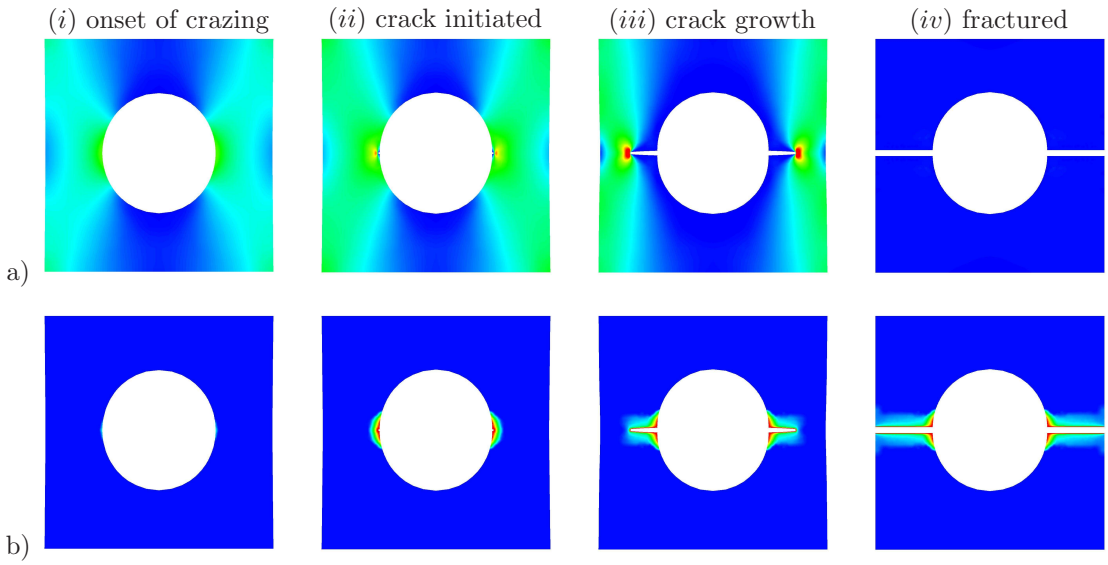

Figure 8.5: Tension test on a micro-structure plate. Contour plots of a) actual driving stress s_M and b) amount of plastic crazing strain ϵ^c at (i) the onset of crazing, (ii) when the crack is initiated, (iii) while the crack grows and (iv) when the specimen fractured into two pieces.

Ductile Fracture. The tension test on the micro-structure plate is repeated with a slightly different set of parameters, in order to show the capability of the model to capture ductile failure, where crazing initiates after a considerable amount of plastic strains. To do so, the parameters of the craze initiation criterion are raised and the crazing induced flow parameters are adjusted, as shown in Table 8.1, parameter set 2. The load-displacement curve resulting from the simulation is shown in Figure 8.4b by the dotted line. The curve consists of a nearly linear path until the yield point, followed by a softening, along with plastic deformations, due to shear yielding. Once the crack is fully developed, the load drops gradually to zero, with further applied displacement until the specimen is fully fractured. The path of unloading of this simulation is more gradual, in comparison to the first example, with steep negative gradient of the load-displacement curve. The marks (i) to (iv) in the load-displacement diagram in Figure 8.4b correspond to the contour plots in Figure 8.6. The principal stresses s_M, the amount of plastic shear yielding strains $|\boldsymbol{\varepsilon}^p|$ and the amount of crazing strains ϵ^c, are depicted in 8.6a,b and c, respectively. The considerable amount of plastic strains, which are not observable in the first example, arises due to the slightly different parameters. As the specimen is deformed, the stresses develop and concentrate at the midplane of the specimen, as is the case in the former example. When the applied stresses reach the yield stress, plastic deformations due to shear yielding accumulate. At the onset of crazing, a partially developed shear band can be observed, which is terminated by the initiation of the craze, see Figure 8.6(i). Plastic strains due to crazing accumulate and as ϵ^c exceeds the threshold $\epsilon_c^\star$ the crack phase field develops. The crack phase field fully develops at the intersection of the circular hole with the mid-plane, leading to the first visible crack. Figure 8.6(ii) shows stresses, plastic strains due to shear yielding and plastic strains due to crazing at the onset of crack, respectively. Figure 8.6(iii) depicts the material state as the crack advances in the horizontal direction. In Figure 8.6(iv), the fully fractured specimen is depicted. Due to the excessive plastic deformations, the specimen cannot recover its initial unloaded shape.

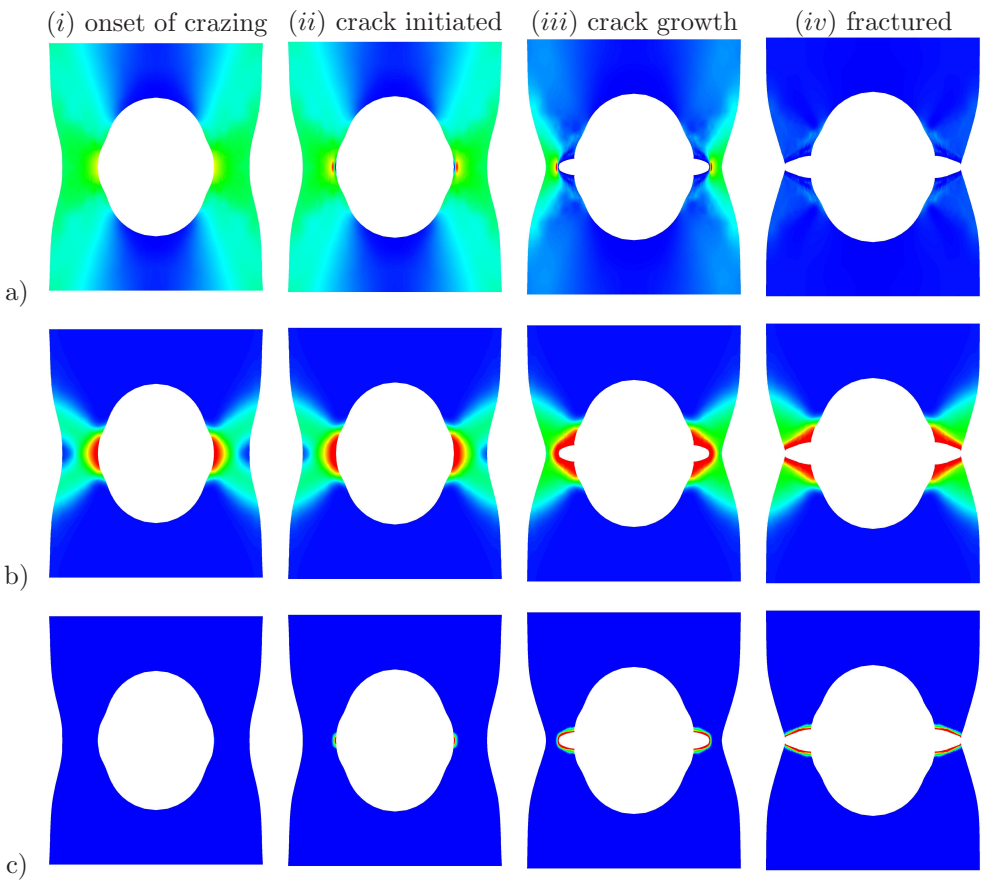

Figure 8.6: Tension test on a micro-structure plate where crazing initiates after a considerable amount of plastic strain. Contour plots of a) effective driving stress s_M, b) amount of plastic shear yielding strain $|\boldsymbol{\varepsilon}^p|$ and c) crazing strain ϵ^c at (i) the onset of crazing, (ii) when crack is initiated, (iii) while crack grows and (iv) when the specimen fractures into two pieces. The specimen cannot recover its initial unloaded shape. The states $(i) - (iv)$ correspond to the points in the load-displacement curve in Figure 8.4.

8.6.2. Tension of a Dumbbell-Shaped Specimen. In this subsection, we analyze the temperature dependent failure mode transition in inhomogeneous tension tests. Experiments performed by Rehage & Goldbach [188] show the brittle failure mode at low temperatures, a transition mode and ductile failure at high temperatures. In order to show that the presented model captures this mode transition, a series of inhomogeneous tension test simulations are performed on a two-dimensional dumbbell-shaped specimen. The geometry and the boundary conditions are depicted in Figure 8.7a. One edge is fixed in all directions, whereas the other edge is fixed in the transverse direction and axially loaded by a prescribed deformation $\bar{u}$. A constant cross-head speed of $\dot{\bar{u}} = 3$ mm/min ensures isothermal conditions. Consequently, the temperature is assumed to be uniform across the specimen and coupled thermomechanical effects are excluded from the deformation process. The simulation is repeated for the prescribed temperatures $\theta = \{0, 20, 40, 60, 80, 90\}^\circ$ C, to analyze the brittle-ductile transition with increasing temperature.[4] The following adjusted parameters $l = 1.0$ mm and $\dot{\gamma}_0^c = 3.0$ s^{-1} are used in addition to parameter set 1 in Table 8.1. The load-displacement curves resulting from the simulations

[4]For a give temperature θ, the parameters μ, μ_p, N_p, c_1 and c_2 are computed by exploiting the equations (8.16), (8.20), (8.22) and (8.32) by substituting $c_0 = 0.0016$, $B = 4.08 \times 10^{18}$, $D = 5.54 \times 10^{21}$, $E_a = 5600$, $c_1(0) = 2.8808$, $Q_1/k_b = 268.40$, $c_2(0) = 364.07$ and $Q_2/k_b = 309.40$.

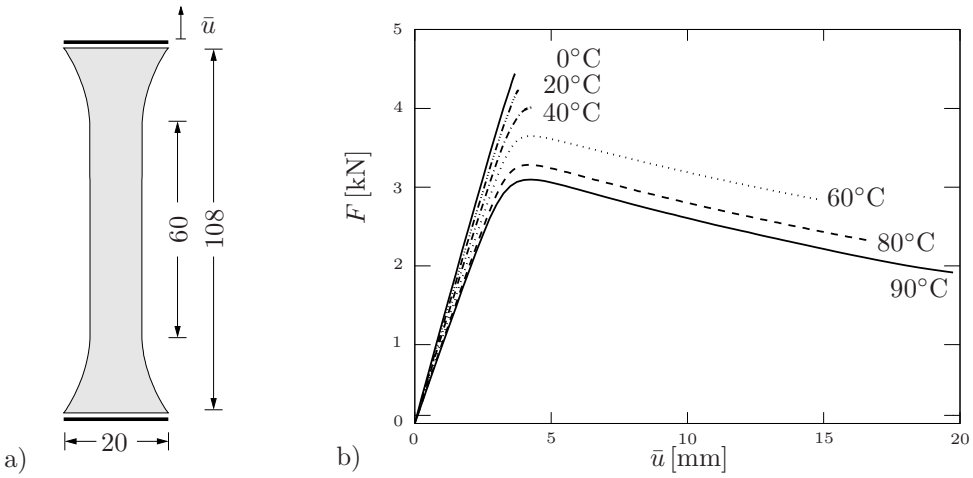

Figure 8.7: a) Geometry of dumbbell-shaped specimen in [mm], discretized by 2462 four-node elements. b) Load-displacemenmt curves resulting from simulations at various temperatures. The transition of the failure mode from brittle at low temperatures, to ductile at high temperatures, is demonstrated.

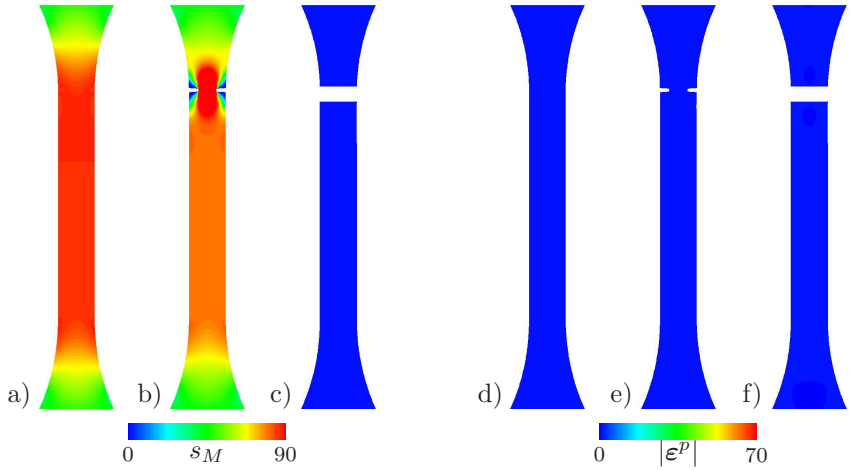

Figure 8.8: Amount of maximum principal stress s_M [N/mm^2] and plastic shear yielding strain $|\varepsilon^p|$ [%] for $\theta = 0$°C. The contour plot shows the onset of crazing in a,d), the crack growth in b,e) and the fully fractured state in c,f).

are shown in Figure 8.7. At 0°C and 20°C, the material shows a linear load-displacement response before brittle failure, without plastic deformations due to shear yielding. For $\theta = 40$°C, a yield point due to shear yielding is observed, which slightly precedes crazing induced fracture. The material behavior converts from the brittle to the ductile regime at this point. From this temperature onwards, the ductility of the specimen gradually increases for increasing temperature. The distribution of stresses and plastic strains is depicted for θ=0° C in Figure 8.8. The stress distribution is homogeneous within the gauge section at the onset of fracture, see 8.8a. The crazes and consequently cracks initiate at the sides of the specimen and grow normal to the loading direction. During crack growth, stresses concentrate at the crack front, see Fig. 8.8b. The crazes and cracks develop without any plastic deformation throughout the specimen, as can be clearly seen in Figure 8.8d-f. The cracks grow, until they meet at the midsection and the specimen fractures into two parts. The two pieces of the specimen recover their initial unloaded shape due to the absence of plastic deformations, see Fig. 8.8c,f. For θ=90°C, the distri-

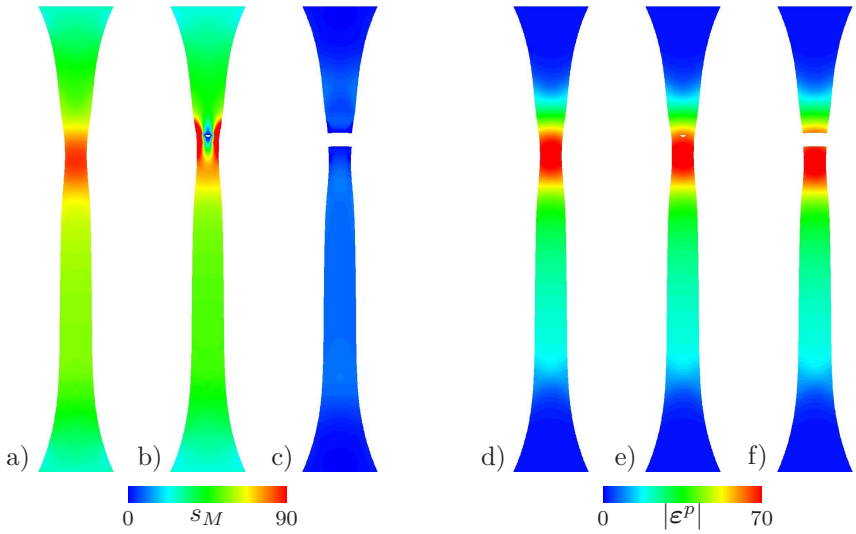

Figure 8.9: Amount of maximum principal stress s_M [N/mm^2] and plastic shear yielding strain $|\boldsymbol{\varepsilon}^p|$ [%] for $\theta = 90°$C. The contour plot shows the onset of crazing in a,d), the crack growth in b,e) and the fully fractured state in c,f).

bution of stresses and plastic strains is depicted in Figure 8.9. Before craze initiation, a significant plastic neck has evolved due to shear yielding, see Fig. 8.9d. Within the neck, the stresses are locally concentrated, see Fig. 8.9a. Due to a high negative pressure within the neck, the crazes initiate in the middle of the neck and grow in both directions normal the loading direction. When the craze strains exceed the threshold $\epsilon_c^\star$, cracks start to grow. During crack growth, stresses concentrate at the crack front, see Fig. 8.9b,e. Due to the extensive plastic deformations prior to crazing, the fractured parts of the specimen cannot recover their unloaded shape, see Figure 8.9c,f. The simulation results are in good qualitative accordance with the experimental observations in e.g. Rehage & Goldbach [188]. This approves the predictive capabilities of the continuum-based model of crazing induced fracture.

9. Conclusion

This thesis outlines a thermodynamically consistent phase field model of diffusive crack propagation in thermo-viscoelastic solids at large strains. A mainly geometric approach to the diffusive approximation of a sharp crack topology is introduced. It is governed by the fracture phase field, which interpolates between the intact and the broken state. The crack topology is approximated by the regularized crack surface functional, which is defined in terms of a crack surface density function, per unit of the reference volume. A balance equation for the crack surface is introduced. Therein, the rate of the crack surface functional is balanced with a crack source and a crack resistance term. From the global balance, a local evolution equation for the fracture phase field is derived. The model is formulated for irreversible crack evolution, with a restriction on the phase field evolution to ensure local crack growth. A modular concept for linking the diffusive crack model to a complex multi-field material response of the bulk material is outlined, where focus is placed on the model problem of finite thermo-viscoelasticity. A concept for brittle and ductile crack initiation and propagation, as well as its regularization in space and time is developed. A key aspect is the definition of crack initiation and crack growth criteria. A staggered scheme is introduced for the numerical solution, which bases on a one-pass operator split. The performance and the vast possibilities of the phase field fracture model at large strains are demonstrated by means of complex numerical examples.

A first application of the proposed general framework for phase field fracture at large strains is discussed in the context of rate-independent crack propagation in elastic rubbery polymers. The approach accounts for micro-mechanically based features of both the elastic bulk response, as well as the crack toughness of idealized polymer networks and can be related to classical statistical network theories of polymers. Starting with a review on the statistically based *fracture toughness* of polymer networks, an energetically based crack driving force is derived. The crack driving state function is expressed in terms of the micro-mechanically based critical energy release rate. The predictive capability of the diffusive fracture model for rubbery polymers is demonstrated by numerical benchmarks. The simulations successfully capture the results observed in experiments.

A further application of the general framework covers fully coupled thermo-mechanical problems at large strains. An important aspect is the constitutive modeling of degrading heat fluxes across cracks, including the generation of convective heat exchanges based on additional constitutive functions defined at the crack faces. This is achieved by approximating surface loads of the sharp crack by distinct volume integrals. A stress-based crack initiation criterion is introduced, which realizes a maximum principal stress criterion with a critical fracture stress threshold. This makes the differentiation between tensile and compression regions simple and is open towards extensions with regard to complex anisotropies in the constitutive modeling. The performance of the fracture phase field model is demonstrated by means of conceptual numerical examples, which illustrate the coupling in the multi-field context.

Another application of the framework is concerned with the rate- and temperature dependent failure of viscoelastic rubbery polymers. The viscoelasticity in rubbery polymers is modeled on a micromechanical basis, where a hierarchy of superimposed networks, related to the ground-state network by entanglement mechanisms, is associated with the modeling of the over-stress response. The rate- and temperature-dependent crack growth is considered by viscous damping in the fracture phase field evolution equation and by a

temperature-dependent, stress-based fracture criterion. A variety of simulations demonstrate the predictive capability of the modular concept applied to rate- and temperature-dependent failure in viscoelastic rubbery polymers.

Additionally, the framework is specified for the description of crazing induced fracture in amorphous glassy polymers. A thermodynamically consistent continuum model for concurrent shear yielding and crazing, coupled with fracture and details of its numerical implementation, are outlined. The proposed formulation in the logarithmic strain space uses an additive split of Lagrangian Hencky-type strains into elastic, plastic shear and plastic crazing parts. A continuum model of visco-plasticity for glassy polymers is enhanced towards the description of dilatational plasticity for crazing, by introducing a nonlinear viscous flow rule. The competition between shear yielding and crazing is controlled by a stress based switch function. The model is constructed such that fracture develops solely under craze flow. The performance of the proposed formulation is demonstrated by means of representative boundary value problems.

The weakness of the phase field model is the enormous number of finite elements which are needed to approximate the sharp crack topology with very small length scale parameters. Hence, continuing research on the computational simulation must account for adaptive remeshing concepts. Apart from this drawback, the model is extremely robust, easy to implement and ideally suited for engineering problems. The approach overcomes difficulties associated with the computational realization of sharp crack discontinuities, in particular when it comes to complex crack topologies. Furthermore, it successfully captures a broad range of specific fracture phenomena, such as crack initiation and crack growth. A vast number of numerical examples demonstrates the predictive quality of the model for rate independent and rate dependent fracture of rubbery polymers, as well as the crazing induced ductile and brittle failure in amorphous glassy polymers. The constitutive formulation is related to the three-dimensional bulk response, which makes it flexible with respect to the constitutive formulation of the crack initiation and crack growth criteria. This feature has already been exploited by considering coupled thermomechanical problems, as well as coupled electro-mechanical problems. It is believed that the model can be further extended to characteristic multi-field fracture problems, induced by chemo-mechanical or solid-fluid interaction. In conclusion, the thermodynamically consistent phase field model for fracture is ideally suited for the modeling of crack propagation in thermo-viscoelastic solids at large strains and has an enormous potential for further research.

A. Compact Implicit Update for Crazing

A compact update scheme is presented for the evolution of the internal variables outlined in Section 8.4.3, by introducing a single residual expression in terms of crazing strains $\boldsymbol{\varepsilon}^c$. A non-linear residual function $\boldsymbol{r}$ of the plastic strain tensor for a frozen deformation state $\boldsymbol{\varepsilon}$ is introduced at time t_{n+1}

$$\boldsymbol{r}(\boldsymbol{\varepsilon}^c) := \boldsymbol{\varepsilon}^c - \boldsymbol{\varepsilon}^c_n - \Delta t\, \dot{\gamma}^c\, \boldsymbol{n}_M \otimes \boldsymbol{n}_M = \boldsymbol{0}\ . \tag{A.1}$$

At the onset of crazing, the eigenvector $\boldsymbol{n}_M$, corresponding to the maximum principal stress s_M is frozen and the craze fibrils align in the direction $\boldsymbol{n}_M$. In the following, the stresses along the fiber direction are defined as $s_M = \boldsymbol{n}_M \cdot \boldsymbol{s} \cdot \boldsymbol{n}_M$ and the crazing strains are redefined as $\boldsymbol{\varepsilon}^c := \epsilon^c\, \boldsymbol{n}_M \otimes \boldsymbol{n}_M$. Making use of the coaxiality of the residual term $\boldsymbol{r}$ and $\boldsymbol{\varepsilon}^c$, the residual expression (A.1) can be simplified to

$$r = \epsilon^c - \epsilon^c_n - \Delta t \dot{\gamma}^c = 0\ . \tag{A.2}$$

The linearization of the residuum r is carried out at k^{th} Newton iteration about ϵ^c_k

$$\mathrm{Lin}\, r(\epsilon^c)\big|_{\epsilon^c_k} = r(\epsilon^c_k) + \mathrm{a}_k \cdot \Delta\epsilon^c = 0 \quad \text{with} \quad \mathrm{a}_k := \left.\frac{\partial r(\epsilon^c)}{\partial \epsilon^c}\right|_{\epsilon^c_k} \tag{A.3}$$

the local tangent of the Newton iteration. The update equation for ϵ^c at the k^{th} step is then obtained by solving (A.3) for $\Delta\epsilon^c$

$$\epsilon^c \leftarrow \epsilon^c_k + \Delta\epsilon^c \quad \text{with} \quad \Delta\epsilon^c := -\mathrm{a}^{-1} \cdot r(\epsilon^c_k)\ . \tag{A.4}$$

The local tangent a is computed from (A.2) as $\mathrm{a} = 1 + \Delta t\, \dot{\gamma}^{c\prime}\, \mathcal{M}$ with$\dot{\gamma}^{c\prime} = \partial_{s_M} \dot{\gamma}^c = \frac{\dot{\gamma}^c_0}{m\, s_{cr}}\, |s_M|^{\frac{1}{m}-1}$ and $\mathcal{M} = \partial_{\epsilon^c} s_M = \kappa + \frac{4}{3}\mu$. The sensitivity of $\boldsymbol{\varepsilon}^c$ with respect to $\boldsymbol{\varepsilon}$ is derived from the total derivative of the residuum with respect to the total strain

$$\mathrm{d}_{\boldsymbol{\varepsilon}} r = \partial_{\epsilon} r|_{\epsilon^c}\ +\ \partial_{\boldsymbol{\varepsilon}^c} r|_{\boldsymbol{\varepsilon}}\ :\ \partial_{\boldsymbol{\varepsilon}} \boldsymbol{\varepsilon}^c\ =\ \boldsymbol{0}\ . \tag{A.5}$$

The desired derivative $\partial_{\boldsymbol{\varepsilon}} \boldsymbol{\varepsilon}^c$ can then be obtained from the condition (A.5) as

$$\partial_{\boldsymbol{\varepsilon}} \boldsymbol{\varepsilon}^c = -\mathrm{a}^{-1} \boldsymbol{n}_M \otimes \boldsymbol{n}_M : \partial_{\boldsymbol{\varepsilon}} r|_{\boldsymbol{\varepsilon}^c}\ . \tag{A.6}$$

Recalling the definition of the residuum (A.2), the derivative $\partial_{\boldsymbol{\varepsilon}} r|_{\boldsymbol{\varepsilon}^c}$ can be expressed as

$$\partial_{\boldsymbol{\varepsilon}} r|_{\boldsymbol{\varepsilon}^c} = -\Delta t\, \dot{\gamma}^{c\prime}\, \boldsymbol{m} : \mathbb{E}^e \tag{A.7}$$

in terms of $\mathbb{E}^e = -\partial_{\boldsymbol{\varepsilon}^c} \boldsymbol{s} := 2\mu\mathbb{P} + \kappa \boldsymbol{1} \otimes \boldsymbol{1}$ and $\boldsymbol{m} = \boldsymbol{n}_M \otimes \boldsymbol{n}_M$. Finally, the insertion of (A.7) into (A.6) leads to the desired sensitivity

$$\partial_{\boldsymbol{\varepsilon}} \boldsymbol{\varepsilon}^c = \mathbb{H} = \mathrm{a}^{-1} \Delta t\, \dot{\gamma}^{c\prime}\, \boldsymbol{m} \otimes \mathbb{E}^e : \boldsymbol{m}\ . \tag{A.8}$$

The consistent algorithmic tangent moduli for crazing can be written as

$$\mathbb{E}^{algo}_c = \mathrm{d}_{\boldsymbol{\varepsilon}} \boldsymbol{s} = \mathbb{E}^e - \mathbb{E}^e : \partial_{\boldsymbol{\varepsilon}} \boldsymbol{\varepsilon}^c\, . \tag{A.9}$$

Incorporation of the sensitivity $\partial_{\boldsymbol{\varepsilon}} \boldsymbol{\varepsilon}^c$ derived in (A.8) into (A.9) yields

$$\mathbb{E}^{algo}_c = \mathbb{E}^e - \mathbb{E}^e : \mathbb{H}\ . \tag{A.10}$$

B. Two-Point Q1-P0-Brick Element Formulation

This chapter presents a mixed Q1P0-element for nearly incompressible materials. This approach was first introduced by Simo et al. [199], influenced by the ideas of Nagtegaal et al. [168]. A summary can be also found in Wriggers [225]. The starting point of such a mixed finite element formulation is the Hu-Washizu variational principle. We deal with nearly incompressible solids, where the volumetric deformation of the body has the constraint $J = 1$. The Hu-Washizu three-field functional is formulated in terms of the deformation map $\boldsymbol{\varphi}$, the pressure p, acting as a penalty parameter, as well as the volume dilatation Θ, satisfying the constraint $J = \Theta$. The considered free energy function is divided into volumetric and isochoric parts, where the unimodular part of the deformation gradient $\bar{\boldsymbol{F}} = J^{-1/3}\boldsymbol{F}$ determines the volume preserving deformation. The well-known formulation is specified for the coupling with phase field fracture, where a degradation of free energy is considered, as described in Chapter 7. The phase field d is considered as a geometric constraint and according to the staggered solution scheme presented in Chapter 4, is considered constant in the following derivation. A decoupling from temperature evolution is obtained by the explicit update of the temperature field.

The decoupled Hu-Washizu potential functional for nearly incompressible materials in the two point setting can be given in a decomposed manner as

$$\pi(\boldsymbol{\varphi}, p, \Theta) = \int_{\mathcal{B}} g(d)\widetilde{\Psi}_{vol}(\Theta, d) + g(d)\widetilde{\Psi}_{iso}(\bar{\boldsymbol{F}}, d) + p(J - \Theta)\, dV - \int_{\partial\mathcal{B}^t} \boldsymbol{\varphi}\bar{\boldsymbol{T}} dA \; . \tag{B.1}$$

Here, Θ is a kinematic variable which will be enforced to be the Jacobian by the Euler-Lagrange equations. The first variation of the three field potential (B.1) results in the three Euler-Lagrange equations

$$\begin{aligned}
\delta_{\boldsymbol{\varphi}}\pi &= \int_{\mathcal{B}} (g(d)\partial_{\boldsymbol{F}}\widetilde{\Psi}_{iso} + pJ\boldsymbol{F}^{-T}) : \delta\boldsymbol{F}\, dV - \int_{\partial\mathcal{B}^t} \delta\boldsymbol{\varphi}\bar{\boldsymbol{T}} dA = 0 \\
\delta_{p}\pi &= \int_{\mathcal{B}} (J - \Theta)\delta p\, dV = 0 \\
\delta_{\Theta}\pi &= \int_{\mathcal{B}} (g(d)\partial_{\Theta}\widetilde{\Psi}_{vol} - p)\delta\Theta\, dV = 0
\end{aligned} \tag{B.2}$$

where we used the derivative $\partial_{\boldsymbol{F}} J = J\boldsymbol{F}^{-T}$ and identify the isochoric first Piola-Kirchhoff stress $\boldsymbol{P}_{iso} = g(d)\partial_{\boldsymbol{F}}\widetilde{\Psi}_{iso}$. The linearization of the mixed setting can be derived by

$$\begin{aligned}
\Delta(\delta_{\boldsymbol{\varphi}}\pi) &= \int_{\mathcal{B}} \delta\boldsymbol{F} : (g(d)\partial^2_{\boldsymbol{F}\boldsymbol{F}}\widetilde{\Psi}_{iso} + pJ\boldsymbol{F}^{-T}\otimes\boldsymbol{F}^{-T} - pJ\boldsymbol{F}^{-T}\odot\boldsymbol{F}^{-T}) : \Delta\boldsymbol{F}\, dV \\
&\quad + \int_{\mathcal{B}} \delta\boldsymbol{F} : \boldsymbol{F}^{-T} J\Delta p\, dV \\
\Delta(\delta_{p}\pi) &= \int_{\mathcal{B}} \delta p(J\boldsymbol{F}^{-T} : \Delta\boldsymbol{F} - \Delta\Theta)\, dV \\
\Delta(\delta_{\Theta}\pi) &= \int_{\mathcal{B}} \delta\Theta(g(d)\partial^2_{\Theta\Theta}\widetilde{\Psi}_{vol}\Delta\Theta - \Delta p)\, dV
\end{aligned} \tag{B.3}$$

with the operations in index notation $\boldsymbol{F}^{-T}\otimes\boldsymbol{F}^{-T} = F^{-1}_{ji}F^{-1}_{lk}$ and $\boldsymbol{F}^{-T}\odot\boldsymbol{F}^{-T} = F^{-1}_{jk}F^{-1}_{li}$. The two additional Euler-Lagrange equations $(\text{B.2})_{2,3}$ need to be satisfied locally within

a finite element due to the discontinuous, constant pressure p and the volume dilatation Θ. We solve these equations directly on the element level with $|\mathcal{B}^e| = \int_{\mathcal{B}^e} dV^e$ obtaining

$$\Theta = \frac{1}{|\mathcal{B}^e|}\int_{\mathcal{B}^e} J\, dV^e = \frac{|\mathcal{S}^e|}{|\mathcal{B}^e|} \quad \text{and} \quad p = \frac{1}{|\mathcal{B}^e|}\int_{\mathcal{B}^e} g(d)\partial_\Theta \widetilde{\Psi}_{vol}(\Theta, d)\, dV^e \ . \tag{B.4}$$

Note again that both Θ and p are assumed to be constant within an element. For the specific choice of $\widetilde{\Psi}_{vol}(\Theta, d) = g(d)\frac{\kappa}{2}(\Theta - 1)^2$, the expression for p reads

$$p = \frac{1}{|\mathcal{B}^e|}\int_{\mathcal{B}^e} g(d)\kappa(\Theta - 1)\, dV^e = \bar{\kappa}(\Theta - 1) \quad \text{with} \quad \bar{\kappa} = \frac{1}{|\mathcal{B}^e|}\int_{\mathcal{B}^e} g(d)\kappa\, dV^e \ . \tag{B.5}$$

Considering the linearization $(\text{B.3})_2$ we obtain the expression for the increment of the volume dilatation $\Delta\Theta$, i.e.

$$\Delta\Theta = \frac{1}{|\mathcal{B}^e|}\int_{\mathcal{B}^e} J\boldsymbol{F}^{-T} : \Delta\boldsymbol{F}\, dV^e \ . \tag{B.6}$$

Performing some algebraic manipulations we obtain

$$\boldsymbol{F}^{-T} : \Delta\boldsymbol{F} = F^{-1}_{ji}\Delta F_{ij} = \frac{\partial X_j}{\partial x_i}\frac{\partial \Delta u_i}{\partial X_j} = \frac{\partial \Delta u_i}{\partial x_i} = \operatorname{div}(\Delta\boldsymbol{u}) \ . \tag{B.7}$$

In complete analogy we obtain the expression $\delta\boldsymbol{F} : \boldsymbol{F}^{-T} = \operatorname{div}(\delta\boldsymbol{u})$. With (B.7), the increment of the volume dilatation reads

$$\Delta\Theta = \frac{1}{|\mathcal{B}^e|}\int_{\mathcal{B}^e} J\operatorname{div}(\Delta\boldsymbol{u})\, dV^e \ . \tag{B.8}$$

From $(\text{B.3})_3$, for $\Delta\Theta = const.$ and $\Delta p = const.$, the increment of the pressure is

$$\Delta p = \frac{1}{|\mathcal{B}^e|}\int_{\mathcal{B}^e} g(d)\partial^2_{\Theta\Theta}\widetilde{\Psi}_{vol}\, dV^e \cdot \Delta\Theta = \bar{\kappa}\Delta\Theta \ , \tag{B.9}$$

with $\bar{\kappa}$ defined in (B.5) for the specific choice $\partial^2_{\Theta\Theta}\widetilde{\Psi}_{vol} = g(d)\kappa$. In the finite element context, we proceed with the assembly of all n_{ele} elements in the domain. In addition, we substitute the increment of the pressure Δp in the linearization $(\text{B.3})_1$, by using $\Delta p = const.$ and equations (B.8) and (B.9), resulting in

$$\begin{aligned}\Delta(\delta_{\boldsymbol{\varphi}}\pi) = \bigwedge_{e=1}^{n_{ele}} \Bigg\{ & \int_{\mathcal{B}^e} \delta\boldsymbol{F} : \mathbb{A} : \Delta\boldsymbol{F}\, dV^e \\ & + \frac{1}{|\mathcal{B}^e|}\int_{\mathcal{B}^e} J\operatorname{div}(\delta\boldsymbol{u})\, dV^e (|\mathcal{B}^e|\bar{\kappa})\frac{1}{|\mathcal{B}^e|}\int_{\mathcal{B}^e} J\operatorname{div}(\Delta\boldsymbol{u})\, dV^e \Bigg\}\end{aligned} \tag{B.10}$$

in terms of the moduli tensor $\mathbb{A} = g(d)\partial^2_{\boldsymbol{FF}}\widetilde{\Psi}_{iso} + pJ(\boldsymbol{F}^{-T}\otimes\boldsymbol{F}^{-T} - \boldsymbol{F}^{-T}\odot\boldsymbol{F}^{-T})$.

The spatial domain $\mathcal{B}$ and the displacement field $\boldsymbol{u} = \boldsymbol{x} - \boldsymbol{X}$, as difference between spatial and material points, will be discretized by isoparametric shape functions such that

$$\begin{aligned}\boldsymbol{u} &= \boldsymbol{N}(\boldsymbol{\xi})\boldsymbol{d} \quad &\Leftrightarrow \quad u_i &= N^I d_{3(I-1)+i} \\ \boldsymbol{X} &= \boldsymbol{N}(\boldsymbol{\xi})\hat{\boldsymbol{X}} \quad &\Leftrightarrow \quad X_i &= N^I \hat{X}_{3(I-1)+i} \\ \boldsymbol{x} &= \boldsymbol{N}(\boldsymbol{\xi})\hat{\boldsymbol{x}} \quad &\Leftrightarrow \quad x_i &= N^I \hat{x}_{3(I-1)+i}\end{aligned} \tag{B.11}$$

where capital letters $\{I, J\}$ indicate the element node and $\boldsymbol{d}$, $\hat{\boldsymbol{X}}$, $\hat{\boldsymbol{x}}$ are the vectors containing the nodal displacements on the element level, the Lagrangian and the Eulerian coordinates. The local coordinates in the parameter space are denoted by $\boldsymbol{\xi} = [\xi, \eta, \zeta]$. The shape functions for an eight-node brick element are given by $N^I(\xi, \eta, \zeta) = \frac{1}{8}(1 + \xi\xi^I)(1 + \eta\eta^I)(1 + \zeta\zeta^I)$. For the computation of the spatial gradients with respect to Lagrangian and Eulerian coordinates, we define the shape functions by application of the chain rule

$$\boldsymbol{N}_{,\boldsymbol{X}} = \boldsymbol{N}_{,\boldsymbol{\xi}} \cdot \boldsymbol{\xi}_{,\boldsymbol{X}} \quad \text{and} \quad \boldsymbol{N}_{,\boldsymbol{x}} = \boldsymbol{N}_{,\boldsymbol{X}} \cdot \boldsymbol{F}^{-1} \ . \tag{B.12}$$

The discrete form of the increment of the volume dilatation (B.8) is

$$\Delta\theta = \frac{1}{|\mathcal{B}^e|} \int_{\mathcal{B}^e} J \operatorname{div}(\Delta\boldsymbol{u}) \, dV^e = \Delta\boldsymbol{d} \frac{1}{|\mathcal{B}^e|} \int_{\mathcal{B}^e} J\boldsymbol{N}_{,\boldsymbol{x}} \, dV^e = \Delta\boldsymbol{d}\bar{\boldsymbol{N}}_{,\boldsymbol{x}} \tag{B.13}$$

with the average shape functions

$$\bar{\boldsymbol{N}}_{,\boldsymbol{x}} = \frac{1}{|\mathcal{B}^e|} \int_{\mathcal{B}^e} \boldsymbol{N}_{,\boldsymbol{x}} J \, dV^e \ . \tag{B.14}$$

Insertion of the finite element approximations $\delta\boldsymbol{F} = \boldsymbol{N}_{,\boldsymbol{X}}\delta\boldsymbol{d}$ yields

$$\begin{aligned} \Delta(\delta_{\boldsymbol{\varphi}}\pi) &= \mathop{\mathsf{A}}_{e=1}^{n_{ele}} \left\{ \delta\boldsymbol{d}^T \left[\int_{\mathcal{B}^e} \boldsymbol{N}_{,\boldsymbol{X}}^T : \mathbb{A} : \boldsymbol{N}_{,\boldsymbol{X}} \, dV^e + \bar{\boldsymbol{N}}_{,\boldsymbol{x}}^T (|\mathcal{B}^e| \partial^2_{\theta\theta}\psi_{vol}) \bar{\boldsymbol{N}}_{,\boldsymbol{x}} \right] \Delta\boldsymbol{d} \right\} \\ &= \mathop{\mathsf{A}}_{e=1}^{n_{ele}} \left\{ \delta\boldsymbol{d}^T \left[\boldsymbol{K}^e_{mat} + \boldsymbol{K}^e_{vol} \right] \Delta\boldsymbol{d} \right\} \end{aligned} \tag{B.15}$$

for the increment of the Euler-Lagrange equation of deformation map (B.10). The discrete expression for the Euler-Lagrange equations reads

$$\begin{aligned} \delta_{\boldsymbol{\varphi}}\pi^h &= \mathop{\mathsf{A}}_{e=1}^{n_{ele}} \left\{ \delta\boldsymbol{d}^T \left[\int_{\mathcal{B}} \boldsymbol{N}_{,\boldsymbol{X}}^T : \boldsymbol{P} \right] dV^e \right] \right\} - \mathop{\mathsf{A}}_{s=1}^{n_{surf}} \left\{ \delta\boldsymbol{d}^T \int_{\partial\mathcal{B}^t} \boldsymbol{N}_{\varphi}^{sT} \bar{\boldsymbol{T}} \, dA \right\} = \boldsymbol{0} \\ &= \mathop{\mathsf{A}}_{e=1}^{n_{ele}} \left\{ \delta\boldsymbol{d}^T \boldsymbol{R}^e \right\} - \mathop{\mathsf{A}}_{s=1}^{n_{surf}} \left\{ \delta\boldsymbol{d}^T \boldsymbol{R}^s \right\} = \boldsymbol{0} \ . \end{aligned} \tag{B.16}$$

The assembly of the element residual and stiffness matrices yields the global residual and tangent matrices

$$\boldsymbol{K}_{glob} = \mathop{\mathsf{A}}_{e=1}^{n_{ele}} [\boldsymbol{K}^e_{mat} + \boldsymbol{K}^e_{vol}] \quad \text{and} \quad \boldsymbol{R}_{glob} = \mathop{\mathsf{A}}_{e=1}^{n_{ele}} \boldsymbol{R}^e - \mathop{\mathsf{A}}_{s=1}^{n_{surf}} \boldsymbol{R}^s \ . \tag{B.17}$$

With these, the linear Euler-Lagrange equation reads

$$\delta_{\boldsymbol{\varphi}}\pi^{lin} = \delta\boldsymbol{D}^T \{ \boldsymbol{K}_{glob} \Delta\boldsymbol{D} + \boldsymbol{R}_{glob} \} = 0 \tag{B.18}$$

which must hold for all variations $\delta\boldsymbol{D}$. We obtain the update of the global displacement vector

$$\boldsymbol{D} \leftarrow \boldsymbol{D} - \boldsymbol{K}^{-1}_{glob} \boldsymbol{R}_{glo} \tag{B.19}$$

until convergence is achieved in the sense $||\boldsymbol{R}|| < tol$.

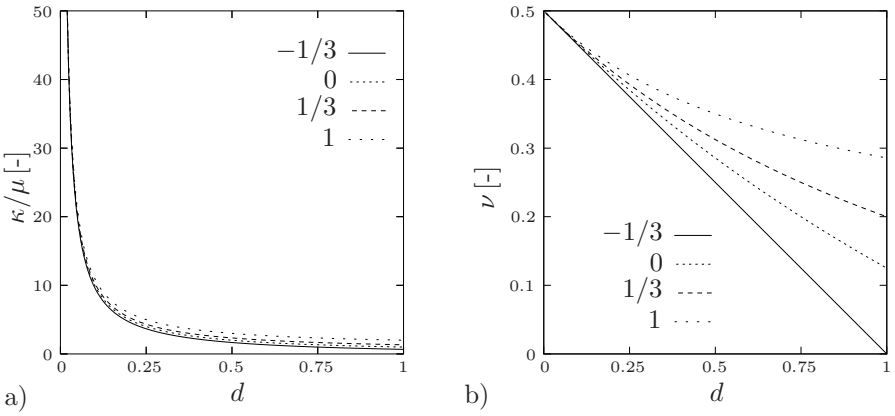

Figure C.1: Bulk modulus in a) and Poisson's ratio in b) decrease with damage d. Sensitivity of the functions with respect to the parameter f_∞.

C. Degradation of the Incompressibility Constraint with Damage

The phase field modeling of crack growth and opening, induces a considerable amount of volume increase in the crack state of the continuum. Isotropic degradation of shear modulus $\mu = (1-d)^2\widetilde{\mu}$ and bulk modulus $\kappa = (1-d)^2\widetilde{\kappa}$ yields a soft, however still incompressible response. To avoid this, a damage dependent release of the incompressibility constraint is proposed, together with isotropic degradation of shear modulus $\mu = (1-d)^2\widetilde{\mu}$. Void growth in incompressible solids yields a macroscopically compressible response. Based on [165], we introduce a constitutive function for the bulk modulus

$$\kappa(d) = \begin{cases} \mu(1/f_0 + f_\infty) & \text{if } d < f_0 \\ \mu(1/d + f_\infty) & \text{otherwise} \end{cases} . \tag{C.1}$$

This function tends to infinity $\kappa \to \infty$ for the intact solid phase $d \to 0$ with parameter $f_0 \ll 1$. On the other hand, for the cracked state of the material, for $d = 1$, the ultimate value is $\kappa/\mu = 1 - f_\infty$. Insertion of (C.1) into the equation of poisson's ratio $\nu = \frac{3\kappa - 2\mu}{2(3\kappa+\mu)}$ yields the dimensionless representation

$$\nu(d) = \frac{3(1/d + f_\infty) - 2}{2(3(1/d + f_\infty) + 1)} . \tag{C.2}$$

Ideal material without imperfections is incompressible, with $\nu = 0.5$. Fully damaged material, with $d = 1$, shows little or no lateral contraction. The functions for the bulk modulus and Poisson's ratio over the void fraction are plotted in Figure C.1. Rubber materials are nearly incompressible. A limit value of $f_0 = 0.02$ yields a Poisson's ratio $\nu = 0.49$ and a ratio of bulk to shear modulus $\kappa/\mu \approx 50$, adequate for the modeling of the intact solid material.

References

[1] Ahagon, A.; Gent, A. N. [1975]: *Threshold fracture energies for elastomers.* Journal of Polymer Science: Polymer Physics Edition, 13: 1903–1911.

[2] Ambrosio, L.; Tortorelli, V. M. [1990]: *Approximation of functionals depending on jumps by elliptic functionals via* Γ*-convergence.* Communications on Pure and Applied Mathematics, 43: 999–1036.

[3] Anand, L.; Gurtin, M. E. [2003]: *A theory of amorphous solids undergoing large deformations, with application to polymeric glasses.* International Journal of Solids and Structures, 40: 1465–1487.

[4] Andrews, E.; Bevan, L. [1972]: *Mechanics and mechanism of environmental crazing in a polymeric glass.* Polymer, 13(7): 337–346.

[5] Argon, A.; Hannoosh, J. [1977]: *Initiation of crazes in polysstyrene.* The Philosophical Magazine, 36(5): 1195–1216.

[6] Argon, A.; Salama, M. [1977]: *Growth of crazes in glassy polymers.* The Philosophical Magazine, 36(5): 1217–1234.

[7] Argon, A. S. [1973]: *A theory for the low-temperature plastic deformation of glassy polymers.* The Philosophical Magazine, 28: 839–865.

[8] Argon, A. S. [1973]: *Physical basis of distortional and dilational plastic flow in glassy polymers.* Journal of Macromolecular Science, Part B: Physics, 8(34): 573–596.

[9] Argon, A. S. [1975]: *Role of heterogeneities in the crazing of glassy polymers.* Pure and Applied Chemistry, 43(1-2): 247–272.

[10] Argon, A. S. [2011]: *Craze initiation in glassy polymers - Revisited.* Polymer, 52(10): 2319–2327.

[11] Armero, F.; Linder, C. [2009]: *Numerical simulation of dynamic fracture using finite elements with embedded discontinuities.* International Journal of Fracture, 160: 119–141.

[12] Arruda, E. M.; Boyce, M. C. [1993]: *A three-dimensional constitutive model for the large stretch behavior of rubber elastic materials.* Journal of the Mechanics and Physics of Solids, 41: 389–412.

[13] Arruda, E. M.; Boyce, M. C. [1993]: *Evolution of plastic anisotropy in amorphous polymers during finite straining.* International Journal of Plasticity, 9: 697–720.

[14] Arruda, E. M.; Boyce, M. C.; Jayachandran, R. [1995]: *Effects of strain rate, temperature and thermomechanical coupling on the finite strain deformation of glassy polymers.* Mechanics of Materials, 19: 193–212.

[15] Ashby, M. F.; Jones, D. R. H. [1986]: *Engineering Materials II.* Pergamon Press.

[16] Ashby, M. F.; Jones, D. R. H. (Editors) [2013]: *An introduction to microstructures and processing.* Butterworth-Heinemann, Oxford, 4th Edition.

[17] Baney, J. M.; Hui, C.-Y. [1999]: *Viscoelastic crack healing and adhesion.* Journal of Applied Physics, 86(8): 4232–4241.

[18] Barenblatt, G. I. [1962]: *The mathematical theory of equilibrium cracks in brittle fracture.* Advances in Applied Mechanics, 7: 55–129.

[19] Basu, S.; Van der Giessen, E. [2002]: *A thermo-mechanical study of mode I, small-scale yielding crack-tip fields in glassy polymers.* International Journal of Plasticity 18 (2002) 1395-1423, 18: 1395–1423.

[20] Bauwens-Crowet, C.; Bauwens, J. C.; Homes, G. [1969]: *Tensile yield-stress behavior of glassy polymers.* Journal of Polymer Science: Part A-2, 7: 735–742.

[21] Benallal, A.; Marigo, J. [2007]: *Bifurcation and stability issues in gradient theories with softening.* Modelling and Simulation in Materials Science and Engineering, 15(1): S283.

[22] Berger, L.; Kramer, E. [1987]: *Chain disentanglement during high-temperature crazing of polystyrene.* Macromolecules, 20(8): 1980–1985.

[23] Bergström, J. S.; Boyce, M. C. [1998]: *Constitutive modeling of the large strain time-dependent behavior of elastomers.* Journal of the Mechanics and Physics of Solids, 46: 931–954.

[24] Bernstein, B.; Kearsley, E. A.; Zapas, L. J. [1963]: *A study of stress relaxation with finite strain.* Transactions of the Society of Rheology, 7: 391–4110.

[25] Bhowmick, A. K. (Editor) [2008]: *Current topics in elastomers research.* CRC Press.

[26] Bird, R. B.; Hassager, O.; Armstrong, R. C.; Curtiss, C. F. [1977]: *Dynamics of Polymeric Liquids. Kinetic Theory*, Vol. 2. John Wiley & Sons.

[27] Borden, M. J.; Verhoosel, C. V.; Scott, M. A.; Hughes, T. J. R.; Landis, C. M. [2012]: *A phase-field description of dynamic brittle fracture.* Computer Methods in Applied Mechanics and Engineering, 217-220: 77–95.

[28] Borden, M. J.; Hughes, T. J. R.; Landis, C. M.; Verhoosel, C. V. [2014]: *A higher-order phase-field model for brittle fracture: Formulation and analysis within the isogeometric analysis framework.* Computer Methods in Applied Mechanics and Engineering, 273: 100–118.

[29] Bourdin, B.; Francfort, G. A.; Marigo, J. J. [2000]: *Numerical experiments in revisited brittle fracture.* J. Mech. Phys. Solids, 48: 797–826.

[30] Bourdin, B.; Francfort, G. A.; Marigo, J.-J. [2008]: *Special invited exposition: The variational approach to fracture.* Journal of Elasticity, 91: 5–148.

[31] Bourdin, B.; Francfort, G.; Marigo, J. [2008]: *The variational approach to fracture.* Journal of Elasticity, 91(1-3): 5–148.

[32] Bowden, P. B.; Jukes, J. A. [1972]: *The plastic flow of isotropic polymers.* Journal of Materials Science, 7: 52–63.

[33] Boyce, M. C.; Arruda, E. M. [2000]: *Constitutive models of rubber elasticity: A review.* Rubber Chemistry and Technology, 73: 504–523.

[34] Boyce, M. C.; Parks, D. M.; Argon, A. S. [1988]: *Large inelastic deformation of glassy polymers. Part I: Rate dependent constitutive model.* Mechanics of Materials, 7: 15–33.

[35] Boyce, M. C.; Montagut, E. L.; Argon, A. S. [1992]: *The effects of thermomechanical coupling on the cold drawing process of glassy polymers.* Polymer Engineering and Science, 32: 1073–1085.

[36] Braides, D. P. [1998]: *Approximation of Free Discontinuity Problems.* Springer Verlag, Berlin.

[37] Braides, D. P. [2002]: Γ-*Convergence for Beginners.* Oxford University Press.

[38] Brown, H. [1991]: *A molecular interpretation of the toughness of glassy polymers.* Macromolecules, 24(10): 2752–2756.

[39] Bucknall, C. [2007]: *New criterion for craze initiation.* polymer, 48: 1030–1041.

[40] Buliga, M. [1999]: *Energy minimizing brittle crack propagation.* Journal of Elasticity, 52: 201–238.

[41] Camacho, G. T.; Ortiz, M. [1996]: *Computational modelling of impact damage*

in brittle materials. International Journal of Solids and Structures, 33: 2899–2938.
[42] Carbone, G.; Persson, B. N. J. [2005]: *Hot cracks in rubber: Origin of the giant toughness of rubberlike materials*. Physical Review Letters, 95: 114301.
[43] Carbone, G.; Persson, B. [2005]: *Crack motion in viscoelastic solids: The role of the flash temperature*. The European Physical Journal E, 17(3): 261–281.
[44] Chadwick, P. [1999]: *Continuum Mechanics*. Dover Publications, Inc., Mineola.
[45] Cohen, A. [1991]: *A Padé approximant to the inverse Langevin function*. Rheological Acta, 30: 270–273.
[46] Coleman, B.; Gurtin, M. E. [1967]: *Thermodynamics with internal state variables*. The Journal of Chemical Physics, 47: 597–613.
[47] Coleman, B.; Noll, W. [1961]: *Foundations of linear viscoelasticity*. Reviews of Modern Physics, 33: 239–249.
[48] Coleman, B.; Noll, W. [1963]: *The thermodynamics of elastic materials with heat conduction and viscosity*. Archive for Rational Mechanics and Analysis, 13: 167–178.
[49] Dal Maso, G. [1993]: *An Introduction to Γ-Convergence*. Birkhäuser.
[50] Dal Maso, G.; Toader, R. [2002]: *A model for the quasistatic growth of brittle fractures: Existence and approximation results*. Archive for Rational Mechanics and Analysis, 162: 101–135.
[51] D'Amico, F.; Carbone, G.; Foglia, M.; Galietti, U. [2013]: *Moving cracks in viscoelastic materials: Temperature and energy-release-rate measurements*. Engineering Fracture Mechanics, 98: 315–325.
[52] Davidge, R.; Green, T. [1968]: *The strength of two-phase ceramic/glass materials*. Journal of Materials Science, 3(6): 629–634.
[53] Gennes, P. G. de [1971]: *Reptation of a polymer chain in the presence of fixed obstacles*. The Journal of Chemical Physics, 55: 572–579.
[54] de Gennes, P. G. [1996]: *Soft adhesives*. Langmuir, 12(19): 4497–4500.
[55] Deam, R. T.; Edwards, S. F. [1976]: *The theory of rubber elasticity*. Philosophical Transactions of the Royal Society London A, 280: 317–353.
[56] Doi, M.; Edwards, S. F. [1986]: *The Theory of Polymer Dynamics*. Clarendon Press.
[57] Döll, W. [1983]: *Optical interference measurements and fracture mechanics analysis of crack tip craze zones*. In Kausch, H. (Editor), *Crazing in Polymers*, Vol. 52-53 of *Advances in Polymer Science*, pp. 105–168. Springer-Verlag.
[58] Donald, A.; Kramer, E. [1981]: *The mechanism for craze-tip advance in glassy polymers*. Philosophical Magazine A, 43(4): 857–870.
[59] Donald, A. M. [1997]: *Crazing*. In Haward, R. N.; Young, R. J. (Editors), *The Physics of Glassy Polymers*, chapter 6, pp. 295–341. Chapman & Hall, 2nd Edition.
[60] Drozdov, A. D. [1996]: *Finite Elasticity and Viscoelasticity: A Course in the Nonlinear Mechanics of Solids*. World Scientific Publishing Co., Singapore.
[61] Drozdov, A. D. [1997]: *A constitutive model for nonlinear viscoelastic media*. International Journal of Solids and Structures, 34: 2685–2707.
[62] Drozdov, A. D.; Dorfmann, A. [2002]: *Finite viscoelasticity of filled rubbers: The effects of pre-loading and thermal recovery*. Continuum Mechanics and Thermodynamics, 14: 337–361.
[63] Eastgate, L. O.; Sethna, J. P.; Rauscher, M.; Cretegny, T. [2002]: *Fracture in mode I using a conserved phase-field model*. Phys. Rev. E, 65: 036117.

[64] Edwards, S. F.; Vilgis, T. A. [1988]: *The tube model theory of rubber elasticity.* Reports on Progress in Physics, 51: 243–297.

[65] Eirich, F. R. (Editor) [1978]: *Science and technology of rubber.* Academic Press, New York.

[66] Elmukashfi, E.; Kroon, M. [2012]: *Numerical analysis of dynamic crack propagation in rubber.* International Journal of Fracture, 177: 163–178.

[67] Estevez, R.; Tijssens, M.; van der Giessen, E. [2000]: *Modeling of the competition between shear yielding and crazing in glassy polymers.* Journal of the Mechanics and Physics of Solids, 48: 2585–2617.

[68] Ferry, J. D. [1980]: *Viscoelastic Properties of Polymers.* John Wiley & Sons, Inc.

[69] Findley, W. N.; Lai, J. S.; Onaran, K. [1989]: *Creep and Relaxation of Nonlinear Viscoelastic Materials.* Dover Publication.

[70] Flory, P. J. [1989]: *Statistical Mechanics of Chain Molecules.* Clarendon Press.

[71] Flory, P. J.; Erman, B. [1982]: *Theory of elasticity of polymer networks. 3.* Macromolecules, 15: 800–806.

[72] Francfort, G. A.; Marigo, J. J. [1998]: *Revisiting brittle fracture as an energy minimization problem.* J. Mech. Phys. Solids, 46: 1319–1342.

[73] Frémond, M. [2002]: *Non-Smooth Thermomechanics.* Springer.

[74] Frémond, M.; Nedjar, B. [1996]: *Damage, gradient of damage, and principle of virtual power.* International Journal of Solids and Structures, 33: 1083–1103.

[75] Furukawa, J. [1955]: *A kinetic interpretation of the rheological behavior of high polymers.* Journal of Polymer Science, 15: 193–202.

[76] Gearing, B.; Anand, L. [2004]: *On modeling the deformation and fracture response of glassy polymers due to shear-yielding and crazing.* International Journal of Solids and Structures, 41: 3125–3150.

[77] Geissler, G.; Kaliske, M. [2010]: *Time-dependent cohesive zone modelling for discrete fracture simulation.* Engineering Fracture Mechanics, 77: 153–169.

[78] Geissler, G.; Kaliske, M.; Nase, M.; Grellman, W. [2007]: *Peel process simulation of sealed polymeric fil computational modelling of experimental results.* International Journal for Computer-Aided Engineering and Software, 24: 586–607.

[79] Geissler, G.; Netzker, C.; Kaliske, M. [2010]: *Discrete crack path prediction by an adaptive cohesive crack model.* Engineering Fracture Mechanics, 77(18): 3541–3557. Computational Mechanics in Fracture and Damage: A Special Issue in Honor of Prof. Gross.

[80] Gent, A.; Schultz, J. [1972]: *Effect of wetting liquids on the strength of adhesion of viscoelastic material.* The Journal of Adhesion, 3(4): 281–294.

[81] Gent, A. N. [1970]: *Hypothetical mechanism of crazing in glassy plastics.* Journal of Material Science, 5: 925–932.

[82] Gent, A. N. [1996]: *A new constitutive relation for rubber.* Rubber Chemistry and Technology, 69: 59–61.

[83] Gent, A. N.; Lai, S.-M. [1994]: *Interfacial bonding, energy dissipation, and adhesion.* J. Polym. Sci. Polym. Phys., 32: 1543–1555.

[84] Gent, A. N. (Editor) [2012]: *Engineering with rubber: How to design rubber components.* Hanser, 3rd Edition.

[85] Geyer, J.; Nemat-Nasser, F. [1982]: *Experimental investigation of thermally induced interacting cracks in brittle solids.* International Journal of Solids and Structures, 18(4): 349–356.

[86] Govaert, L. E.; Timmermans, P. H. M.; Brekelmans, W. A. M. [2000]: *The influence of intrinsic strain softening on strain localization in polycarbonate: Modeling and experimental validation.* Journal of Engineering Materials and Technology, 122: 177–185.

[87] Govindjee, S.; Simó, J. C. [1992]: *Mullins' effect and the strain amplitude dependence of the storage modulus.* International Journal of Solids and Structures, 29: 1737–1751.

[88] Green, M. S.; Tobolsky, A. V. [1946]: *A new approach to the theory of relaxing polymeric media.* The Journal of Chemical Physics, 14: 80–92.

[89] Greensmith, H. [1960]: *Rupture of rubber. VIII. Comparisons of tear and tensile rupture measurements.* J. Appl. Polym. Sci., III, Issue No. 8: 183–193.

[90] Greensmith, H. [1963]: *Rupture of rubber. X. The change in stored energy on making a small cut in a test piece held in simple extension.* Journal of Applies Polymer Science, 7: 993–1002.

[91] Greensmith, H.; Thomas, A. [1955]: *Rupture of rubber. III. Determination of tear properties.* Journal of Polymer Science, 18: 189–200.

[92] Greensmith, H. W. [1964]: *Rupture of rubber. XI. Tensile rupture and crack growth in a noncrystallizing rubber.* Journal of Applied Polymer Science, 8(3): 1113–1128.

[93] Greenwood, J. A. [2004]: *The theory of viscoelastic crack propagation and healing.* Journal of Physics D: Applied Physics, 37(18): 2557.

[94] Grellmann, W.; Heinrich, G.; Kaliske, M.; Klüppel, M.; Schneider, K.; Vilgis, T. [2013]: *Fracture Mechanics and Statistical Mechanics of Reinforced Elastomeric Blends.* Springer.

[95] Griffith, A. A. [1920]: *The phenomena of rupture and flow in solids.* Philosophical Transactions of the Royal Society London A, 221: 163–198.

[96] Griffith, A. A. [1924]: *The theory of rupture.* In Biezeno, C. B.; Burgers, J. M. (Editors), *Proceedings of the First International Congress for Applied Mechanics, Delft*, pp. 55–63.

[97] Griffith, A. [1921]: *The phenomena of rupture and flow in solids.* Philosophical Transactions of the Royal Society of London A, 221: 163–198.

[98] Gross, D.; Seelig, T. [2011]: *Bruchmechanik mit einer Einführung in die Mikromechanik.* Springer-Verlag, 5th Edition.

[99] Gürses, E.; Miehe, C. [2009]: *A computational framework of three dimensional configurational force driven brittle crack propagation.* Computer Methods in Applied Mechanics and Engineering, 198: 1413–1428.

[100] Gurson, A. L. [1977]: *Continuum theory of ductile rupture by void nucleation and growth, Part I - Yield criteria and flow rules for porous ductile media.* Journal of Engineering Materials and Technology-Transactions of the ASME, 99: 2–15.

[101] Hakim, V.; Karma, A. [2009]: *Laws of crack motion and phase-field models of fracture.* Journal of the Mechanics and Physics of Solids, 57: 342–368.

[102] Hasan, O. A.; Boyce, M. C. [1995]: *A constitutive model for the nonlinear viscoelastic viscoplastic behavior of glassy polymers.* Polymer Engineering and Science, 35: 331–344.

[103] Haupt, P. [2002]: *Continuum Mechanics and Theory of Materials.* Springer-Verlag, 2nd Edition.

[104] Haupt, P.; Sedlan, K. [2001]: *Viscoplasticity of elastomeric materials: Experi-*

mental facts and constitutive modelling. Archive of Applied Mechanics, 71: 89–109.

[105] Heinrich, G.; Kaliske, M. [1997]: *Theoretical and numerical formulation of a molecular based constitutive tube-model of rubber elasticity.* Computational and Theoretical Polymer Science, 7: 227–241.

[106] Heinrich, G.; Straube, E. [1983]: *On the strength and deformation dependence of the tube-like topological constraints of polymer networks, melts and concentrated solutions, i. the polymer network case.* Acta Polymerica, 34: 589–594.

[107] Hill, R. [1968]: *On constitutive inequalities for simple materials I.* Journal of the Mechanics and Physics of Solids, 16: 229–242.

[108] Hocine, N.; Abdelaziz, M.; Imad, A. [2002]: *Fracture problems of rubbers: J-integral estimation based upon η factors and an investigation on the strain energy density distribution as a local criterion.* International Journal of Fracture, 117: 1–23.

[109] Holzapfel, G. A.; Simó, J. C. [1996]: *A new viscoelastic constitutive model for continuous media at finite thermomechanical changes.* International Journal of Solids and Structures, 33: 3019–3034.

[110] Holzapfel, G. [2000]: *Nonlinear Solid Mechanics.* John Wiley & Sons.

[111] Hui, C.; Ruina, A.; Creton, C.; Kramer, E. [1992]: *Micromechanics of crack growth into a craze in a polymer glass.* Macromolecules, 25: 3948–3955.

[112] Irwin, G. R. [1957]: *Analysis of stresses and strains near the end of a crack traversing a plate.* Journal of Applied Mechanics, 24: 361–364.

[113] Irwin, G. R. [1958]: *Fracture.* In Flügge, S. (Editor), *Encyclopedia of Physics*, Vol. 6, Elasticity and Plasticity, pp. 551–590. Springer.

[114] Itskov, M.; Dargazany, R.; Hörnes, K. [2011]: *Taylor expansion of the inverse function with application to the Langevin function.* Mathematics and Mechanics of Solids, pp. 1–9.

[115] James, H. M.; Guth, E. [1943]: *Theory of elastic properties of rubber.* The Journal of Chemical Physics, 11: 455–481.

[116] Kadir, A.; Thomas, A. G. [1981]: *Tear behavior of rubbers over a wide range of rates.* Rubber Chemistry and Technology, 54: 15–23.

[117] Kaliske, M.; Rothert, H. [1997]: *Formulation and implementation of three-dimensional viscoelasticity at small and finite strains.* Computational Mechanics, 19: 228–239.

[118] Kaliske, M.; Dal, H.; Fleischhauer, R.; Jenkel, C.; Netzker, C. [2012]: *Characterization of fracture processes by continuum and discrete modelling.* Computational Mechanics, 50: 303–320.

[119] Kambour, R. [1973]: *A review of crazing and fracture in thermoplastics.* Journal of Polymer Science: Macromolecular Reviews, 7: 1–154.

[120] Karma, A.; Kessler, D. A.; Levine, H. [2001]: *Phase-field model of mode III dynamic fracture.* Physical Reviev Letters, 87: 045501.

[121] Kaye, A. [1962]: *Non-newtonian flow in incompressible fluids.* Technical Report 134, College of Aeronautics, Cranfield CoA.

[122] Keck, J.; Miehe, C. [1997]: *An Eulerian overstress-type viscoplastic constitutive model in spectral form. formulation and numerical implementation.* In Owen, D.; Hinton, E.; Onate, E. (Editors), *Proceedings of the V International Conference on Computational Plasticity*, pp. 996–1003. CIMNE, Barcelona.

[123] Kinloch, A. J.; Young, R. J. [1983]: *Fracture Behaviour of Polymers.* Applied

Science Publishers, London and New York.

[124] Kramer, E. [1983]: *Microscopic and molecular fundamentals of crazing*. Advances in Polymer Science, 52/53: 1–56.

[125] Kramer, E.; Berger, L. [1990]: *Fundamental processes of craze growth and fracture*. In Kausch, H. (Editor), *Crazing in Polymers Vol. 2*, Vol. 91 of *Advances in Polymer Science*, pp. 1–68. Springer-Verlag.

[126] Kroon, M. [2011]: *Steady-state crack growth in rubber-like solids*. International Journal of Fracture, 169: 49–60.

[127] Kuhn, C.; Müller, R. [2011]: *A new finite element technique for a phase field model of brittle fracture*. Journal of Theoretical and Applied Mechanics, 49(4): 1115–1133.

[128] Kuhn, W. [1934]: *Über die Gestalt fadenförmiger Moleküle in Lösungen*. Kolloid-Zeitschrift, 68: 2–15.

[129] Kuhn, W. [1936]: *Beziehungen zwischen Molekülgröße, statistischer Molekülgestalt und elastischen Eigenschaften hochpolymerer Stoffe*. Kolloid-Zeitschrift, 76: 258–271.

[130] Kuhn, W.; Grün, F. [1942]: *Beziehungen zwischen elastischen Konstanten und Dehnungsdoppelbrechung hochelastischer Stoffe*. Kolloid-Zeitschrift, 101: 248–271.

[131] Kuna, M. [2010]: *Numerische Beanspruchungsanalyse von Rissen. Finite Elemente in der Bruchmechanik*. Springer-Verlag, New York, 2nd Edition.

[132] Lake, G. [1995]: *Fatigue and fracture of elastomers*. Rubber Chemistry and Technology, 68: 435–460.

[133] Lake, G.; Thomas, A. [1967]: *The strength of highly elastic material*. Proceedings of the Royal Society of London. Series A, Mathematical and Physical Sciences, 300: 108–119.

[134] Lauterwasser, B. D.; Kramer, J. [1979]: *Microscopic mechanisms and mechanics of craze growth and fracture*. Philosophical Magazine, 39: 469–495.

[135] Linder, C.; Armero, F. [2009]: *Finite elements with embedded branching*. Finite Elements in Analysis and Design, 45: 280–293.

[136] Linder, C.; Tkachuk, M.; Miehe, C. [2011]: *A micromechanically motivated diffusion-based transient network model and its incorporation into finite rubber viscoelasticity*. Journal of the Mechanics and Physics of Solids, 59: 2134–2156.

[137] Lion, A. [1996]: *A constitutive model for carbon black filled rubber. Experimental investigations and mathematical representations*. Continuum Mechanics and Thermodynamics, 8: 153–169.

[138] Lion, A. [1997]: *On the large deformation behaviour of reinforced rubber at different temperatures*. Journal of the Mechanics and Physics of Solids, 45: 1805–1834.

[139] Lion, A.; Johlitz, M. [2012]: *On the representation of chemical ageing of rubber in continuum mechanics*. International Journal of Solids and Structures, 49(10): 1227 – 1240.

[140] Lion, A.; Peters, J. [2010]: *Coupling effects in dynamic calorimetry: Frequency-dependent relations for specific heat and thermomechanical responses - a one-dimensional approach based on thermodynamics with internal state variables*. Thermochimica Acta, 500: 76–87.

[141] Lodge, A. S. [1956]: *A netowork theory of flow birefringence and stress in concentrated polymer solutions*. Transactions of the Faraday Society, 52: 120–130.

[142] Lu, S.; Pister, K. [1975]: *Decomposition of the deformation and representation*

of the free energy function for isotropic thermoelastic solids. International Journal of Solids and Structures, 11: 927–934.

[143] Lubliner, J. [1985]: *A model of rubber viscoelasticity.* Mechanics Research Communications, 12: 93–99.

[144] Lulei, F.; Miehe, C. [2001]: *A physically-based constitutive model for the finite viscoelastic deformations in rubbery polymers based on a directly evaluated micro-macro transition.* In Besdo, D.; Schuster, R.; Ihlemann, J. (Editors), *Constitutive Models for Rubber II*, pp. 117–125. Balkema Publications, Lisse.

[145] Marsden, J. E.; Hughes, T. J. R. [1983]: *Mathematical Foundations of Elasticity.* Prentice-Hall, Englewood Cliffs, New Jersey.

[146] Maugin, G. A. [1999]: *The Thermomechanics of Nonlinear Irreversible Behaviors. An Introduction.* World Scientific Publishing Co. Pte. Ltd.

[147] Maugis, D.; Barquins, M. [1980]: *Fracture mechanics and the adherence of viscoelastic bodies.* Journal of Physics D: Applied Physics, 11(14): 203–277.

[148] Miehe, C.: *Geometrical methods for nonlinear continuum mechanics and continuum thermodynamics.* Lecture notes.

[149] Miehe, C.: *Theoretical and computer-oriented material theory.* Lecture notes.

[150] Miehe, C. [1995]: *Entropic thermoelasticity at finite strains. aspects of the formulation and numerical implementation.* Computer Methods in Applied Mechanics and Engineering, 120: 243–269.

[151] Miehe, C. [1995]: *Discontinuous and continuous damage evolution in ogden-type large-strain elastic materials.* European Journal of Mechanics A/Solids, 14: 697–720.

[152] Miehe, C.; Göktepe, S. [2005]: *A micro-macro approach to rubber-like materials. Part II: The micro-sphere model for finite rubber viscoelasticity.* Journal of the Mechanics and Physics of Solids, 53: 2231–2258.

[153] Miehe, C.; Gürses, E. [2007]: *A robust algorithm for configurational-force-driven brittle crack propagation with r-adaptive mesh alignment.* International Journal for Numerical Methods in Engineering, 72: 127–155.

[154] Miehe, C.; Keck, J. [2000]: *Superimposed finite elastic-viscoelastic-plastoelastic stress response with damage in filled rubbery polymers. Experiments, modelling and algorithmic implementation.* Journal of the Mechanics and Physics of Solids, 48: 323–365.

[155] Miehe, C.; Lambrecht, M. [2001]: *Algorithms for computation of stresses and elasticity moduli in terms of Seth-Hill's family of generalized strain tensors.* Communications in Numerical Methods in Engineering, 17: 337–353.

[156] Miehe, C.; Schänzel, L. [2014]: *Phase field modeling of fracture in rubbery polymers. Part I: Finite elasticity coupled with brittle failure.* Journal of the Mechanics and Physics of Solids, 65: 93–113.

[157] Miehe, C.; Apel, N.; Lambrecht, M. [2002]: *Anisotropic additive plasticity in the logarithmic strain space: Modular kinematic formulation and implementation based on incremental minimization principles for standard materials.* Computer Methods in Applied Mechanics and Engineering, 191: 5383–5425.

[158] Miehe, C.; Göktepe, S.; Lulei, F. [2004]: *A micro-macro approach to rubber-like materials. Part I: The non-affine micro-sphere model of rubber elasticity.* Journal of the Mechanics and Physics of Solids, 52: 2617–2660.

[159] Miehe, C.; Göktepe, S.; Mendez, J. [2009]: *Finite viscoplasticity of amorphous*

glassy polymers in the logarithmic strain space. International Journal of Solids and Structures, 46: 181–202.

[160] Miehe, C.; Hofacker, M.; Welschinger, F. [2010]: *A phase field model for rate-independent crack propagation: Robust algorithmic implementation based on operator splits.* Computer Methods in Applied Mechanics and Engineering, 199: 2765–2778.

[161] Miehe, C.; Welschinger, F.; Hofacker, M. [2010]: *Thermodynamically consistent phase-field models of fracture: Variational principles and multi-field fe implementations.* International Journal of Numerical Methods in Engineering, 83: 1273–1311.

[162] Miehe, C.; Méndez Diez, J.; Göktepe, S.; Schänzel, L. [2011]: *Coupled thermoviscoplasticity of glassy polymers in the logarithmic strain space based on the free volume theory.* International Journal of Solids and Structures, 48: 1799–1817.

[163] Miehe, C.; Schänzel, L.; Ulmer, H. [2015]: *Phase field modeling of fracture in multi-physics problems. Part I. balance of crack surface and failure criteria for brittle crack propagation in thermo-elastic solids.* Computer Methods in Applied Mechanics and Engineering. doi:10.1016/j.cma.2014.11.016.

[164] Miehe, C. [2012]: *Mixed variational principles for the evolution problem of gradient-extended dissipative solids.* GAMM-Mitteilungen, 35: 8–25.

[165] Mori, T.; Tanaka, K. [1973]: *Average stress in matrix and average elastic energy of materials with misfitting inclusions.* Acta Metallica, 21: 571–573.

[166] Mumford, D.; Shah, J. [1989]: *Optimal approximations by piecewise smooth functions and associated variational problems.* Communications on Pure and Applied Mathematics, 42: 577–685.

[167] Müller, H. K.; Knauss, W. G. [1971]: *The fracture energy and some mechanical properties of a polyurethane elastomer.* Journal of Rheology, 15: 217–233.

[168] Nagtegaal, J.; Parks, D.; Rice, J. [1974]: *On numerically accurate finite element solutions in the fully plastic range.* Computer Methods in Applied Mechanics and Engineering, 4: 153–177.

[169] Narisawa, I.; Yee, A. F. [1993]: *Crazing and fracture of polymers.* In Thomas, E. L. (Editor), *Structure and Properties of Polymers, Materials Science and Technology*, Vol. 12, chapter 15, pp. 699–765. VCH.

[170] Nase, M.; Langer, B.; Baumann, H.; Grellmann, W.; Geissler, G.; Kaliske, M. [2009]: *Evaluation and simulation of the peel behavior of polyethylene/polybutene-1 peel systems.* Journal of Applied Polymer Science, 111: 363–370.

[171] Netzker, C.; Horst, T.; Reincke, K.; Behnke, R.; Kaliske, M.; Heinrich, G.; Grellmann, W. [2013]: *Analysis of stable crack propagation in filled rubber based on a global energy balance.* International Journal of Fracture, 181: 13–23.

[172] Nguyen, T.; Govindjee, S. [2006]: *Numerical study of geometric constraint and cohesive parameters in steady-state viscoelastic crack growth.* International Journal of Fracture, 141: 255–268.

[173] Nguyen, T.; Govindjee, S.; Klein, P.; Gao, H. [2005]: *A material force method for inelastic fracture mechanics.* Journal of the Mechanics and Physics of Solids, 53: 91–121.

[174] Ogden, R. W. [1972]: *Large deformation isotropic elastictiy: On the correlation*

of theory and experiment for incompressible rubberlike solids. Proceedings of the Royal Society London A, 326: 565–584.

[175] Ogden, R. W. [1984]: *Non-linear elastic deformations.* Ellis Horwood, Chichester.

[176] Oxborough, R.; Bowden, P. [1973]: *A general critical-strain criterion for crazing in amorphous glassy polymers.* Philosophical Magazine, 28(3): 547–559.

[177] Pandolfi, A.; Ortiz, M. [2002]: *An efficient adaptive procedure for three-dimensional fragmentation simulations.* Engineering with Computers, 18: 148–159.

[178] Persson, B. N. J.; Brener, E. A. [2005]: *Crack propagation in viscoelastic solids.* Physical Review E, 71: 036123.

[179] Persson, B. N. J.; Albohr, O.; Heinrich, G.; Ueba, H. [2005]: *Crack propagation in rubber-like materials.* Journal of Physics: Condensed Matter, 17(44): R1071.

[180] Pham, K.; Amor, H.; Marigo, J.; Maurini, C. [2011]: *Gradient damage models and their use to approximate brittle fracture.* International Journal of Damage Mechanics, 20(4): 618–652.

[181] Phan-Thien, N. [1978]: *A nonlinear network viscoelastic model.* Journal of Rheology, 22: 259–283.

[182] Rabinowitz, S.; Ward, I. M.; Parry, J. S. C. [1970]: *The effect of hydrostatic pressure on the shear yield behaviour of polymers.* Journal of Materials Science, 5: 29–39.

[183] Raha, S.; Bowden, P. B. [1972]: *Birefringence of plastically deformed poly(methyl methacrylate).* Polymer, 13: 174–183.

[184] Rahul-Kumar, P.; Jagota, A.; Bennison, S. J.; Saigal, S.; Muralidhar, S. [1999]: *Polymer interfacial fracture simulations using cohesive elements.* Acta Metallurgica, 47: 4161–4169.

[185] Rahul-Kumar, P.; Jagota, A.; Bennison, S.; Saigal, S. [2000]: *Cohesive element modeling of viscoelastic fracture: Application to peel testing of polymers.* International Journal of Solids and Structures, 37: 1873–1897.

[186] Reese, S. [2003]: *On a consistent hourglass stabilization technique to treat large inelastic deformations and thermo mechanical coupling in plane strain problems.* International Journal for Numerical Methods in Engineering, 57: 1095–1127.

[187] Reese, S.; Govindjee, S. [1998]: *Theoretical and numerical aspects in the thermo-viscoelastic material behaviour of rubber-like polymers.* Mechanics of Time-Dependent Materials, 1: 357–396.

[188] Rehage, G.; Goldbach, G. [1967]: *Zur Spannungsrißbildung von Hochpolymeren.* Die Angewandte Makromolekulare Chemie, 1(1): 125–149.

[189] Richeton, J.; Ahzi, S.; Vecchio, K. S.; Jiang, F. C.; Makradi, A. [2007]: *Modeling and validation of the large deformation inelastic response of amorphous polymers over a wide range of temperatures and strain rates.* International Journal of Solids and Structures, 44: 7938–7954.

[190] Richteton, J.; Ahzi, S.; Daridon, L. [2007]: *Thermodynamic investigation of yield-stress models for amorphous polymers.* Philosophical Magazine, 87: 3629–3643.

[191] Rivlin, R.; Thomas, A. [1953]: *Rupture of rubber. I. Characteristic energy for tearing.* Journal of Polymer Science, X(3): 291–318.

[192] Rouse, P. E. [1953]: *A theory of the linear viscoelastic properties of dilute solutions of colling polymers.* The Journal of Chemical Physics, 21: 1272–1280.

[193] Scott, K. W.; Stein, R. S. [1953]: *A molecular theory of stress relaxation in*

polymeric media. The Journal of Chemical Physics, 21: 1281–1286.

[194] Seelig, T.; van der Giessen, E. [2002]: *Localized plastic deformation in ternary polymer blends*. International Journal of Solids and Structures, 39: 3505–3522.

[195] Seelig, T.; Van der Giessen, E. [2007]: *Effects of microstructure on crack tip fields and fracture toughness in pc/abs polymer blends*. International Journal of Fracture, 145: 205–222.

[196] Seth, B. R. [1964]: *Generalized strain measure with application to physical problems*. In Reiner, M., A. D. (Editor), *Second-Order Effects in Elasticity, Plasticity and Fluid Dynamics*, pp. 162–172. Pergamon Press, Oxford.

[197] Sicsic, P.; Marigo, J. J.; Maurini, C. [2014]: *Initiation of a periodic array of cracks in the thermal shock problem: A gradient damage modeling*. Journal of the Mechanics and Physics of Solids, pp. 256–284.

[198] Sidoroff, F. [1974]: *Un modèle viscoélastique non linéaire avec configuration intermédiaire*. Journal de Mécanique, 13: 679–713.

[199] Simo, J.; Taylor, R.; Pister, K. [1985]: *Variational and projection methods for the volume constraint in finite deformation elasto-plasticity*. Computer methods in applied mechanics and engineering, 51: 177–208.

[200] Simó, J. C. [1987]: *On a fully three-dimensional finite-strain viscoelastic damage model: Formulation and computational aspects*. Computer Methods in Applied Mechanics and Engineering, 60: 153–173.

[201] Sternstein, S.; Myers, F. [1973]: *Yielding of glassy polymers in the second quadrant of principal stress space*. Journal of Macromolecular Science, Part B, 8(3): 539–571.

[202] Sternstein, S.; Ongchin, L. [1969]: *Yield criteria for plastic deformation of glassy high polymers in general stress fields*. Polymer preprints, 10: 1117–1124.

[203] Strobl, G. R. [1997]: *The Physics of Polymers. Concepts for Understanding Their Structures and Behavior*. Springer-Verlag, 2nd Edition.

[204] Tanaka, F.; Edwards, S. F. [1992]: *Viscoelastic properties of physically crosslinked networks Part 3. Time-dependent phenomena*. Journal of Non-Newtonian Fluid Mechanics, 43: 289–309.

[205] Tanaka, F.; Edwards, S. F. [1992]: *Viscoelastic properties of physically crosslinked networks. transient network theory*. Macromolecules, 25: 1516–1523.

[206] Tanner, R. I. [1985]: *Engineering Rheology*. Oxford University Press, revised Edition.

[207] Tanner, R. I. [1988]: *From a to (bk)z in constitutive relations*. Journal of Rheology, 32: 673–702.

[208] Thomas, A. [1955]: *Rupture of rubber. II. The strain concentration at an incision*. Journal of Polymer Science, 18: 177–188.

[209] Thomas, A. [1994]: *The development of fracture mechanics for elastomers*. Rubber chemistry and technology, 67: 50–60.

[210] Thomas, A. G. [1960]: *Rupture of rubber. VI. Further experiments on the tear criterion*. Journal of Applied Polymer Science, 3(8): 168–174.

[211] Tijssens, M.; van der Giessen, E.; Sluys, L. [2000]: *Modeling of crazing using a cohesive surface methodology*. Mechanics of Materials, 32: 19–35.

[212] Tijssens, M.; van der Giessen, E.; Sluys, L. [2000]: *Simulation of mode I crack growth in polymers by crazing*. International Journal of Solids and Structures, 37: 7307–7327.

[213] Tomita, Y.; Tanaka, S. [1995]: *Prediction of deformation behavior of glassy polymers based on molecular chain network model.* International Journal of Solids and Structures, 32: 3423–3434.

[214] Treloar, L. R. G. [1944]: *Stress-strain data for vulcanised rubber under various types of deformation.* Transactions of the Faraday Society, 40: 59–70.

[215] Treloar, L. R. G. [1954]: *The photoelastic properties of short-chain molecular networks.* Transactions of the Faraday Society, 50: 881–896.

[216] Treloar, L. R. G. [1975]: *The Physics of Rubber Elasticity.* Clarendon Press, 3rd Edition.

[217] Treloar, L. R. G.; Riding, G. [1979]: *A non-Gaussian theory of rubber in biaxial strain. I. Mechanical properties.* Proceedings of the Royal Society London A, 369: 261–280.

[218] Truesdell, C.; Noll, W. [1965]: *Handbuch der Physik Bd. III/3*, chapter The nonlinear field theories of mechanics. Springer, Berlin.

[219] Tvergaard, V.; Needleman, A. [1984]: *Analysis of the cup-cone fracture in a round tensile bar.* Acta Metall, 32: 157–169.

[220] University of Cambridge. Micrograph Library.

[221] Verhoosel, C. V.; Borst, R. de [2013]: *A phase-field model for cohesive fracture.* International Journal for Numerical Methods in Engineering, 96: 43–62.

[222] Wang, M. C.; Guth, E. [1952]: *Statistical theory of networks of non-Gaussian flexible chains.* The Journal of Chemical Physics, 20: 1144–1157.

[223] Wientjes, R. H. W.; Jongschaap, R. J. J.; Duits, M. H. G.; Mellema, J. [1999]: *A new transient network model for associative polymer networks.* Journal of Rheology, 43: 375–391.

[224] Williams, M.; Landel, R.; Ferry, J. [1955]: *The temperautre dependence of relaxation mechanisms in amorphous polymers and other glass forming liquids.* Journal of the American Chemical Society, 77: 3701–3707.

[225] Wriggers, P. [2008]: *Nonlinear Finite Element Methods.* Springer-Verlag.

[226] Wu, P. D.; van der Giessen, E. [1993]: *On improved network models for rubber elasticity and their applications to orientation hardening in glassy polymers.* Journal of the Mechanics and Physics of Solids, 41: 427–456.

[227] Wu, P. D.; van der Giessen, E. [1994]: *Analysis of shear band propagation in amorphous glassy polymers.* International Journal of Solids and Structures, 31: 1493–1517.

[228] Wu, P. D.; van der Giessen, E. [1995]: *On neck propagation in amorphous glassy polymers under plane strain tension.* International Journal of Plasticity, 11: 211–235.

[229] Xu, X. P.; Needleman, A. [1994]: *Numerical simulations of fast crack growth in brittle solids.* Journal of the Mechanics and Physics of Solids, 42: 1397–1434.

[230] Yamamoto, M. [1956]: *The visco-elastic propoerties of network structure I. General formalism.* Journal of the Physical Society of Japan, 11: 413–421.

[231] Yang, A.; Kramer, E.; Kuo, C.; Phoenix, S. [1986]: *Craze fibril stability and breakdown in polystyrene.* Macromolecules, 19: 2010–2019.

[232] Zimm, B. H. [1956]: *Dynamics of polymer molecules in dilute solution: Viscoelasticity, flow birefringence and dielectric loss.* The Journal of Chemical Physics, 24: 269–278.

In dieser Schriftenreihe bisher erschienene Berichte:

I-1 (1996) *Theoretische und algorithmische Konzepte zur phänomenologischen Beschreibung anisotropen Materialverhaltens*, J. Schröder, Dissertation, 1996.

I-2 (1996) *Zur Theorie und Numerik finiter elastoplastischer Deformationen von Schalentragwerken*, B. Seifert, Dissertation, 1996.

I-3 (1996) *Zur Modellierung des künstlichen Infrarot-Dichroismus in Poymerfolien bei großen Verformungen*, J. Buhler, Dissertation, 1996.

I-4 (1998) *Verfahren zur Ermittlung der Erdbebenlasten mit Berücksichtigung des stochastischen Charakters des Bebens*, S. Zhang, Dissertation, 1998.

I-5 (1998) *Zur Beschreibung finiter Deformationen von Polymeren: Experimente, Modellbildung, Parameteridentikation und Finite-Elemente- Formulierung*, J. Keck, Dissertation, 1998.

I-6 (1999) *Berechnungsverfahren instationär erregter Systeme im Frequenzbereich*, A. Jaworek, Dissertation, 1999.

I-7 (2000) *Homogenisierungsmethoden der nichtlinearen Kontinuumsmechanik unter Beachtung von Stabilitätsproblemen*, J. Schröder, Habilitation, 2000.

I-8 (2002) *Theorie und Numerik von Materialinstäbilitaten elastoplastischer Festkörper auf der Grundlage inkrementeller Variationsformulierungen*, M. Lambrecht, Dissertation, 2002.

I-9 (2002) *Mikromechanisch motivierte Modelle zur Beschreibung finiter Deformationen gummiartiger Polymere: physikalische Modellbildung und numerische Simulation*, F. Lulei, Dissertation, 2002.

I-10 (2003) *Adaptive Finite-Elemente-Berechnungen der nichtlinearen Festkörpermechanik bei kleinen und großen Verzerrungen*, A. Koch, Dissertation, 2003.

I-11 (2003) *Theorie und Numerik der Parameteridentikation von Materialmodellen der finiten Elastizität und Inelastizität auf der Grundlage optischer Feldmeßmethoden*, G. Scheday, Dissertation, 2003.

I-12 (2004) *Approaches to the Description of Anisotropic Material Behaviour at Finite Elastic and Plastic Deformations, Theory and Numerics*, N. Apel, Dissertation, 2004.

I-13 (2004) *Temperaturabhängige Beschreibung visko-elasto-plastischer Deformationen kurzglasfaserverstärkter Thermoplaste: Modellbildung, Numerik und Experimente*, S. Rieger, Dissertation, 2004.

I-14 (2005) *Zur Parameteridentikation komplexer Materialmodelle auf der Basis realer und virtueller Testdaten*, A. Rieger, Dissertation, 2005.

I-15 (2005) *Viskoelastisches Verhalten von Elastomeren bei finiten Verzerrungen: Experimente, Modellierung und Simulationen*, H. Zecha, Dissertation, 2005.

I-16 (2005) *Mehrskalenmodelle in der Festkörpermechanik und Kopplung von Mehrgittermethoden mit Homogenisierungsverfahren*, C. G. Bayreuther, Dissertation, 2005.

I-17 (2005) *Static and Dynamic Homogenization Analyses of Discrete Granular and Atomistic Structures on Different Time and Length Scales*, J. Dettmar, Dissertation, 2005.

I-18 (2006) *Incompatibility and Instability Based Size Effects in Crystals and Composites at Finite Elastoplastic Strains*, M. Becker, Dissertation, 2006.

I-19 (2007) *Aspects of Energy Minimization in Solid Mechanics: Evolution of Inelastic Microstructures and Crack Propagation*, E. Gürses, Dissertation, 2007.

I-20 (2007) *Micro-Macro Approaches to Rubbery and Glassy Polymers: Predictive Micromechanically-Based Models and Simulations*, S. Göktepe, Dissertation, 2007.

I-21 (2008) *Material Forces in Finite Inelasticity and Structural Dynamics: Topology Optimization, Mesh Refinement and Fracture*, D. Zimmermann, Dissertation, 2008.

I-22 (2010) *Thermoviscoplasticity of Glassy Polymers: Experimental Characterization, Parameter Identification and Model Validation*, J. Méndez Diez, Dissertation, 2010.

I-23 (2010) *On the Formulation and Numerical Implementation of Dissipative Electro-Mechanics at Large Strains*, D. Rosato, Dissertation, 2010.

I-24 (2010) *A variational framework for gradient-extended dissipative continua: Application to damage mechanics, fracture, and plasticity*, F. Welschinger, Dissertation, 2010.

I-25 (2013) *Variational Multifield Modeling of the Formation and Evolution of Laminate Microstructure*, F. Hildebrand, Dissertation, 2013.

I-26 (2013) *On the Computational Modeling of Micromechanical Phenomena in Solid Materials*, C. Linder, Habilitation, 2013.

I-27 (2013) *Hybrid Micro-Macro Modeling of Texture Evolution in Polycrystal Plasticity Based on Microstructural Reorientation Continua*, I. Zimmermann, Dissertation, 2013.

I-28 (2014) *Finite Element based Electronic Structure Calculations*, V. Schauer, Dissertation, 2014.

I-29 (2014) *A Thermodynamically Consistent Phase Field Approach to Fracture*, M. Hofacker, Dissertation, 2014.

I-30 (2014) *Multi-level descriptions of failure phenomena with the strong discontinuity approach*, A. Raina, Dissertation, 2014.

I-31 (2015) *Phase Field Modeling of Fracture in Rubbery and Glassy Polymers at Finite Thermo-Viscoelastic Deformations*, L. Schänzel, Dissertation, 2015.